January 2019

Fracture Detection And Prediction In Unconventional Reservoirs For Finding Sweet Spot

Sofiane Djezzar

FRACTURE DETECTION AND PREDICTION IN UNCONVENTIONAL RESERVOIRS FOR FINDING SWEET SPOT

by

Sofiane Djezzar

Engineer in Structural Geology, University of Sciences and Technology, Algiers, 1993

Magister in Structural Geology, University of Sciences and Technology, Algiers, 2012

A Dissertation

Submitted to the Graduate Faculty of the

University of North Dakota

In fulfillment of the requirements
For the degree of

Doctor of Philosophy

Grand Forks, North Dakota

August
2019

This dissertation, submitted by Sofiane Djezzar in partial fulfillment of the requirements for the Degree of Doctor of Philosophy from the University of North Dakota, has been read by the Faculty Advisory Committee under whom the work has been done and is hereby approved.

Dr. Vamegh Rasouli

Dr. Mehdi Ostadhassan

Dr. Minou Rabiei

Dr. Hui Pu

Dr. Naima Kaabouch

This dissertation is being submitted by the appointed advisory committee as having met all of the requirements of the School of Graduate Studies at the University of North Dakota and is hereby approved.

Chris Nelson

Interim Dean of the School of Graduate Studies

7/8/19

Date

PERMISSION

Title: Fracture Detection and Prediction in Unconventional Reservoirs for Finding Sweet Spot.

Department: Petroleum Engineering

Degree: Doctor of Philosophy

In presenting this document in partial fulfillment of the requirements for a graduate degree from the University of North Dakota, I agree that the library of this University shall make it freely available for inspection. I further agree that permission for extensive copying for scholarly purposes may be granted by the professor who supervised my dissertation work or, in her/his absence, by the Chairperson of the department or the Dean of the Graduate School. It is understood that any copying or publication or other use of this dissertation or part thereof for financial gain shall not be allowed without my written permission. It is also understood that due recognition shall be given to me and to the University of North Dakota in any scholarly use which may be made of any material in my dissertation.

Name: Sofiane Djezzar

Date: 7/15/2019

Table of Contents

List of Figures

List of Tables

ACKNOWLEDGEMENTS

I am so thankful and grateful to the University of North Dakota and the College of Engineering and Mines, which gave me the opportunity, the financial support, and material means to do this thesis.

I am greatly indebted to Sonatrach Exploration, Algeria, for the permission to use its data and for the strong oil and gas industry knowledge that I acquired.

I would like to express my gratitude to my supervisor and Chair of the Petroleum Engineering Department, Dr Vamegh Rasouli, who offered me the chance to pursue this PhD degree at the University of North Dakota. Also, for his precious instructions and valuable comments.

I express my gratefulness to the director of graduate student at the Petroleum Engineering Department, Dr Mehdi Ostadhassan, who accepted to be member of my thesis committee and for the chance that he gave me to teach the PTRE401 course.

I thank my co-Advisor, Dr Minou Rabiei for her valuable instructions and valued commentaries.

I am deeply thankful to Dr Naima Kaabouch and Dr Hui Pu, who honoured me by accepting to be members of my committee.

I would like to give my great thanks to my wife Aldjia for all what she has done for me.

I would like to thank my American friends for their help and encouragements; I name Beth, Doris, Chad, Kathy, John, Jane, deceased Leroy, Lori, Malcom, and all my friends at Christus Rex.

I thank my Algerian friends who encouraged me to do this thesis. I name Badreddine, Nacer, Azzedine, Mustapha, Maamar, Chems-edinne, Nabil, and Reda.

Finally, I want to thank my mother for her precious prayers and good thoughts. Also, my brothers, my sisters, and my brothers in law for all their support and patience during my studies in the US.

In the memory of my Dad, who was my mentor and my friend.

ABSTRACT

The Cambro-Ordovician in the Algerian Saharan platform is characterized by tight sandstone formations with very low petrophysical characteristics where the natural fractures play an important role in their productivity. The Mouydir basin is the less explored basin in Algeria where no 3D seismic data exist and only low quality of seismic 2D surveys are available. In addition, few wells were drilled in the fifties exist in this basin. They were drilled based on the field observations, gravity data, geological maps, and seismic refraction data. Unfortunately, these wells were all negative. The Mouydir basin is limited in the west by the Ahnet and Timimoun basins, which are considered as the main gas provinces in the western part of the Saharan plate-form. In addition, The Mouydir basin is limited in the north and the east by Oued Mya and Illizi basins, which are considered as prospective oil provinces. These basins have the same petroleum system as the Mouydir basin where the Silurian hot shale is the principal source rock and Ordovician the main reservoirs, which produce tremendous quantity of oil and gas from naturally fractured reservoirs.

To overcome this lack of data, a specific and an innovative workflow is proposed to analyze and characterize the natural fractures in the Cambro-Ordovician reservoir by using an analog that appears in the southern edge of the Mouydir basin in order to bring a new insight and guide the future exploration wells in this basin. This workflow integrates multiple data that help to build a deterministic fracture model. This model highlights the major and minor fractures that aid to understand the basin's geological evolution as well as the impact of the basement's fractures on the basin structuration and on the sedimentary cover. The 3D fracture model is used to understand the fractures' distribution, fractures' connectivity, and fractures' kinematics. The outcomes could be used to predict fractures' extension and occurrence in the subsurface and could be used to explain the negative results of the drilled wells. Different scales of observation have enabled to highlight a fractal dimension of natural fracturing in these unconventional reservoirs.

The fracture characterization using core and borehole imagery data including the fracture attributes, breakouts, and induced fractures help to determine the in-situ stress, fracture morphology, and fracture typology. The 3D seismic attributes and the interpretive criteria of seismic 2D support to determine the intensity, density and fracture kinematics of natural fractures. These approaches allow up understanding the geological processes that affect the area of study, which are responsible for the generation of the complex fracture patterns. These approaches will aid to predict the occurrence of these fracture patterns in the area where no data is available.

The drilling of a horizontal pilot well on the positive structures already discovered, perpendicular to the Maximum Horizontal stress, having as target the Cambro-Ordovician reservoir in the depocenter of the Mouydir basin, could be a decelerator of a new exploration era in this unexplored basin.

Chapter I: General Introduction

I-1-Introduction

The Saharan platform is an epicontinental margin that includes a series of basins separated by positive North-South oriented structural trends, such as the Amguid–El Biod and the Idjerane spur that separate the Mouydir basin from the Illizi and the Ahnet basins respectively. These sub-meridian trends are controlled by basement accidents inherited from the Pan-African orogeny (Fig.1).

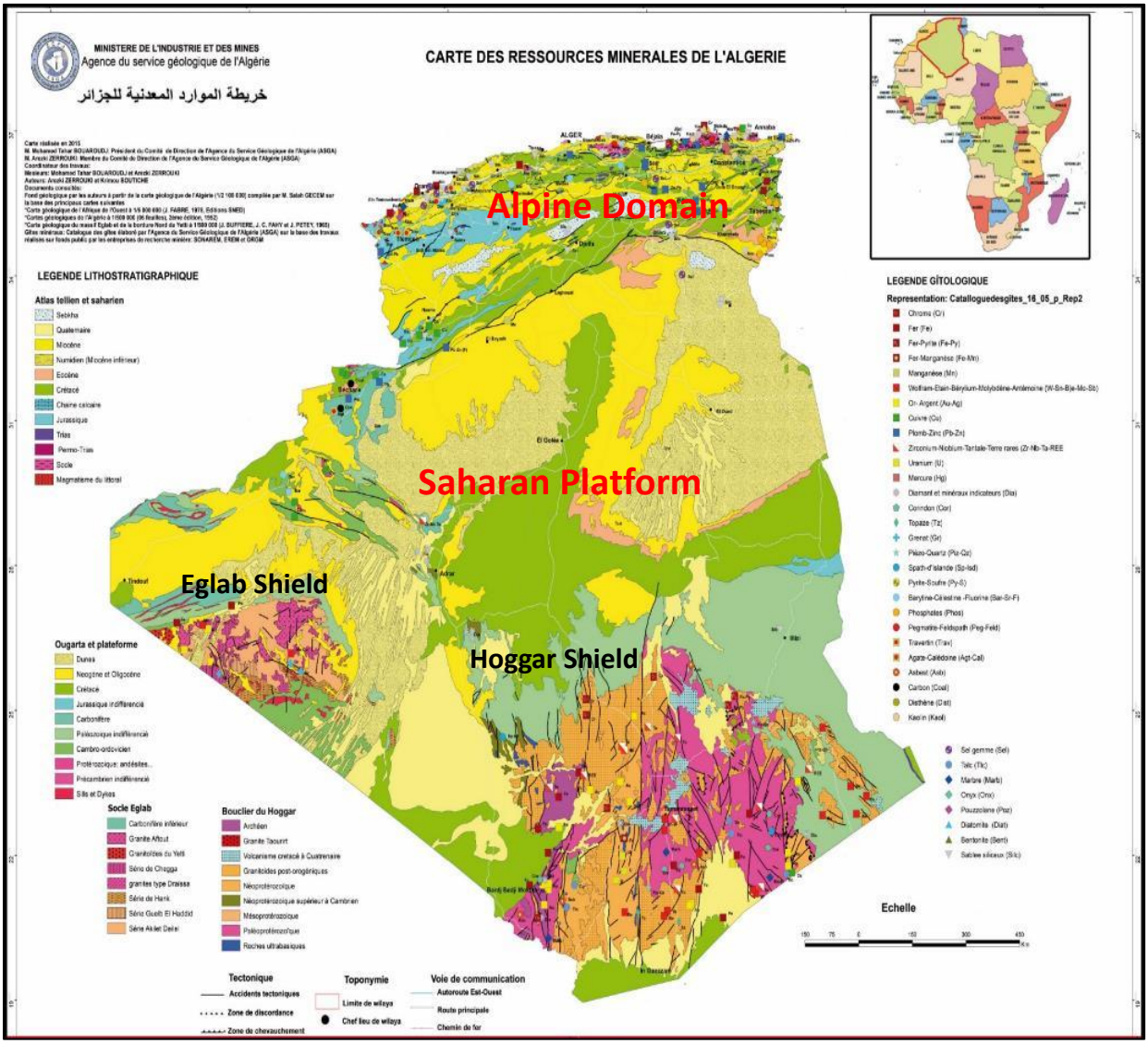

Figure 1: Main geological domains in Algeria

The current structural image of this basin is the result of the succession of several tectonic episodes during the Paleozoic, Mesozoic, and Cenozoic eras. The Mouydir basin is an intracratonic platform basin with a sedimentary cover up to 3500 meters. The series thin towards the Southern part of the basin where they end with outcrops. The pre-Mesozoic sketch shows the Upper Devonian and Carboniferous are eroded over a large part of the basin by Hercynian erosion. On the other hand, the Cambro-Ordovician to Lower Devonian series are preserved in the basin.

The Mesozoic subsidence decreases from the north where it reaches more than 2000 meters to the south where it records depths of a few hundred meters. The exploration activity in the Mouydir basin is resumed by the acquisition of 5710 km of 2D seismic and the drilling of 14 exploration wells (Issad et al.2011). The different wells in various reservoirs of the drilled wells revealed only water with a variable salinity and some gas indices from the Ordovician reservoirs and from the Lower Devonian (Issad et al. 2011).

The Petroleum system in the Mouydir basin consists on the Silurian source rock, the Cambro-Ordovician reservoirs, the Ordovician, Silurian and Upper Devonian clays, which form the seal rocks. The age of expulsion of hydrocarbons is Paleozoic. Knowing that the source rock is in dry gas phase, the basin is perspective in gas. Although a large part of the expelled hydrocarbons was dismigrated before the formation of the traps (Hercynian), the presence of gas showings in certain drilled structures indicates a trapping at the same time as the Hercynian uplift and erosion (case of the basins Ahnet-Timimoun).

The Cambro-Ordovician in the Algerian Saharan platform is characterized by tight sandstone formations with very low petrophysical characteristics whither the natural fractures play an important role in their productivity. The Mouydir basin is the less explored basin in Algeria where no 3D seismic data is available and only few wells and less quality seismic 2D survey exist to characterize these reservoirs. In addition, it should be noted that these wells were implanted on structures defined by satellite images, by field observation, gravity data, geological maps, seismic refraction data, and low quality and density of 2D seismic profiles. The Cambrian-Ordovician reservoir and the Lower Devonian reservoirs are generally compact, so their productivity depends largely on natural fractures. Hence the need to study the distribution of fracture networks. The Mouydir basin is close to Ahnet and Timimoun basins, which are considered as the main important gas provinces in the western part of the Saharan plate-form. These basins have the same petroleum system as the Mouydir basin where the Ordovician reservoir produces tremendous quantity of gas

in naturally fractured reservoir. However, in the Mouydir basin, the few wells drilled were all negative.

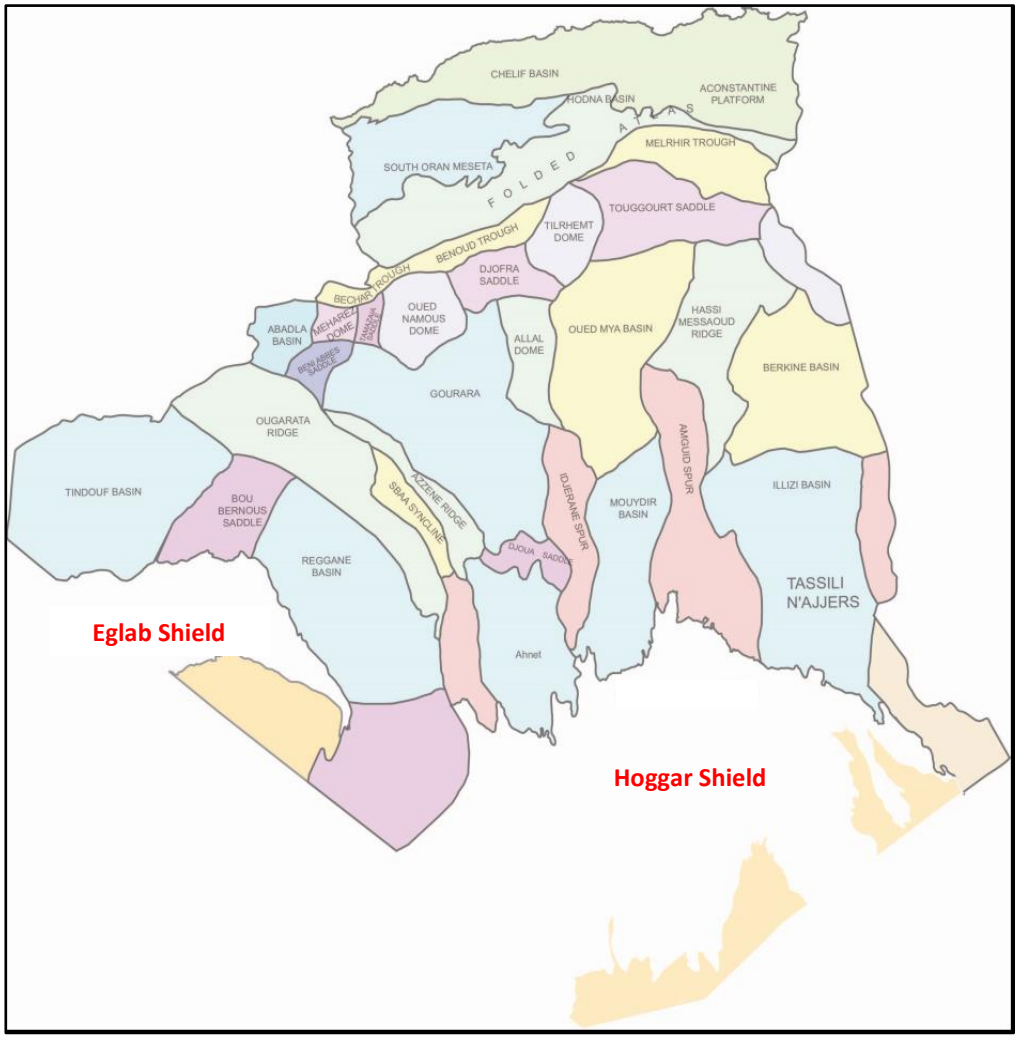

Figure 2: Algerian basins

I-2-Geological background

The area of study is located in the north part of Hoggar shield. It is situated between latitudes 24º30'N and 28º00'N, longitudes 3º00'E and 6º00'E. It is limited on the west by the Idjerane spur and Ahnet basin, on the east by the Amguid spur and Illizi basin and on the South by the Hoggar shield uplift (Fig.3). The area of study covers a large area where the Paleozoic formations appear in outcrop at Ain-Tadjoubar, Arak, Iftessene, and Khanget-El-Hadid regions.

It is delimited by large sub-meridian faults that compartmentalized the Mouydir basin during the different orogeny.

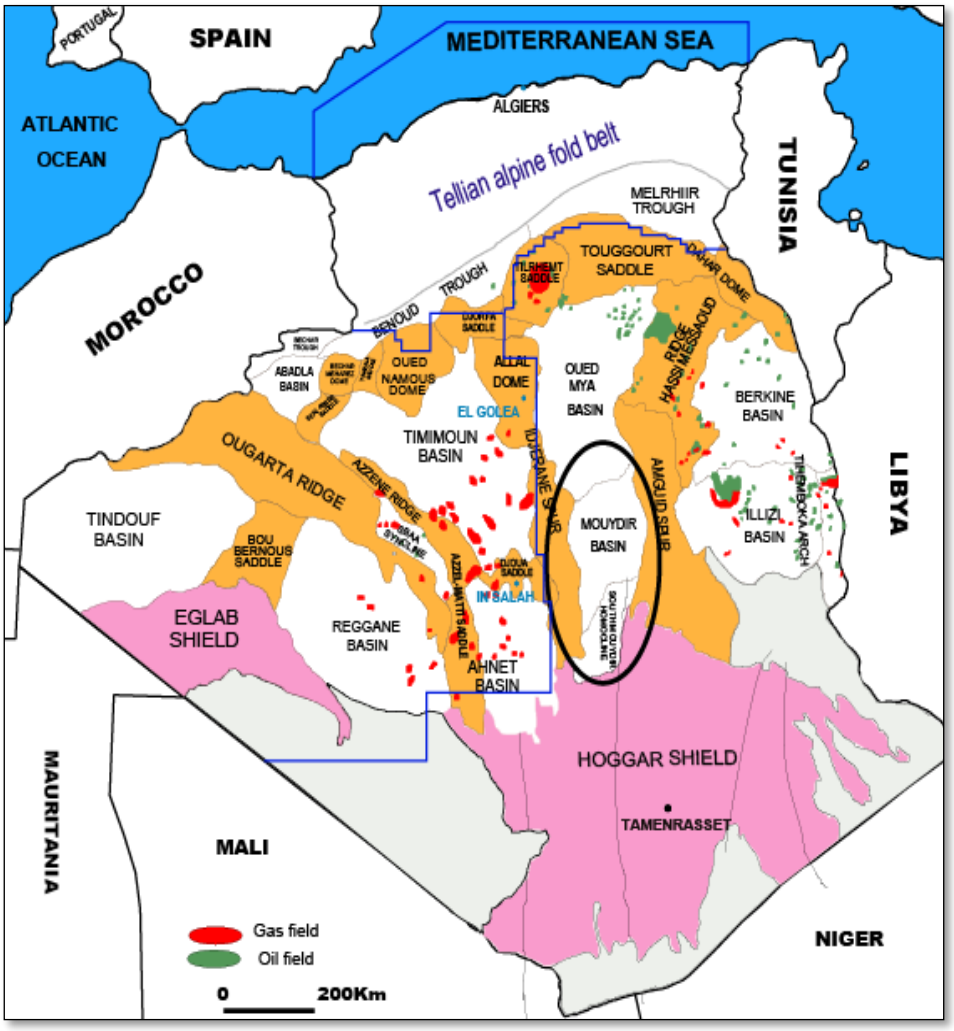

Figure-3: Location of the area of study.

The Cambro-Ordovician is well known in the Algerian basins where the Ordovician reservoirs are considered as the second most important oil and gas bearing formations producing naturally due to the existence of natural fractures (WEC, 2005). Three main formations, Ajjers, In-Tahouite, and Tamadjert compose the Cambro-Ordovician. These layers appear at subsurface in all the Saharan Platform basins and expose at outcrops in several areas in the north part of the Hoggar shield (Fig.4).

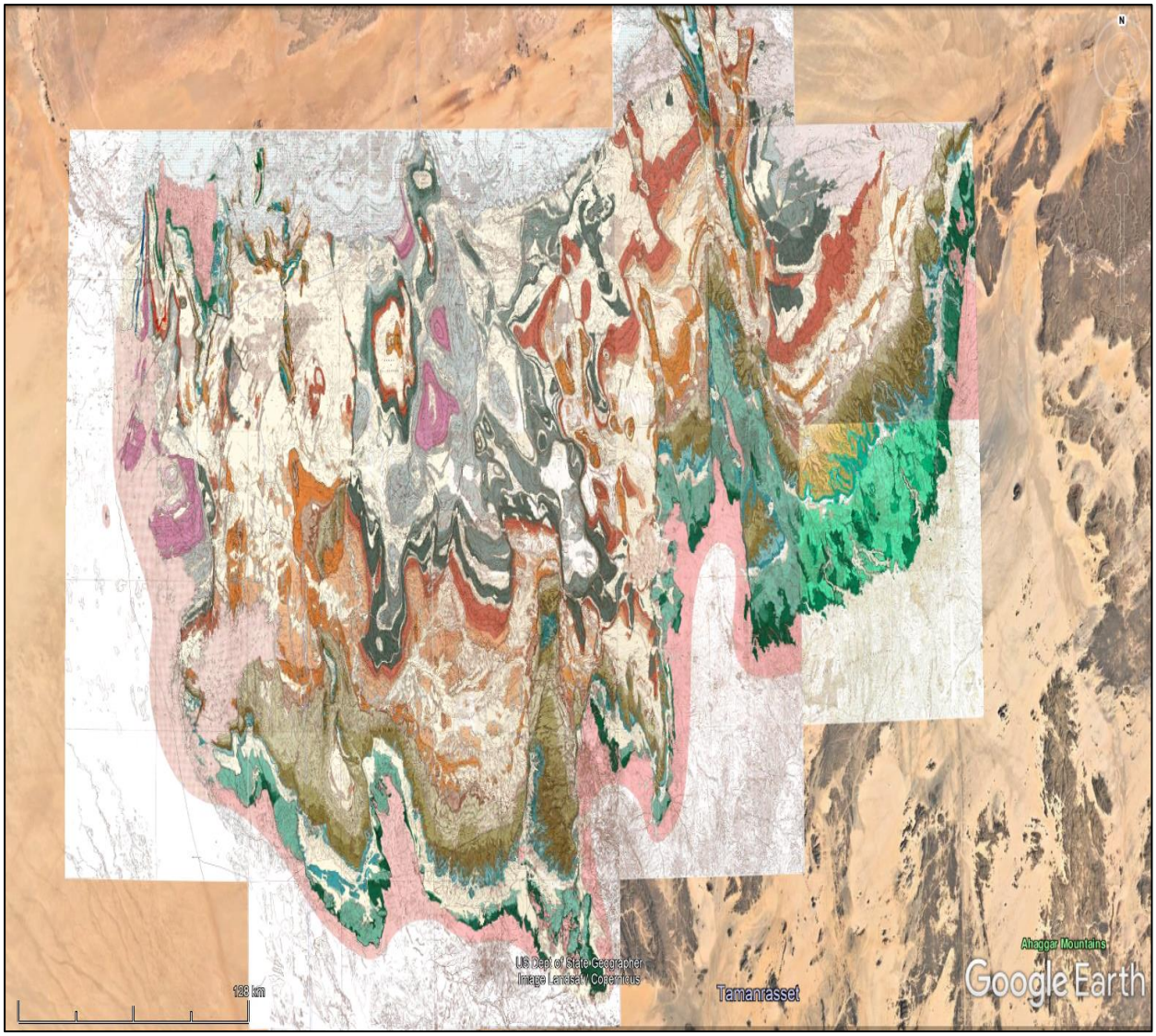

Figure 4: Paleozoic series in the Ahnet and Mouydir southern edges

The Ordovician formations have an age span varying from the Tremadocian to Ashgill. However, the recent palynological investigation indicates that most of the Ajjers Formation belongs to the Middle Cambrian age (Vecoli et al., 2008).

The Ordovician reservoirs composed of El Atchane sandstones (Tremadocian); Hamra Quartzites (Arenigian); Ouargla sandstone (Llanvirnian); Oued Saret sandstone (Lower Caradocian); Ramade or M'kratta sandstone (Upper Caradocian-Ashgillian). (WEC, 2005).

The deposition of the Ajjers formation is followed by the Ordovician transgression resulted due to the accumulation of the In-Tahouite formation (Bennacef et al., 1971).

During the latest Ordovician, due to polycyclic glaciations, the shallow-marine/fluvial system underwent a change into the glacio-marine system (Craig et al. 2008). Its record consists of the diamictites, glacio-fluvial sandstones, with a wide spectrum of sedimentary structures described as the Tamadjert Formation (Beuf et al., 1971). The Cambro-Ordovician falls under two types of classification.

The first classification is mainly used to describe the Cambro-Ordovician in subsurface and divides it into six units; Unit I, including El Moungar conglomerate, Unit II, including Hassi Leila series, Unit III-1, age Tremadocian, including Meribel sandstone, El-Gassi shale, and El Atchane sandstone. Unit III-2, age Lower to Middle Arenig, is represented by Hamra Quartzites. Unit III-3, age Llanvirn-Llandellian-Caradoc, is composed by Ouargla sandstone, Azzel shale, and the Oued-Saret sandstone. Unit IV, age Ashgill, is represented by a silico-clastic complex corresponding to the Micro-conglomeratic shale and the M'Kratta sandstone.

On the other hand, the second classification is used to describe the Cambro-Ordovician at outcrops. It splits the Cambro-Ordovician in three different geological formations including Ajjers, In-Tahouite, and Tamadjert. Ajjers formation is composed by El-Moungar conglomerate, Tin-Taradjelli sandstone, Vire-du-Mouflon sandstone, and Hamra-Quartzites.

They correspond to the units I & II (Cambrian), III-1, and III-2, respectively. The second formation is In-Tahouite, which corresponds to unit III-3. The third formation is Tamadjert, which is equivalent to unit IV (Fig.5 and Fig.6).

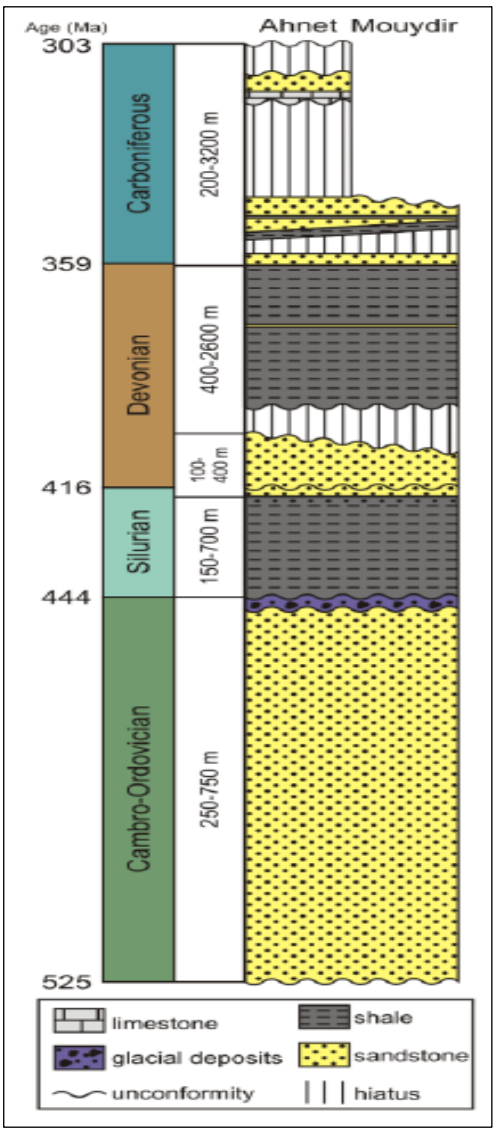

Figure-5: Schematic lithostratigraphic column of the Ahnet and Mouydir basins (compiled after Follot, 1952; Beuf &. 1971; Wenddt & al. 2006, 2009 and Vecoli &al., 2008 in Zieliński, 2011)

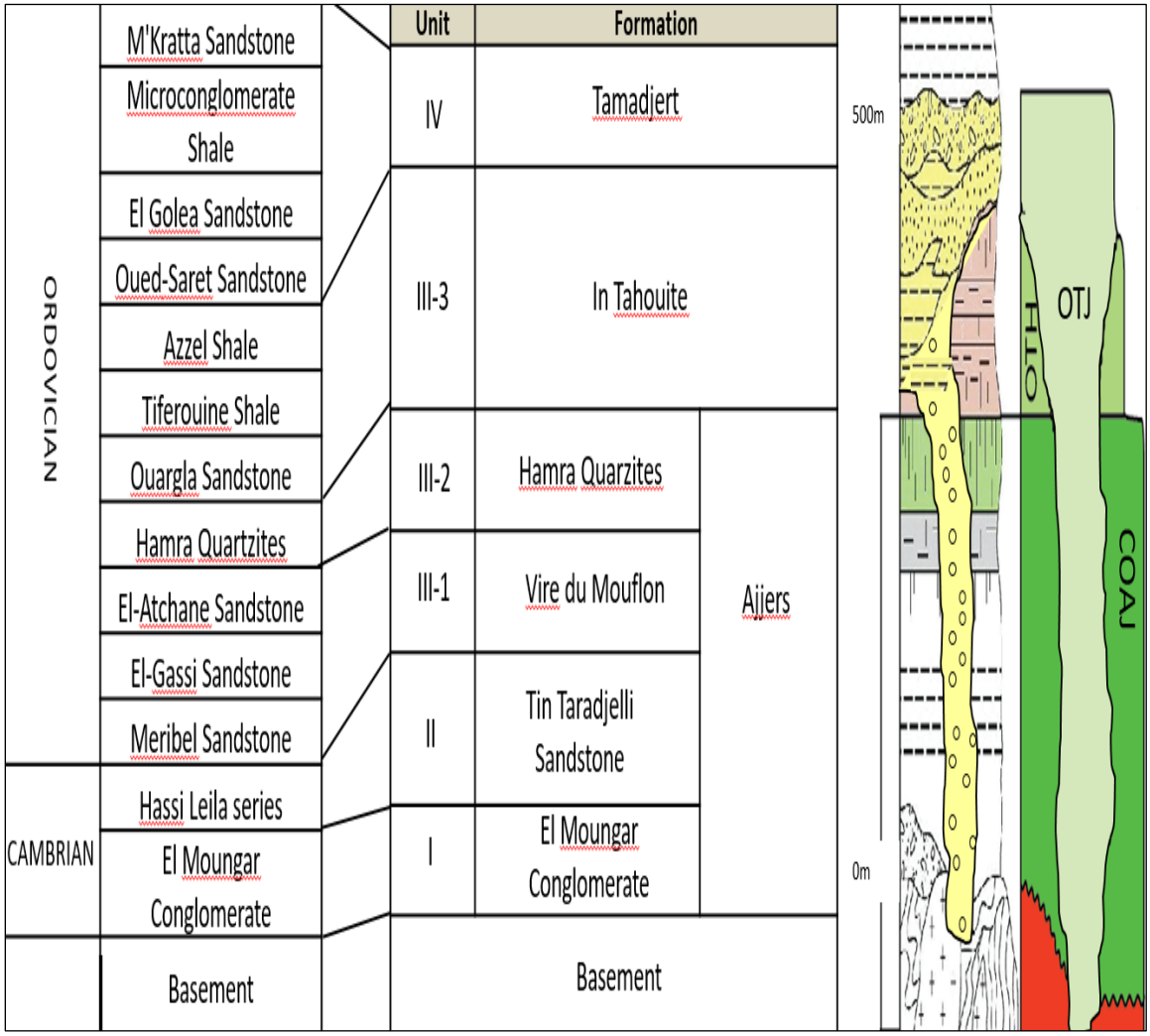

Figure-6: The Cambro-Ordovician Units in the area of the Mouydir basin (in Zegrir, 2014, modified)

The area of study is prone to several tectonic phases where some of Precambrian lineaments may have experienced strike-slip displacements during the Cambro-Ordovician (Coward & Ries, 2003). In the Late Silurian-Early Devonian regionally, extensive inversion of the basins occurred due to the Caledonian orogeny (Follot, 1952; Beuf et al., 1971; Fekirine & Abdallah, 1998). Middle Devonian tectonic movements reactivated the Precambrian faults that bordered the basin creating basin-and-ridge topography (Wendt et al., 2006). The Variscan compression leaded also to the origin of numerous, mainly N-S trending, reverse faults into Paleozoic rocks (Zieliński, 2011).

During the Mesozoic, the Hoggar Shield was uplifted and this took place before the Cretaceous time and is connected with the Alpine tectonics (Liégeois et al., 2005).

This movement resulted in a partial inversion of the sedimentary basins along the northern margin of the Hoggar Shield and eroded significant portion of the Paleozoic sedimentary cover. Between the Cretaceous and the early Cenozoic, the sedimentary basins underwent tectonic inversion caused by a collision between Europe and Africa inducing the reactivation of the Precambrian faults (Zieliński, 2011).

The El-Atchane sandstone, Hamra Quartzites, Ouargla sandstone, Oued Saret sandstone, and M'Kratta sandstone are the main reservoirs in the Cambro-Ordovician formation, deposited in a fluviatile and fluvio-glacial environment.

They are considered as secondary oil targets in the Algerian basins. The M'Kratta sandstone reservoir produced oil in some wells, and similar to the Hamra Quartzite reservoir has revealed large accumulations of oil in the Oued Mya basin, which is now considered as an oil target in the region.

The Ordovician reservoirs are compact (average porosity of 7% and permeability less than 10 mD) where their productivity depends on the existence of opened fractures (WEC, 2007).

I-3-Methodology

A specific and an innovative workflow is proposed to analyze and characterize the natural fracture in the Mouydir basin to bring a new insight in order to guide a prospective petroleum exploration in this basin. This workflow integrates two approaches where multiple outcrops and subsurface data are used to build a deterministic fault model (Fig.7).

The model can be used to study the impact of the faults and fractures on fluid migration, reserves accumulation, and basin's geological evolution, as well as assessing the impact of the basement faults on the basin and the sedimentary cover.

The 3D static structural model merges the surface and subsurface models and populates the geological data such as discontinuities and geological formations. The model presents information about the basin's paleo-evolution and the actual basin architecture. In order to determine the presence of faults at the outcrop, the seismic attributes, such as curvature are mapped onto the digital elevation model (DEM).

The application of seismic attributes integrated with the digital elevation model is an innovative approach proposed as part of the workflow to signify the presence of faults and fractures in the underburden and generation of a surface deterministic fault model.

This model represents a temporal and a spatial faults and fractures distribution model. In addition, this workflow uses temporal and spatial fracture distributions in both outcrops and subsurface to compare their density, frequency, and extension in order to generate a unique deterministic fault model.

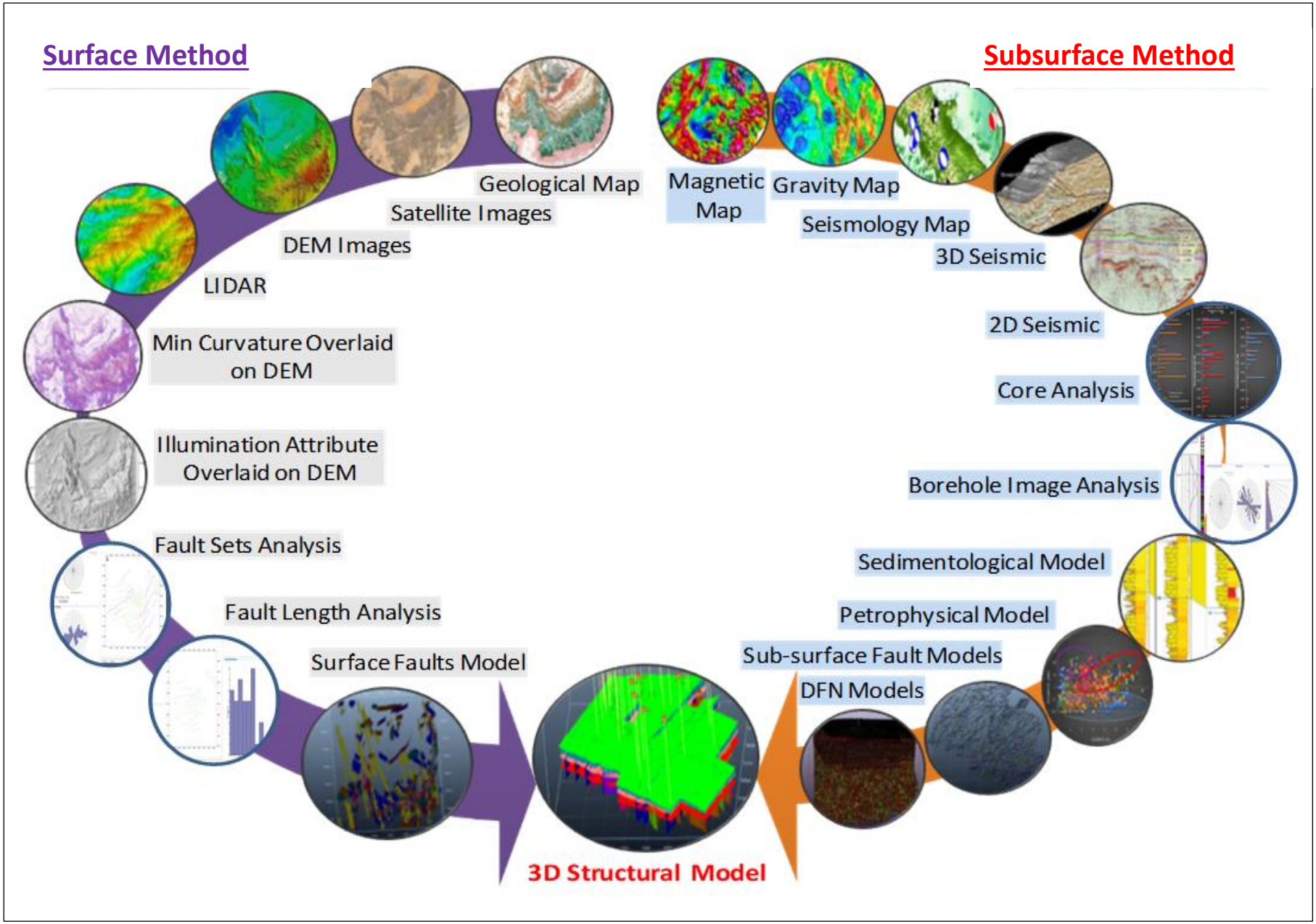

Figure 7: The proposed fracture analysis workflow

I-3.1-The first method

This method is the study of the Cambro-Ordovician analog which helps to understand the fractures distribution, fracture connectivity, fracture length, and fractures kinematics to predict their occurrence and frequency in subsurface. The Cambro-Ordovician formations are characterized by stiff tectonic style, showing a dense fault network that affected the Paleozoic series. The outcomes are the determination of fault sets, length distributions, correlation coefficients, power law coefficients, and fractal dimensions.

The fault network helps to generate a 3D deterministic fault model which illustrates the fractures distribution in space, determine their origin, relationship, kinematics, and the impact of the basement's faults on the sedimentary cover. The analysis composed of two main steps. Firstly, the major fault map corresponding to the area of study, generated from the combination of curvature and illumination attributes, geological maps, satellite images, and digital elevation models are built.

The outcomes are the determination of fault sets, length distributions, correlation coefficients, power law coefficients, and fractal dimensions. Secondly, minor fault maps corresponding to the basement formation and different Cambro-Ordovician units are generated. The proposed methodologies help to determine the major and minor fault sets at different scales to understand the fractography and typology of fractures affecting the basement and Cambro-Ordovician units.

The different faults sets help to generate 3D deterministic fault model for each formation to illustrate the fractures distribution in space and geological age. The combination of the different fracture models helps to determine the fracture origin, their relationship, kinematics, and illustrate the impact of the basement's faults on the sedimentary cover.

The study of the Cambro-Ordovician analogue becomes necessary to analyse the natural fractures that affect this basin to guide the oil and gas exploration and the drilling of prospective wells in Mouydir basin. Geological studies provide a regional overview of the major faults in and around the target formation. However, geological maps alone cannot provide an accurate representation of the complexity of the subsurface structures.

I-3.2-The second method

This method is based on the analyses and studies of different subsurface data. The Bouguer's gravity anomaly map is constructed to determine the positive and negative anomalies corresponding to the high and low structural zones. Integration of the Bouguer anomalies signify the main lineament directions, which are associated with major basement faults and their impact on the sedimentary cover.

The petrophysical model illustrates the reservoir characteristics, their distribution and extension at the reservoir and basin scale. The storage and the flow capacity of the flow units characterize the reservoir heterogeneity and illustrate the impact of fractures on the permeability. The hydrogeological model captures the water flow regime. For example, the water salinity and potentiometric pressure distribution ranges at basin scale indicate the water seepage and its direction.

The fracture model is based on the study of the natural fractures which constitute most often-preferential drains or barriers of permeability that partially control the movement of fluids being produced. In the tight reservoir, the fracture modeling is very important.

The wells' productivity in these low permeability reservoirs is attributed to interconnected fracture networks. The borehole imagery data (UBI-OBMI-FMI) were used to determine the fracture attributes, breakout & drilling induced fractures, fractures permeability, in-situ stress, fracture morphology (open, mineral-filled, vuggy), healed / mineralized fractures, total loss of mud circulation around sub-vertical open fracture or fault, fracture aperture calculation and statistical diagrams.

The core's analysis goals are to determine the distribution and typology of fractures in Ordovician reservoir in the Mouydir basin. The cores were described based on their lithological variations, grain-size distribution, mineralogical composition, fossils, sedimentary structures, and the presence of faults and fractures. Several types of fractures and faults characterize the Ordovician formations.

The first type is related to the tectonic fractures named, which are frank fractures with presence of cement, breccia or slickensides. The second fracture is related to stylolites, they are

due to the sediments' compaction. They are vertical or oblique and always connected to a horizontal stylolites.

The core fracture analysis is focused on the tectonic fracture, which are classified in Mode I, and Mode II fractures. They appear on cores and both have an impact on the fluid flow.

The cores and borehole image analysis help to determine the fracture types (diffuse, swarms), their connectivity and length, and the relationship between the facies and faults/fractures. For the subsurface deterministic fault model, 2D seismic data from Mouydir basin were used to generate a 3D fault model and to analyze the kinematics of the faults in the edges of the two basins.

This model aids to understand the faults kinematics, chronology, and the relationship between the basement faults and the sedimentary cover at basin scale. Because of the low quality of 2D seismic profiles and the lack of recent seismic data in the Mouydir basin, a 3D seismic volume in the Ahnet basin was used to enhance the fault networks that affect the Cambro-Ordovician reservoir.

Several seismic attributes were used for the natural fracture detection, including curvature attribute, dip maps, dip azimuth attribute maps, seismic volume frequency maps, variance, edge detection, Ant Tracking algorithm. A unique 3D fault model is built merging the deterministic surface and subsurface fault models, which gives an insight about the relationship between the two faults models in term of fault continuity, fault density, fault frequency, and the fractures-faults relationship at micro and macro scales.

Chapter II: Multiscale Fracture Analysis

II-1-Introduction

The unconventional reservoirs have rapidly evolved over the last years and a significant increase in hydrocarbon discoveries where natural fractures play a significant role in the production. This has helped to enhance the understanding of the effect of fracturing on fluid flow mechanism.

During the development of the fields, the wells of the implementation strategy are determined by the spatial distribution of fractures across the field or reservoir. The geoscientists seek to intersect areas with high density of fractures and good connectivity, where the drainage of the matrix is more effective. The orientation of the wells should be in accord to the geometrical and geomechanical parameters such as the orientation of fracture planes and the maximum horizontal stress.

The study of the naturally fractured reservoirs is very challenging with the main difficulty being how to model and predict the fracture networks at different scales extending from outcrops and shallow depth to the reservoir and basin depths. Advanced 3D seismic and well data are needed to characterize and model the fractures. This process requires great effort in terms of time, data collection, and analysis. The study of the reservoir analog can be a substitute approach with more readily accessible data.

II-2-The Problematic

The Mouydir basin is the less explored basin in Algeria where no 3D seismic data exist and only low quality of seismic 2D surveys are available. The few wells drilled in this basin were all negative. The Cambrian-Ordovician reservoir are generally compact, so their productivity depends largely on natural fractures.

To overcome this lack of data, a specific and an innovative workflow is proposed to analyze and characterize the natural fractures in the Cambro-Ordovician reservoir analog that appear in the southern edge of the Mouydir basin in order to bring a new insight and guide the future petroleum exploration wells in this basin.

A deterministic fracture model highlights the major and minor fractures that aid to understand the basin's geological evolution as well as the impact of the basement's fractures on the basin structuration and on the sedimentary cover.

II-3-The Specific Workflow

In the proposed workflow, satellite images, geological maps, and digital elevation models are used as input data to recognize and enhance the fault planes (Fig.8).

Several attributes such as curvature, slopes, and illumination are applied on digital elevation model (DEM) to detect both the major faults and small-scale fractures. These are digitized and analyzed based on their orientation, length distribution, and density using FracaFlow software. The fracture analyses are based on two aspects:

The first aspect is related to the study of the major faults that affect the zone of interest. These faults are digitalized using the combination of several inputs; geological maps, satellite images, and digital elevation models.

The second aspect focuses on the fracture analyses that affect the basement and the Cambro-Ordovician units, by using the same input data at different scales to determine the same parameters and outputs.

The results are the generation of different diagrams, cross plots, and histograms related to the fault sets orientation, length attributes, length distribution, correlation coefficient, and power law coefficient. These help to understand the fractography and typology of fractures affecting the reservoir analog.

The 3D deterministic fault models established at formations scale and at area of interest are built to illustrate the fractures' distribution in time and space.

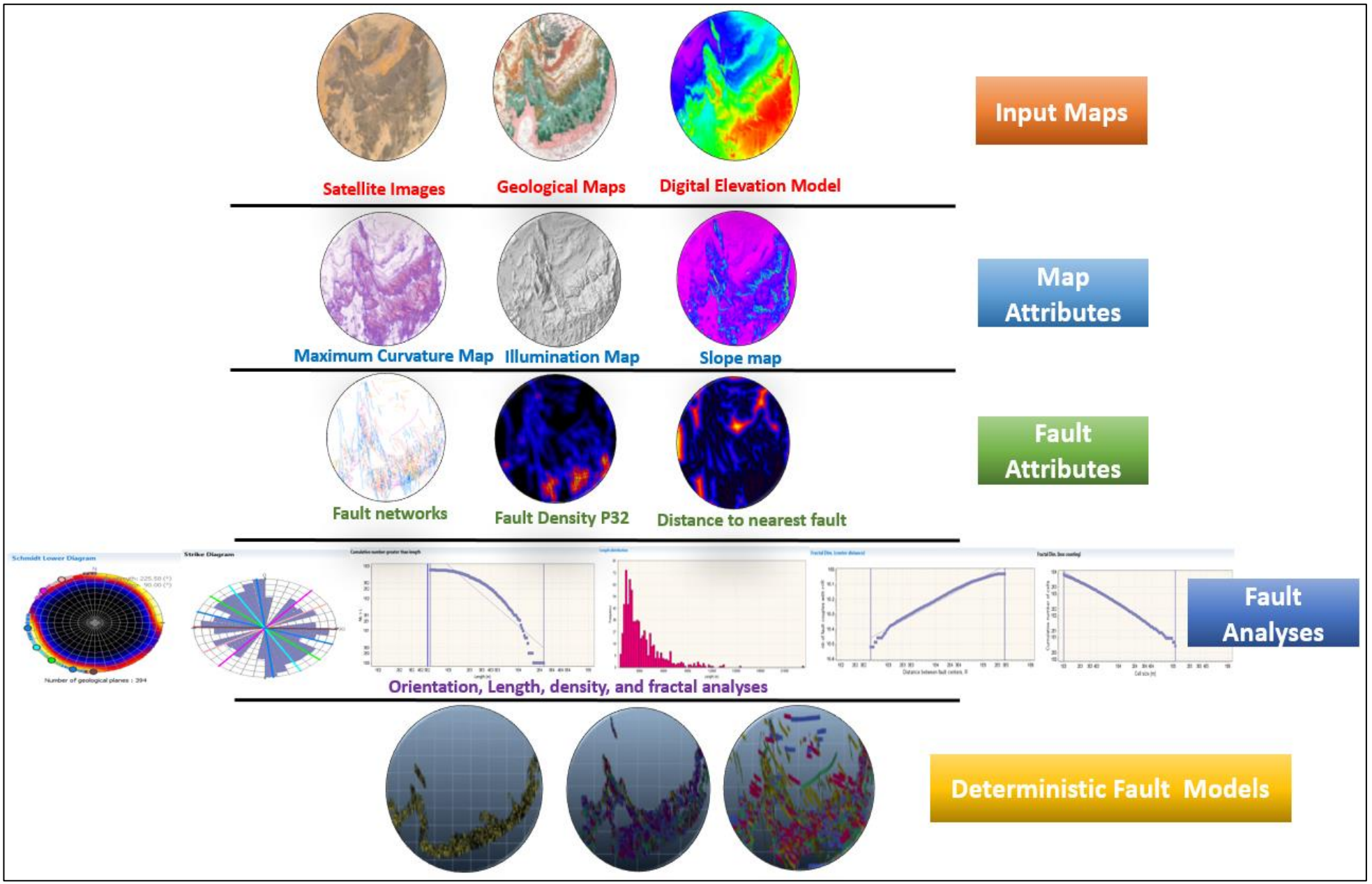

Figure 8: The specific workflow for the multiscale fracture analysis.

II-4-Data and Methodology

The data used in the multiscale fracture analysis include geological maps with scale of 1:100000, satellite images with a resolution of 30 meters (m), and Digital Elevation Models (DEM) with a resolution of 65 m. Different data sets were georeferenced and merged using Global Mapper software.

The faults detection and digitization were done based on the satellite images, curvature attributes, and illumination attributes maps. The latter attributes maps were generated based on the digital elevation model using FracaFlow software. The histograms, maps, rose diagrams, and graphs were created to determine the fault orientations, length distribution, and statistical parameters.

The 3D deterministic fault models represent the outcome of the fracture analysis that gives a realistic image of fracture distribution in the Cambro-Ordovician and the basement units. For each stratigraphic unit composing the Cambro-Ordovician, a 3D model was built to understand the relation between the stratigraphic units and the fracture occurrence.

The basement's fault characterization gives an overview about the impact of the basement faulting on the Cambro-Ordovician sedimentary cover. The kinematics analysis is based mainly on the geological maps. Two observation scales were chosen for this study to determine the fracture typology and fracture distribution law.

The first one is a mega-scale 1:100.000, which was used to digitalize and analyze the lineaments that represent the major faults that affect the area of study located between the north part of Hoggar shield and the south edges of Mouydir basin.

The second one is mesoscale 1:25000, which was used to represent the minor lineaments at formation scale.

Four approaches were applied to define the different networks and define the fractal dimension based on the fault's length and lithology:

- The first approach was related to the Major faults' analysis.
- The second approach was related to the analysis of the Minor faults that affect each geological formation separately including the basement and the Cambro-Ordovician units.
- The third approach was related to the analysis of the whole Minor fault network that affect the basement and the Cambro-Ordovician units.

- The fourth approach consisted to the analysis of the Major and Minor fault network that affects the area of study.

II-4.1-Fracture Detection

Seismic attributes are a powerful methods used in the seismic interpretation. They provide alternative images of fractures and other features such as channels (Chopra and Marfrut, 2007). Curvature is one of several geometric seismic attributes, which measures how bent a curve is at a particular point on a two-dimensional or three-dimensional surface (SEG Wiki). Curvature attributes have shown to be highly correlated with fractures, some of them measured on outcrops (Lisle, 1994; Roberts, 2001).

More recently, volumetric curvature attributes have become popular, enabling interpreters to delineate small flexures, folds, mounds, and differential compaction features on horizons that have not been explicitly picked and that are otherwise continuous and not seen by coherence (Chopra and Marfrut, 2007).

Illumination is another attribute showing the illumination of a surface as if a light source at some low elevation angle and azimuth were casting shadows, thus indicating relief on the surface being displayed (Beicip, 2018). This attribute computes an artificial illumination of a map. The rays are supposed to be parallel and horizontal.

The chosen direction of computation represents the azimuth of the source light, counted clockwise to the North (Beicip, 2018). Only one source of directional light is used and only the specular illumination defined with the cosines of the angle between the incident light and the normal of a triangle. This property is defined on the triangle surface and not at the vertices (Beicip, 2018).

In addition, this attribute is the local slope (slope gradient) of the map. It is defined by a plane tangent to a topographic surface, as modeled by the topography at a point (Burrough, 1986). Slope is classified as a vector; as such it has a quantity (gradient) and a direction (aspect). Slope gradient is defined as the maximum rate of change in altitude as the compass direction of this maximum rate of change (Beicip, 2018).

For the fracture detection, the main input used for this approach are the geological maps, satellite images, and the digital elevation models that can be displayed with different distributions

(Fig.9, 10 & 11). The numerical surface was loaded on software where different attributes were applied on them to enhance and detect fractures that affect this reservoir analog.

The first attribute applied on the digital elevation model is the illumination. Light is applied on this surface in a specific direction in order to highlight the lineaments that could be interpreted as faults. Eight (8) maps were generated using different light direction NS, NE-SW, E-W, SE-NW, highlighting the major and minor lineaments (Fig.12).

The second attribute applied on the Digital elevation model is curvature. Several curvature attributes were applied namely maximum curvature, minimum curvature, mean curvature, first principal curvature, Gaussian curvature, azimuthal curvature, and oriented curvature (Fig.13 & Fig.14).

Also, slope maps were generated based on the digital elevation models, which helped also in the lineaments' detection (Fig.15).

The fracture digitalization is generated using all fracture traces were drawn on to these attributes map digitally using the line tool in FracaFlow.

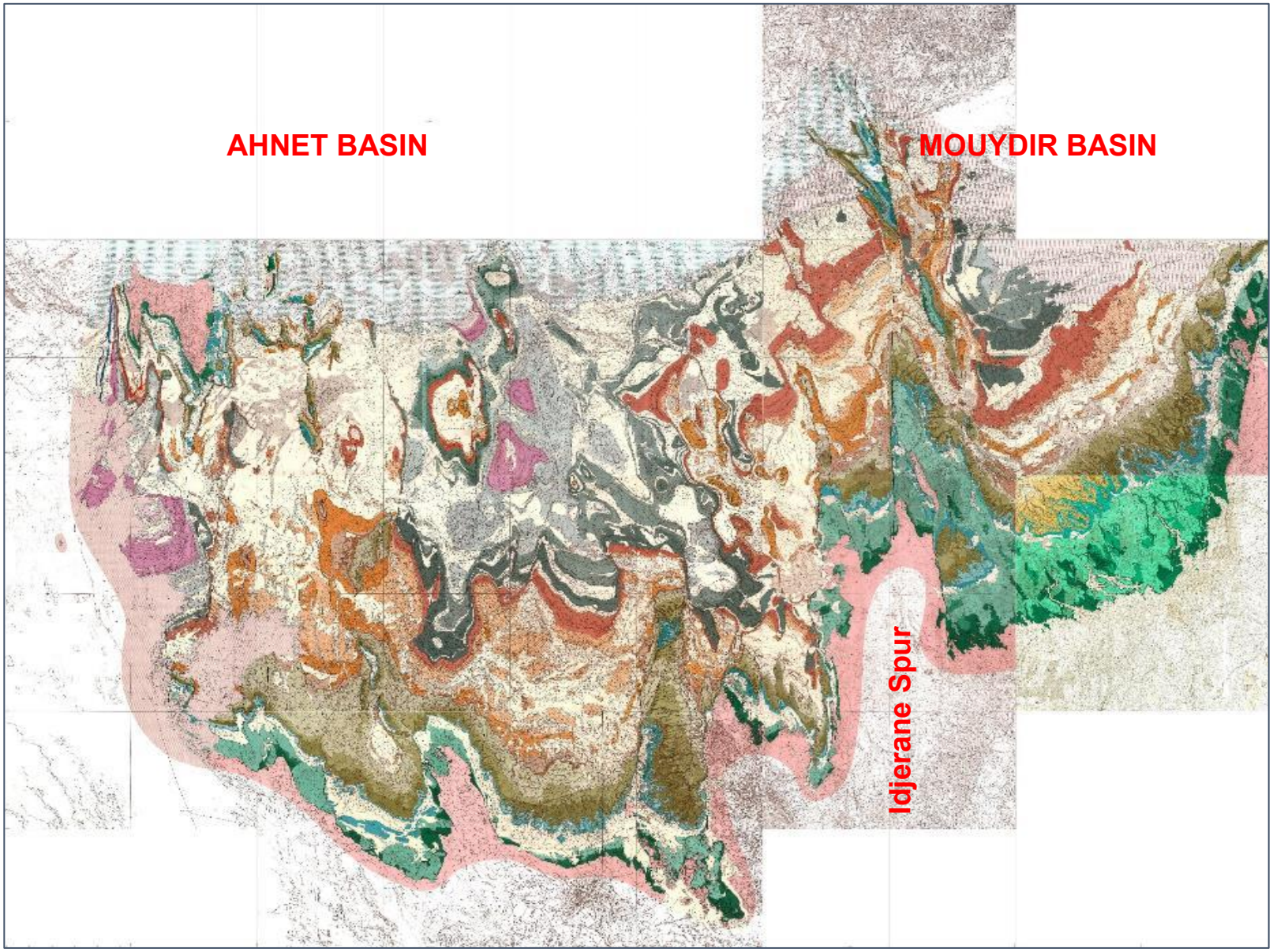

Figure 9: Composed Geological Maps

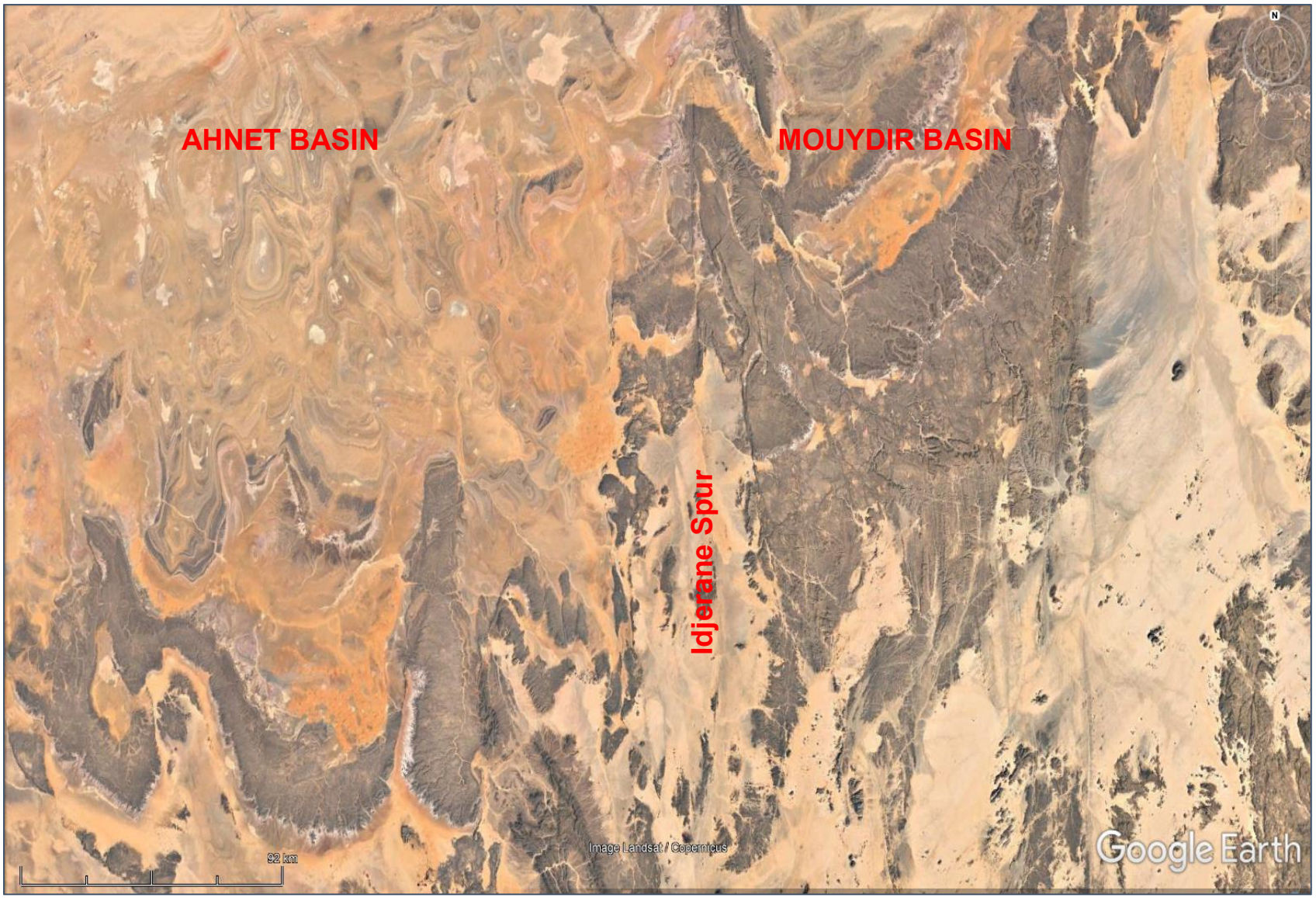

Figure 10: Satellite Image from Google Earth

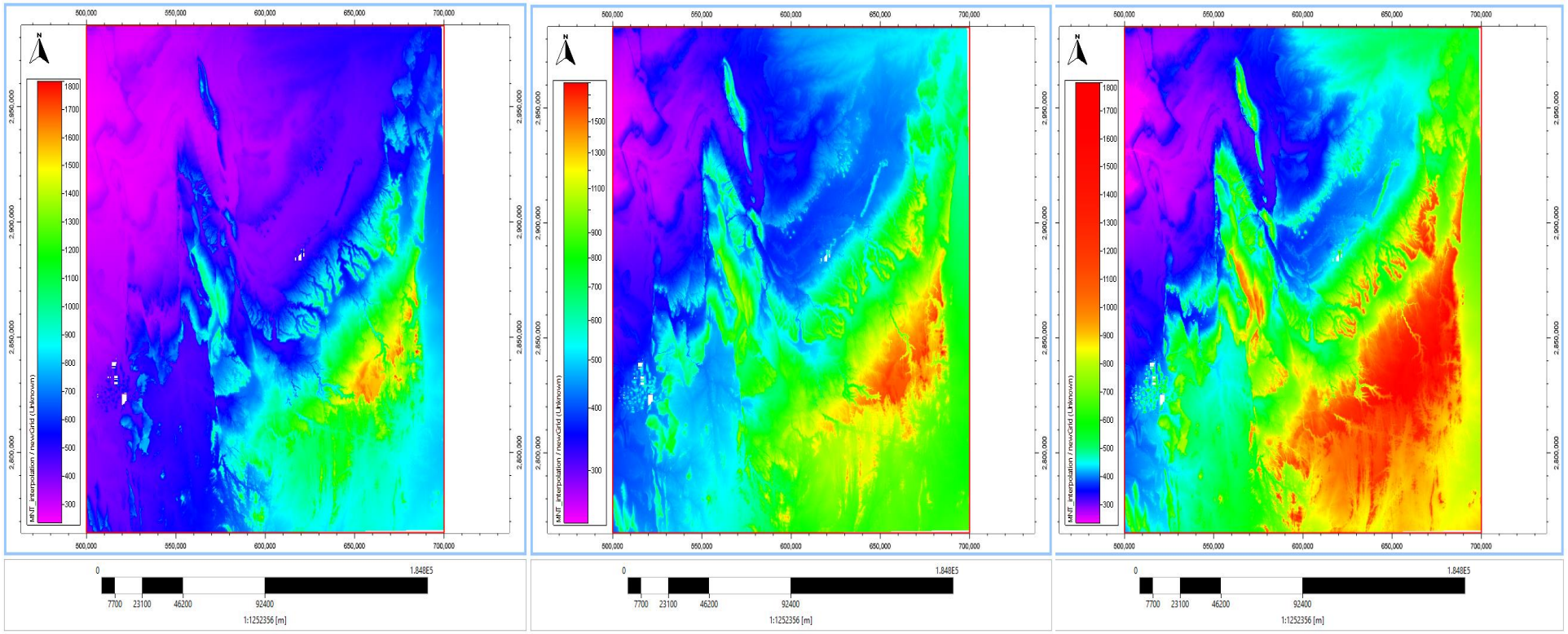

Linear Distribution

Log Distribution

Histogram Distribution

Figure-11: Digital Elevation Models.

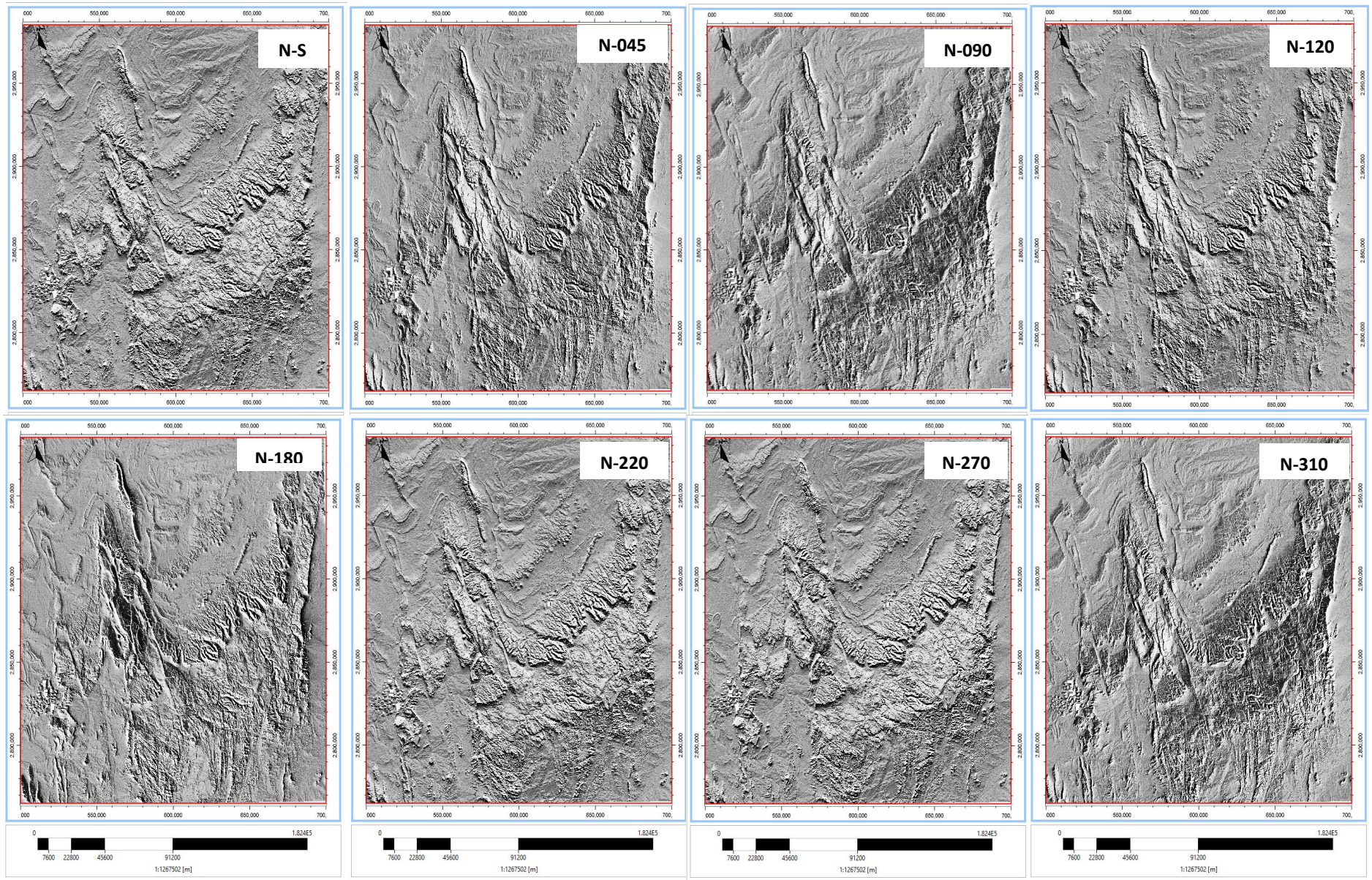

Figure-12: Illuminations Maps with different light direction

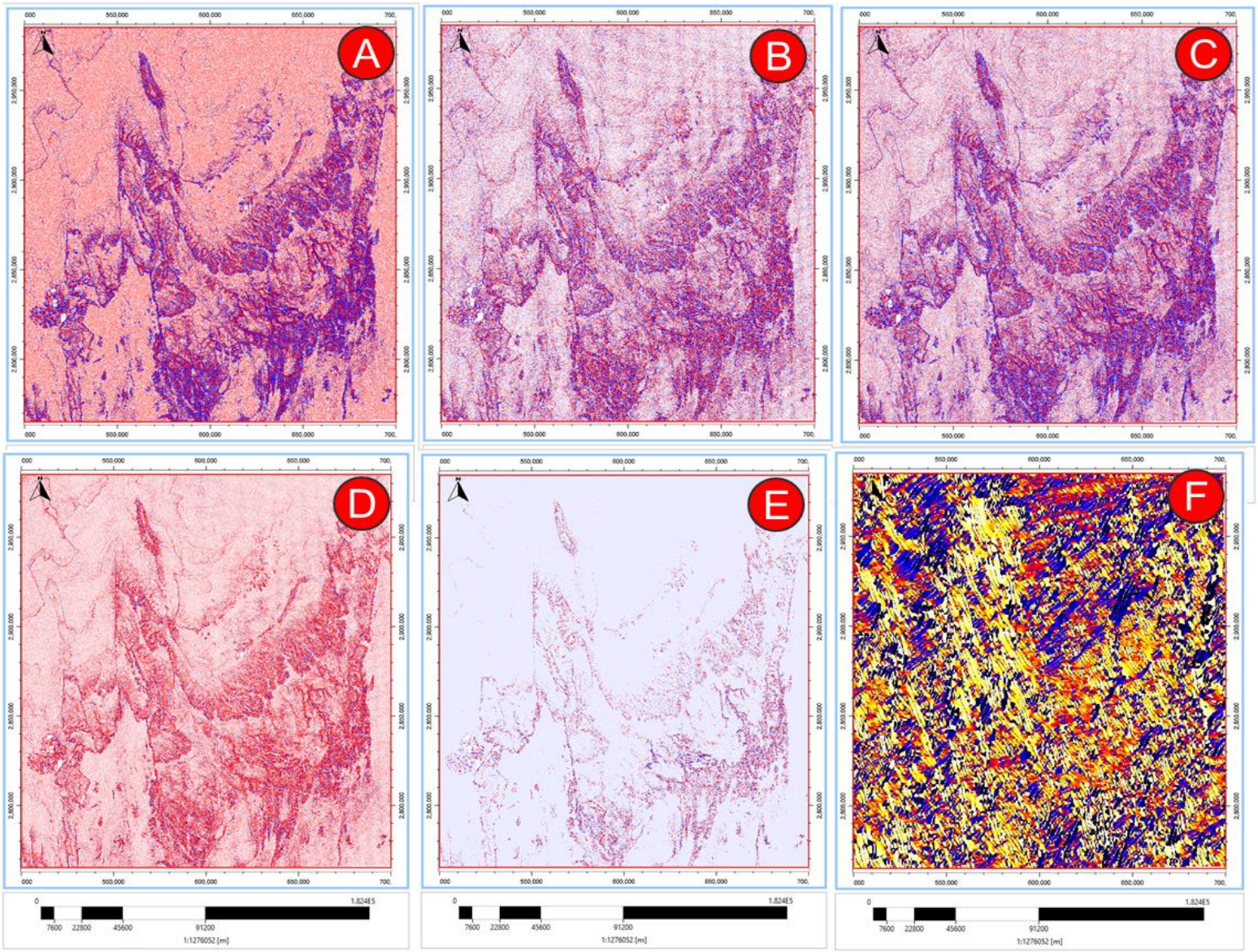

Figure-13: Curvature attributes; A- Maximum B- Minimum C- Mean D- First principal E- Gaussian F- Azimuthal

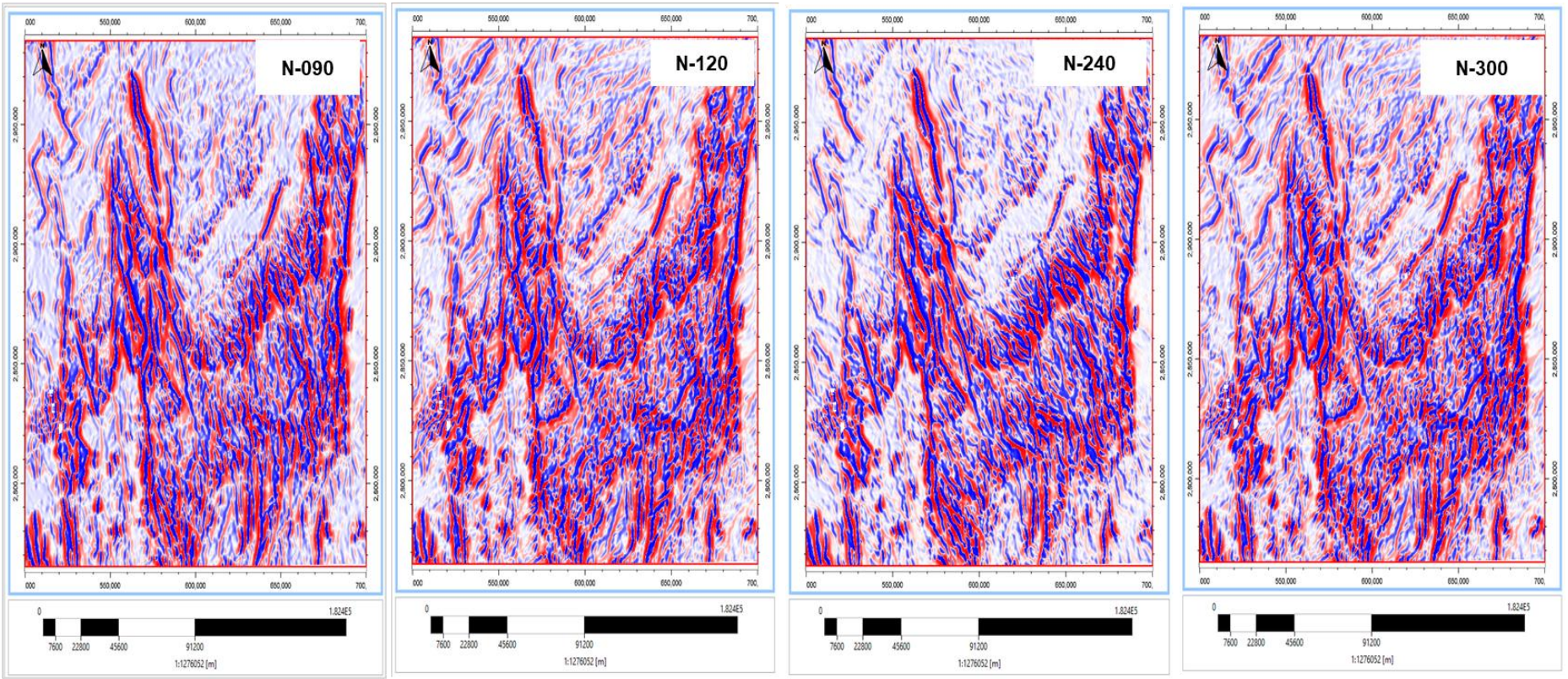

Figure-14: Oriented Curvature attributes

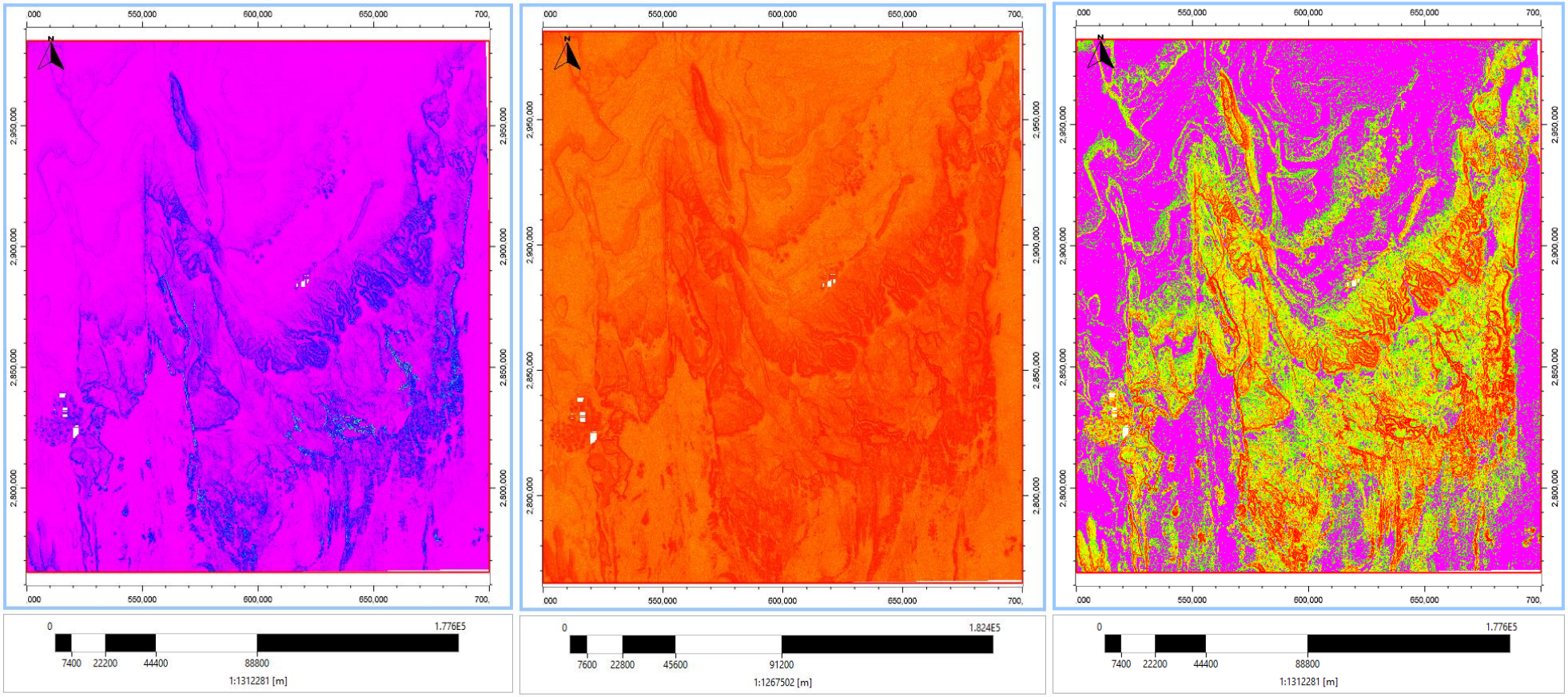

Linear Distribution

Log Distribution

Histogram Distribution

Figure-15: Slope Maps with different distribution

II-5-Fracture analysis

The fracture is defined as break that appears on a rock mass due to stress. According to Bonnet (2001), fractures are classified in mode I and mode II where in mode I, fracture is in tensile or opening mode and the displacement is normal to the discontinuity walls (e.g. joint). On the other hand, the mode II fracture is in an in-plane shear mode, where the displacement is in the plane of the discontinuity (e.g. fault). The fractures occur on a varied range of scales from microns to hundreds of kilometers, where they have a strong impact on the fluid flow and other rock parameters (Bonnet et al, 2001).

The pole diagrams are used in the fault analysis to better and faster analyze the faults' orientation. Each fault set is represented on stereo-diagram, which represent a group of poles built manually or automatically. The length distribution plays an important role because, for the same density and orientation distribution, collections of short fractures are less well-connected than those of long fractures (Balberg and Binenbaum, 1983; Balberg et al., 1991).

Many field studies around the world have confirmed that fracture sets have a power law length distribution (Davy et al., 1990, 1992; Davy, 1993; Pickering et al., 1995; Bour, 1997; Bour and Davy, 1998; Odling et al., 1999; Bonnet et al., 2001; Darcel et al., 2003a, b). The power law exponent "a" is generally in the range $1 < a < 3$ (Segall and Pollard, 1983; Davy, 1993; Berkowitz et al., 2000; Bonnet et al., 2001). According to Odling et al. (1999), when the exponent "a" is different from 2.0, the length populations lack either short fractures ($a < 2$) or long fractures ($a > 2$).

In the area of study, faults and joins represent the discontinuities. The length populations are plotted as normalized cumulative frequency distribution where Nb is the number of fractures with length greater than length, L per m^2. The logarithmic axes are used where a straight line indicates that the length distribution is power law with an exponent "a" given by the slope of the graph. The quantitative analyses of fractures in the Cambro-Ordovician are conducted with respect to the major faults affecting the zone of interest as well as analysis of the affecting the basement and Cambro-Ordovician formations.

The fault map is generated from the combination of the curvature attributes, illumination, geological maps, satellite images, and digital elevation model, by determining fracture sets, fracture lengths, and fractal dimension for different fracture sets (Fig.16). This allows us to

determine the major and minor fault sets in the area and understand the fractography of each formation.

The 3D deterministic fault model for each formation was built to illustrate the fracture distribution in space to determine their origin and relationship, and predict their continuity in the subsurface. The details of fracture analysis for different formations are described in the following subsections.

II-5.1-Detection of Major Faults

This approach took into account only the Major fractures that affected the area of study. They affect the basement and all the Paleozoic series. These fractures are Mode II fracture, characterized by long length, strike-slip kinematics, and affect all the Paleozoic series and continue in the Mouydir basin subsurface. According to Haddoum, 2001, the main fracture sets that affect the Paleozoic series correspond to strike-slip faults and reverse faults.

The Major structures correspond to N-S-trending dextral strike-slip faults, and NNW-SSE to N-S trending reverse faults.

The Minor NE-SW-trending dextral or NW-SE-trending sinistral strike-slip faults cut the N-S-trending faults (Haddoum, 2001). These fractures are an inheritance of the Pan-African orogeny and they were reactivated during the Hercynian and Alpine orogenies (Haddoum, 2001).

The pole diagrams are used in the fracture analysis to better and faster analyze the fractures' orientation. Each fracture set is represented on stereo-diagram, which represent a group of poles built manually or automatically. The global lineaments map was generated at scale of 1:100000. It gives an illustration of the major fault sets and their length distributions.

Almost 400 faults were digitized and analyzed based on geological, curvature, and illumination maps (Fig.11). The fracture system in this area has several orientations and was classified into seven distinct sets of N000, N040, N060, N090, N110, N130 and N150, respectively (Fig.17).

The length distribution is plotted as a bar chart that displays the distribution of the fracture length in meter versus their frequency, highlighting the most, least, and mean frequent length observed in the field. The length distribution follows the power law with the N000, N090, and N130 being the most dominant fracture sets.

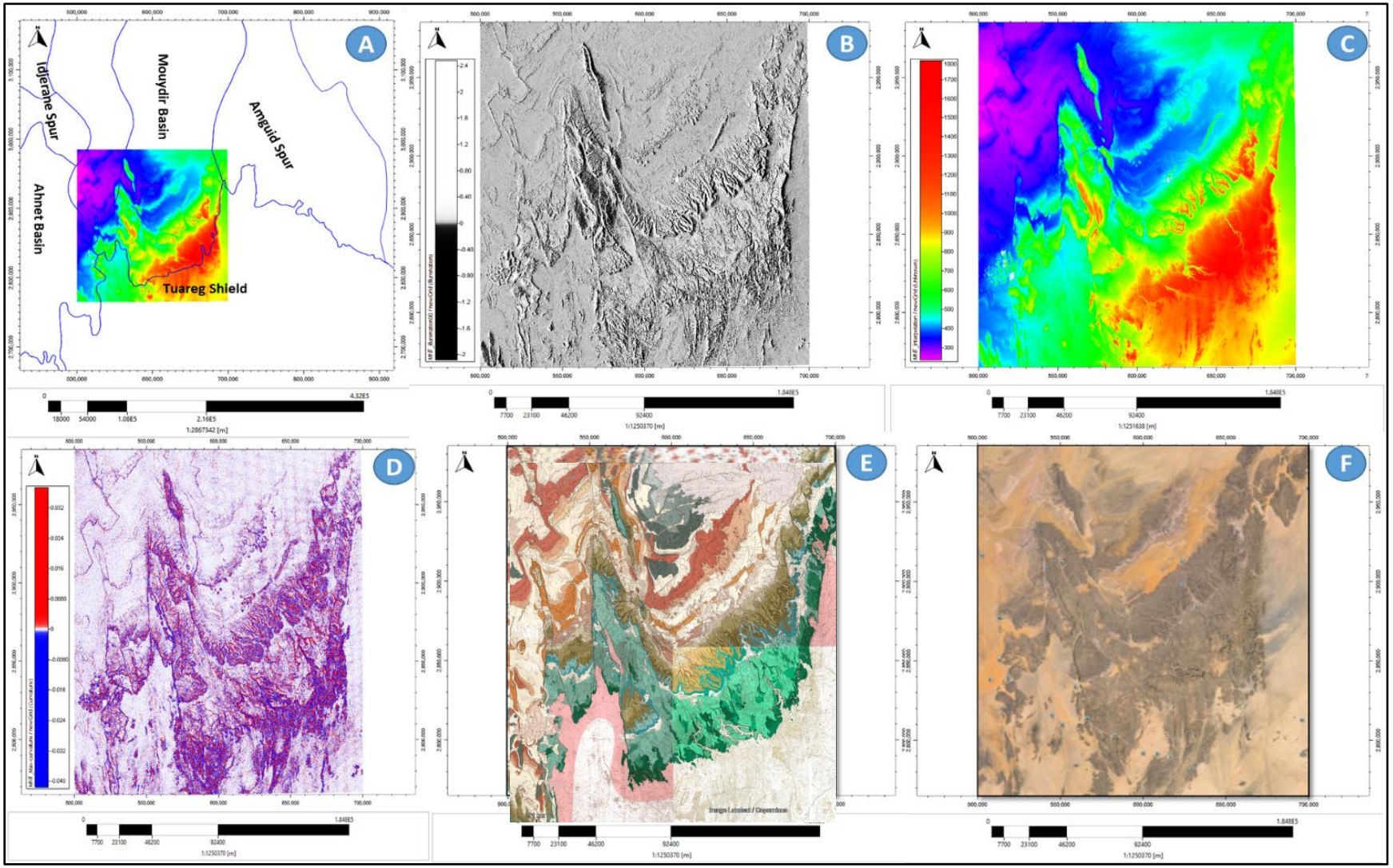

Figure-16: Workflow application on the major faults. A- Location of the zone of interest (ZOI) in relation to the basin's location. B- Illumination of the ZOI. C-digital elevation model of the ZOI. D- Maximum curvature map of the ZOI. E-Geological maps of the ZOI.

The faults' length corresponding to these fracture sets range from 4km to 166 km, 2km to 37km, and 1.6km to 47km, respectively. Due to the large fracture lengths, it is likely that they intersect each other at some depth. The fault set N000 is the most important fault network affecting the area as it is represented by 100 faults extending to the basement and affecting all the Paleozoic series, including the Cambro-Ordovician, Silurian and the Devonian formations.

The geological maps analysis confirm that these fractures are strike-slip faults. The global fractures length and the length of each fracture set were analyzed based on statistical parameters such as the most, least, and mean frequent lengths, correlation coefficient, and power law exponent (Fig.14 & Tab.1). The coefficient correlation ranges from 0.93 and 0.97. In addition, the power law coefficient oscillates between 1.97 and 2.42.

Table-1: Length distribution and parameters related to the Major faults

Data	Points	a	LMin (m)	LMax (m)	LMean (m)	Correlation coeff.	Distribution
All faults	394	2.14	1507.63	165100	5970.73	-0.95	Power law
Major Faults-N000	100	1.98	3139.7	165700	12980	-0.94	Power law
Major Faults-N040	38	2.24	1657.57	67450	5098.77	-0.94	Power law
Major Faults-N060	44	1.97	1492.24	21440	4339.57	-0.93	Power law
Major Faults-N090	59	2.42	1857.17	37870	4574.26	-0.97	Power law
Major Faults-N110	37	2.32	1590.77	63890	4581.38	-0.95	Power law
Major Faults-N130	59	2.02	1696.32	47580	5758.45	-0.93	Power law
Major Faults-N150	57	2.06	3273.61	66770	9997.34	-0.97	Power law

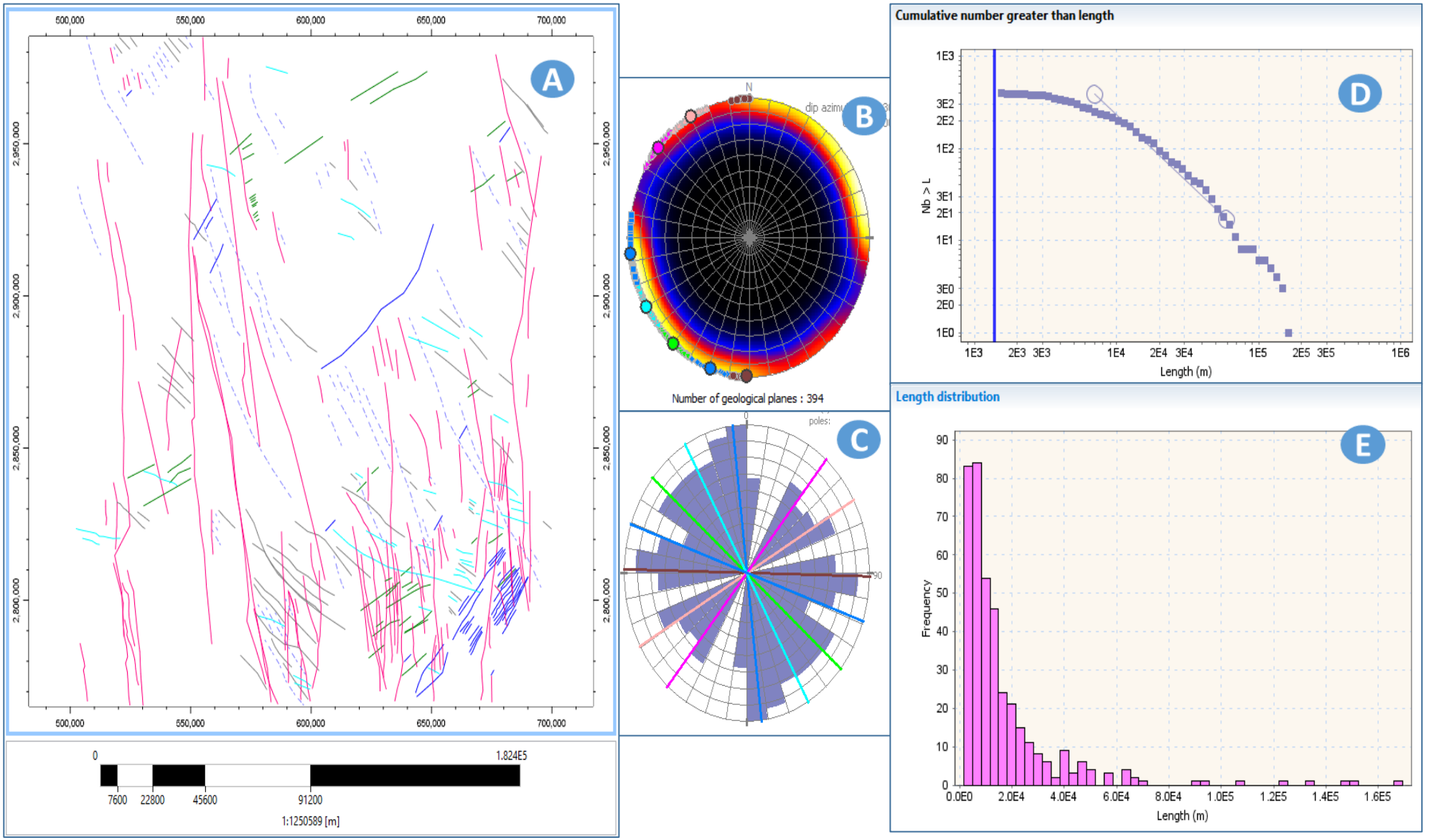

Figure-17: Major faults characteristics. A- Major faults map in the area of study. B- Major faults' pole orientation. C- Major Faults sets orientation. D- Length Power Law distribution, E- Length distribution

II-5.2-Detection of Minor Faults

This approach is applied on the different geological formations including the basement and the three Cambro-Ordovician units. Each unit is studied separately in order to understand the fractography of each unit that composes the Cambro-Ordovician reservoir and the basement formation. This will help to understand the relation between the facies and the different fracture networks. For each unit, the fracture sets are determined and the length distribution is calculated.

The fractal dimensions using center dimension and box-counting algorithms are estimated for the whole fracture network and for each fracture set, which composes the fracture network. As mentioned, the analysis of fracture sets that intersect the basement rocks and the three formations that constitute the Cambro-Ordovician is an important step in the fracture analysis workflow.

The fractures were digitalized based on the curvature and illumination maps and other input data and the results were used to define the fracture orientation and determine the fracture density of each stratigraphic unit, deducted from the analysis of rose diagrams and other statistical parameters. The length distribution was plotted to identify the largest and smallest frequent length. The length of each fracture set was analyzed based on the correlation coefficient, power law exponent, and the maximum, minimum, and mean length.

II-5.2.1-Basement formation

The basement formation in the area of study belongs to the Hoggar shield. It is mainly composed of metamorphic and igneous rocks. The Hoggar shield is a Cenozoic swell with a surface of 550,000 km^2 made of Precambrian rocks surrounded in the north part by the Paleozoic series deposited after the end of the Pan-African orogeny (Liégeois, 2019). Twenty-three terranes have been identified in the Hoggar Shield, separated either by subvertical mega-shear zones or by thrust fronts; these terranes differ by lithologic, metamorphic, magmatic or tectonic characteristics (Black et al. 1994).

The basement is affected by 640 faults where the fracture network is grouped into five sets oriented N000, N050, N090, N120, and N160, respectively (Fig.18 and Fig.19). The N000 and N160 fault sets are the dominant fault sets and represented by 256 and 145 fault planes, and their lengths range between 500 m to 13 km and 1 to 10km, respectively (Fig.19E & Tab.2).

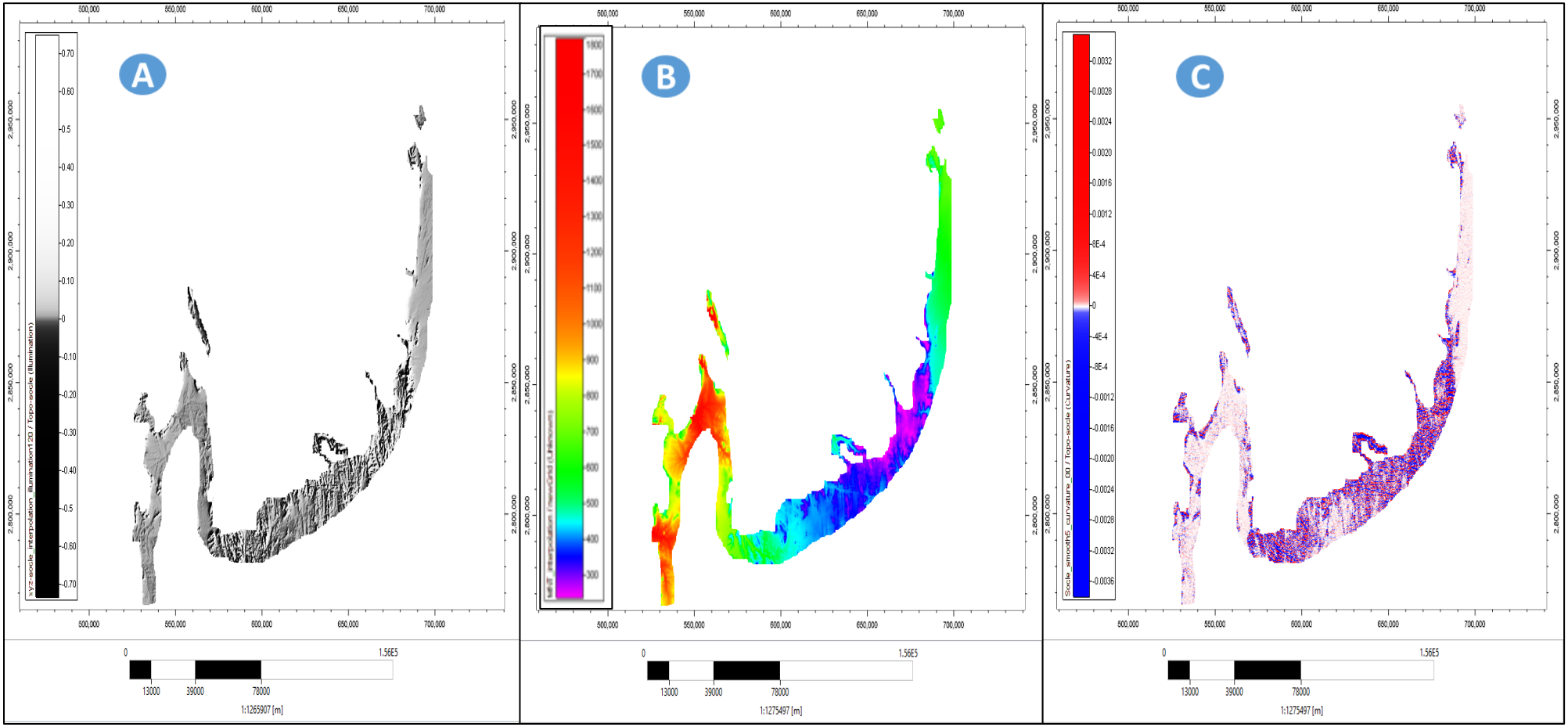

Figure-18: Basement Minor faults. A- Illumination map of the basement formation. B- Digital Elevation Model of the basement formation. C-Curvature map of the basement formation.

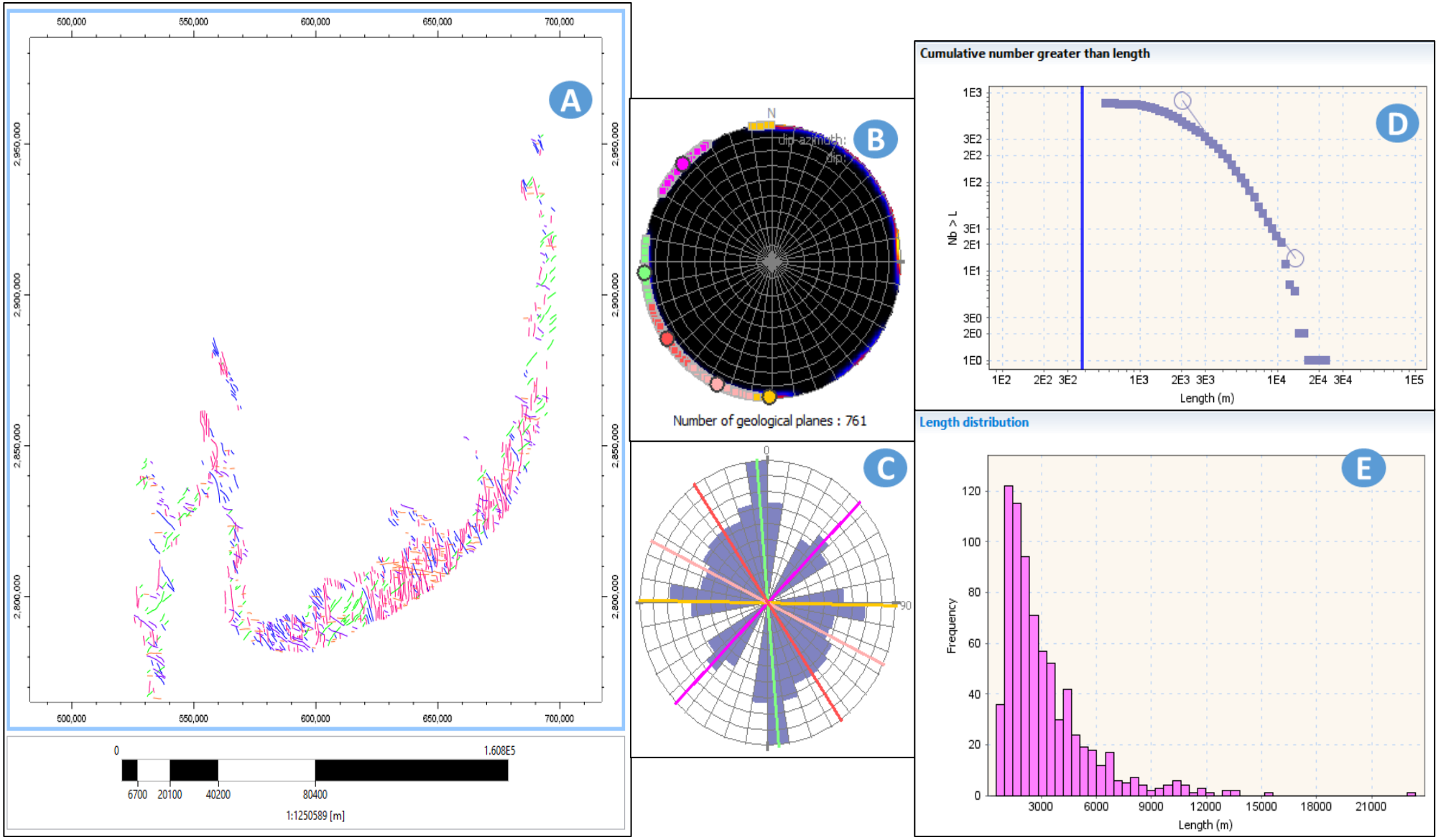

Figure-19: Basement Minor faults characteristics. A- Minor faults map in the Basement formation. B- Minor faults' pole orientation. C- Manor Faults sets orientation. D- Length Power Law distribution, E- Length distribution.

The log–log diagram of the fracture length attests that the basement's fracture length distribution follows a power law distribution with correlation coefficients of 0.89-0.97 corresponding to a power law coefficient of 2.36-2.89 (Fig.19 & Tab.2).

Table 2: Length distribution and parameters related to the Basement faults

Data	Points	a	LMin (m)	LMax (m)	LMean (m)	Correlation coeff.	Distribution
Selected Faults	761	2.89	551.54	22950	1132.38	-0.93	Power law
Basement-N000	256	2.36	609.52	15290	1601.27	-0.89	Power law
Basement-N050	123	2.6	549.43	10710	1226.41	-0.91	Power law
Basement-N090	121	2.83	718.86	22980	1497.33	-0.97	Power law
Basement-N120	116	2.43	646.6	9570.19	1508.62	-0.94	Power law
Basement-N160	145	2.62	885.08	11870	1877.66	-0.95	Power law

II-5.2.2-The Ajjers formation

Sandstone units, including Hamra Quartzites, Vire-du-Mouflon sandstone, and Tin-Taradjelli sandstone are the main formation of the Ajjers formation. The latter is intersected by 492 faults. The fracture network is grouped into five sets with orientations of N000, N050, N090, N110, N130 and N150 (Fig.20 & Fig.21). The fault sets N000 and N090 are the dominant sets represented by 120 and 123 fault planes, respectively. The Ajjers fractures length distribution shows that the N-S and N090 fault sets have the largest length ranging between 750m and 10km and 800m and 5.5km, respectively.

The log–log diagram of length distribution shows that the Ajjers fracture length distribution follows a power law trend as depicted in Fig. 10. The correlation coefficient ranges from 0.93 to 0.96 and the power law coefficient is 2.27-3 (Fig.21E & Tab.3).

Table 3: Length distribution and parameters related to the Ajjers' faults

Data	Points	a	LMin (m)	LMax (m)	LMean (m)	Correlation coeff.	Distribution
All Faults	492	2.47	357.83	16030	936.88	-0.9	Power law
Ajjers-N000	120	2.19	357.83	16030	1168.08	-0.89	Power law
Ajjers-N050	36	2.52	843.7	6966.39	1713.95	-0.95	Power law
Ajjers-N090	123	3.12	645.12	9842.41	1166.97	-0.96	Power law
Ajjers-N110	52	3.05	1110.37	8108.58	1933.39	-0.95	Power law
Ajjers-N130	92	2.33	663.03	13160	1703.08	-0.93	Power law
Ajjers-N150	69	2.74	1003.68	11270	1997.4	-0.95	Power law

II-5.2.3-In-Tahouite formation

The In-Tahouite formation composed mostly of bioturbated siltstones and very-fine to fine-grained sandstones (Bennacef et al., 1971). It also includes Azzel shale, Tiferouine shale, and Ouargla sandstone. The In-Tahouite formation is intersected by 172 faults and the fracture network is classified into five sets of N000, N040, N060, N090, N120 and N130 (Fig.22 and Fig.23). The fault sets N000, N090 and N130 are the most dominant fault networks represented by 40, 49, and 51 fault planes, respectively.

The In-Tahouite fractures length shows that the N-S, N090 and N130 fault sets have the largest length ranging from 350m to 16km, 650 to 10km, and 660m to 13km, respectively (Fig.18E). The log–log diagram of the length distribution confirms that the basement's fracture length distribution follows a power law trend. The correlation coefficients and power law coefficients range from 0.89-0.95 and 2.19-3.12, respectively (Fig.23 &Tab.4).

Table 4: Length distribution and parameters related to the In-Tahouite's faults

Data	Points	a	LMin (m)	LMax (m)	LMean (m)	Correlation coeff.	Distribution
All Faults	172	2.9	518.09	10180	1021.16	-0.94	Power law
In-Tahouite-N000	40	2.67	752.79	10200	1569.66	-0.96	Power law
In-Tahouite-N050	15	2.54	579.87	4593.54	1162.1	-0.93	Power law
In-Tahouite-N060	17	2.55	532.86	6983.19	1157.13	-0.93	Power law
In-Tahouite-N090	49	3	807.65	5494.03	1407.55	-0.99	Power law
In-Tahouite-N130	51	2.27	516.52	5563.09	1211.6	-0.94	Power law

II-5.2.4-The Tamadjert formation

The Tamadjert formation is a heterogeneous reservoir. According to Bennacef et al. (1971), the stratigraphic and sedimentological characteristics of the Tamadjert glacial formation are very Different from those of the other main detrital Paleozoic units in the Sahara.

This originality is linked with specific processes of glacial phenomena (Biju-Duval et al., 1974). The Tamadjert formation has at its base either an angular unconformity or a disconformity, which caused very abrupt thickening and lithological variations (Bennacef et al., 1971). The formation is composed of M'Kratta sandstone, El-Goléa sandstone, and micro-conglomerate shale.

The Tamadjert formation is affected by 843 faults where the fracture network is clustered into five sets of: N000, N040, N070, N090 and N130, respectively (Fig.24 and Fig.25). The fault

sets N000, N090, and N0130 are the dominant fault networks represented by 212, 178, and 171 faults, respectively.

The Tamadjert fracture length analysis shows that the N070 and N090 fault sets have the largest length ranging from 500m-9 km and 530m-8.7km, respectively (Fig.25).

The log–log diagram of length distribution confirms that the basement's fracture length distribution follows a power law function with a high correlation coefficient of 0.91-0.97 and a power law coefficient of 2.37-2.81 (Fig.25 &Tab.5).

Table 5: Length distribution and parameters related to the Tamadjert's faults

Data	Points	a	LMin (m)	LMax (m)	LMean (m)	Correlation coeff.	Distribution
All Faults	843	2.73	516.16	79370	1195.95	-0.97	Power law
Tamadjert-N000	212	2.37	516.16	79370	1614.87	-0.97	Power law
Tamadjert-N040	84	2.58	648.57	6233.58	1328.5	-0.91	Power law
Tamadjert-N070	57	2.56	514.66	9283.62	1161.36	-0.94	Power law
Tamadjert-N090	178	2.75	530.2	8750.73	1093.91	-0.91	Power law
Tamadjert-N120	171	2.81	684.66	17110	1422.51	-0.95	Power law
Tamadjert-N150	141	2.53	890.15	21920	2118.6	-0.97	Power law

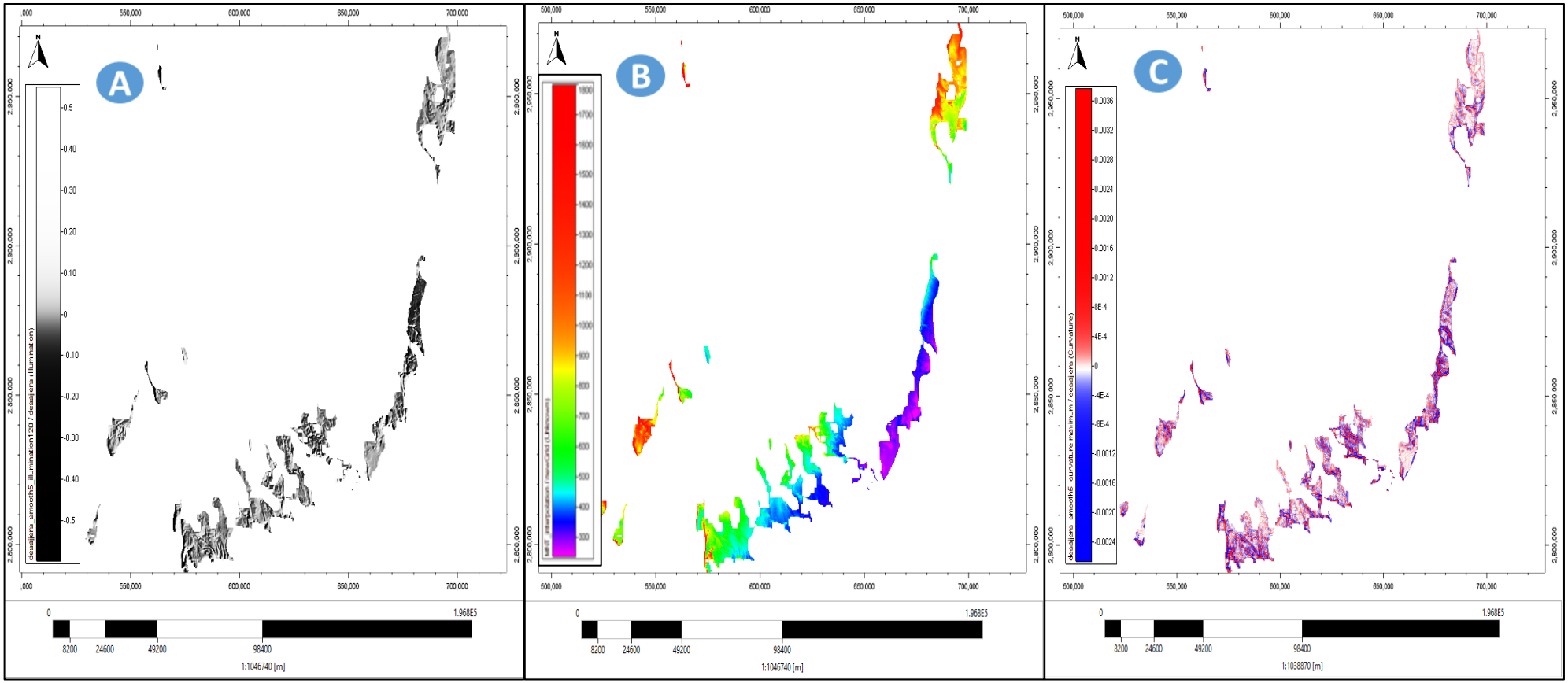

Figure 20: Ajjers Minor faults. A- Illumination map of the Ajjers formation. B- Digital Elevation Model of the Ajjers formation. C-Curvature map of the Ajjers formation

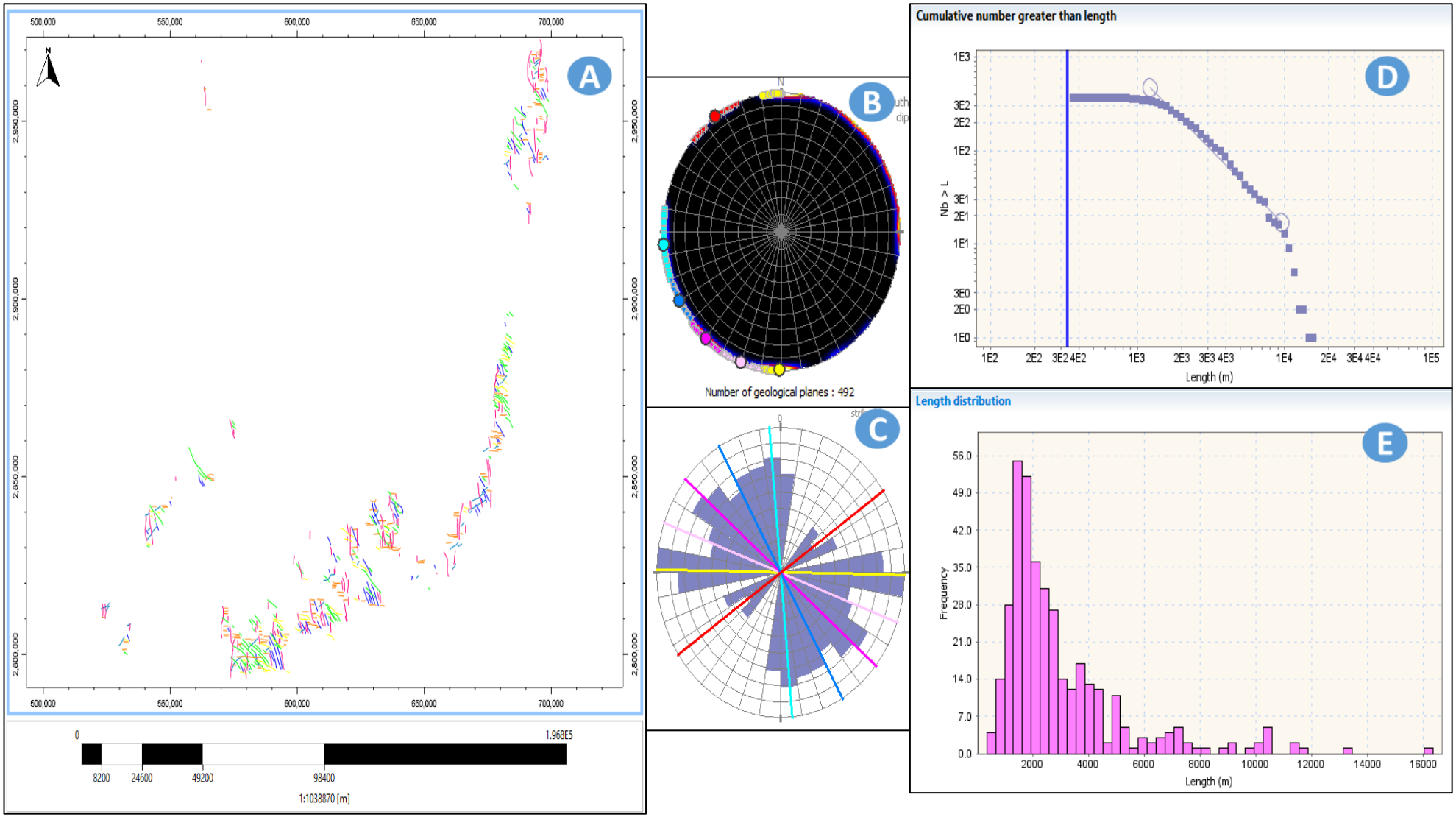

Figure 21: Ajjers Minor faults characteristics. A- Minor faults map in the Ajjers formation. B- Minor faults' pole orientation,. C- Minor Faults sets orientation. D- Length Power Law distribution, E- Length distribution

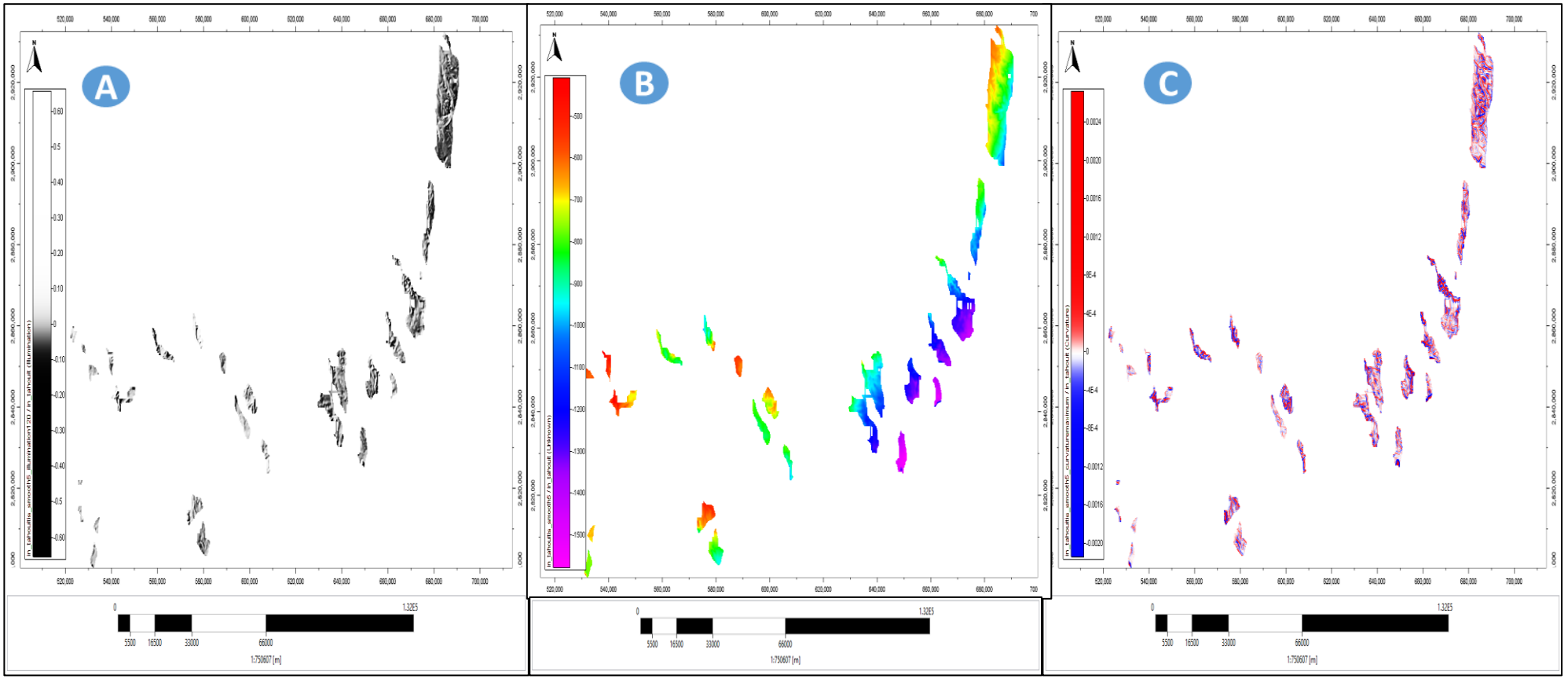

Figure 22: In-Tahouite Minor Faults. A- Illumination map of the In-Tahouite formation. B- Digital Elevation Model of the In-Tahouite formation. C- Curvature map of the In-Tahouite formation

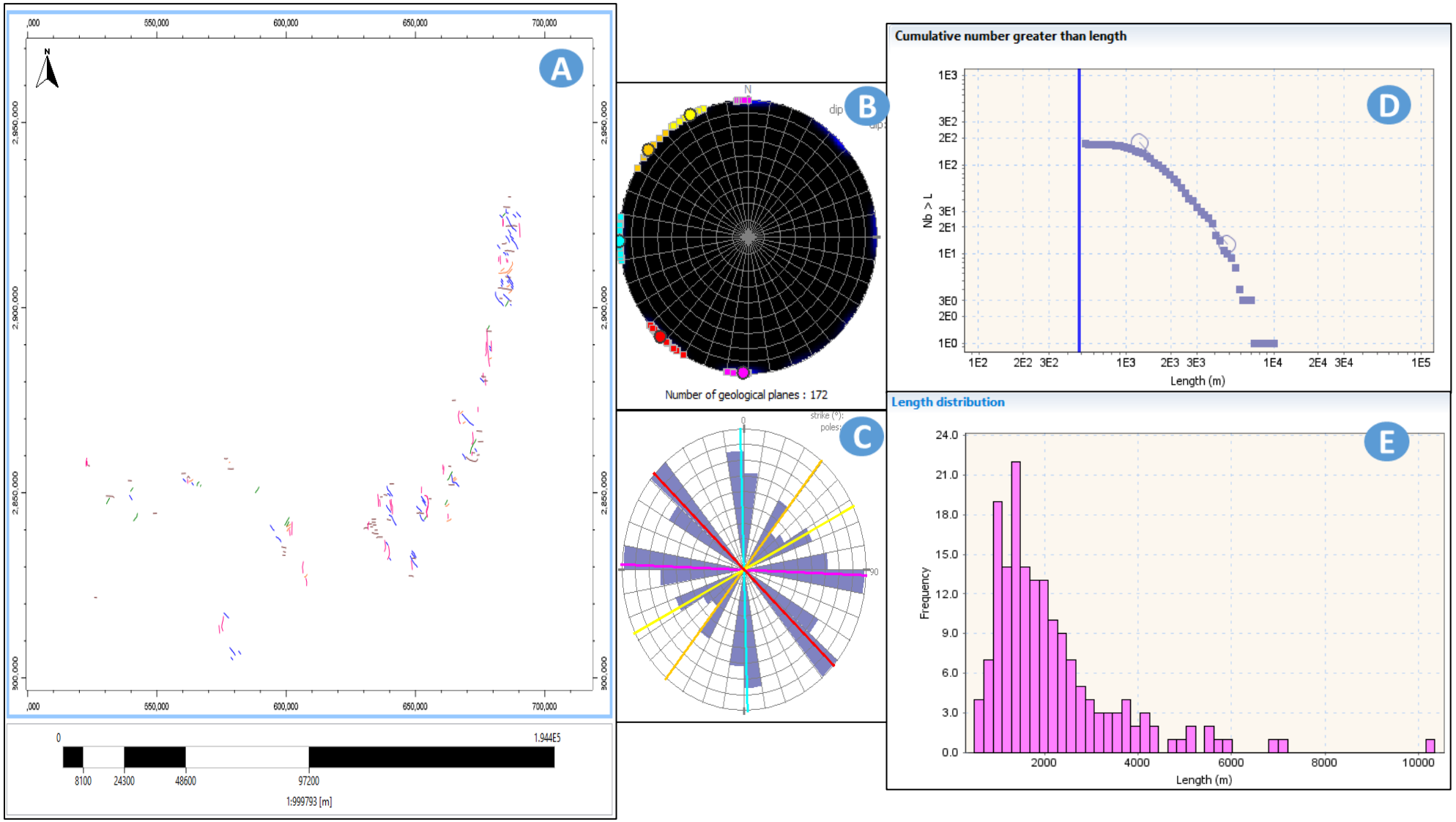

Figure 23: In-Tahouite Minor faults characteristics. A- Minor faults map in the In-Tahouite formation. B- Minor faults' pole orientation,. C- Minor Faults sets orientation. D- Length Power Law distribution, E- Length distribution.

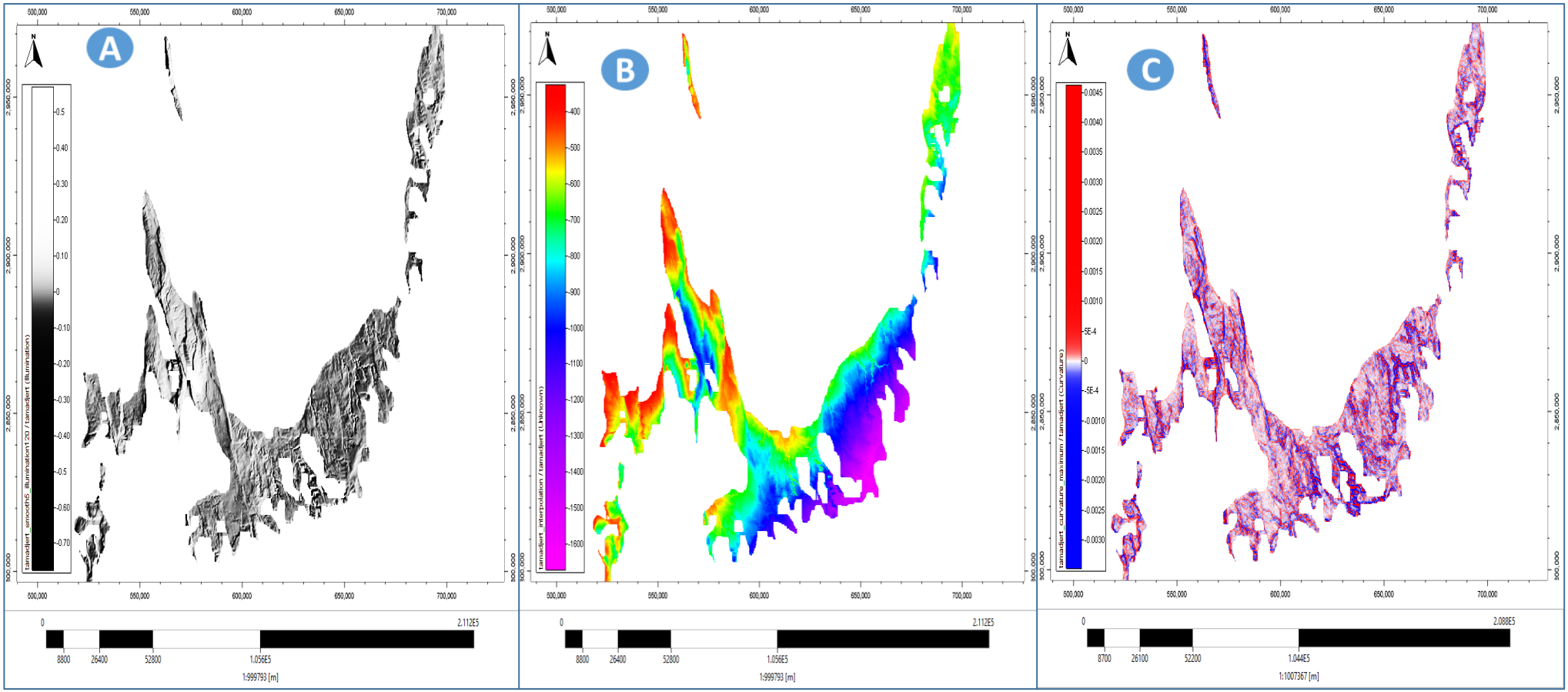

Figure 24: Tamadjert Minor Faults. A- Illumination map of the Tamadjert formation. B- Digital Elevation Model of the Tamadjert formation. C-Curvature map of the Tamadjert formation.

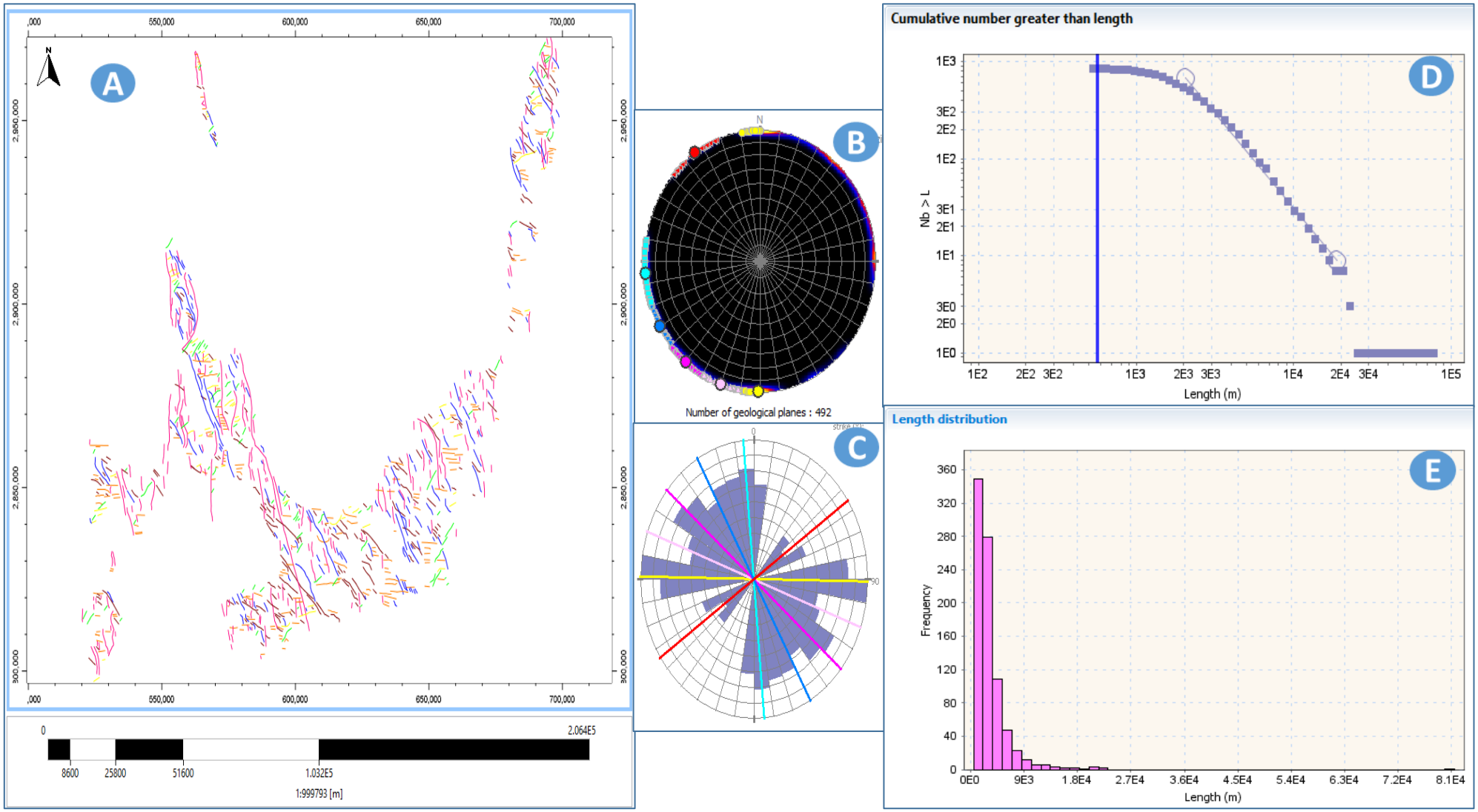

Figure 25: Tamadjert Minor Faults characteristics. A- Minor faults map in the Tamadjert formation. B- Minor faults' pole orientation. C- Minor Faults sets orientation. D- Length Power Law distribution, E- Length distribution.

II-6-Global Faults

This third approach is applied only on the Minor fracture networks that affect the basement and the Cambro-Ordovician units. This will help to understand the behavior and the fractography of each unit. In addition, it will help to understand the relationship and the impact of the basement fractures on the different units of the Cambro-Ordovician reservoir analog by comparing the orientation of the different fracture sets, their length, their kinematics, and their fractal dimensions. The basement, Ajjers, In-Tahouite, and Tamadjert fracture networks are merged into a Global fracture network. This approach is applied on the whole fault network that affect the basement and the Cambro-Ordovician units together.

The basement, Ajjers, In-Tahouite, and Tamadjert fault networks are merged into a global fault network. The fracture orientation and fractal dimensions are calculated using center dimension and box-counting algorithms for the global faults and compared to the fractal dimension of each fault set that composes this fracture network. The global fault network is composed by 1891 faults and characterized by five fault sets: N000, N050, N090, N120, and N150 respectively where the N-S and N150 fault sets are the most important groups in term of faults' number and length (Fig.26).

The log–log diagram of length distribution confirms that the basement's fracture length distribution follows a power law function with a high correlation coefficient of 0.91-0.97 and a power law coefficient of 2.55-3.12 (Fig.26 & Tab.6).

Table 6: Length distribution and parameters related to the Global faults

Data	Points	a	LMin (m)	LMax (m)	LMean (m)	Correlation coeff.	Distribution
All faults	1891	2.79	360.72	79230	803.42	-0.96	Power law
Global-Faults-N000	628	2.55	360.72	79230	967.32	-0.95	Power law
Global-Faults-N050	258	2.85	549.43	10710	1104.75	-0.91	Power law
Global-Faults-N090	471	3.12	532.77	22950	994.27	-0.97	Power law
Global-Faults-N120	482	2.78	519.44	17080	1111.73	-0.93	Power law
Global-Faults-N150	355	2.83	887.81	21920	1826.91	-0.96	Power law

II-7-Total faults

This approach studies the Major and Minor fracture networks that affect the area of study. This approach helps to comprehend the behavior and the relationship between the Major and Minor fractures in terms of space and time.

In addition, it brings a new insight about the effect of the basement fracture on the sedimentary cover and the geological age of the different fracture sets. Also the impact of the major fracture on the basin structuration. Both Minor and Major fracture networks are merged to a unique Total fracture network.

The fracture orientation and fractal dimensions are calculated using center dimension and box-counting algorithms for the total faults and compared to the fractal dimension of each fault set that composes this fracture network.

The total network is composed by 2544 faults and characterized by five fault sets: N000, N050, N090, N120, and N150 respectively (Fig.27). The N-S, N090 and N160 fault sets are the most important groups in term of faults' number and length.

The log–log diagram of length distribution confirms that the basement's fracture length distribution follows a power law function with a high correlation coefficient of 0.97-0.99 and a power law coefficient of 1.97-2.57 (Fig.27 & Tab.7).

Table 7: Length distribution and parameters related to the Total faults

Data	Points	a	LMin (m)	LMax (m)	LMean (m)	Correlation coeff.	Distribution
All Faults	2544	2.2	362.04	163900	1527.92	-0.97	Power law
Total-faults-N000	728	1.97	362.04	163900	2388.24	-0.97	Power law
Total-faults-N050	296	2.44	554.52	67080	1601.48	-0.97	Power law
Total-faults-N090	530	2.57	534.1	37640	1340.72	-0.98	Power law
Total-faults-N120	578	2.36	522.88	63530	1620.84	-0.97	Power law
Total-faults-N150	412	2.27	892.76	66340	2886.56	-0.99	Power law

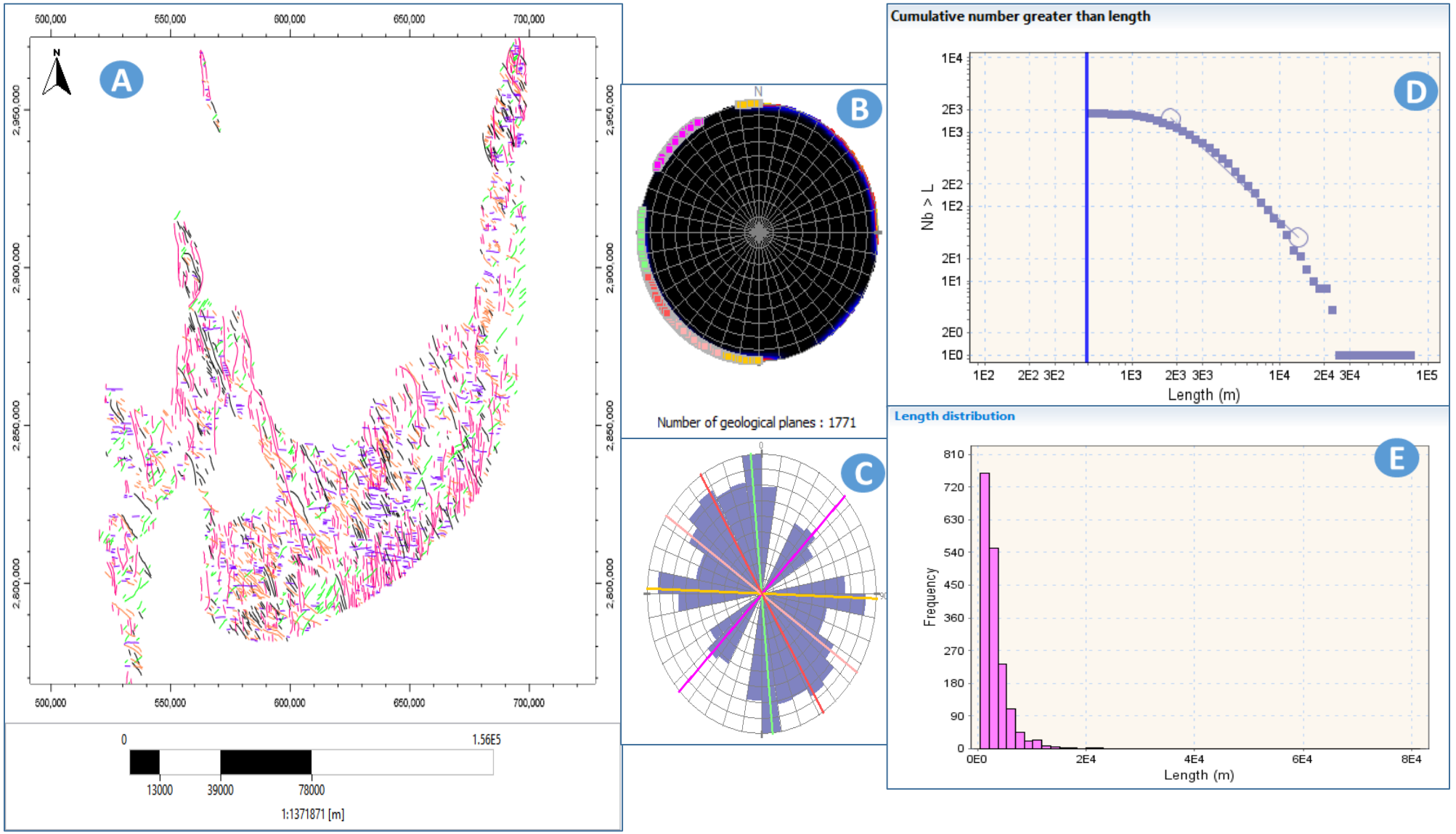

Figure 26: Global Faults characteristics. A- Global Minor faults map in the area of study. B- Faults' pole orientation, C- Faults sets orientation. D- Length's Power Law distribution, E- Length distribution.

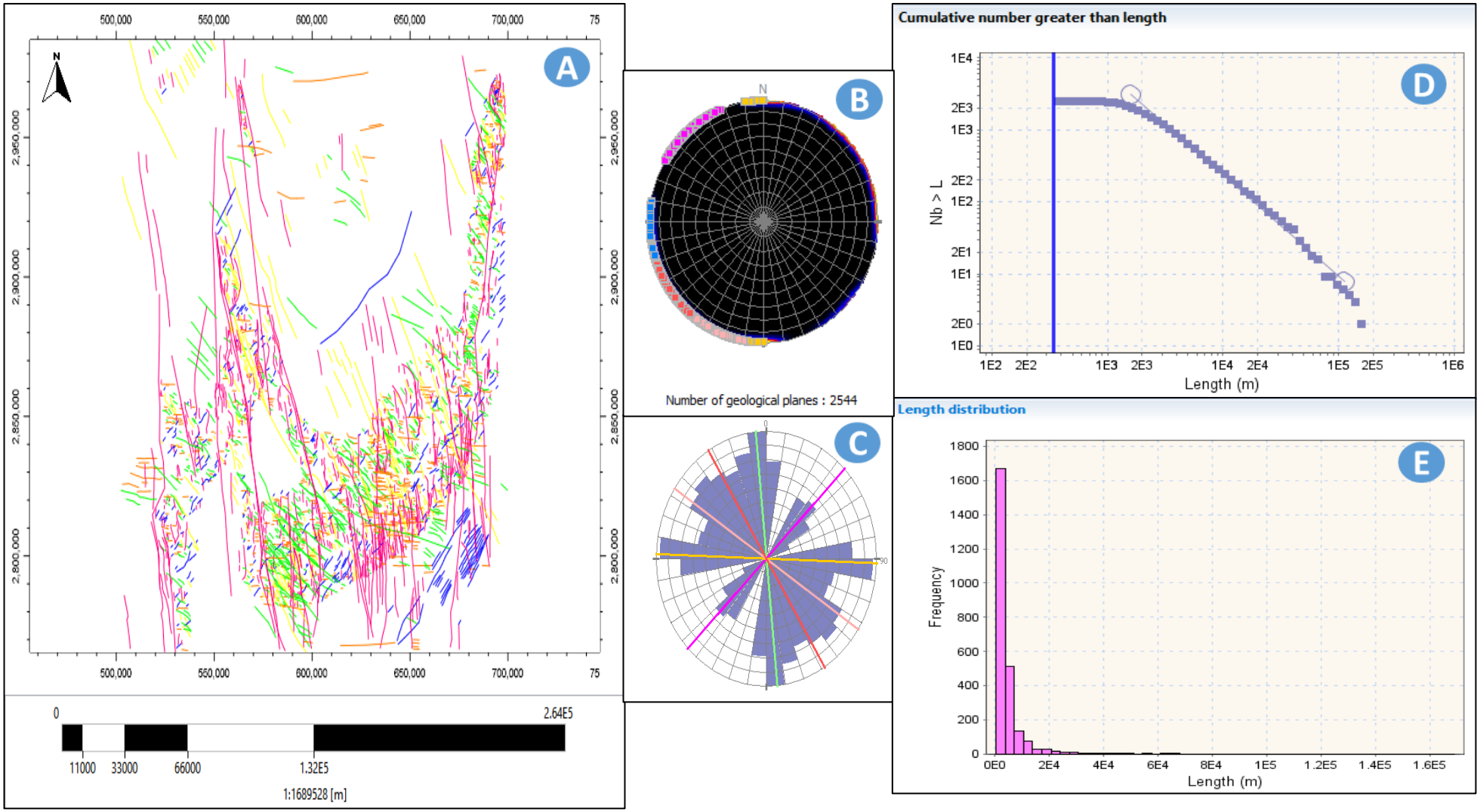

Figure 27: Total faults characteristics. A- Total Major & Minor faults map in the area of study. B- Faults' pole orientation. C-Faults sets orientation. D- Length's Power Law distribution, E- Length distribution.

II-8-3D Fault Models

The 3D fault models are built based on different stratigraphic units in the area of study and the faults' length including the basement, Ajjers, In-Tahouite, and Tamadjert faults, respectively (Fig.28A, Fig.28B, Fig.29A, Fig.29B) and the major faults that affect the area of study (Fig.30B).

The Global 3D deterministic fault model built from the merge of all other models is used to illustrate different fracture sets, their density and analyze their interconnection in space, which help to understand fractures relationship, their chronology, origin and their discontinuity or continuity in the subsurface (Fig.30A).

The analysis of different models demonstrates that the Cambro-Ordovician formations have different mechanical stratigraphy units based on their thickness and lithology. The unique 3D deterministic fault model illustrates the faults distribution and helps to distinguish the mechanical Cambro-Ordovician units and the relationship between them (Fig.31).

The Tamadjert formation appears to be the most fractured unit due to the lithological characteristics. On the other hand, the In-Tahouite is the least fractured formation due probably to its shaly nature. The basement fracture has a different impact on the Cambro-Ordovician sedimentary cover and it appears that it structured the Cambro-Ordovician units.

The Cambro-Ordovician formations are characterized by brittle tectonic style, linked with major basement faults inherited from the Pan-African orogeny, which is responsible for the creation of an extensive fracture network comprising major vertical faults. The analysis of geological maps show that a dense net of faults and folds have affected the Paleozoic.

The major structures correspond to N-S-trending dextral strike-slip faults and NNW-SSE to N-S faults. Two major fault corridors can be distinguished which design the Mouydir basin edges. They start from the Hoggar shield and continue to the north in divergent directions in the Saharan platform. They are oriented NNE to NS and NNW to NS constituting Amguid and Idjerane spur respectively.

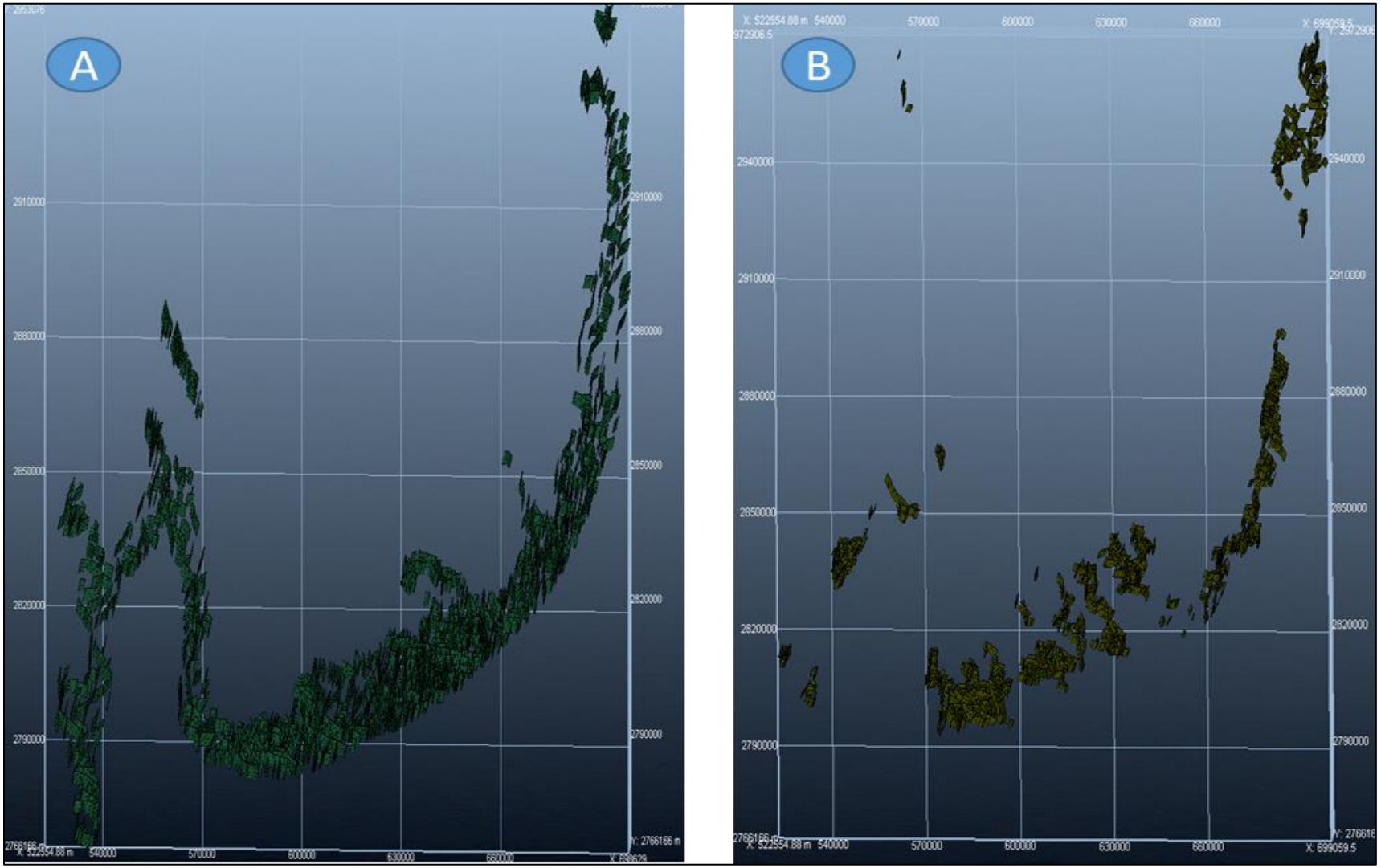

Figure 28: A- The 3D basement faults model. B- The 3D Ajjers' faults model

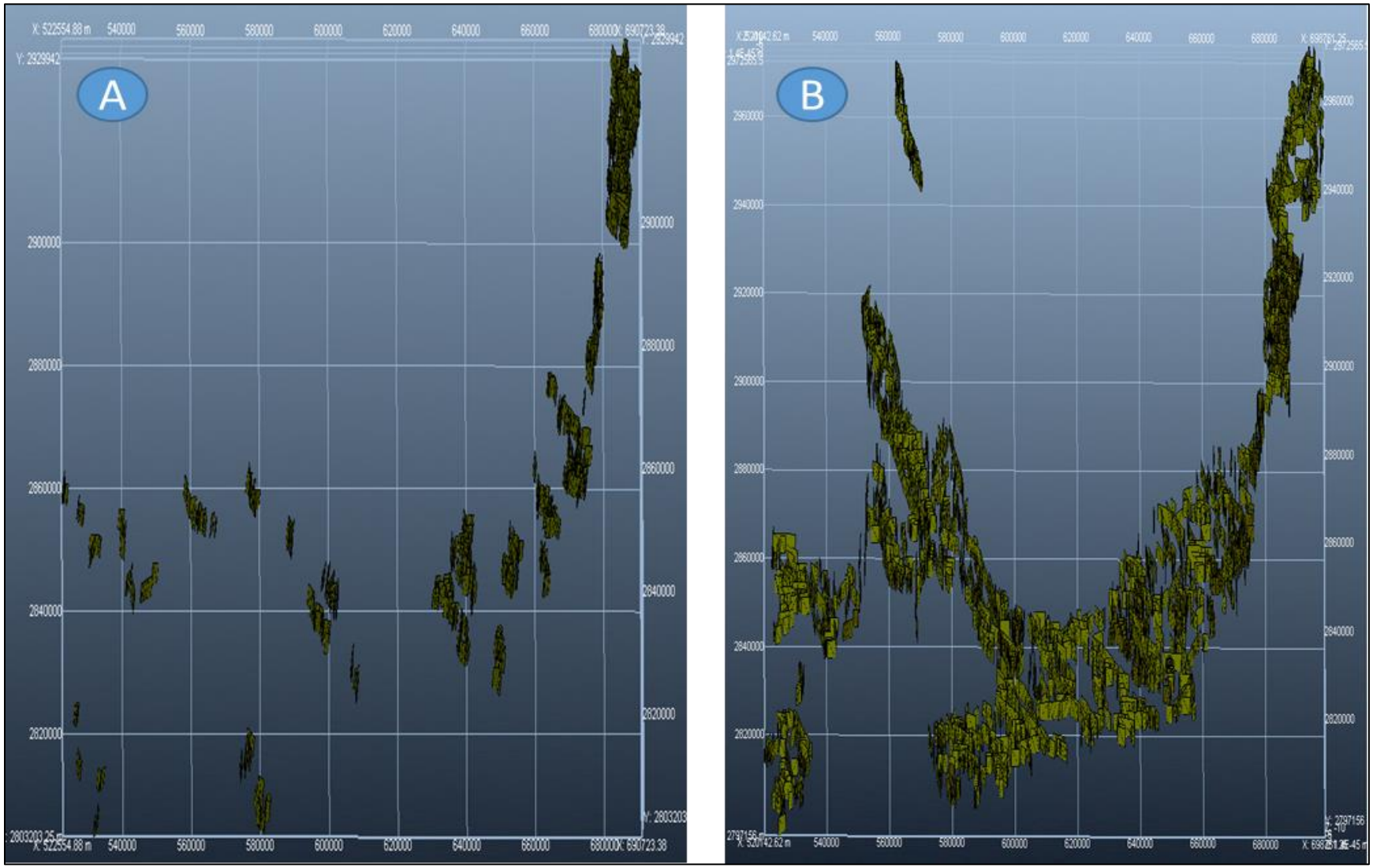

Figure 29: A- 3D In-Tahouite faults model. B- 3D Tamadjert faults model.

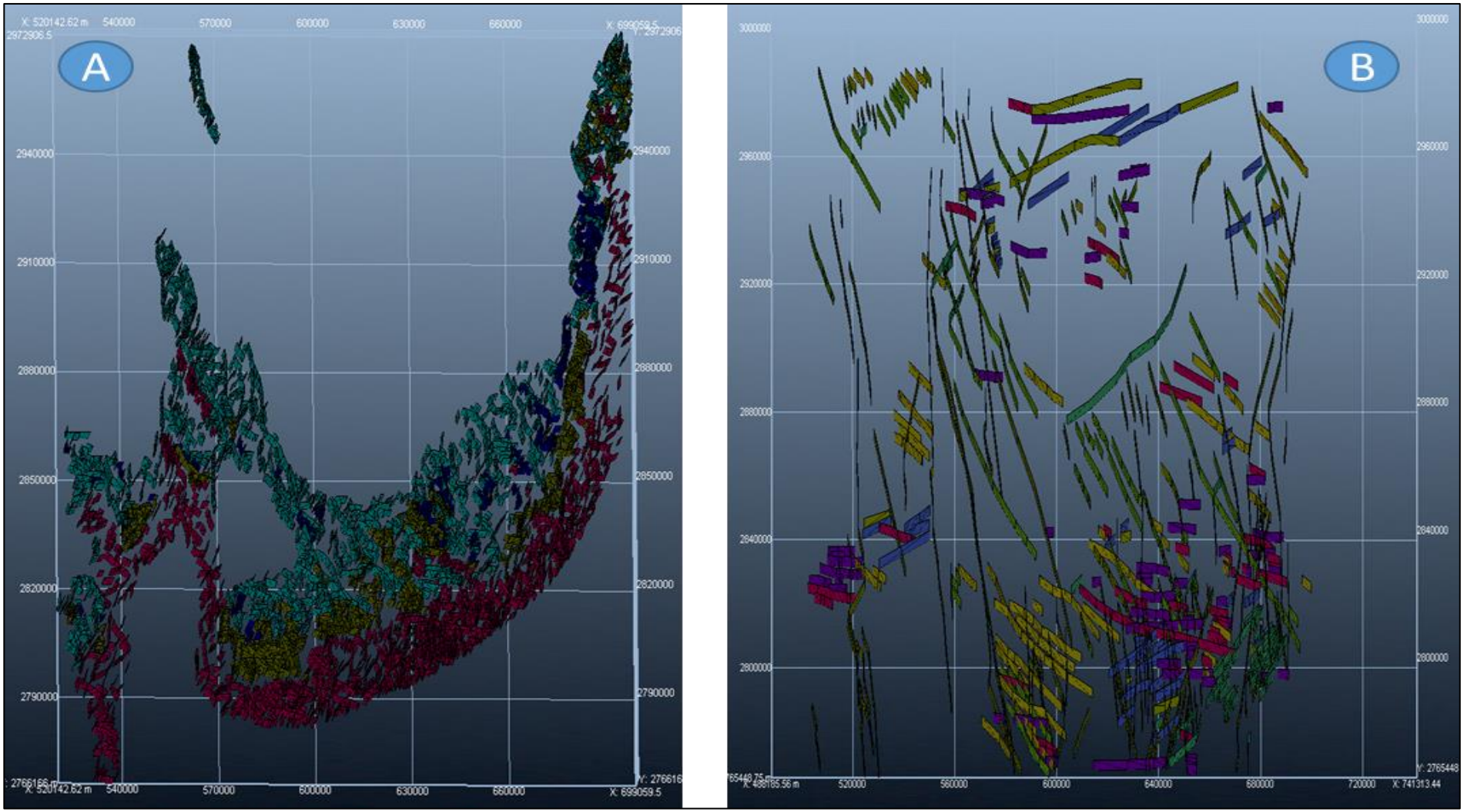

Figure 30: A- The 3D global faults model. B- The 3D Major faults model.

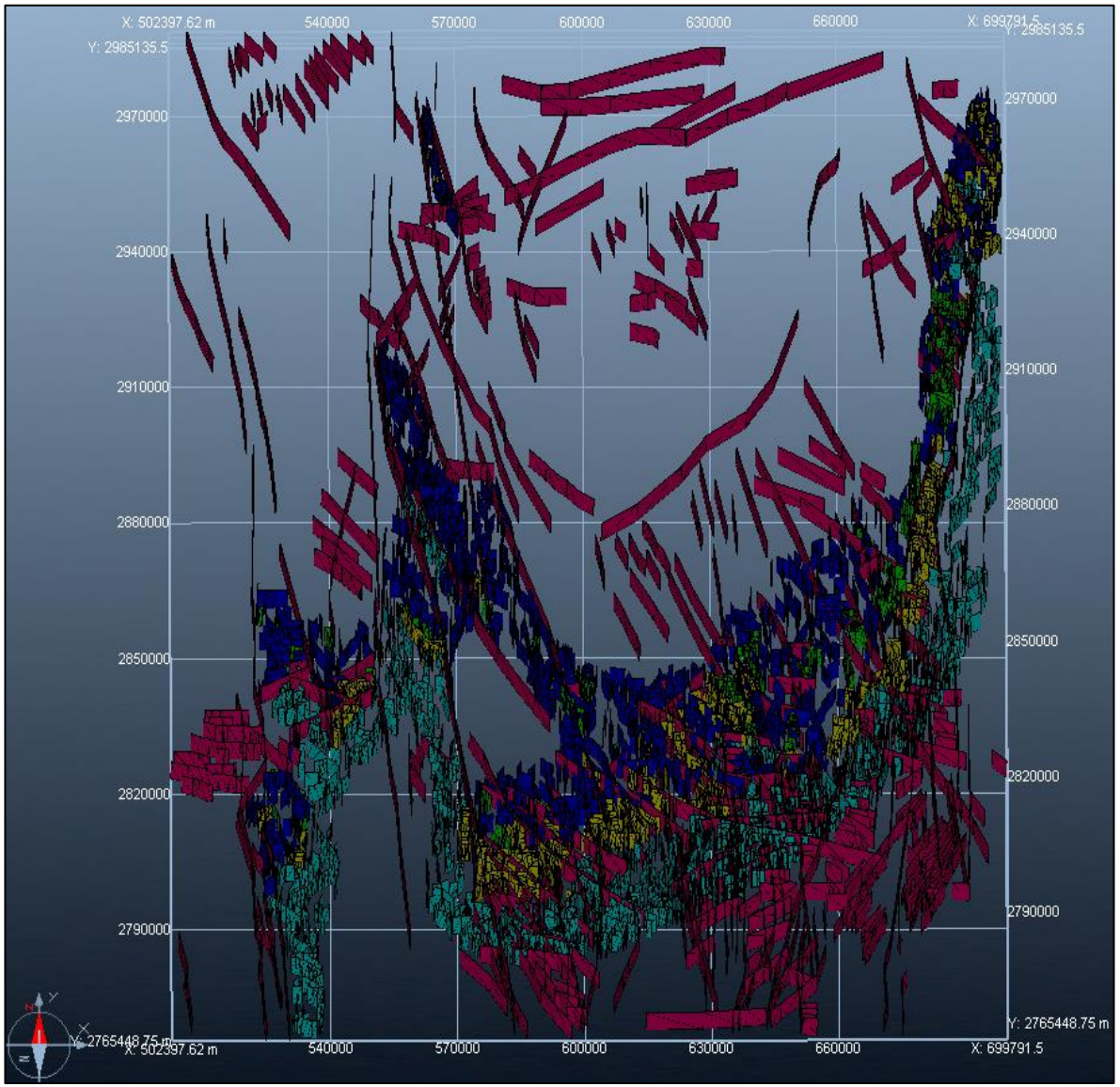

Figure 31: 3D Total faults model.

II-9-Fracture Intensity and Density

The spatial density of fractures is known to vary as a function of distance from larger structures and is a critical attribute for assessing the transport properties of a rock mass (Healy et al, 2017). Maps of spatial density can provide insight into the processes of shear fracture growth from the interaction and coalescence of constituent small fracture (Moore and Lockner, 1995).

FracPaQ™ is A MATLAB™ toolbox for the quantification of fracture patterns developed by Healy et al, 2017, it provides two measures of spatial density calculated from the input 2D fracture data. Fracture intensity, labelled P21 by Dershowitz and Herda (1992), has units of m−1 and is defined as the total length of fracture in a given area (hence units of m/m2 = m−1). Fracture density, labelled P20 by Dershowitz and Herda (1992), has units of m−2 and is defined as the number of fractures per unit area.

Circular scan window method of Mauldon et al. (2001) was used to calculate an estimate of fracture density and intensity of the area of study by generating 'Estimated Density, P20' and 'Estimated Intensity, P21' maps of the fracture in the area of study (Fig. 32A). The fractures related to the Total fracture network were digitalized using Neuralog software and loaded as an ASCII file on FracPaQ toolbox.

The estimated fracture intensity map shows high intensity that is defined as the larger length of fractures per unit area in border of the zone of interest, which correspond to the edges of the Mouydir basin (Fig.32B). This pattern of fracture abundance is consistent with the through-going strike slip fractures oriented N-S and NW-SE. The density map show 2 main trends oriented in the same direction of the major faults N000 and N150 (Fig.32C).

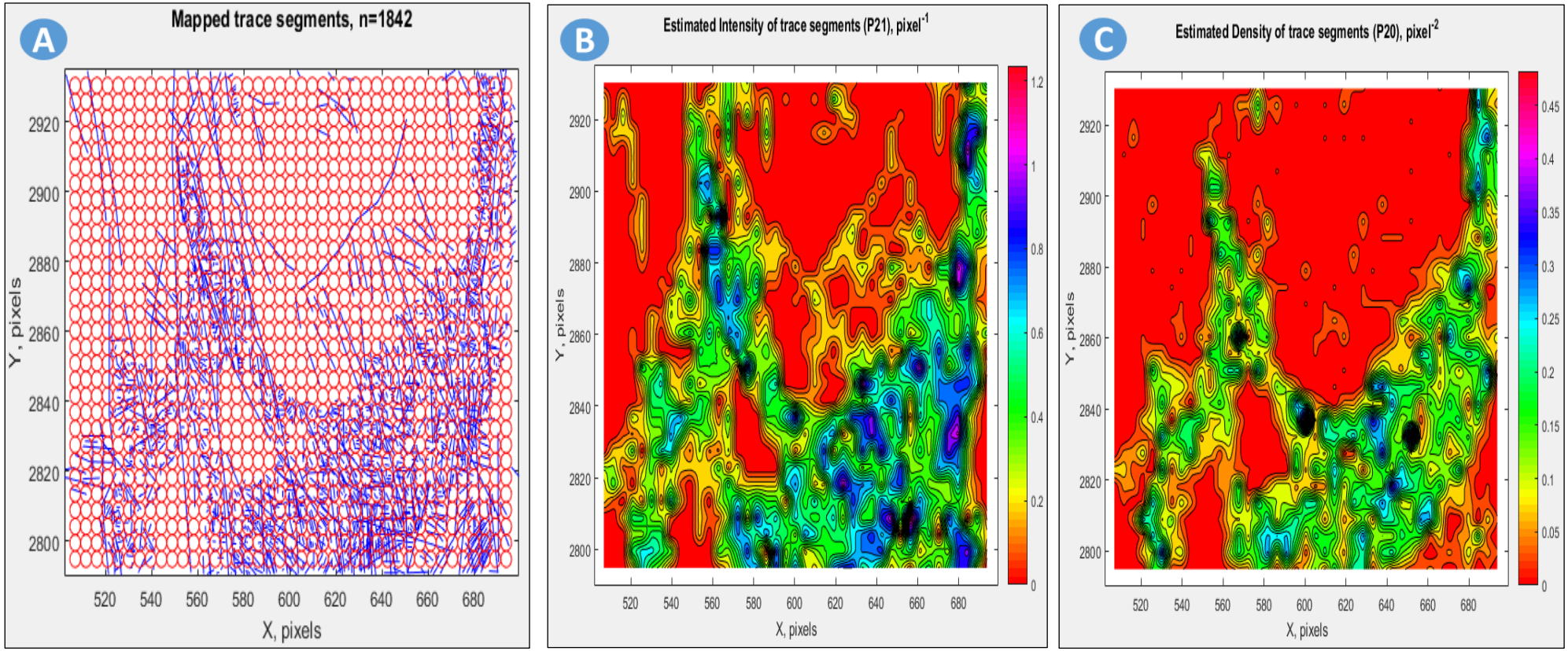

Figure 32: Scan circle using the method of Mauldon et al. (2001), Estimated fracture intensity (P21) and Estimated fracture density (P20) maps in the area of study.

II-10-Fracture Connectivity, permeability, and wavelet analysis

FracPaQ currently assumes that the input fracture traces lie on a statistically flat 2D surface, so that the effects of topography on the appearance of fracture traces does not require correction (Healy et al, 2017). The quantification of lengths and orientations is then reduced to simple operations in coordinate geometry.

The orientation distribution in a fracture pattern is important for unravelling the tectonic history of the rocks and in controls rock mass behavior with respect to attributes such as permeability and strength (Healy et al, 2017). Crack tensor plot is used to generate 2-dimensional crack tensors from the fracture traces (Oda et al., 1983 and Suzuki et al., 1998).

The crack tensor combines data from the orientation distribution (angles) with the sizes (lengths) of the fractures and their spatial density to provide a single dimensionless measure of a crack pattern (Fig.33).

The crack tensors of 0th, 2nd, 4th and 8th rank can be related to other physical properties, such as bulk permeability, bulk elasticity and the acoustic velocities such as P- and S-wave anisotropy (Healy et al, 2017).

The orientations used in the crack tensor calculation are the poles to the fracture trace segments; and therefore the magnitude of the tensor is largest in directions perpendicular to those shown in the rose diagram for the same data, which uses the angles of the trace segments, and not the poles (Healy et al, 2017).

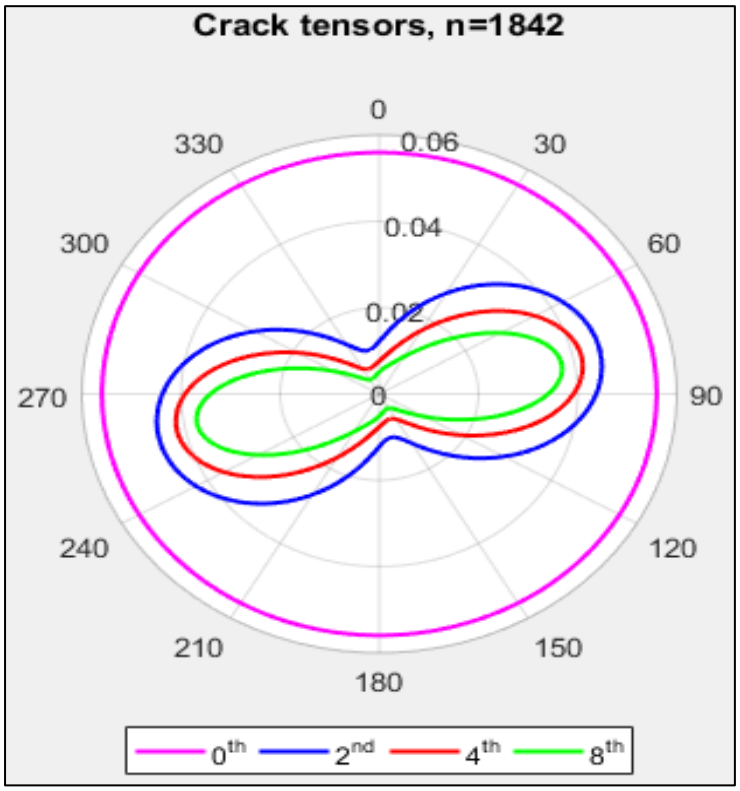

Figure 33: Crack tensors for the fracture pattern. 0th, 2nd, 4th and 8th rank crack tensors are shown in different colors.

According to Healy (2017), FracPaQ also provides an estimate of permeability in 2D using the cubic law, a parallel plate assumption and the crack-tensor formulation. (Suzuki et al. 1998); and (Brown and Bruhn, 1998). The crack tensor (Oda et al., 1983) incorporates information about fracture sizes, orientations and spatial densities in a single measure.

The Ternary plot of segment connectivity is generated for the fracture that affect the area of study (Fig.34). The ternary plot (Manzocchi, 2002), shows the relative proportions of isolated (I), splay or abutment (Y), and intersection (X) nodes in the fracture network. Better connected fracture patterns plot towards the base of the triangle (i.e. a higher proportion of X+Y nodes) and the worst towards the summit of the triangle.

The fracture network in the area of study shows that 2% of fractures are slay, 13% have intersection with each other, and 85 % of fractures are isolated. The Connectivity line in this case is less than 1. If the hydraulic conductivity of the fractures differs significantly from that of the rock matrix (either higher or lower) then the connectivity of the network has implications for fluid flow through the rock mass (Healy et al, 2017).

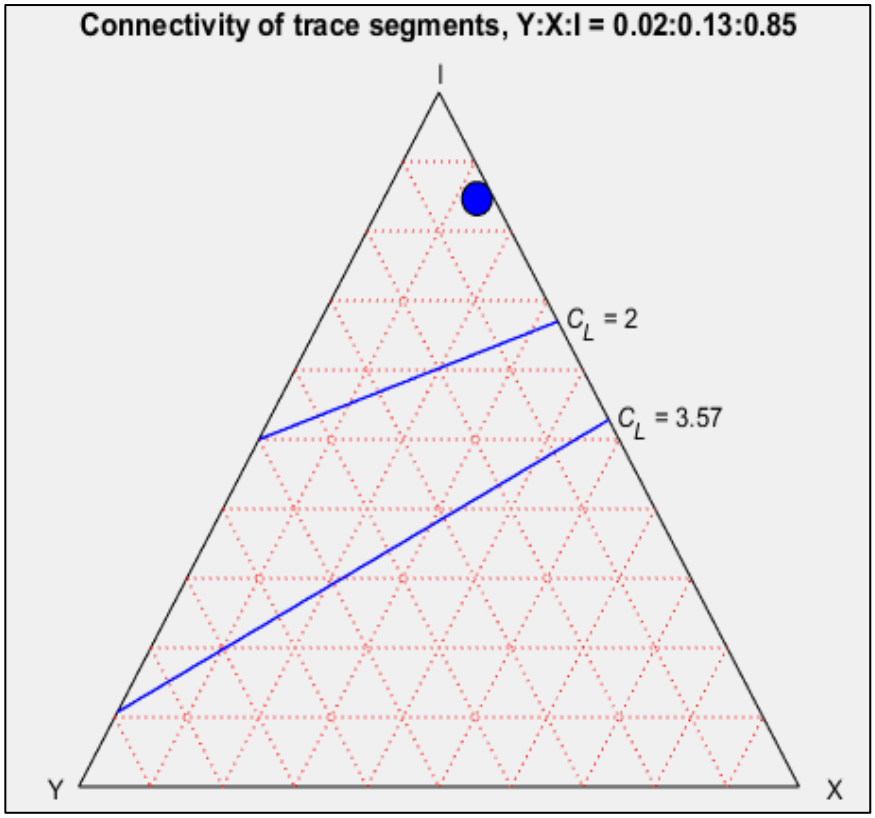

Figure 34: A ternary plot of fracture segment connectivity for the fracture pattern in the area of study. Two contour lines for Connections per Line (CL) are also shown, using indicative values described by Sanderson & Nixon (2015).

FracPaQ has a Permeability ellipse option to generate two plots of permeability anisotropy, one in the direction of flow and one in the direction of fluid pressure gradient (Long et al., 1982). However, surface roughness of fractures is not considered in the estimate of 2D permeability.

The different Permeability are calculated using the 2nd rank crack tensor using the method of Oda et al. (1983) and Suzuki et al. (1998). Plotting of the ellipses follows the method of Long et al. (1982), with the semi-axes scaled as √k1 and √k2 for the direction of flow, and scaled as 1/√k1 and 1/√k2 for the direction of gradient, where k1 is the maximum permeability and k2 is the minimum (Fig.35 A &B).

The permeability calculation is based on a parallel plate model of fractures, and a constant default aperture of 1 x 10^{-3} units is assumed. The units of permeability calculated in FracPaQ default to pixels^2, where a constant aperture applied to all fractures in the network (Healy et al, 2017).

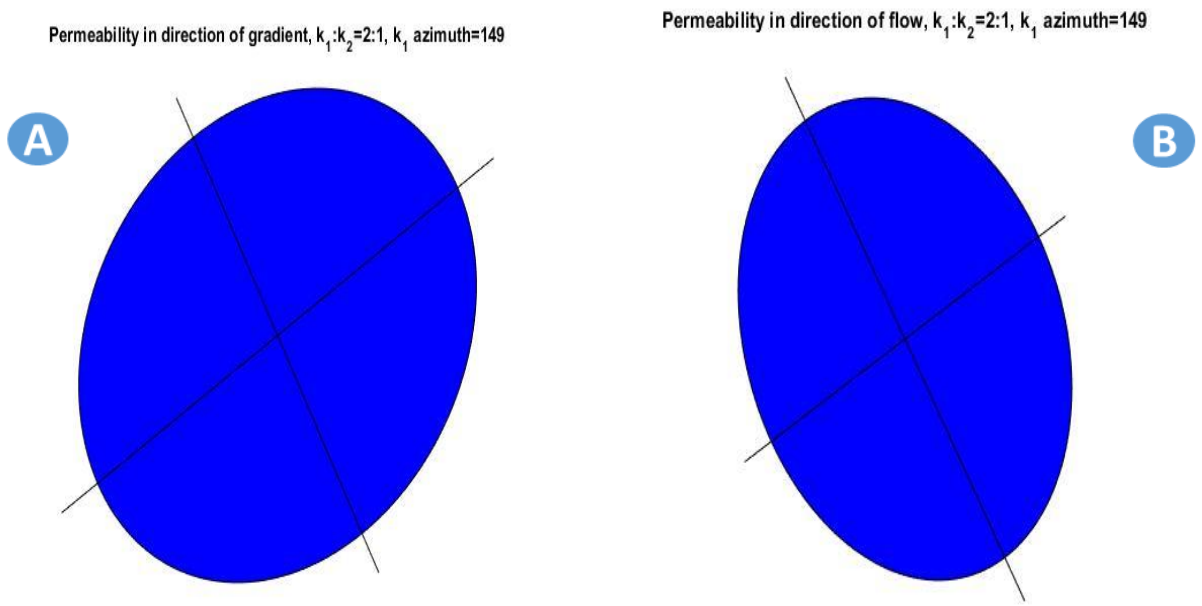

Figure 35: Permeability of a fracture network in the area of study, plotted as 2-D ellipses to visualize the anisotropy in the direction of pressure gradient (A) and the direction of flow (B).

The permeability k1 azimuth in the direction of gradient is oriented parallel to the shorter, high-density fracture set. On the other hand, the permeability k1 azimuth in the direction of flow is oriented parallel to the higher, high-density fracture set. The smaller fracture set may have dominated the k_1 azimuth.

FracPaQ version implements 2D wavelet analysis of fracture maps, using either Morlet or Mexican hat wavelet filters (Rizzo et al., 2017b). Wavelet analysis (WA) is based on scaling and moving a filter, the selected wavelet, onto a signal, which is a binary fracture trace map (Fig.36 & Fig.37). Compared to the classical Fourier Transform, WA results are better for two reasons; the first one is the size of the wavelet can be adjusted according to the scale of the entity under consideration.

The second one is the wavelet can be selected to best match the geometry of the entity, i.e. cracks. The Morlet wavelet is superior to the Mexican hat wavelet in quantifying scale transitions in 2D fracture maps (Rizzo et al., 2017b). For each 'a' value (selected length scale), three plots are produced: the Wavelet Coefficient (WC) map, the rose diagram of optimal orientations and the histogram of WC values.

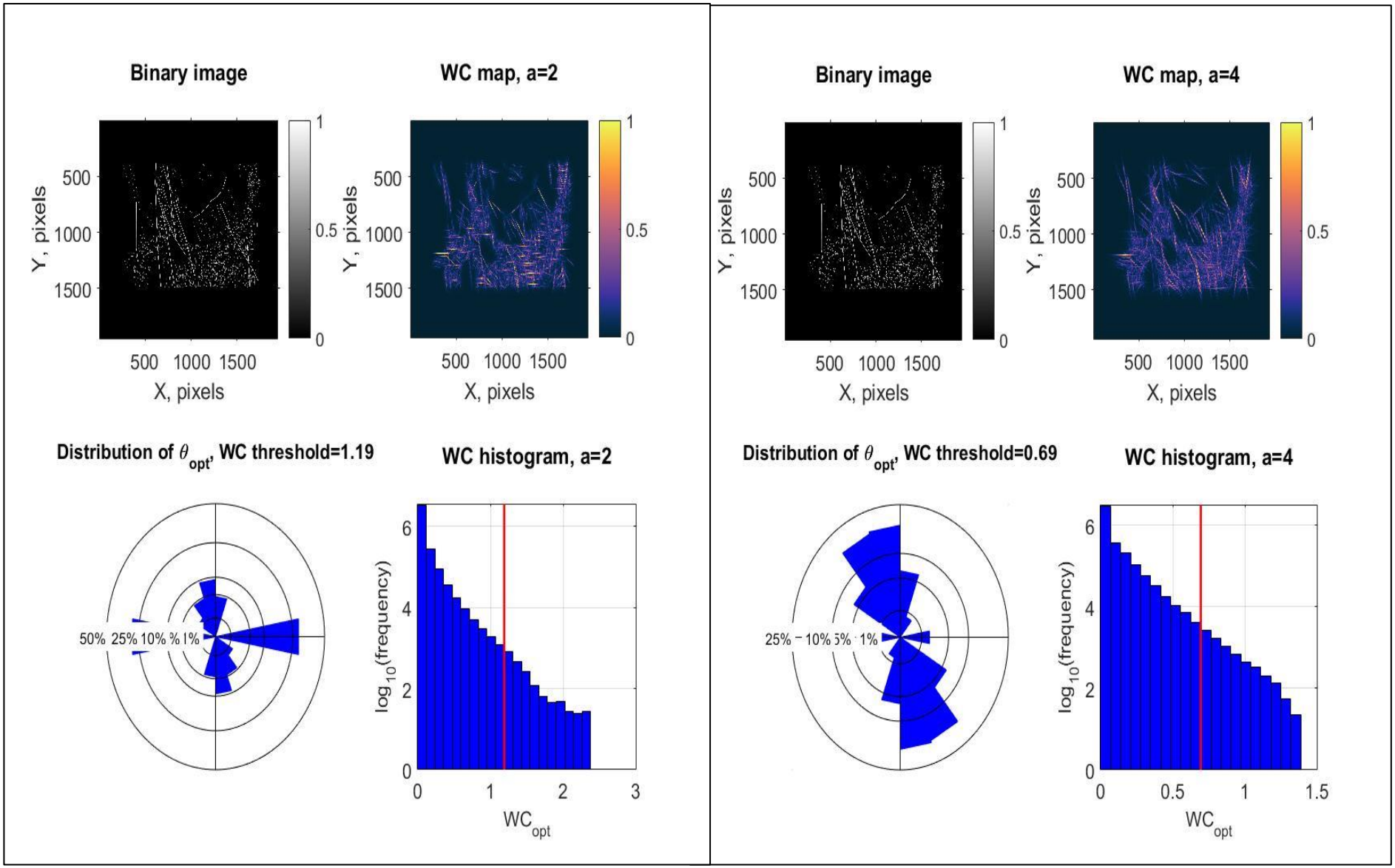

Figure 36: Wavelet analysis in FracPaQ. Left side shows results from Morlet wavelet analysis at a length scale of a=2, and right side shows same analysis for a length scale a=4. Note how the orientation distribution (rose diagrams) change at bigger length scales.

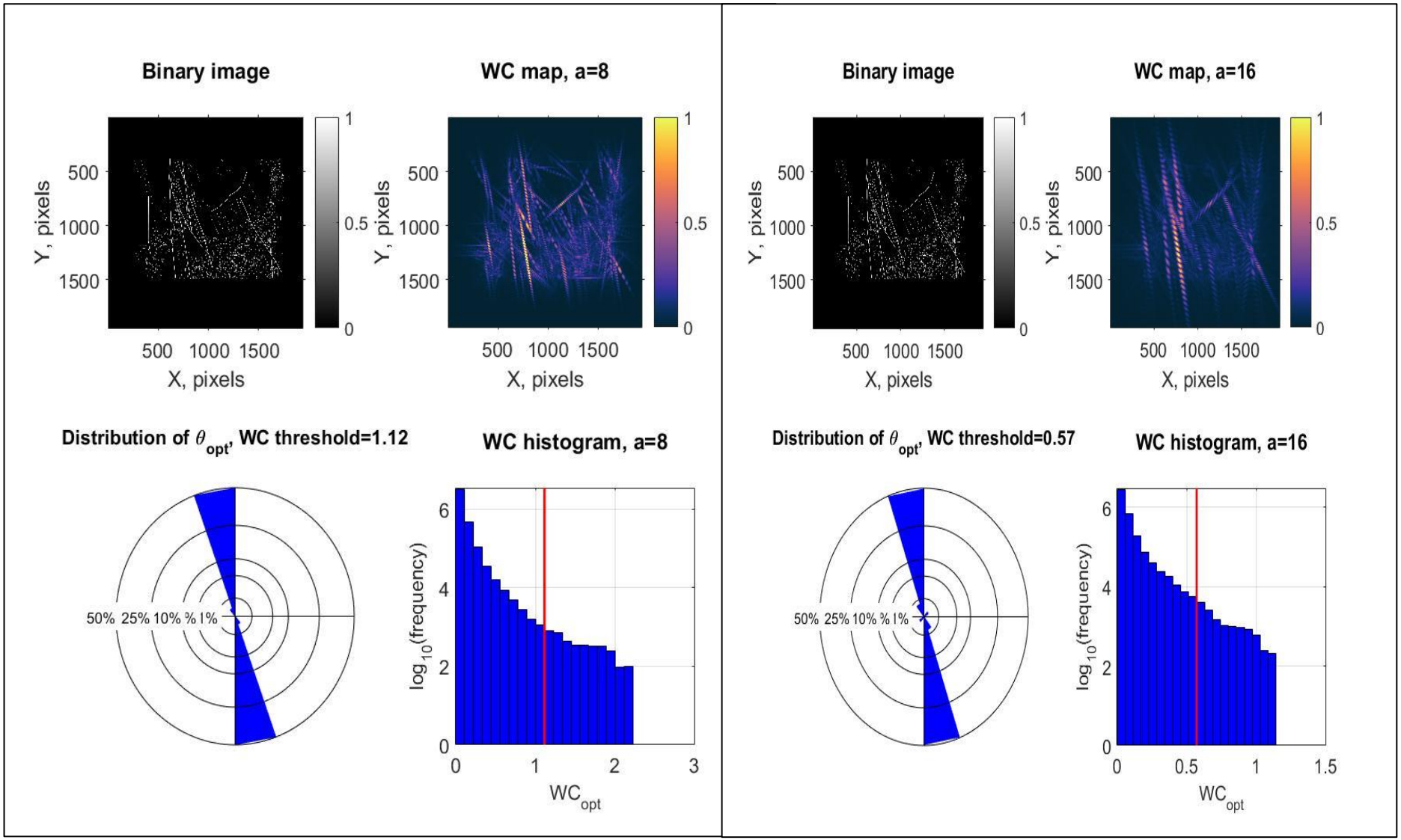

Figure 37: Examples of output from Wavelet analysis in FracPaQ. Left side shows results from Morlet wavelet analysis at a length scale of a=8, and right side shows same analysis for a length scale a=16. Note how the orientation distribution (rose diagrams) change

II-11-Discussion

The 3D surface fault models related to different units are generated using digitized fault lineaments showing faults length, connectivity and orientation, which aid in the understanding of their continuity, kinematics and chronology using other data like geological maps. Each formation of the Cambro-Ordovician shows a specific mechanical stratigraphy unit based on its thickness and lithology. The merge of these fault models helps to generate a unique deterministic fault model, which illustrates the spatial faults distribution and the relationship between the basement's faults and the sedimentary cover.

The analysis of different fracture networks affecting the basement and the Cambro-Ordovician units show that they carry fractal nature with some exceptions due to the few number of fracture. The Cambro-Ordovician formations are characterized mainly by brittle tectonic style, linked with major basement faults inherited from the Pan-African orogeny, which is responsible for the creation of an extensive fracture network comprising major vertical faults (WEC, 2005). The major structures correspond to N-S-trending dextral strike-slip faults, and NNW-SSE to N-S trending reverse faults and folds. (Haddoum & al, 2001).

Two major faults can be distinguished which design the Mouydir basin edges, they start from the Hoggar shield and continue in diverge direction in the Saharan platform. They are oriented NNE to NS and NNW to NS constituting Amguid and Idjerane spur, respectively. The longer the fracture the greater its width (Barlberg & al. 1991). These major faults constitute large fracturing corridors with an intense deformation generating the secondary faults and folds that can be notable from geological maps.

According to Haddoum (2001), the deformation and stratigraphic analysis show that this basin underwent a NNE-SSW to ENE-WSW shortening at about the Carboniferous/Permian transition or, more probably, during the Early Permian.

The faults sets N040, N060, and N090 constitute the fracture system compatible with the Hercynian shortening direction oriented N040 (Boudjema, 1987; Haddoum et al., 2001; Zazoun, 2001). The other fault sets could be attributed to the post-Hercynian tectonic events (Boudjema, 1987).

II-12-Conclusions

This study highlights a dense fracture networks that affect the Paleozoic series and Cambro-Ordovician units in the northern Hoggar shield. The fracture analysis illustrates different fracture sets, fracture density, fracture interconnection in space and in time. These helped to understand fractures chronology, their origin and their discontinuity or continuity in the subsurface. The area of study is characterized by statabound and non-statabound fracture models where the analysis of different outcomes demonstrates that the Cambro-Ordovician formations have different mechanical stratigraphy units based on their thickness and lithology. The unique deterministic fracture model illustrates the fractures' distribution and helps to distinguish the mechanical Cambro-Ordovician units and the relationship between them.

The Tamadjert formation appears to be the most fractured unit due to the lithological characteristics. On the other hand, the In-Tahouite is the least fractured formation due probably to its shaly nature. The basement fracture has a different impact on the sedimentary cover and it appears that it structured the Cambro-Ordovician units. The Cambro-Ordovician formations are characterized mainly by brittle tectonic style, linked with Major basement fractures inherited from the Pan-African orogeny, which is responsible for the creation of an extensive fracture network comprised of Major vertical fractures. The analysis of geological maps show that a dense fracture networks have affected the Paleozoic. The Major structures correspond to N-S-trending dextral strike-slip fractures and NNW-SSE trending sinistral strike-slip fracture.

Two Major fracture corridors can be distinguished which design the western and the eastern Mouydir basin's edges. They start from the basement in the Hoggar shield and continue to the north in divergent directions in the Saharan platform. They are oriented NNE to NS and NNW to NS constituting the Amguid and the Idjerane spurs respectively. The fracture analysis showed that the main fault sets in the Cambro-Ordovician reservoirs are oriented N000, N050, N090, N120, and N160 where the major structures correspond to N-S-trending dextral strike-slip faults, and NNW-SSE to N-S trending reverse faults.

The structural and stratigraphic analysis show a strong variation of the impact of the basement fracture on the Cambro-Ordovician sedimentary rocks. The same fracture sets affect the basement and all the Cambro-Ordovician units, which means that the basement's faults had a role on basin structuration and the sedimentary cover.

The fractures are more important in tight formations such as Ajjers and Tamadjert but less important in In-Tahouite formation due probably to its shaly units. The Tamadjert is the most fractured formation mainly due to its tight sandstone units (Dalle-de-M'kratta). On the other hand, the In-Tahouite formation is the less fractured formation due the presence of several shale units such as Azzel and Tiferouine units.

The N-S and N160 are major faults that affect the basement and the Paleozoic series. They are an inheritance of the Pan-African orogeny but they were reactivated later during different tectonic phases.

The fractures' length distribution shows a power law distribution with a coefficient ranging between 2.31 and 2.69 and high correlation coefficients. The fracture network in the area of study shows that 2% of fractures are slay, 13% have intersection with each other, and 85 % of fractures are isolated. The Connectivity line in this case is less than 1.

Chapter III: Fractal Analysis of 2-D Fracture Network

III-1-Introduction

The fractal analysis has been used by many authors to illustrate the two-dimensional geometry of fracture networks (Allegre & al., 1982; Davy & al., 1990, 1992; Davy, 1993; Cowie & al., 1995, 1996; Bour & Davy, 1998, 1999; Bour & al., 2002; Bonnet & al., 2001; Darcel & al., 2003a, b). The fractal geometry is a technique that can recognize and calculate how the geometry of patterns occurs from one magnitude to another (Mandelbrot, 1982). The fractal geometry provides a method for measuring the size scaling and spatial clustering of the full range of complex fracture networks (Barton, 1995).

Many studies have investigated the fractal nature of fracture networks at different scales and report varied values which range from 1 to 2 (Bonnet & al, 2001).

In our case study, the fractal dimension concept is applied on the 2D fracture networks that affect the basement and the Cambro-Ordovician in the northern part of the Hoggar shield, Algeria. The fractal dimension for these 2-D fracture networks is estimated using two methods.

The first method is the center distance algorithm, which considers only the fault centers distribution as a fractal. If the center's population is fractal, this function is proportional to a power law distribution. This dimension correlation gives an indicator of faults' center's spatial distribution (Beicip, 2018).

The second method is the box-counting algorithm, which considers the entire network to be fractal. The box-counting algorithm consists in discretizing a 2D fault trace map with different grids successively. The latter are square grids with constant limits but with a decreasing cell size. For each iteration, the cells intersected by at least one fracture trace are counted. The number of intersected cells is plotted versus the grid cell size, on a log-log scale (Beicip, 2018, Cacas & al, 2001).

The concept of fractal dimension is applied to verify whether or not the 2-D fracture networks that affect the basement and the Cambro-Ordovician reservoirs analog in the north Hoggar shield, Algeria have fractal dimension. The Ajjers, the In-Tahouite, and the Tamadjert units compose the Cambro-Ordovician reservoirs analog. They are characterized by stiff tectonic style showing dense fault network that affects all the Paleozoic series. The fractal dimension D_m

is estimated using the center distribution and box-counting algorithms. According to geometry and structure, the fractures are gathered into major and minor faults where the fractal analysis is estimated for the whole fault network and the different fractures sets.

III-2-Material and Methods

The fractal dimension for these 2-D fracture networks is estimated using two methods; the center distance algorithm, which considers only the fault centers distribution as a fractal and the box-counting algorithm, which considers the entire network to be fractal. Two main parameters were calculated; the fractal dimensions D_m and Rmin for the different networks and different fault sets. The data used for the 2-D fracture networks analysis include geological maps, satellite images, and digital elevation models.

The faults detection and digitalization are made on satellite images, curvature attribute map, and illumination attribute map (Fig.38). Two observation scales were chosen for this analysis. The first one is a mega-scale 1:100000, to analyze the lineaments that represent the major faults that affect the Paleozoic series in the area of study. The second scale is 1:25000, which is used to analyze the minor faults that affect the basement and the three units that compose the Cambro-Ordovician.

The fractal analysis used FracaFlow™ software to generate the different maps, histograms and plots. Four approaches were applied to define the different faults sets and fractal dimension.

The first approach was related to the Major faults' analysis.

The second approach was related to the analysis of the Minor faults that affect each geological formation separately including the basement and the Cambro-Ordovician units.

The third approach was related to the analysis of the whole Minor fault network that affect the basement and the Cambro-Ordovician units.

The fourth approach was consisted in the analysis of the merged Major and Minor fault network that affects the area of study

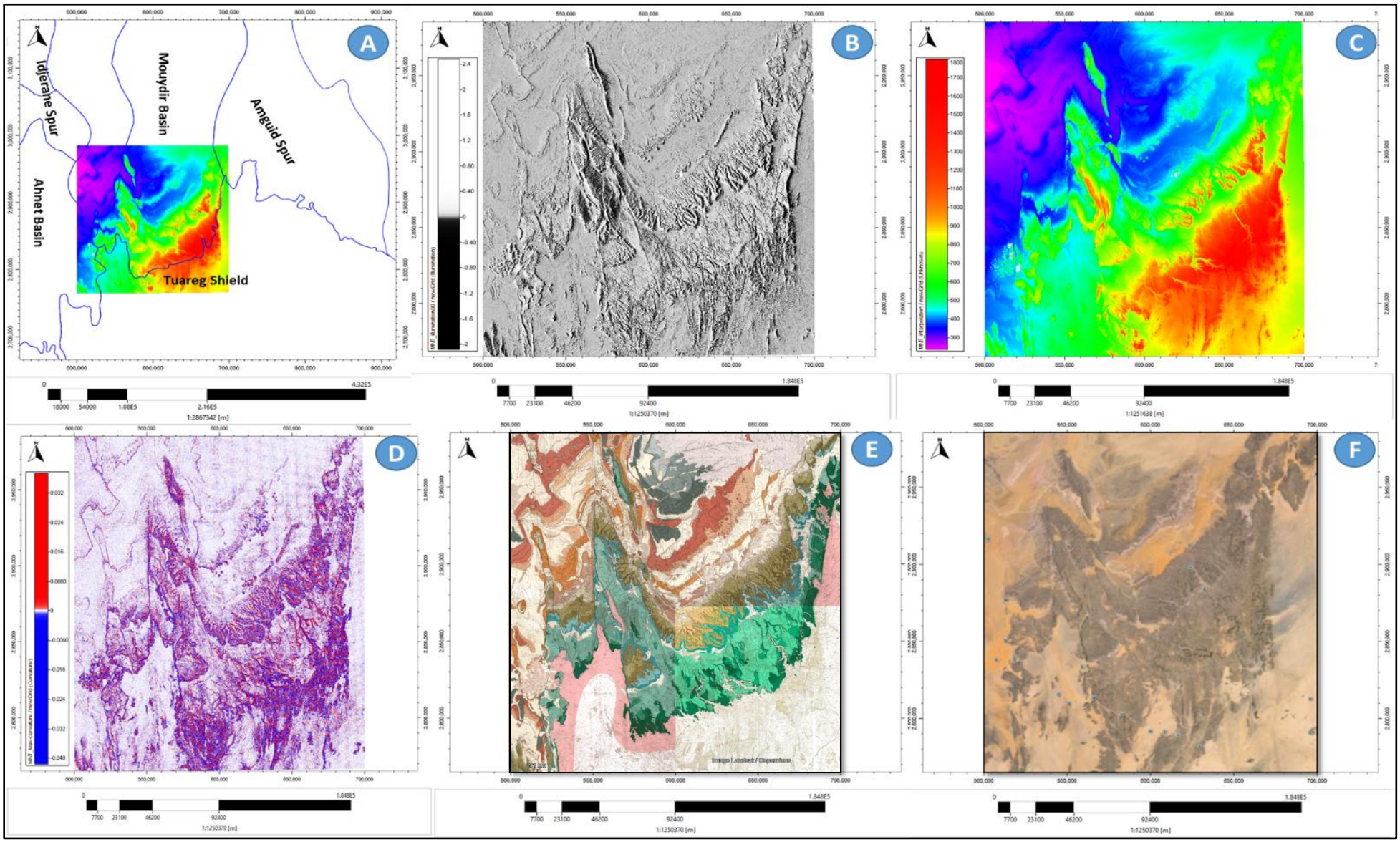

Figure 38: Input data for the applied method. A-Location of the area of study. B- Illumination map of the area of study. C- Digital Elevation Model of the area of study. D-Curvature map of the area of study. E-Geological maps of the area of study. F-Satellite images

III-3-Fractal Analysis

The fractal dimension for these 2-D fracture networks is estimated using two methods. The first method is the center distance algorithm, which considers only the fault centers distribution as a fractal and the second method is the box-counting algorithm, which considers that the entire network is a fractal. The fractal dimension for the major and minor faults were determined for the whole networks and for the different fracture sets.

In addition, Rmin, which is the distance between two centers for which the curve is not linear, was calculated for the whole networks and for the different fracture sets.

III-3-1-The first approach

This approach took into account only the Major fractures that affected the area of study. These fractures affect the basement and all the Paleozoic series. These fractures are Mode II fracture, characterized by long length, strike-slip kinematics, and affect all the Paleozoic series and continue in the Mouydir basin subsurface.

According to Haddoum, 2001, the main fracture sets that affect the Paleozoic series correspond to strike-slip faults and reverse faults.

This approach is applied to the whole area of the study where the fractal dimension is calculated for the major faults affecting the Paleozoic series. The area of study is affected by 394 major faults where seven faults sets are distinguished, N000, N040, N060, N090, N110, N130, and N150 respectively.

The whole fault network has a fractal dimension of 1.7114 and 1.57 using the center distance and the box-counting algorithm respectively. On the other hand, the different fault sets have a fractal dimension D_m ranging from 1.0536 to 1.5939 using the center distance algorithm and from 1.0091 to 1.3798 using the box-counting algorithm.

However, we have noticed that three fault sets have no fractal dimension using the box-counting algorithm, and they are, respectively, N060, N090, and N110 (Table-8, Fig.39 & Fig.40).

Table 8: Fractal dimensions related to the Major faults affecting the area of study

Data	Points	Fract dim.(center distance)	Fract dim.(box counting)	Rmin
All faults	394	1.7114	1.57	425.956
Major Faults-N000	100	1.5939	1.3798	1409.9569
Major Faults-N040	38	1.0573	1.0091	851.6644
Major Faults-N060	44	1.0637	novalue	843.3506
Major Faults-N090	59	1.2378	novalue	524.139
Major Faults-N110	37	1.2903	novalue	1493.9429
Major Faults-N130	59	1.5116	1.0802	1670.2399
Major Faults-N150	57	1.4246	1.1566	2543.0053

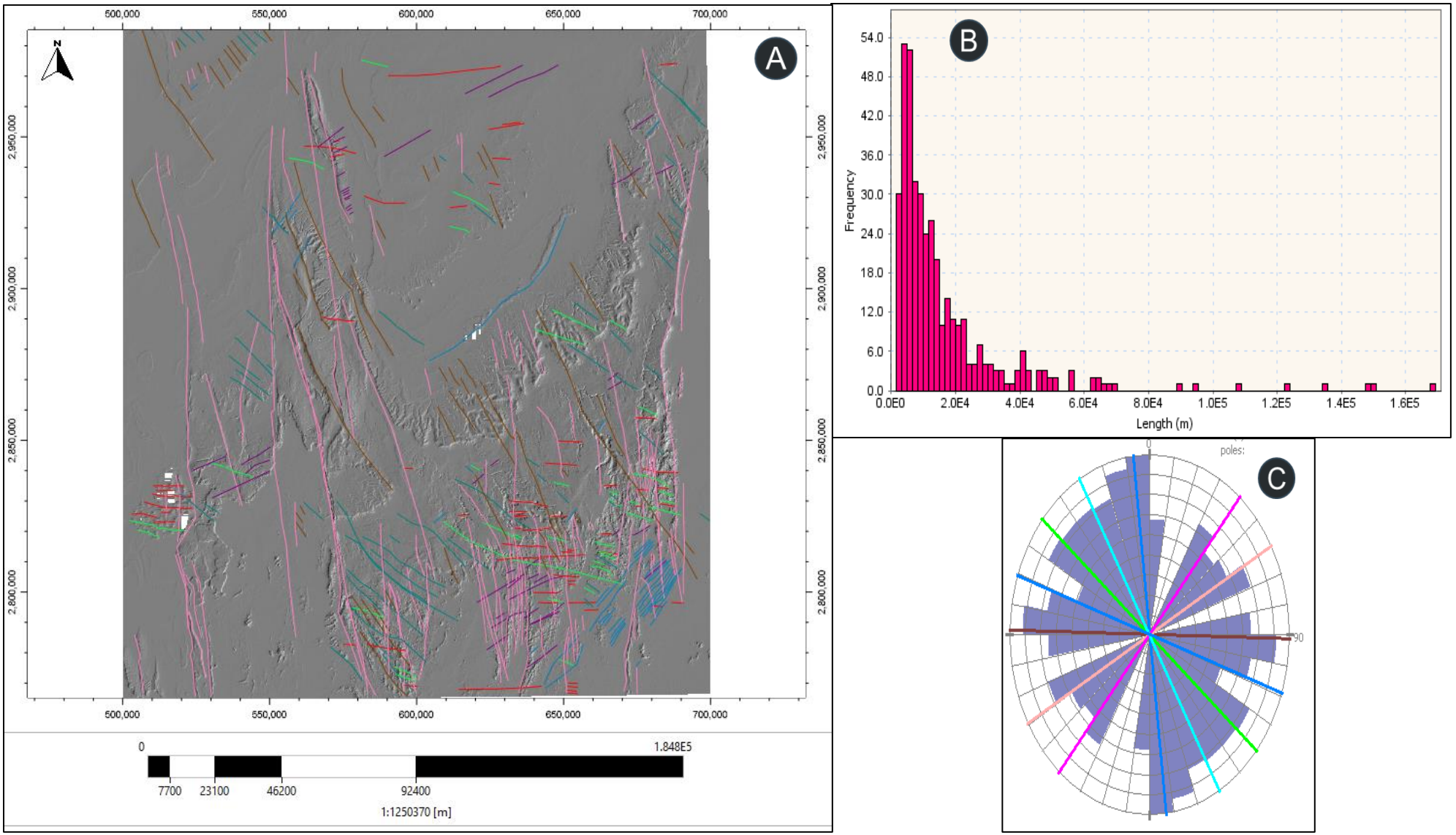

Figure 39: Major faults characteristics. A- Major faults map in the area of study. B- Major faults' length distribution. C- Major fault sets orientation

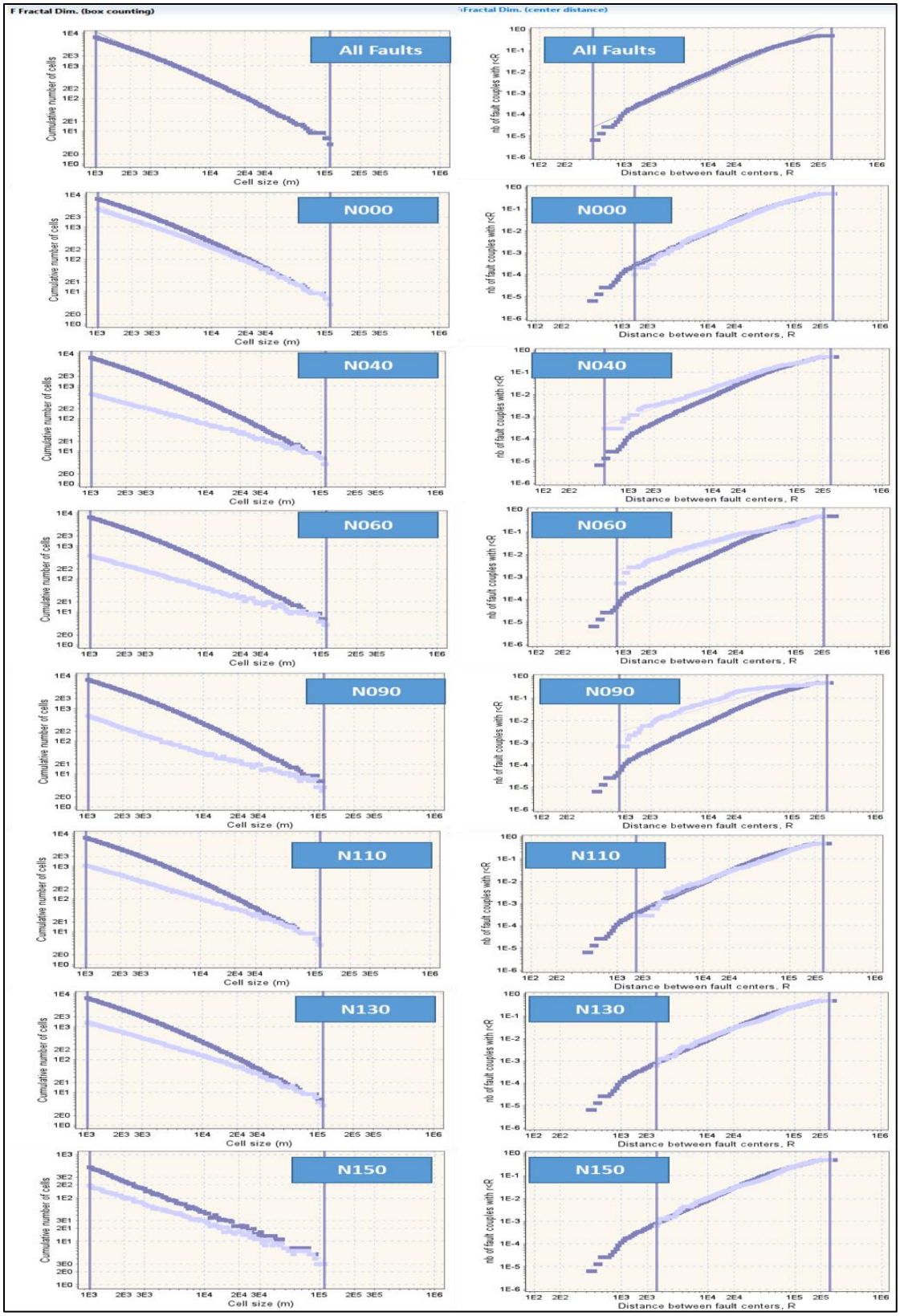

Figure 40: Fractal dimension distributions for the Major faults by fault set using the center distance and the box-counting algorithms

III-3-2-The second approach

This approach is applied on the different geological formations including the basement and the three Cambro-Ordovician units (Ajjers, In-Tahouite, and Tamadjert). Each unit is studied separately in order to understand the fractography of each unit that composes the Cambro-Ordovician reservoir and the basement formation based on their lithology.

This will help to understand the relation between the facies and the different fracture networks. For each unit, the fracture sets are determined and the length distribution is calculated. The fractal dimensions using center dimension and box-counting algorithms are estimated for the whole fracture network and for each fracture set, which composes the fracture network.

III-3-2.1- The basement formation

The basement is affected by 761 faults and it is considered to be one of the most fractured formation in the area of study. It is characterized by five fault sets, N000, N050, N090, N120, and N160, respectively.

The whole fault network has fractal dimension D_m of 1.705 and 1.3993 using the center distance and box-counting algorithm respectively. On the other hand, the different fault sets have a fractal dimension D_m ranging from 1.376 to 1.4693 using the center distance algorithm and from 1.0091 to 1.3798 using the box-counting algorithm. However, we noticed that the fault set N090 has no fractal dimension using the box-counting algorithm (Table-9, Fig.41 & Fig.43).

Table 9: Fractal dimensions related to the Minor faults affecting Basement formation

Data	Points	Fract dim.(center distance)	Fract dim.(box counting)	Rmin
All faults	761	1.705	1.3993	107.415
Basement-N000	256	1.4693	1.2163	385.8096
Basement-N050	123	1.3783	1.0512	453.2459
Basement-N090	121	1.376	novalue	661.2585
Basement-N120	116	1.4425	1.0149	632.9037
Basement-N160	145	1.4009	1.086	314.4352

III-3-2.2- The Ajjers formation

The Ajjers unit is affected by 492 faults. It is characterized by six fault sets, N000, N050, N090, N110, N130, and N150, respectively. The whole faults network has fractal dimension of

1.5945 and 1.2125 using the center distance and the box-counting algorithm respectively. On the other hand, the different fault sets have a fractal dimension D_m ranging from 1.1119 to 1.3777 using the center distance algorithm. For the box-counting algorithm, none of the fault sets have fractal dimension except for the set N000, where the fractal dimension is equal to 1 (Table-10 & Fig.42 & Fig.44).

Table 10: Fractal dimensions related to the Minor faults affecting Ajjers formation

Data	Points	Fract dim.(center distance)	Fract dim.(box counting)	Rmin
All faults	492	1.5945	1.2125	113.9189
Ajjer-N000	120	1.3777	1	293.8084
Ajjer-N50	36	1.1119	novalue	716.8985
Ajjer-N90	123	1.2062	novalue	285.2209
Ajjer-N110	52	1.2444	novalue	439.7315
Ajjer-N130	92	1.1953	novalue	518.2868
Ajjer-N150	69	1.2012	novalue	592.9249

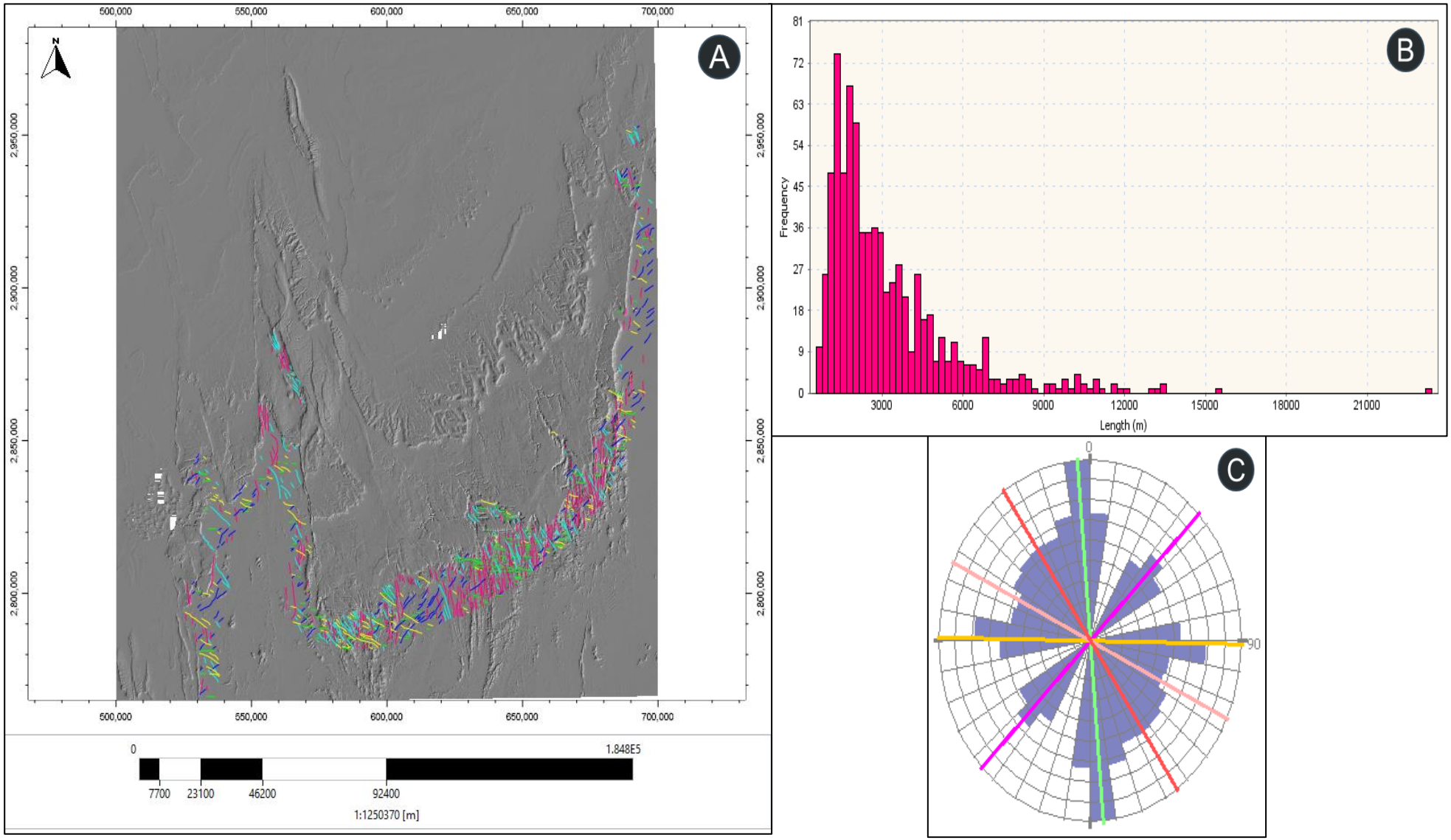

Figure 41: Basement faults characteristics. A- Minor faults map in the basement formation. B- Minor faults' length distribution. C- Minor fault sets orientation.

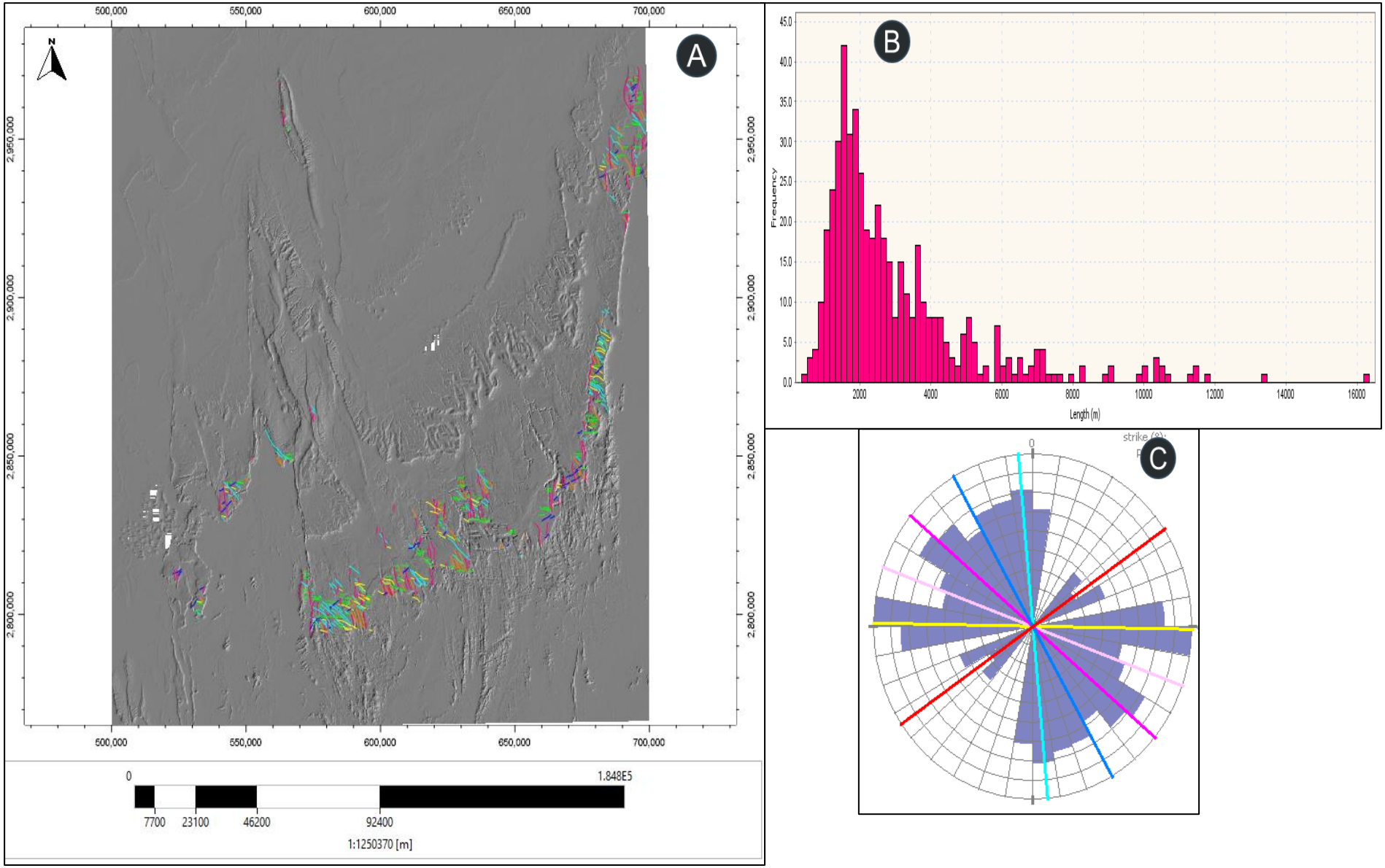

Figure 42: Ajjers faults characteristics. A- Minor faults map in the Ajjers formation. B- Minor faults' length distribution. C- Minor fault sets orientation.

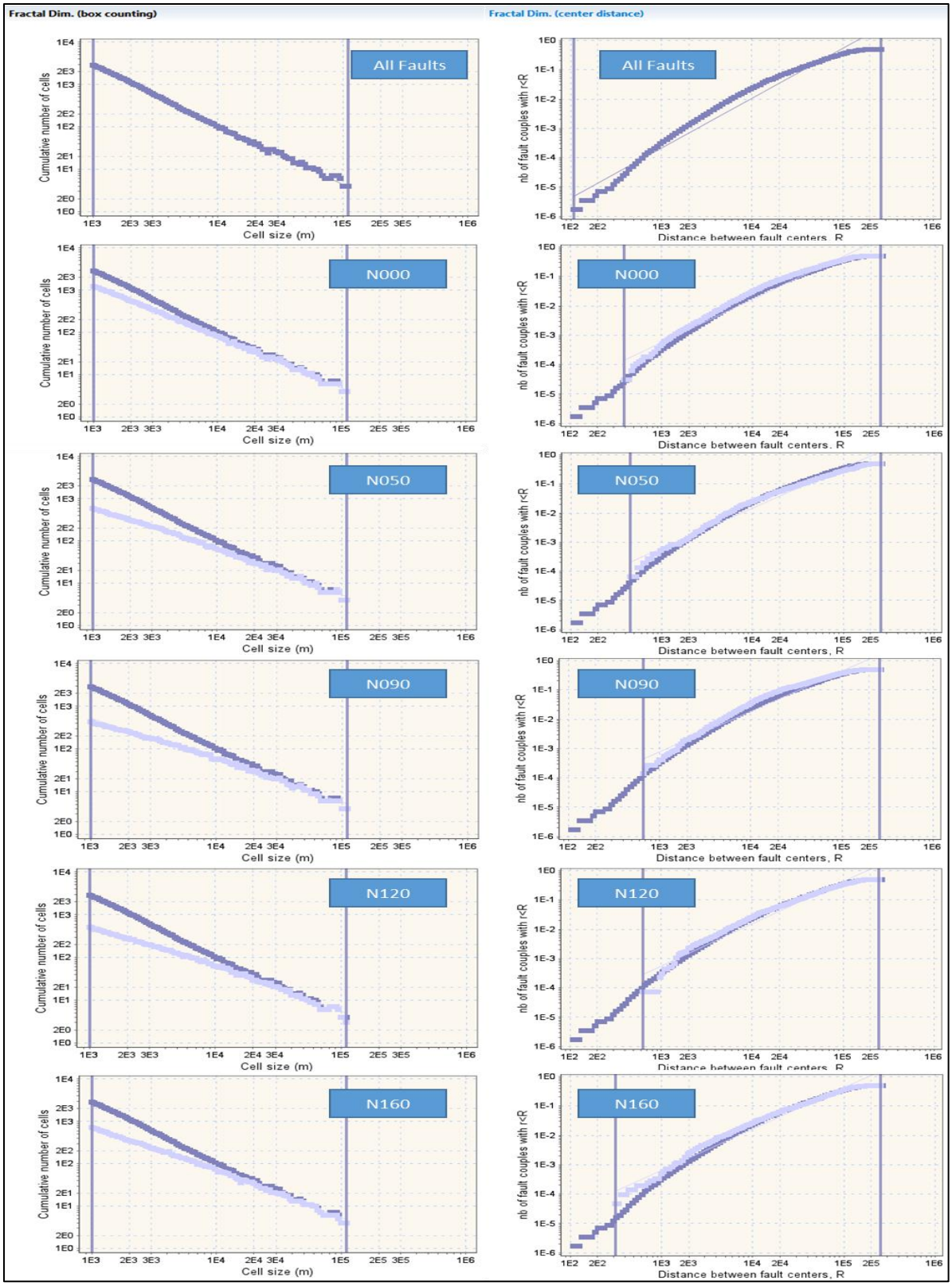

Figure 43: Fractal dimension distributions for the Minor faults in the Basement formation by fault set using the center distance and the box-counting algorithms.

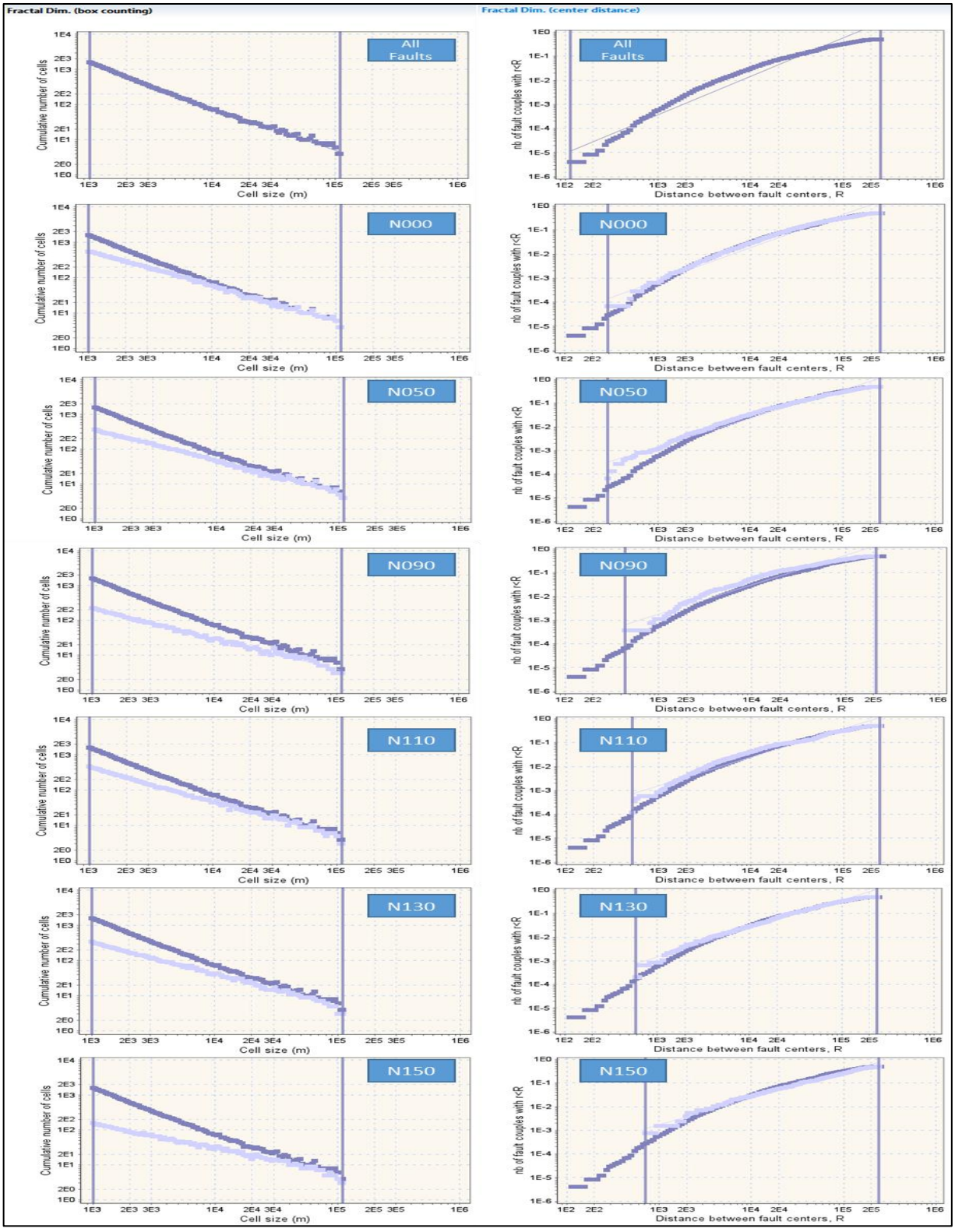

Figure 44: Fractal dimension distributions for the Minor faults in the Ajjers formation by fault set using the center distance and the box-counting algorithms.

III-3-2.3- In-Tahouite formation

The In-Tahouite unit is affected by 172 faults and it is considered the less fractured formation, probably due to the shaly units that compose it. It is characterized by five fault sets: N000, N050, N060, N090, and N130, respectively.

The whole fault network has fractal dimensions D_m of 1.3722 and 1.04 using the center distance and the box-counting algorithm respectively. On the other hand, none of the different fault sets have a fractal dimension D_m using the center distance or the box counting algorithms, except for the fault sets N090 and N130 which have fractal dimensions D_m of 1.0946 and 1.1392 using the center distance algorithm (Table-11, Fig.45 & Fig.47).

Table 11: Fractal dimensions related to the minor faults affecting In-Tahouite formation.

Data	Points	Fract dim.(center distance)	Fract dim.(box counting)	Rmin
All faults	172	1.3722	1.04	220.1225
In-Tahouite-N000	40	novalue	novalue	266.3499
In-Tahouite-N050	15	novalue	novalue	997.2087
In-Tahouite-N060	17	novalue	novalue	549.5823
In-Tahouite-N090	49	1.0946	novalue	615.7739
In-Tahouite-N130	51	1.1392	novalue	600.7082

III-3-2.4- Tamadjert formation

The Tamadjert unit is affected by 843 faults and is considered the most fractured formation due to the units' stiffness that compose it. It is characterized by five fault sets: N000, N050, N090, N120, and N160, respectively.

The whole fault network has fractal dimensions of 1.705 and 1.3993 using the center distance and the box-counting algorithm respectively. On the other hand, the different fault sets have a fractal dimension D_m ranging from 1.376 to 1.4693 using the center distance algorithm, and from 1.0091 to 1.3798 using box-counting algorithm. However, the fault set N090 has no fractal dimension using the box-counting algorithm (Table-12, Fig.46 & Fig.48).

Table 12: Fractal dimensions related to the minor faults affecting Tamadjert formation.

Data	Points	Fract dim.(center distance)	Fract dim.(box counting)	Rmin
All faults	843	1.6962	1.4099	82.0379
Tamadjert-N000	212	1.618	1.1874	427.2758
Tamadjert-N040	84	1.2823	novalue	969.4864
Tamadjert-N070	57	1.0858	novalue	787.2807
Tamadjert-N090	178	1.4913	1.0213	142.9118
Tamadjert-N120	171	1.4854	1.0853	466.2224
Tamadjert-N150	141	1.4881	1.1093	634.168

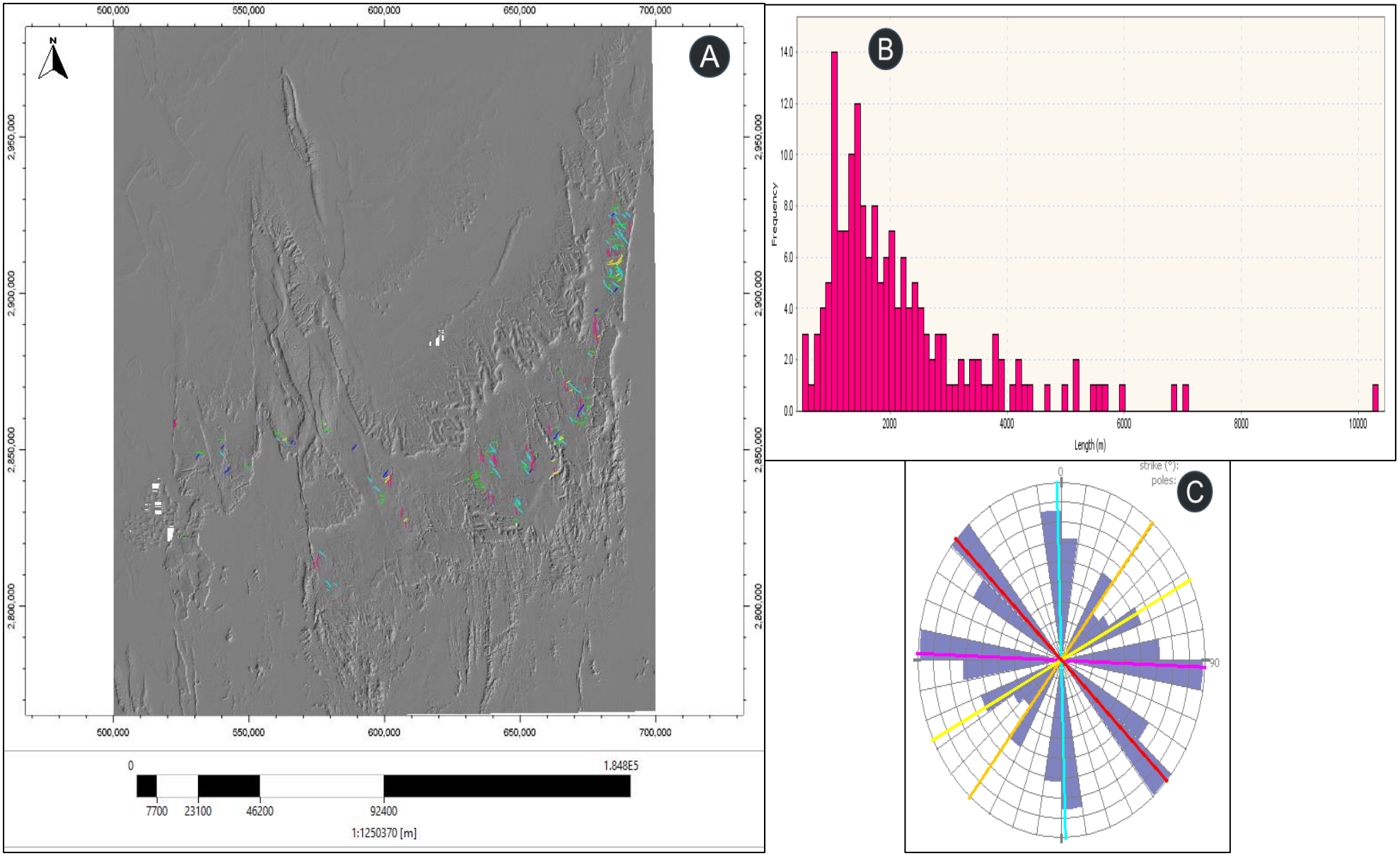

Figure 45: In-Tahouite faults characteristics. A- Minor faults map in the In-Tahouite formation. B- Minor faults' length distribution. C- Minor fault sets orientation.

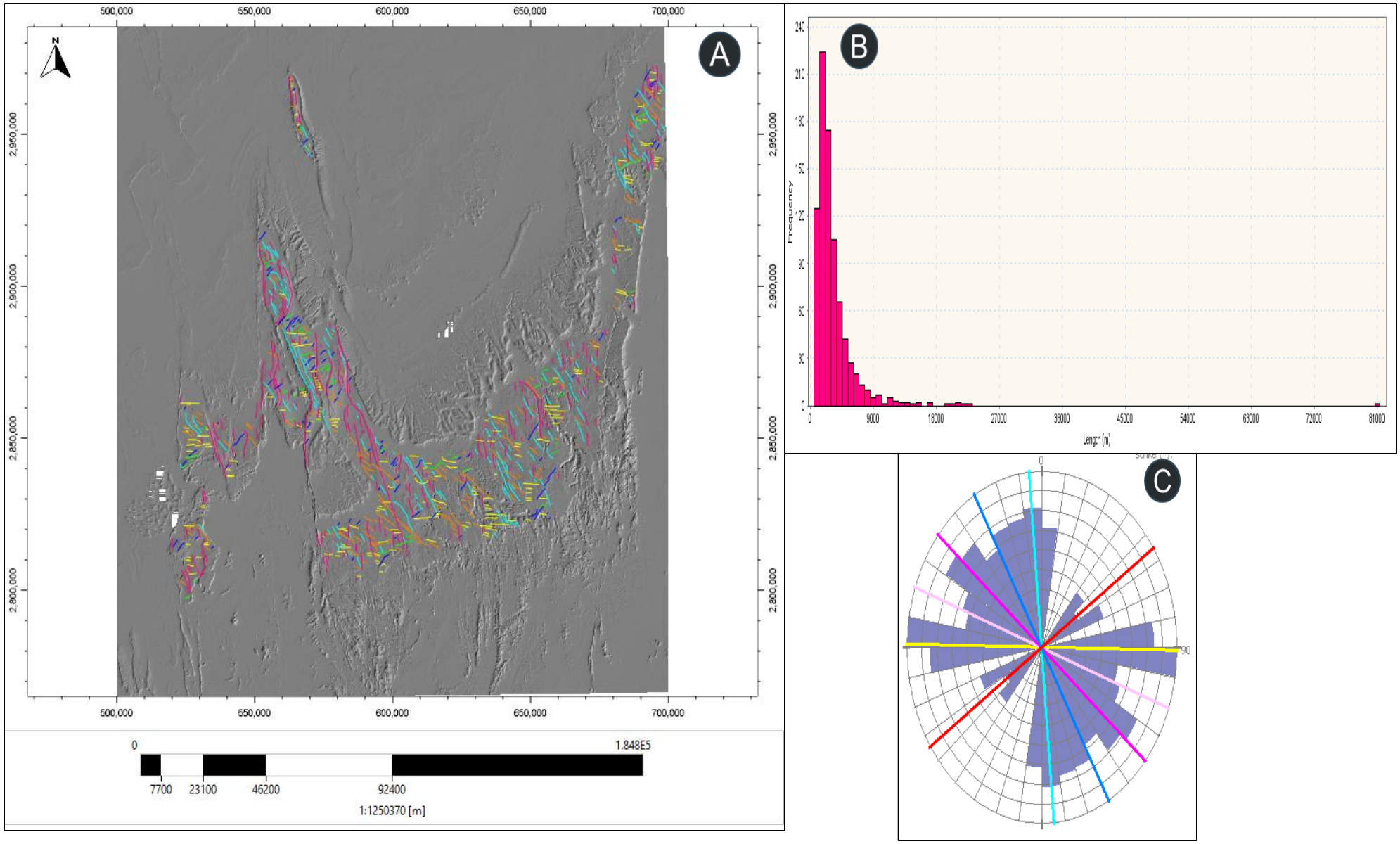

Figure 46: Tamadjert faults characteristics. A- Minor faults map in the Tamadjert formation. B- Minor faults' length distribution. C- Minor fault sets orientation.

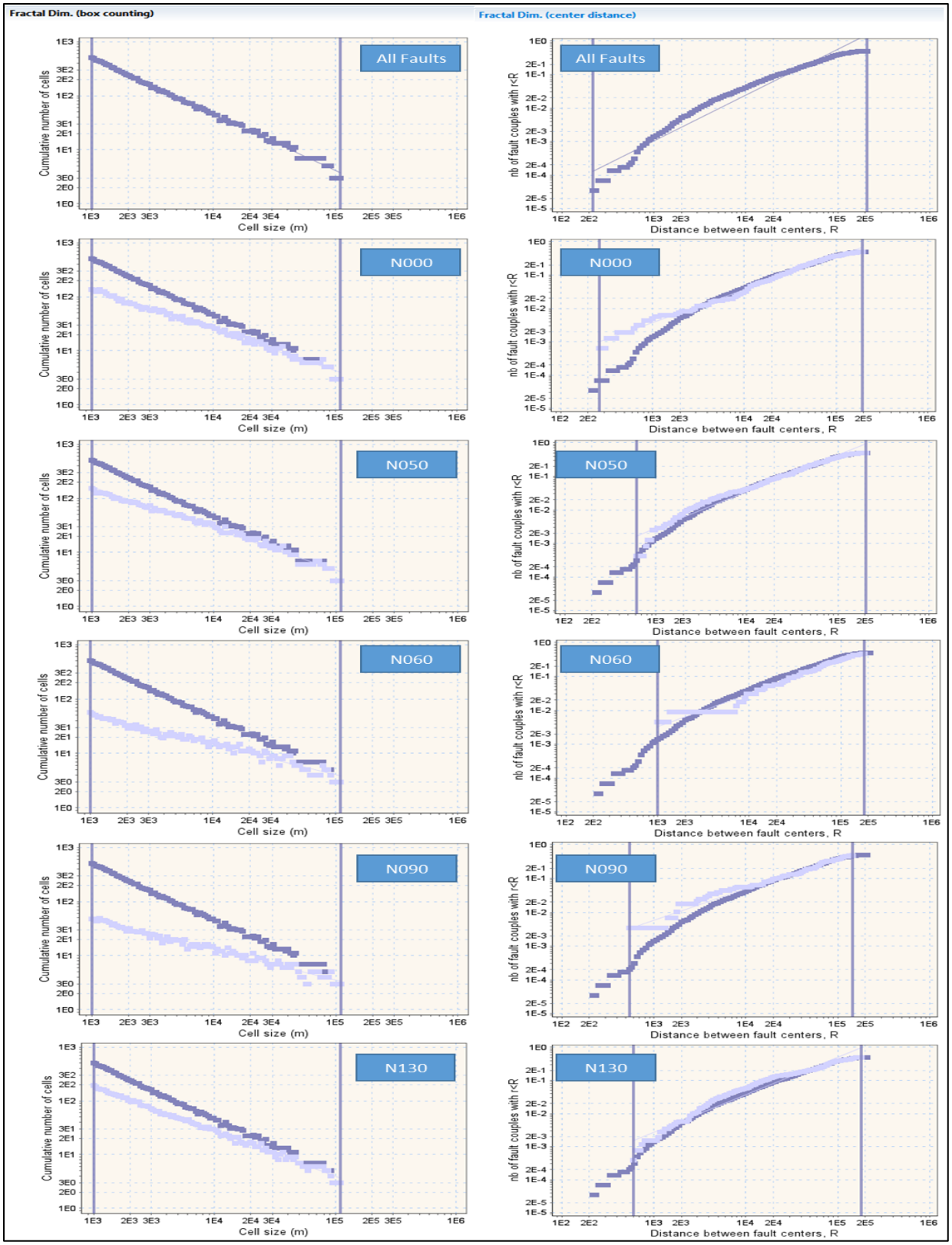

Figure 47: Fractal dimension distributions for the Minor faults in the In-Tahouite formation by fault set using the center distance and the box-counting algorithms.

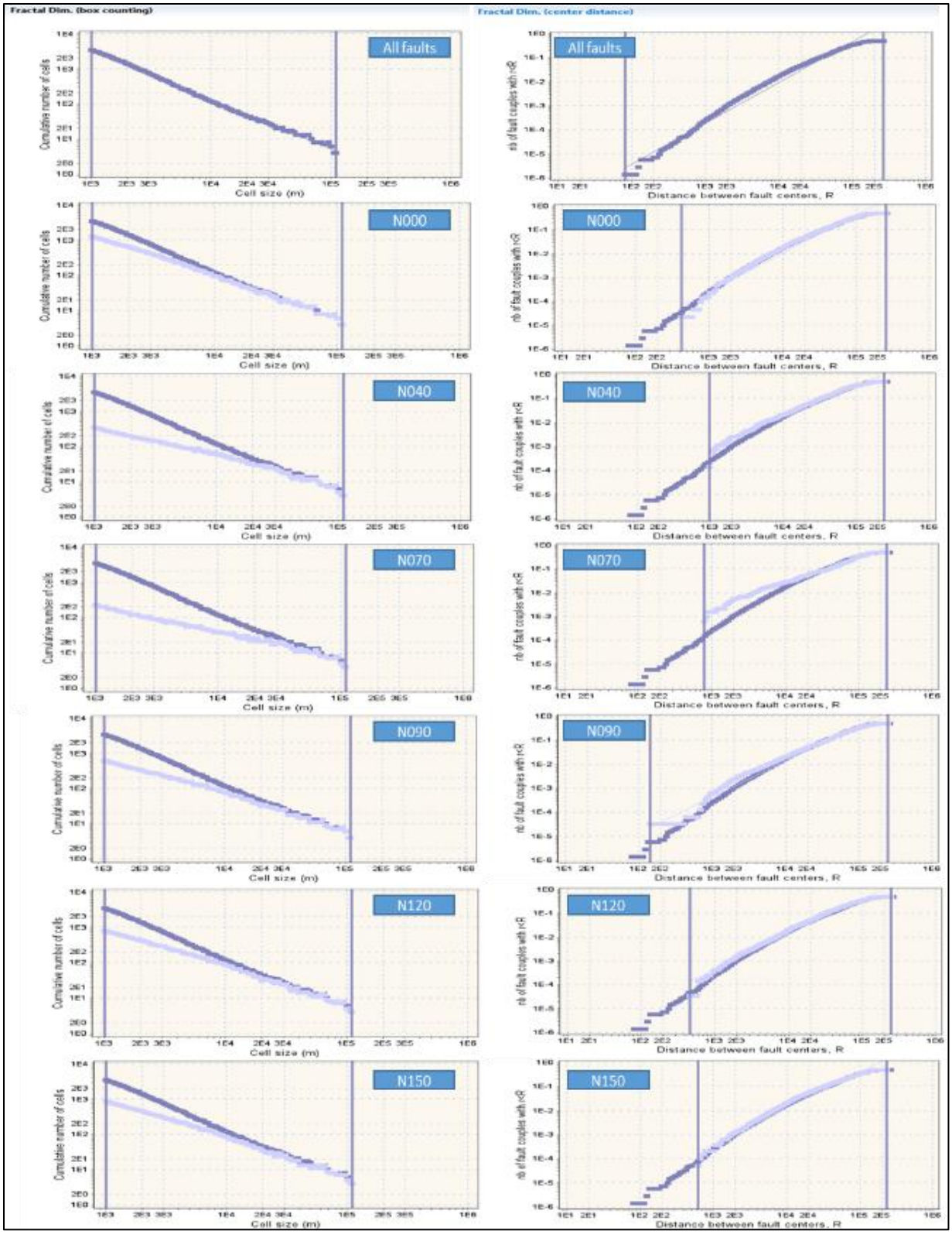

Figure 48: Fractal dimension distributions for the Minor faults in the Tamadjert formation by fault set using the center distance and the box-counting algorithms.

III-3-3-The third approach

This third approach is the merged of all the Minor fracture networks that affect the basement and the Cambro-Ordovician units. This helps to recognize the relationship and the impact of the basement fractures on the different units of the Cambro-Ordovician reservoir analog by comparing the orientation and fractography of the different fracture sets, length, kinematics, and fractal dimensions.

The basement, Ajjers, In-Tahouite, and Tamadjert fracture networks are merged into a Global fracture network which is composed by 1891 faults and characterized by five fault sets: N000, N050, N090, N120, and N150 respectively where the N-S and N150 fault sets are the most important groups in term of faults' number and length.

The Global faults network has fractal dimensions of 1.7946 and 1.5754 using the center distance and box-counting algorithm respectively. On the other hand, the different fault sets have a fractal dimension D_m ranges from 1.4796 to 1.6716 using center distance algorithm and from 1.1149 to 1.3984 using box-counting algorithm (Table-13, Fig.49 & Fig.51).

Table 13: Fractal dimensions related to the Global faults.

Data	Points	Fract dim.(center distance)	Fract dim.(box counting)	Rmin
All faults	1891	1.7946	1.5754	88.0436
Global-Faults-N000	628	1.6716	1.3984	91.1372
Global-Faults-N050	222	1.4796	1.1149	453.5019
Global-Faults-N090	348	1.5941	1.1774	143.0563
Global-Faults-N120	338	1.6271	1.2284	466.4582
Global-Faults-N150	355	1.6259	1.2821	88.0078

III-3-4-The fourth approach

The fourth approach studies the merged of the Major and Minor fracture network that affects the area of study. This approach comforts to comprehend the behavior and the relationship between the Major and Minor fractures. In addition, it brings a new insight about the effect of the basement fracture on the sedimentary cover and the chronology of the different fracture sets. Both Minor and Major fracture networks are merged to a unique Total fracture network. This approach is applied on all fault networks that affect all the Paleozoic series.

The fracture orientation and fractal dimensions are calculated using center dimension and box-counting algorithms for the whole fault network and each fracture set. The total network is composed by 2544 faults and characterized by five fault sets: N000, N050, N090, N120, and N150 respectively. The N-S, N090 and N160 fault sets are the most important groups in term of faults' number and length.

The total faults network has fractal dimensions of 1.7798 and 1.6742 using the center distance and box-counting algorithm respectively. On the other hand, the different fault sets have a fractal dimension D_m ranges from 1.1.4115 to 1.6825 using center distance algorithm and between 1.2158 and 1.5061 using box-counting algorithm (Table-14, Fig.50 & Fig.52).

Table 14: Fractal dimensions related to the Total faults.

Data	Points	Fract dim.(center distance)	Fract dim.(box counting)	Rmin
All faults	2544	1.7798	1.6742	65.0631
Total-faults-N000	728	1.5451	1.5061	91.1792
Total-faults-N050	296	1.5234	1.2158	250.3348
Total-faults-N090	530	1.4725	1.2691	143.0568
Total-faults-N120	578	1.6825	1.3583	209.6989
Total-faults-N150	412	1.4115	1.3484	88.0078

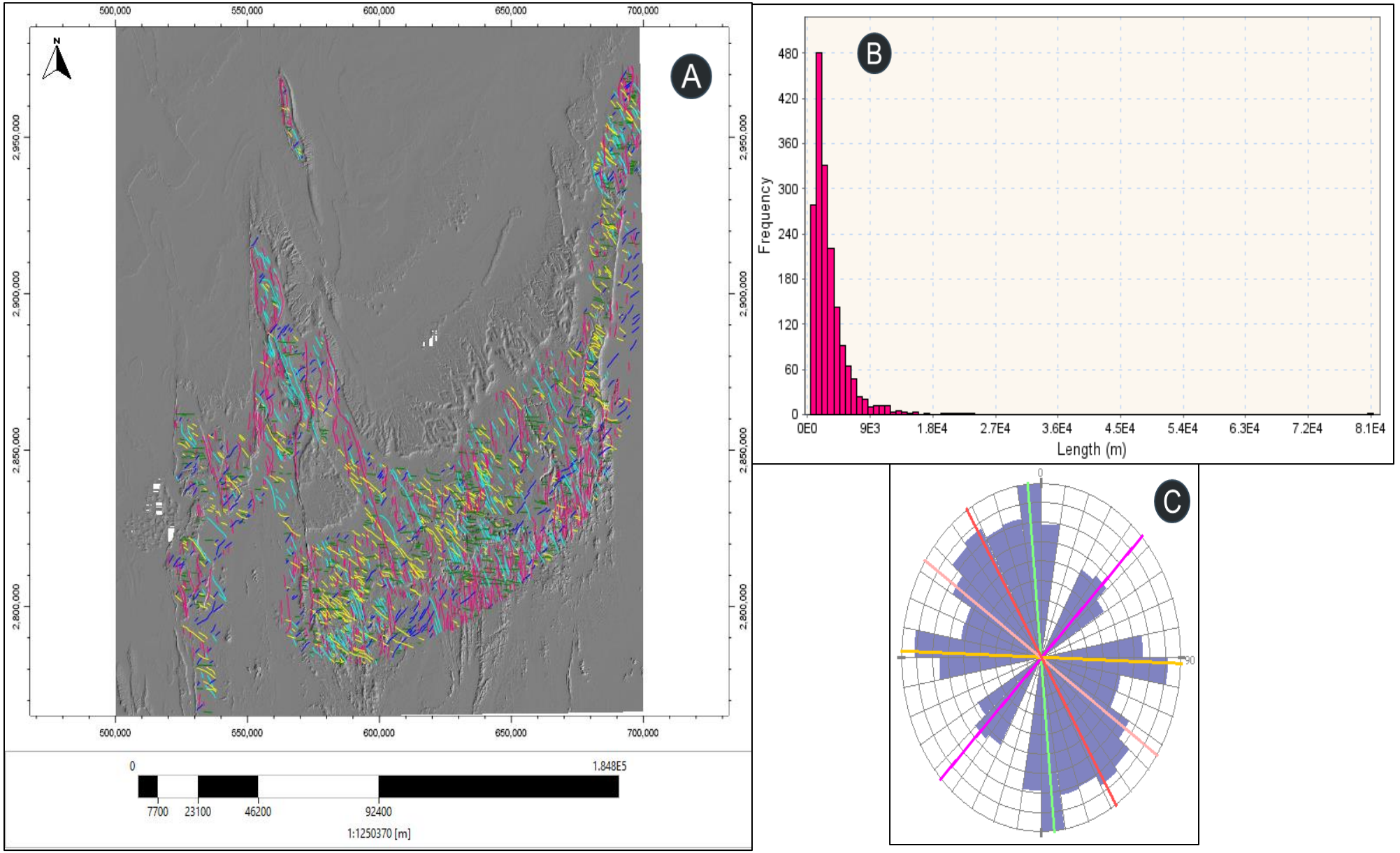

Figure 49: Global faults characteristics. A- Minor Global Faults map (Basement and Cambro-Ordovician formations). B—Minor faults' length distribution. C-Minor fault sets orientation.

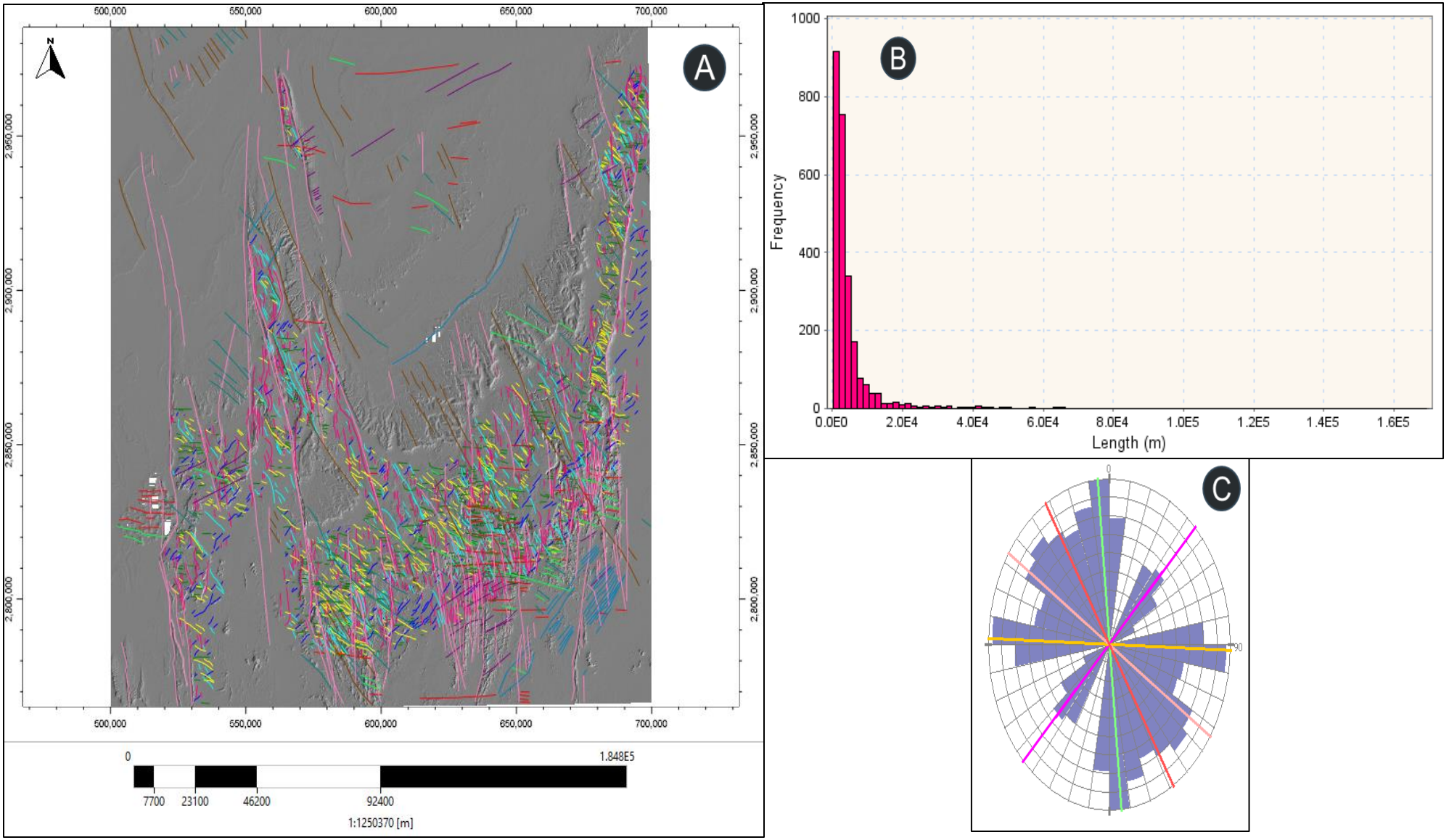

Figure 50: Total faults characteristics. A- Total Faults map (Major faults, Basement, and Cambro-Ordovician formations). B--Faults' length distribution. C-Fault sets orientation.

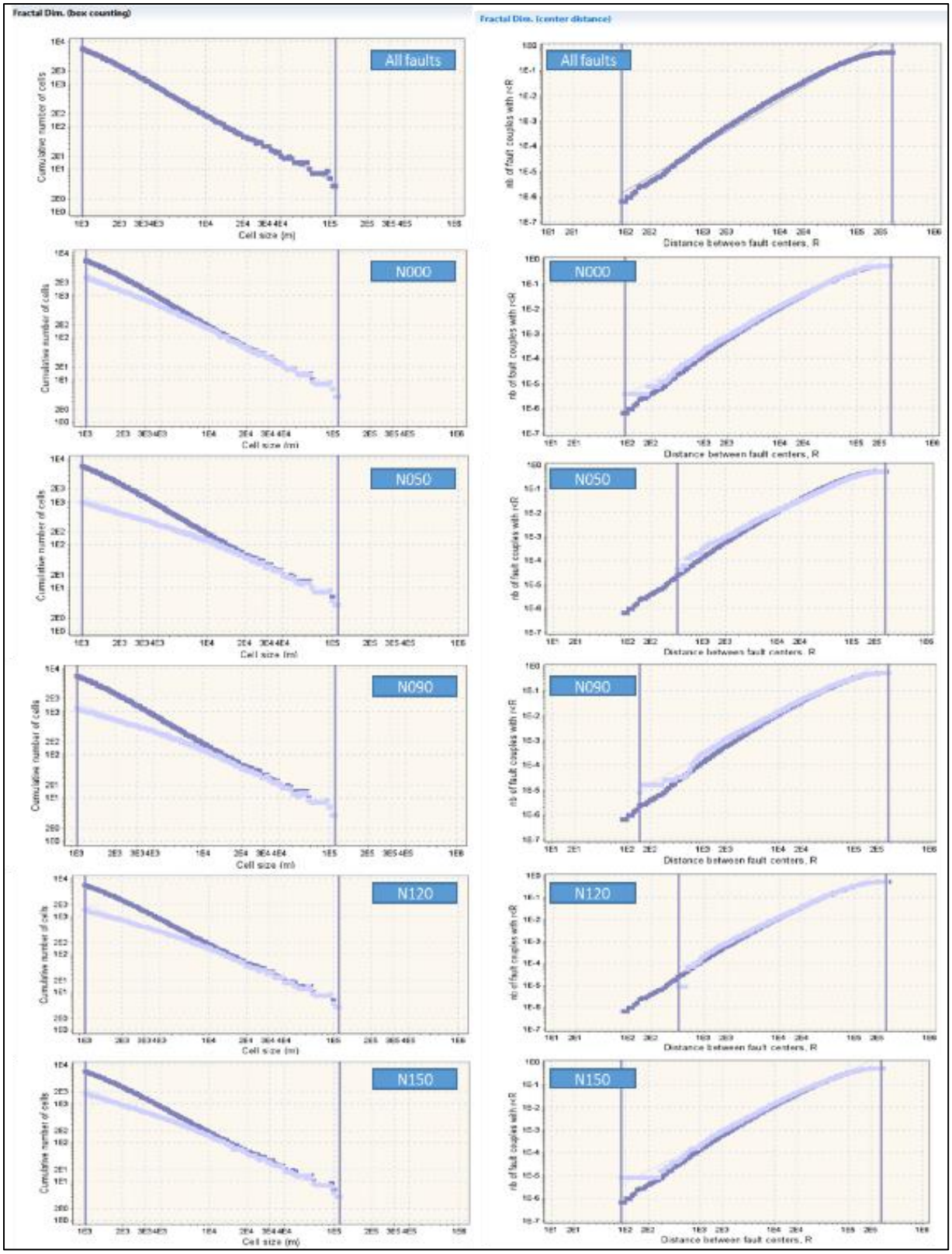

Figure 51: Fractal dimension distributions for the Minor Global faults in the area of study by fault set using the center distance and the box-counting algorithms.

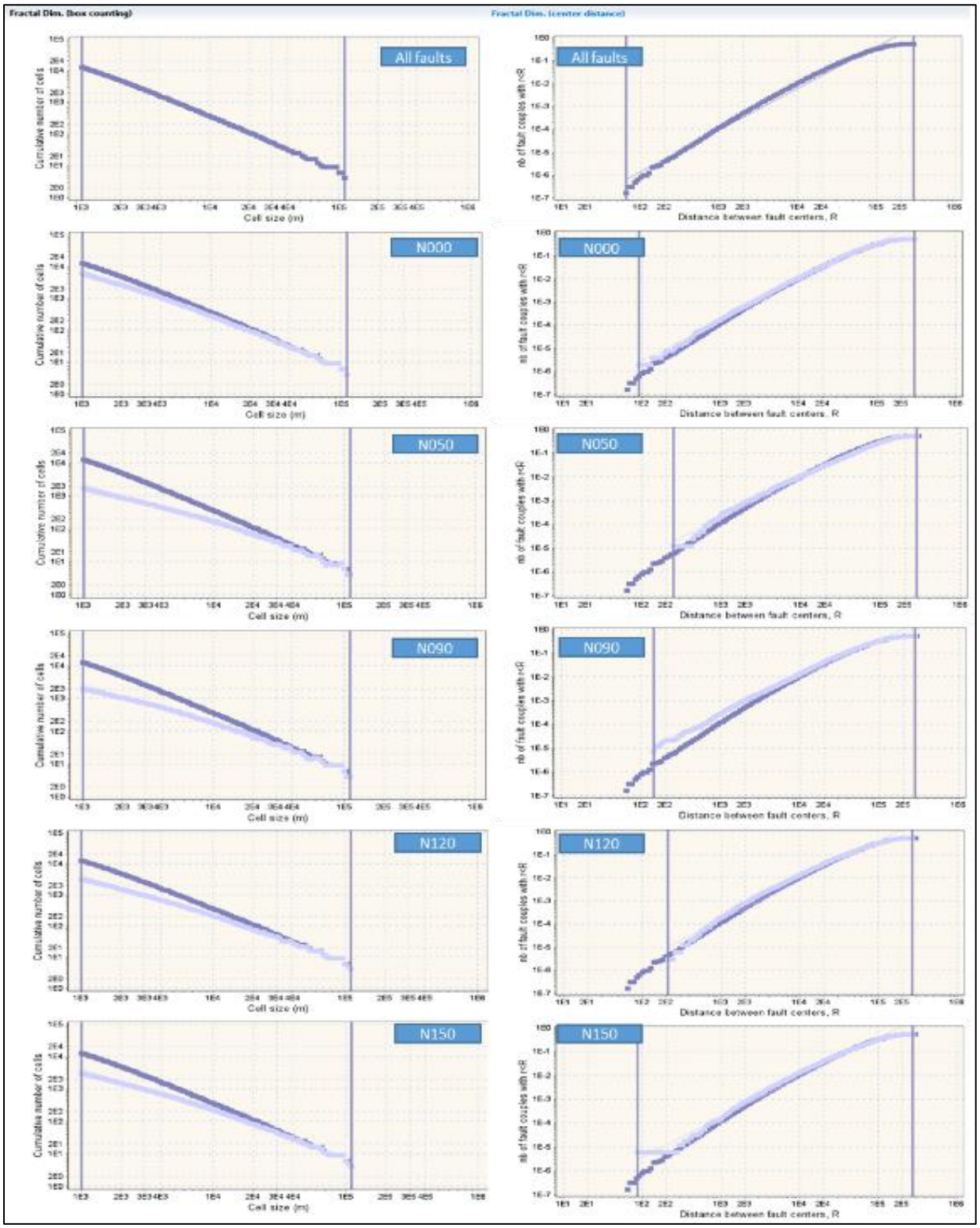

Figure 52: Fractal dimension distributions for the Major and Minor faults in the area of study by fault set using the center distance and the box-counting algorithms.

III-4- Conclusions

The Cambro-Ordovician formations are characterized by brittle tectonic style, linked with Major basement fractures inherited from the Pan-African orogeny, which is responsible for the creation of an extensive fracture network. The analysis of geological maps shows that a dense fracture networks had affected the Paleozoic.

The Major structures correspond to N-S-trending dextral strike-slip fractures and NNW-SSE trending sinistral strike-slip fracture. Two Major fracture corridors can be distinguished which design the western and the eastern Mouydir basin's edges. They start from the basement in the Hoggar shield and continue to the north in divergent directions in the Saharan platform. They are oriented NNE to NS and NNW to NS constituting the Amguid and the Idjerane spurs respectively.

The fractures' length distribution shows a power law distribution with a coefficient ranging between 2.31 and 2.69 and high correlation coefficients. The fractal analysis of the entire 2D fracture networks and the different fracture sets that affect the basement and the Cambro-Ordovician units show that they have fractal dimensions based on both the center distance and the box-counting algorithms with values ranging between 1 and 2.

Though, very few fracture sets do not show any fractal dimension. Both methods display that the fracture networks that affect the area of study have a fractal dimension. However, the fractal dimension using the box-counting algorithm is 0.2 to 0.3 less than the fractal dimension using the center surface algorithm for the different networks and in the different fracture sets.

The main fault sets are oriented N000, N050, N090, N120, and N160, where the major structures correspond to N-S-trending dextral and sinistral strike-slip faults. The fractal analysis D_m of the entire 2D fracture networks and the different faults sets that affect the basement and the Cambro-Ordovician units show that they have fractal dimensions based on both the center distance and the box-counting algorithms with values ranging between 1 and 2. However, very few fault sets do not show any fractal dimension.

The analysis of different fractures networks affecting the basement and the Cambro-Ordovician units showed that they have fractal distribution using center distance and box-counting algorithms with a power law coefficient ranging from 2.31 to 2.69 and high correlation coefficients. However, a few sets do not show fractal dimension maybe due to the scattered of

fractures in the area of study. The fractal dimension using the box-counting algorithm is 0.2 to 0.3 less than the fractal dimension using the center surface algorithm for the different networks and in the different fracture sets.

Chapter IV: Core Fracture Analysis

IV-1-Introduction

Fracture is a general term used to describe any discontinuity within a rock mass that developed as a response to stress (Bour & al, 2001). The fracture could be a fault, which is a mode II fracture, displaying in-plane shear displacement; or a joint, which is mode I fracture, displaying displacement normal to the discontinuity walls (Bour & al, 2001). The length distribution plays an important role in reservoir engineering. The long fractures are more well-connected than those of short fractures (Balberg and Binenbaum, 1983; Balberg et al., 1991).

Natural fractures constitute most often-preferential drains or barriers of permeability that partially control the movement of fluids being produced. In the tight reservoir, the fracture modeling is very important. The wells' productivity in these low permeability reservoirs is attributed to interconnected fracture networks. The core's analysis goals are to determine the distribution and typology of fractures in Ordovician reservoir in the Mouydir basin. Three (3) wells, namely GM-1, ME-1, and EA-1 were described for this purpose (Fig.53).

The core dataset is available at Sonatrach Core Library in Hassi Messaoud City, Algeria. The cores were described based on their lithological variations, grain-size distribution, mineralogical composition, fossils, sedimentary structures, and the presence of faults and fractures.

Several types of fractures and faults characterize the Cambro-Ordovician formations in Mouydir basin. Some of them are related to the sediment compaction and other to the basin tectonic evolution. They are represented by several fracture sets, parallel or secant to each other and their dip could be horizontal, vertical or oblique.

The closed fractures are characterized by a dip that varies from 0 to 90 degrees and they are filled essentially with quartz. The partially open fractures have a dip that varies between 0 to 90 degrees and they are filled by the quartz and sometimes with pyrite. They are parallel or oblique to the stratification. The opened fractures are rare and we can detect them in all the Cambro-Ordovician formation. In addition, the presence of normal and reverse micro-scale faults is highlighted and they are located only in the Ordovician formation.

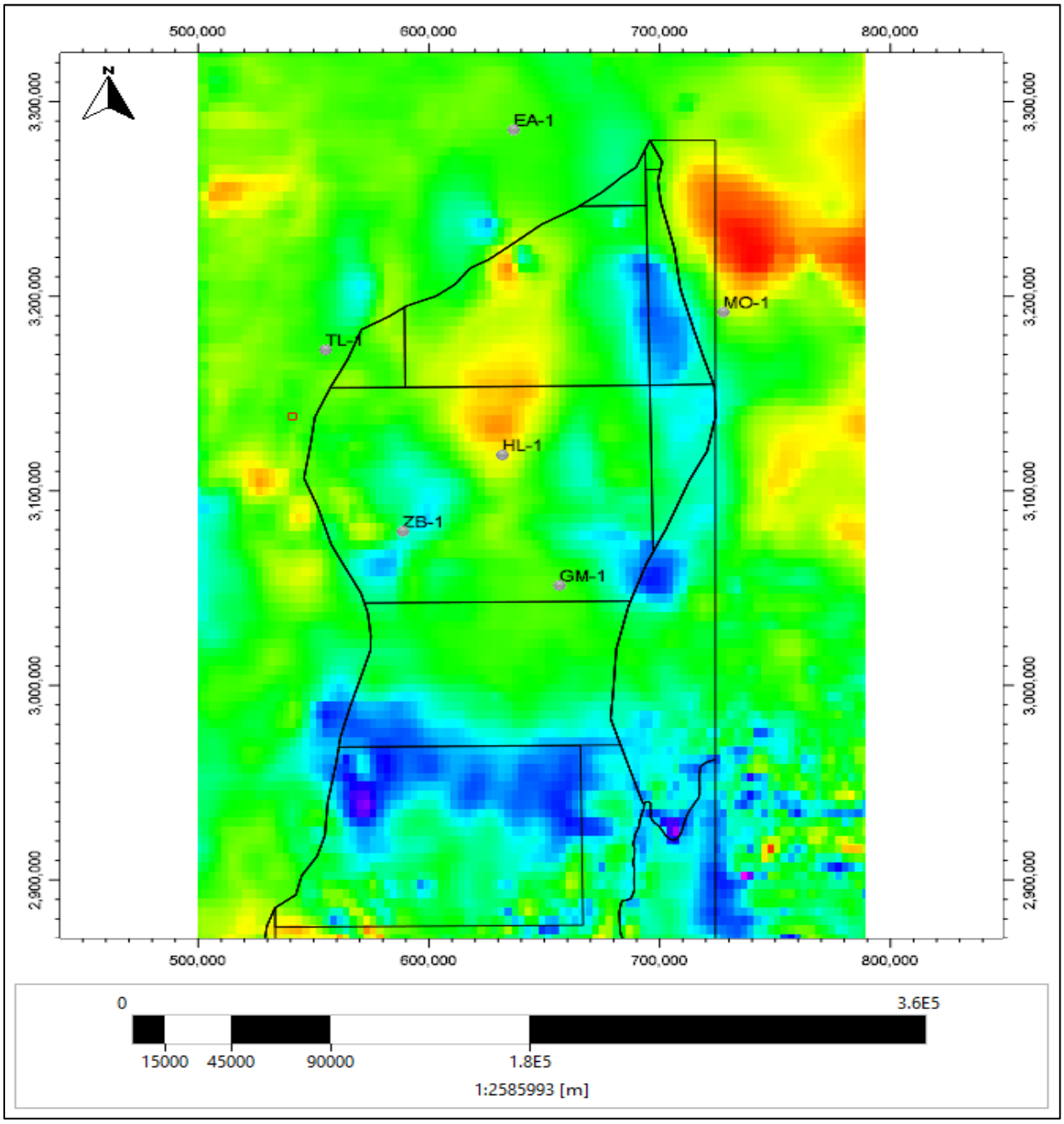

Figure 53: Location of some drilled wells in the area of study on the Gravity map.

IV-2-Fracture Types

According to Bonnet, 2001, the fracture is classified in mode I and mode II where in mode I, fracture is in tensile or opening mode and the displacement is normal to the discontinuity walls (e.g. joint). On the other hand, the mode II fracture is in an in-plane shear mode, where the displacement is in the plane of the discontinuity (e.g. fault). The fractures occur on a varied range

of scales from microns to hundreds of kilometers; where they have a strong impact on the fluid flow and other rock parameters (Bonnet et al, 2001). The first type of fracture is related to the tectonic fractures, which are frank fractures with presence of cement, breccia or slickenside. The second fracture is related to stylolites; they are due mainly to the sediments' compaction. They are vertical or oblique and always connected to a horizontal stylolites (Fig.54).

The results are presented by integrating the various elements in the form of histograms or graphs showing the fractures distribution by type, by fracture length as well as by their frequency in order to estimate their impact on the reservoirs. Fractures are represented by several fracture sets, parallel or secant to each other. The cemented fractures are mainly present in the different Ordovician units. They are represented by several fracture sets, horizontal, vertical, parallel or secant to each other. They are filled essentially by quartz and sometimes with pyrite. The fracture could be single, conjugate, en-echelon or anastomosed (Fig.54).

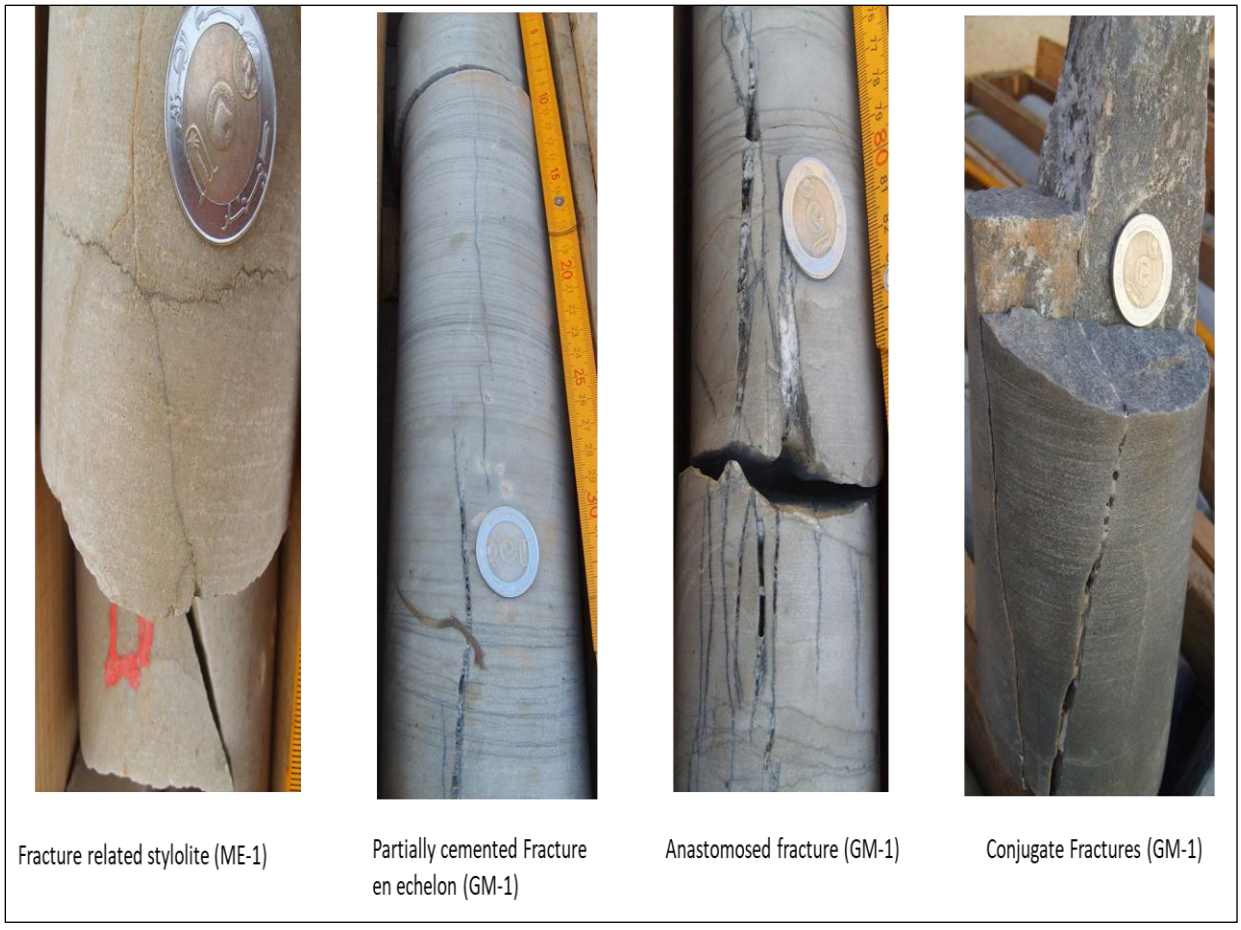

Figure 54: Example of Mode IV and Mode I fractures that affect the Ordovician reservoir.

In addition, the presence of infrequent breccia is noticed with a presence of sulfur. It could be the result of coring operation in an interval where several fracture sets are present, secant or parallel to each other, or due to the presence of a fault in this interval (Fig.55). The presence of open, partially open and closed fractures throughout the cores and the relationship between them are an evidence of multiple episodes of fracturing and/or diagenesis. The normal micro-faults are represented by slickensides (Fig.55). On the other hand, the micro-scale reverse faults are organized in reverse structure and they evolve in some cases to micro-thrust faults (Fig.55). The faults' dip is between 45 to 60 degrees.

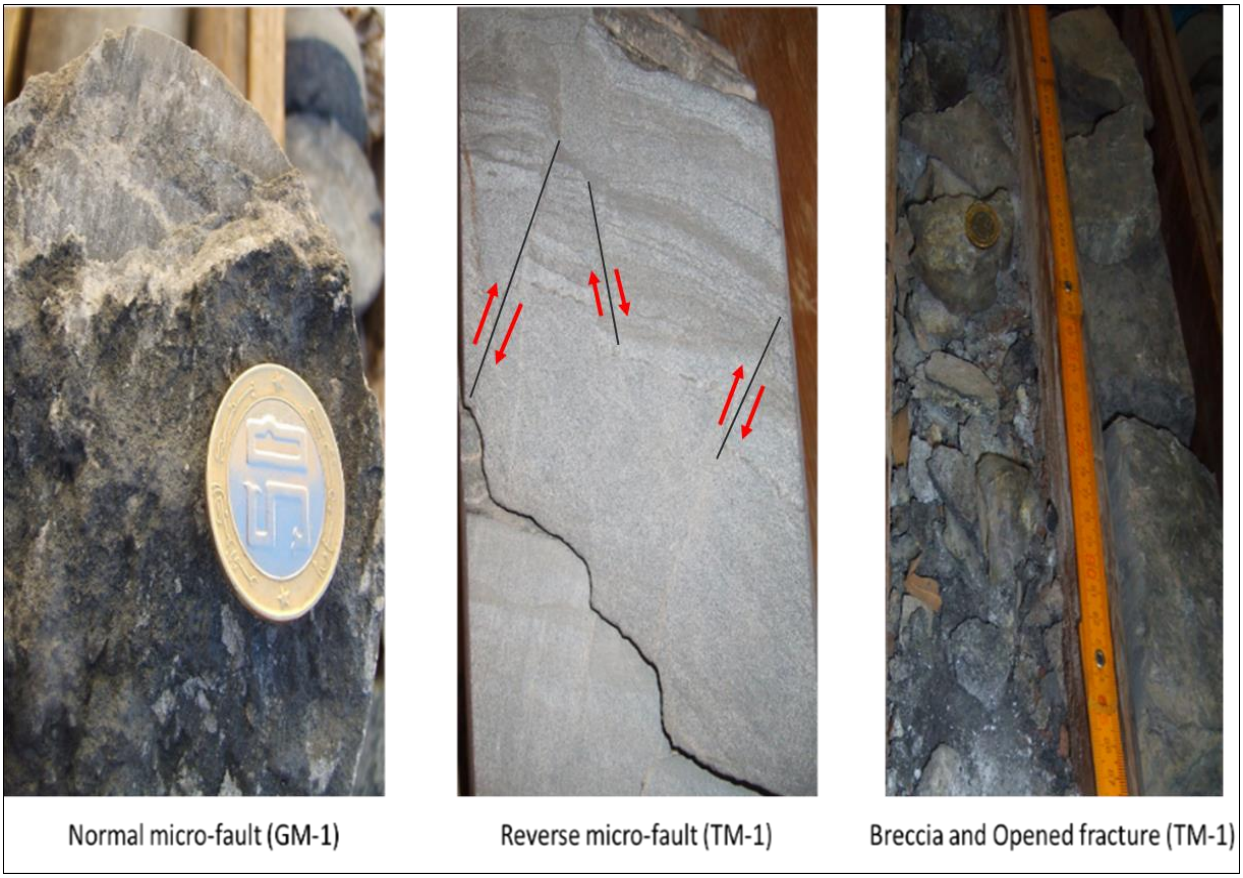

Figure 55: Examples of Mode II fractures that affect the Ordovician reservoir.

IV-3-Fracture Analysis

The core fracture analysis is mainly focused on the tectonic fractures, which are classified in Mode I, and Mode II fractures. They appear on cores and both have an impact on the fluid flow. The Mode I is represented by vertical fractures that appear to be the most important in term of

length and frequency comparing to the oblique and horizontal fractures. The Unit IV appears to be the most fractured reservoir mainly due to the tight sands that compose it (Fig.56). The fracture analysis per well shows that the ME-1 is the most fractured well and especially in the Ordovician units and the TM-1 as the less fractured well (Fig.57).

The wells are affected mainly by cemented and partially cemented fractures. They are located in the different units of Ordovician reservoir. Their frequency is well expressed in the unit III-1 and III-3 in the ME-1 (Fig.58 & Fig.59). On the other hand, The Mode II fracture is represented by of two types of micro-fault. They are exclusively located in the Ordovician units. These micro-faults have a normal and reverse faults kinematics.

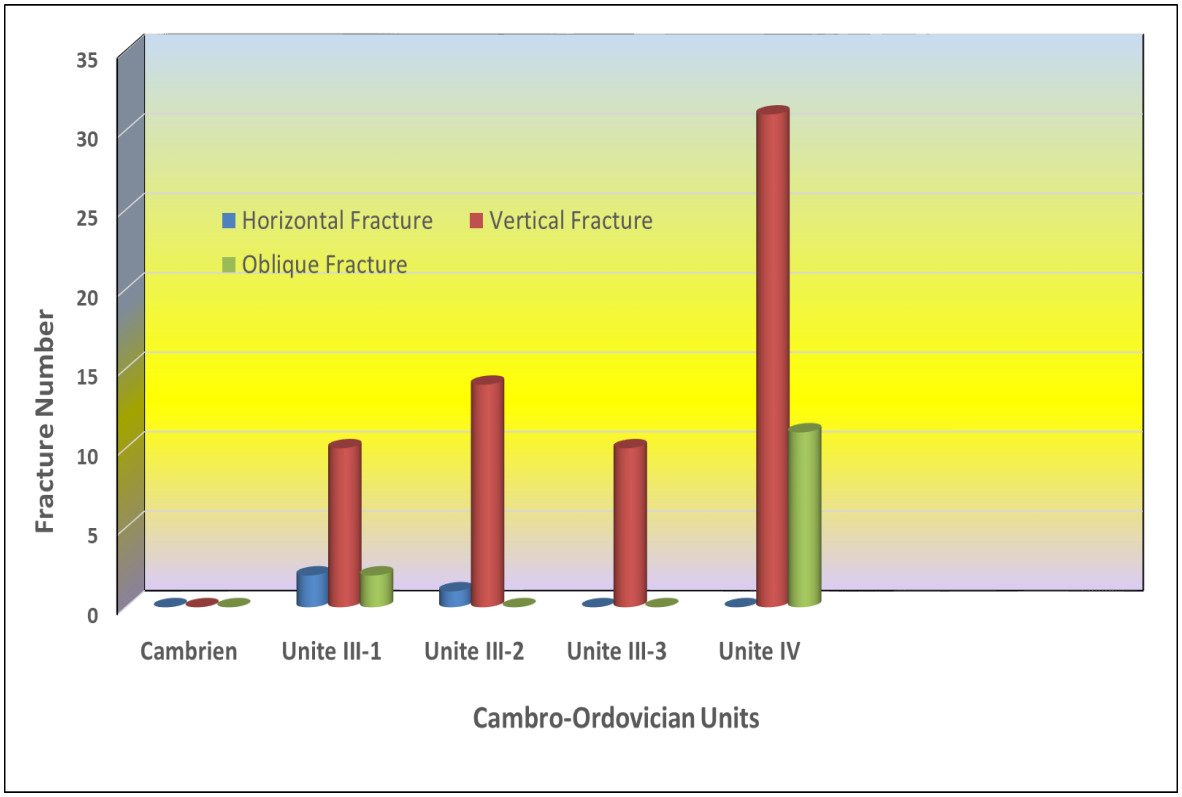

Figure 56: Fracture distribution in the Cambro-Ordovician Units

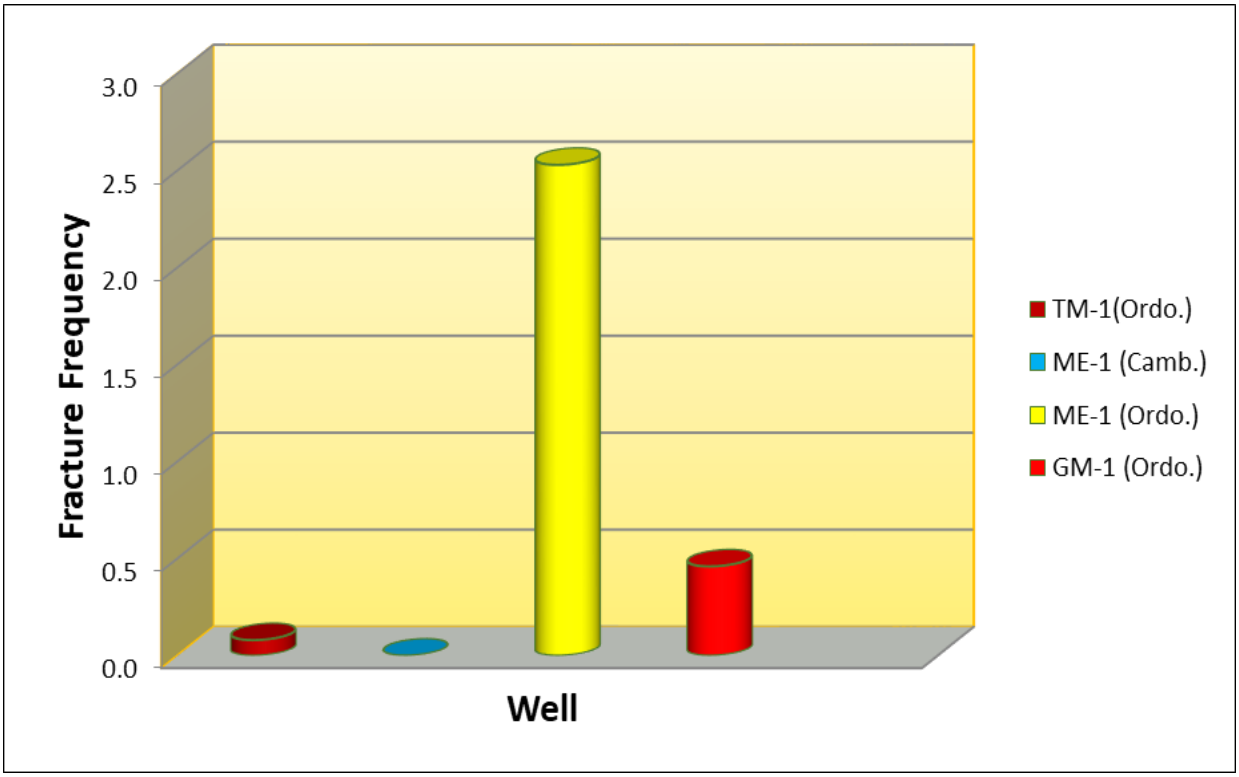

Figure 57: Fracture frequency in the different wells

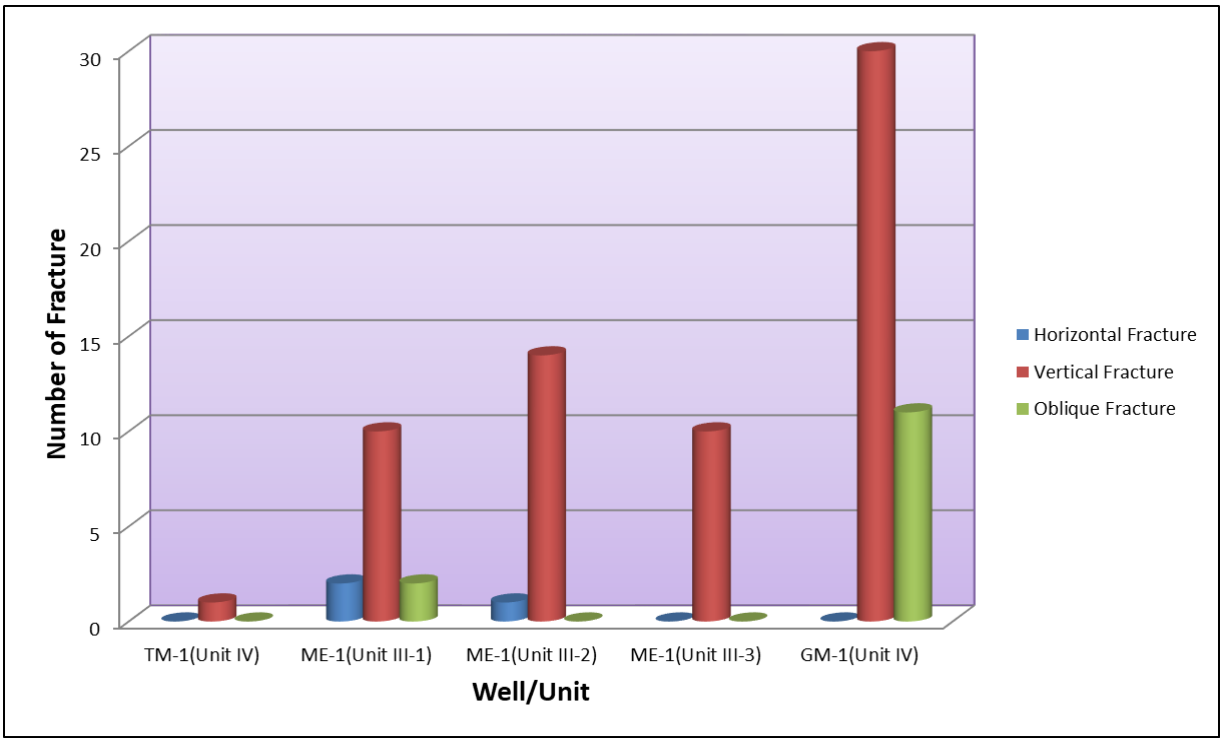

Figure 58: Fracture distribution per well in the Ordovician units

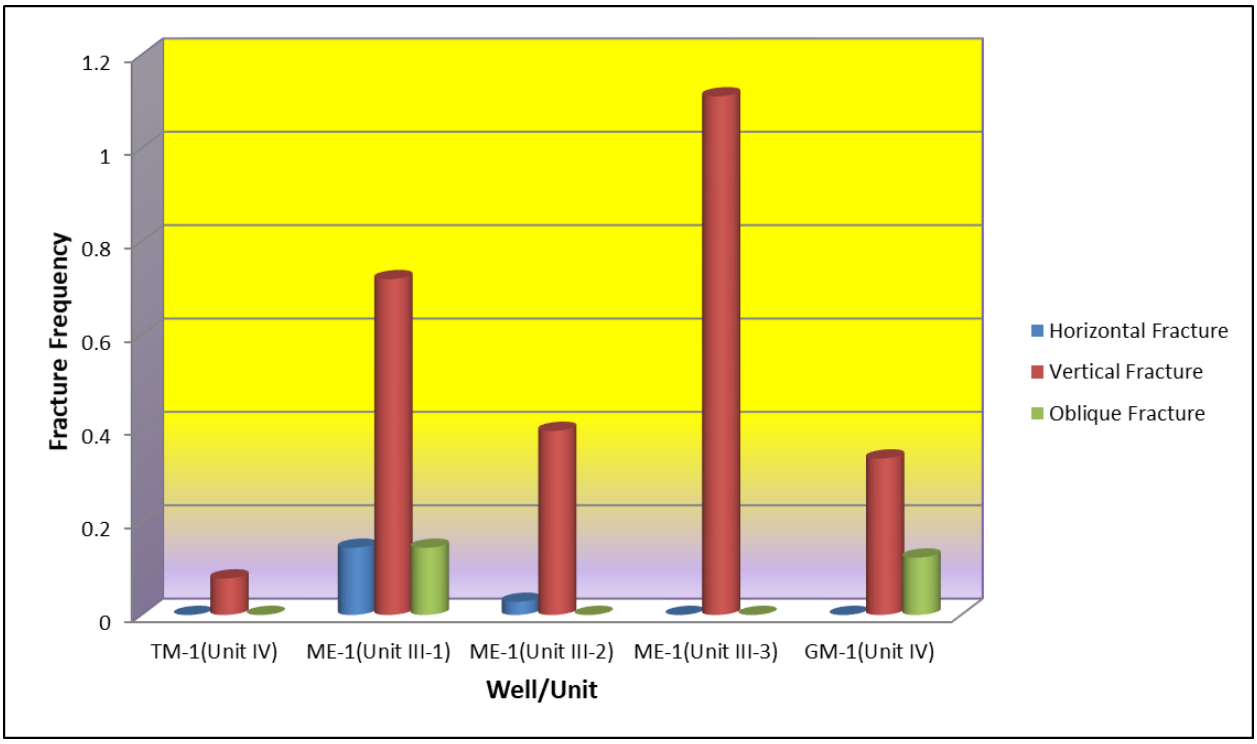

Figure 59: Fracture frequency per well and Ordovician's unit

IV-4-Fracture Length Analysis

The fracture length analysis focuses on the distribution of the Mode I and II fractures and their cumulative length per well that affect the well wells in the area of study. The well TM-1 appears to be the less fractured well. It is affected by 2 Mode I fractures and 3 Mode II fractures because only the Unit-IV's cores were available for the study. The Mode II fractures are represented by normal and reverse micro-faults. On the other hand, the stylolites are well distributed in this unit (Fig.60). The well ME-1 is exclusively affected by the Mode I fractures. They are mainly cemented fractures and affected the different Ordovician units. The stylolites are less present in this well (Fig.61). At the well GM-1, only the Unit-IV of was studied. The upper part of this unit is mostly affected by Mode I fractures represented by cemented and partially cemented fractures. The Mode II fractures are represented by one normal and two reverse micro-faults. On the other hand, the stylolites well represented in the bottom of this unit (Fig.62). The global distribution of fracture types per reservoir shows that the studied wells are moderately fractured, with a predominance of tectonic fractures in number and length, and which are generally cemented. The fracture distribution along wells as a function of fracture type and cement type

shows that tectonic fractures are predominant and the opened fractures are less represented. The analysis of the cumulative lengths of the stylolites shows that the stylolites are present practically throughout the entire cores with cumulative lengths that varies between 10 and 40cm. The core fractures analysis shows that fracture density is variable. The global distribution of fracture types per reservoir shows that the wells studied are less fractured with the predominance of cemented tectonic fractures in number and length. The global distribution of apparent dip values for the studied wells shows that vertical fractures with a dip varying between 75 ° and 90 ° are the most frequent, while a second less representative family corresponding to oblique fractures which dips between 45° and 75°. The presence of Mode I and II fractures throughout the cores and the relationship between them are an evidence of multiple episodes of fracturing and/or diagenesis.

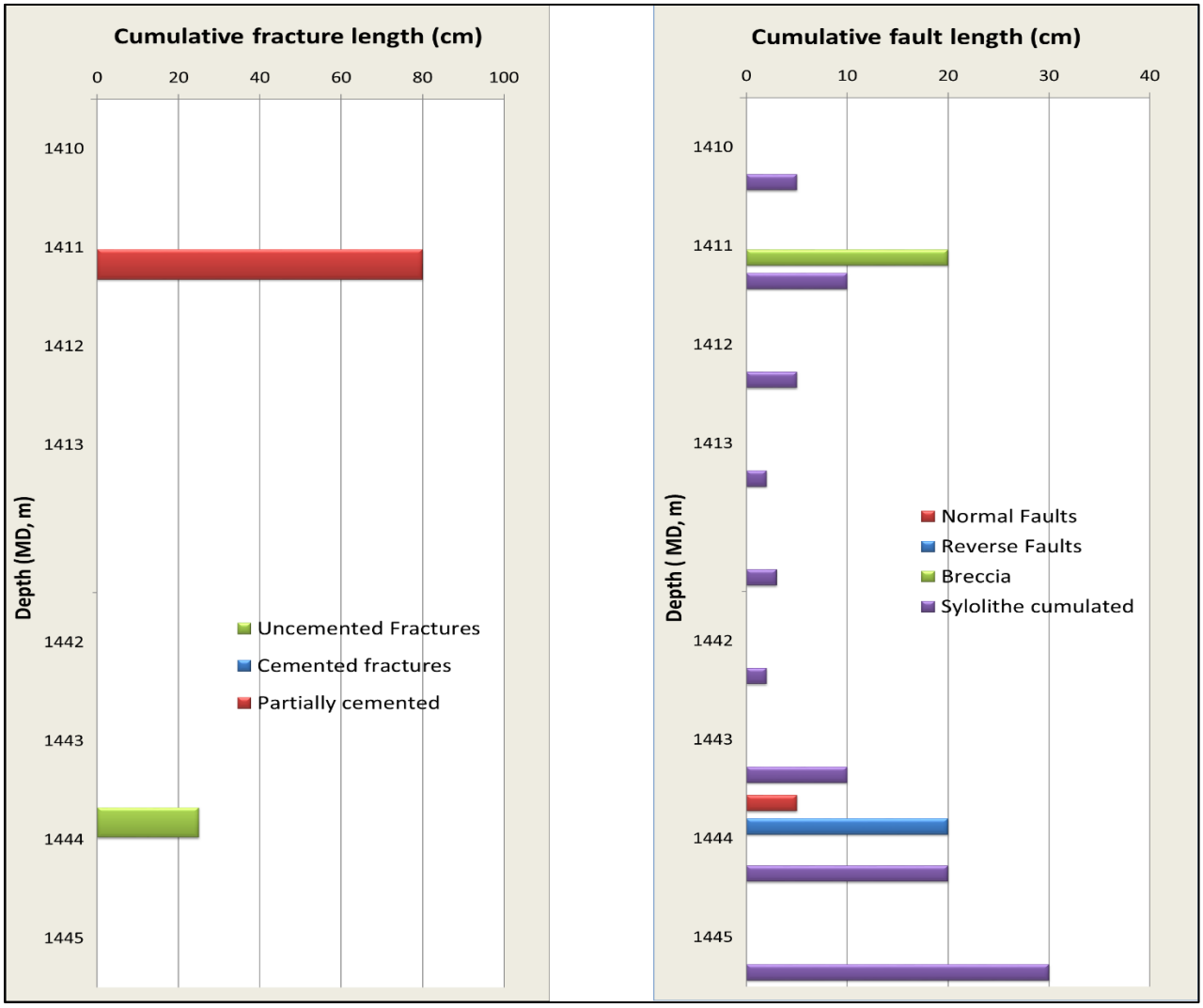

Figure 60: Cumulative fracture and fault length distribution in the TM-1.

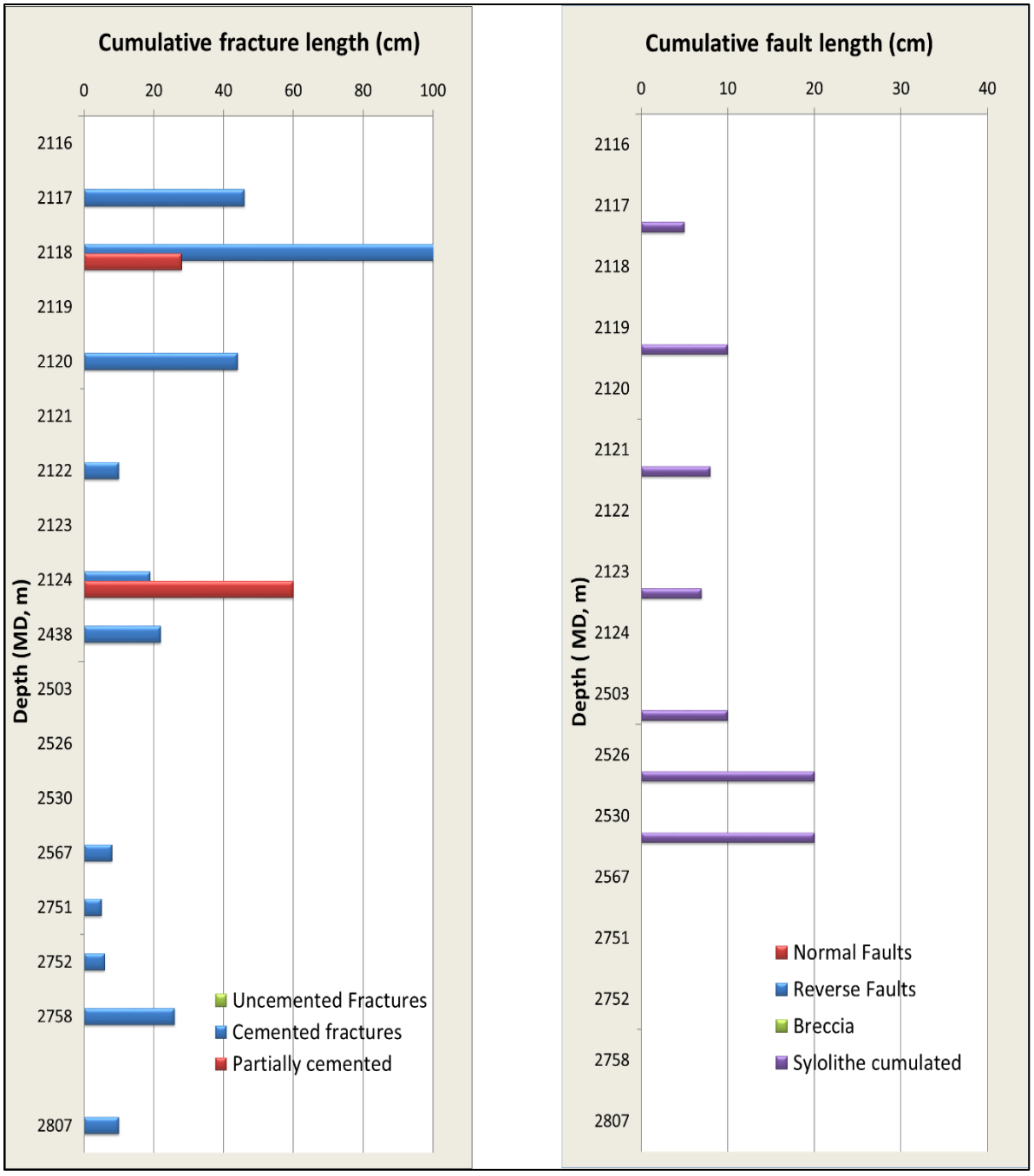

Figure 61: Cumulative fracture and fault length distribution in the ME-1.

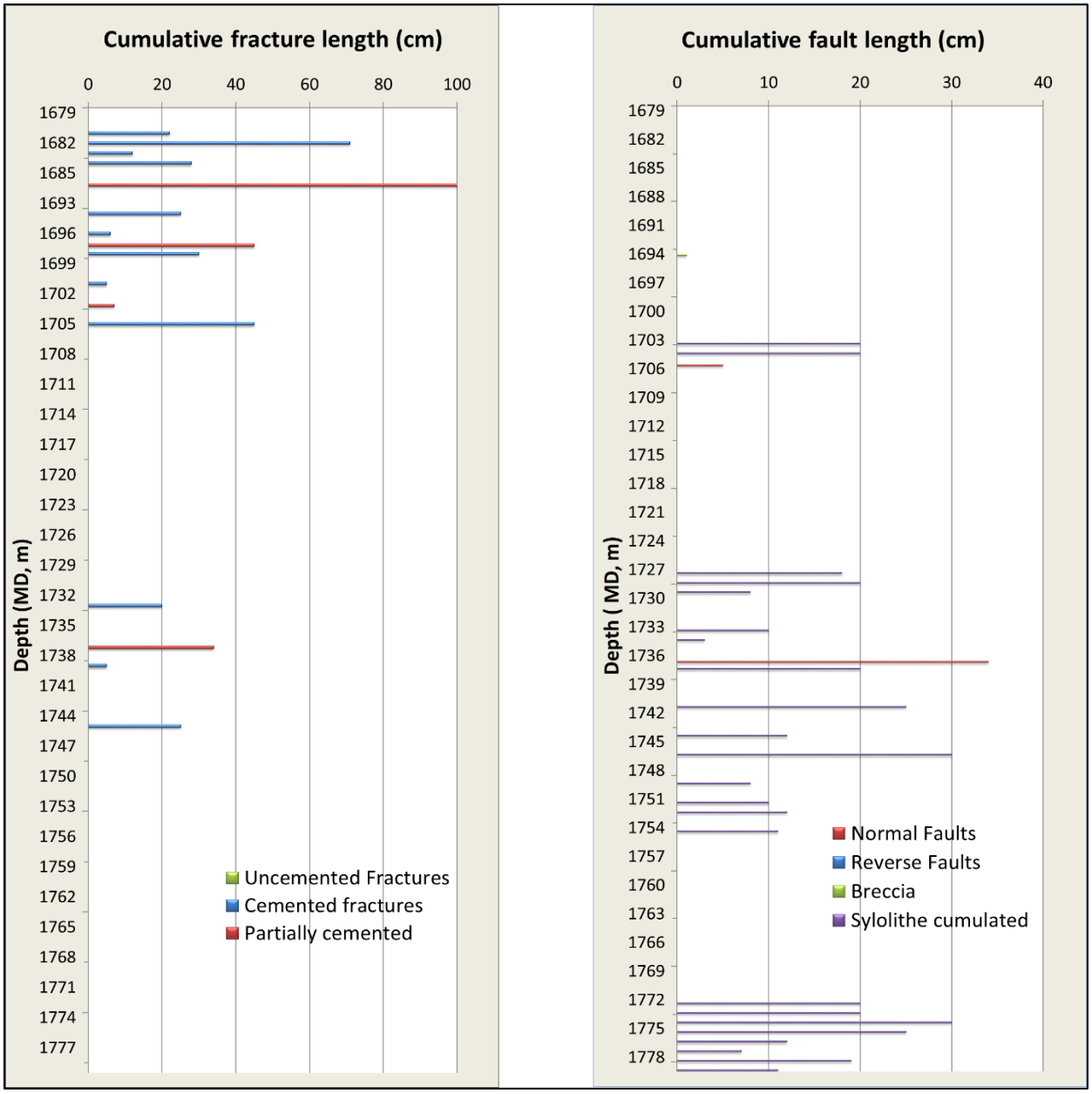

Figure 62: Cumulative fracture and fault length distribution the GM-1.

IV-5-Conclusion

The fracture networks affect the reservoir properties namely, porosity, permeability, and connectivity. This will depend on the fracture's type and state of opening. On a larger scale, major fracture trends, corridors, and fault zones will also have an impact on reservoirs in the definition of compartments and the anisotropy of permeability. The analysis of the core fractures of the three wells of the Mouydir basin shows that the fracture density varies from 2.14 fractures/meter to 0.07

fractures/meter, whereas their openings vary from one millimeter to one centimeter. A proportion of 20% of fractures appear partially clogged with essentially quarzitic cements and 70% of fractures are totally clogged with quartz with presence of pyrite and rarely with calcite. The rest of the fractures described from the cores are opened or reopened during drilling, it should be recalled that the induced fractures were not taken into account in the study of natural fracturing. Direct measurements of fracture openings from cores are not considered representative.

The opening of the fractures is the critical uncertainty thus for openings> 0.001 mm, the fracture permeability is probably> 10md. Some partially clogged fractures, observed locally on cores, have larger openings. These fractures can have a great contribution in the production of hydrocarbons in boreholes, if they form a connected network.

The density of the fractures is close to and sometimes exceeds 1/m of fracture in the different reservoir levels, assuming an ideal level of connectivity, would produce a network of significant permeability. Most of the fractures are steeply dipping, and the observation of some intersections of core fractures probably illustrates the presence of a network of connected fractures.

The global distribution of fracture types per reservoir shows that the studied wells are generally moderately fractured with a predominance of vertical fractures that affect almost all wells and are very pronounced at Ordovician reservoirs. Horizontal fractures showing striated surfaces (slickensides), where the analysis of kinematics reveals in reverse and normal movement. The fracture intensity characterized by the number of fractures per linear meter (f/m).

For all the soundings, the latter oscillates between 0.057 fracture/m and 2.14 fracture/m. The analysis of fracture frequency allows us to attest that the wells studied are moderately fractured. For the studied wells, the global distribution of dip values shows that vertical fractures with a dip varying from 75° to 90° are the most frequent affecting almost all the reservoirs.

The second family represents by horizontal to sub-horizontal fractures with a dip oscillating between 0° and 40°. The third family corresponding to oblique fractures whose dips oscillate between 45° and 70°.

Chapter V: Borehole Imagery Analysis

V-1-Introduction

The acoustic and electrical imaging methods are very useful in the oil and gas industry for the recognition of sub-surface formations by providing information related to the fractures and the deposit environments. These methods bring a better knowledge about the sediments' deposit, and types of faults and fractures that affect the reservoirs. They are essential for the determination of the formations' dip and azimuth, borehole diameter, cores' orientation, direction of the horizontal stresses (SHmax, Shmin), sedimentological features such as lamination and cross-bedding, tectonic features such as faults and fractures, and recognize induced tectonic structures such as breakouts and induced fractures (Fig.63).

The wells in the Mouydir basin were drilled the fifties and no borehole imagery were recorded on them. For this purpose, the borehole imagery data of three (3) vertical wells located in the eastern edge of Ahnet basin and close to the area of study were chosen for this study. Their analysis help to identify the stratification, the fracture types, the dip-Azimuth, the dip, the fracture density, as well as the maximum horizontal stress deduced from the analysis of the breakouts.

The three wells are namely Well-2, Well-3, and Well-4 (Fig.64). UBI and FMI are the two type of borehole imagery used to interpret these fracture types. The Hamra Quartzite covered by these borehole imageries is considered as the second target in the all-Algerian basins and the main reservoir in the Ahnet basin, which is known as a potential gas province in Algeria.

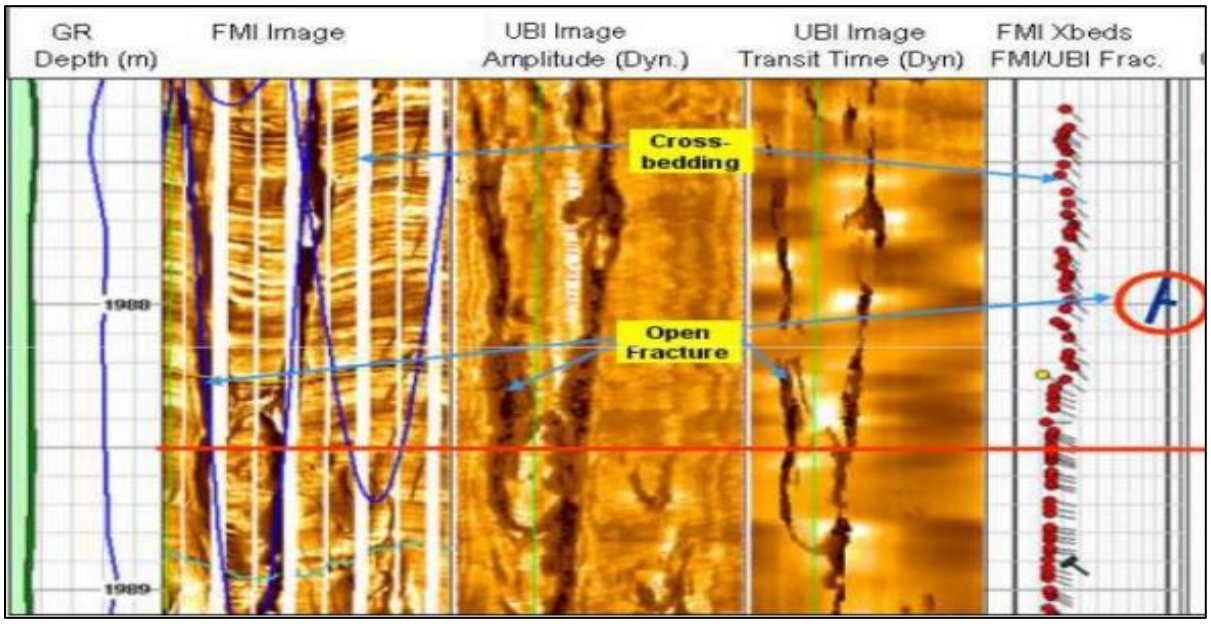

Figure 63: Example of FMI and UBI image showing an open fracture and cross-bedding (Schlumberger document).

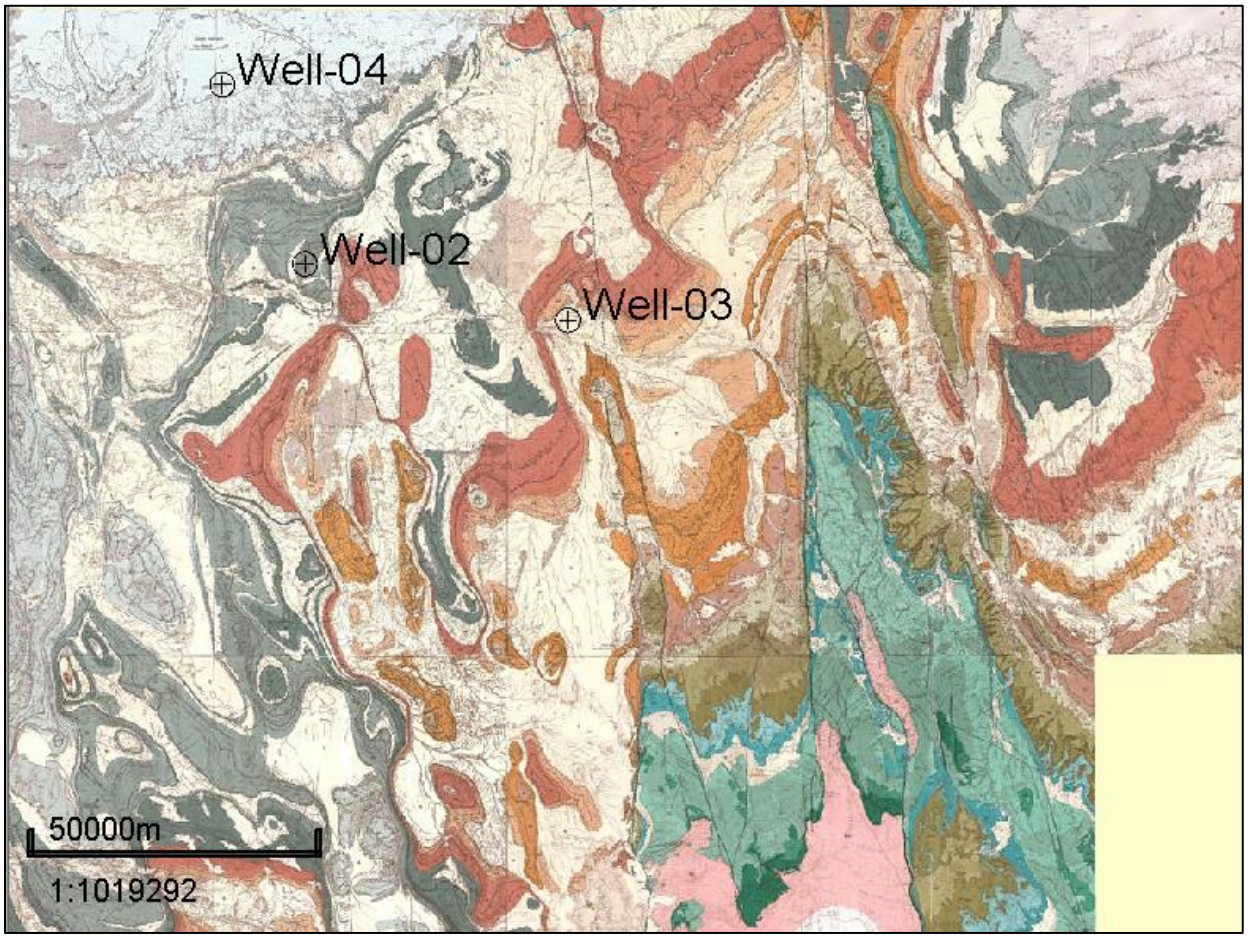

Figure 64: Location of the studied wells

V-2-Fracture Analysis

The fracture analysis consists to determine the dip-azimuth and the dip of the stratification, the conductive fractures, the resistive fractures, the breakouts and the fracture density in each well. The different parameters are represented under the form of tables, rose diagrams and curves.

V-2.1-Fracture analysis for the Well-2

The stratification is represented by almost 400 measurements showing a strike of N070 dipping 6 degrees to the NW and the SE (Fig.65). The breakouts represented by 5 measurements are oriented NE-SW with a dip around 90° (Fig.66). This help to conclude that the Maximum Horizontal Stress (SHMax) is oriented NW-SE.

Three conductive fracture sets were determined (Fig.67). The main fracture set is oriented N135 represented by 19 fractures having an average dip of 83° and dipping to the Ne and sometime to the SW. The second is represented by one fracture and oriented N108 and dip of 67 degrees to the NNE. The third set is represented by one fracture oriented N177 and dip of 71 to the ENE. Only one resistive fracture was determined oriented N106 with a dip of 52° to the NNE (Fig.68).

The fracture density for each fracture set is represented by a curve showing the minimum and maximum fracture density with the projection of tadpoles representing the dip and the dip-azimuth of fractures. The fracture set density varies between 0.005 to 0.2 fracture/meter (Fig.69 & Fig.70).

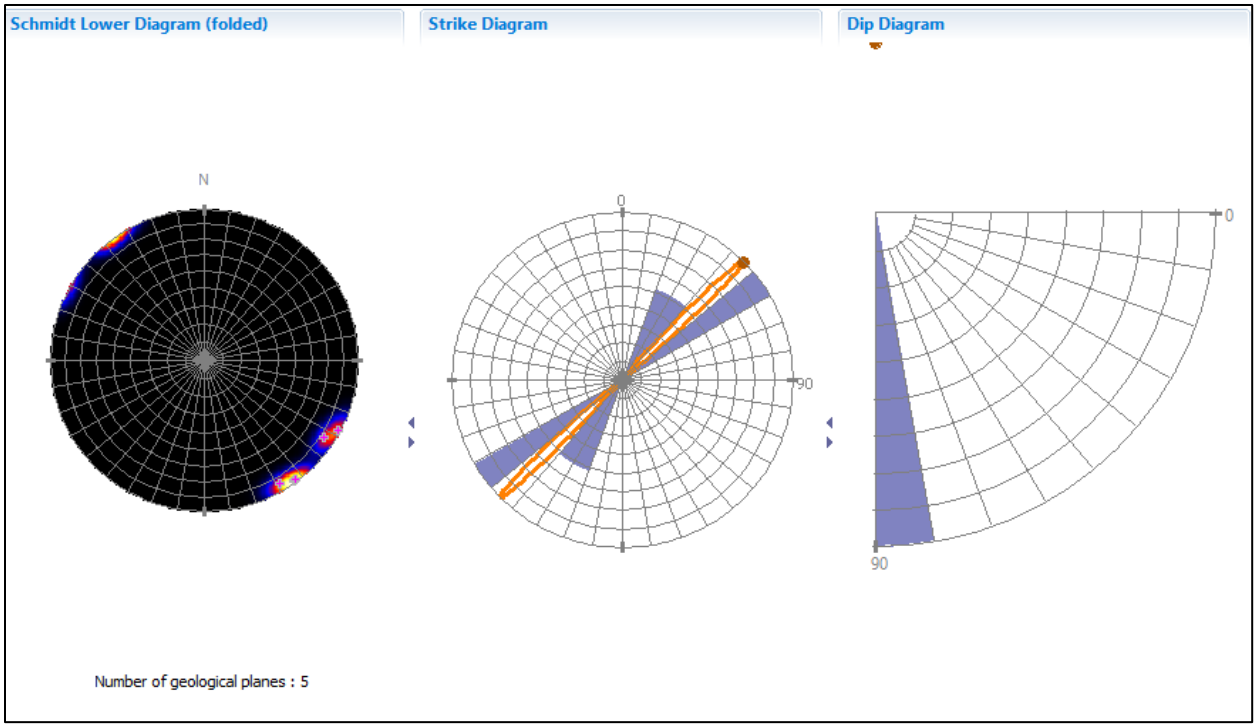

Figure 65: Stratification distribution (Pole, Strike and Dip)

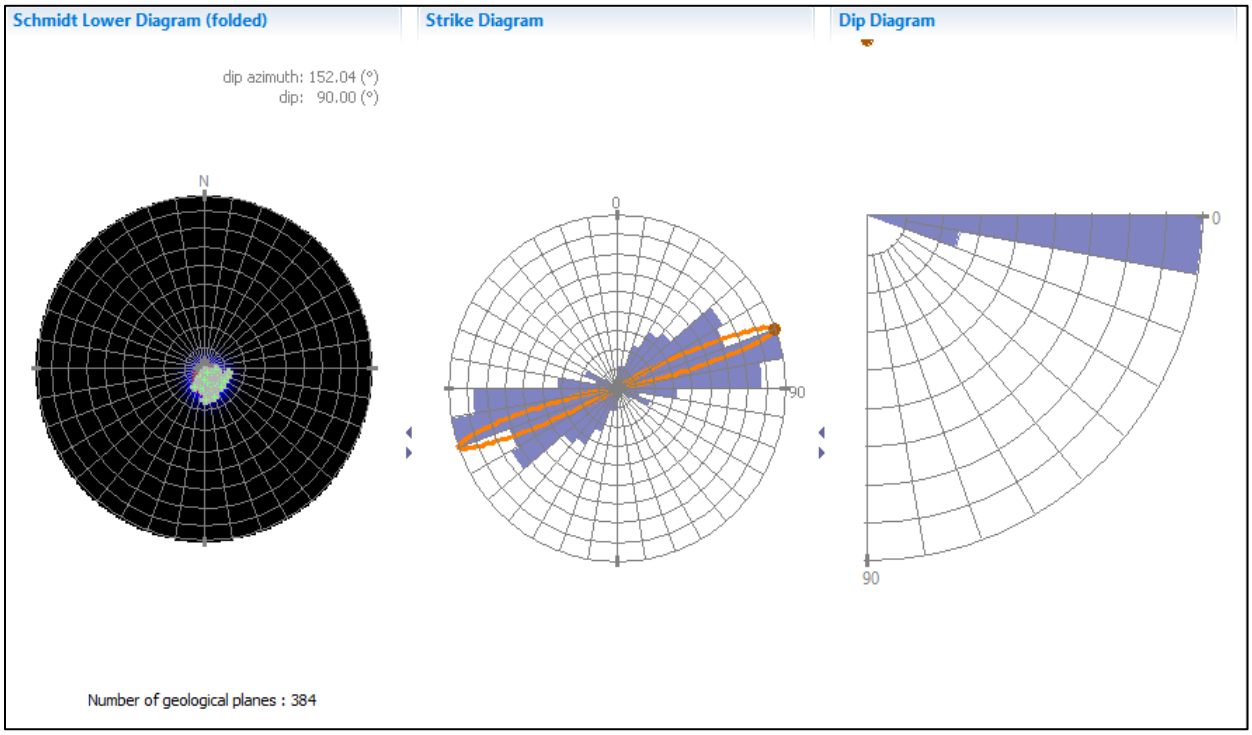

Figure 66: Breakouts distribution (Pole, Strike and Dip)

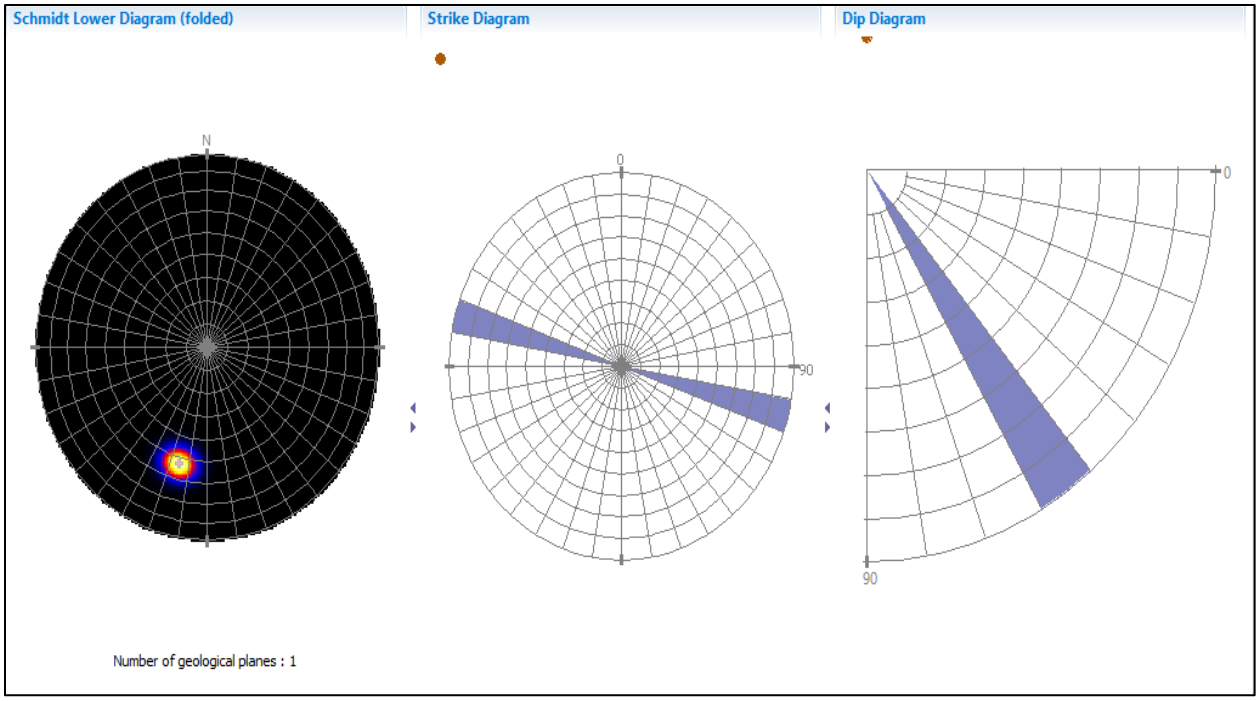

Figure 67: Conductive facture distribution (Pole, Strike and Dip)

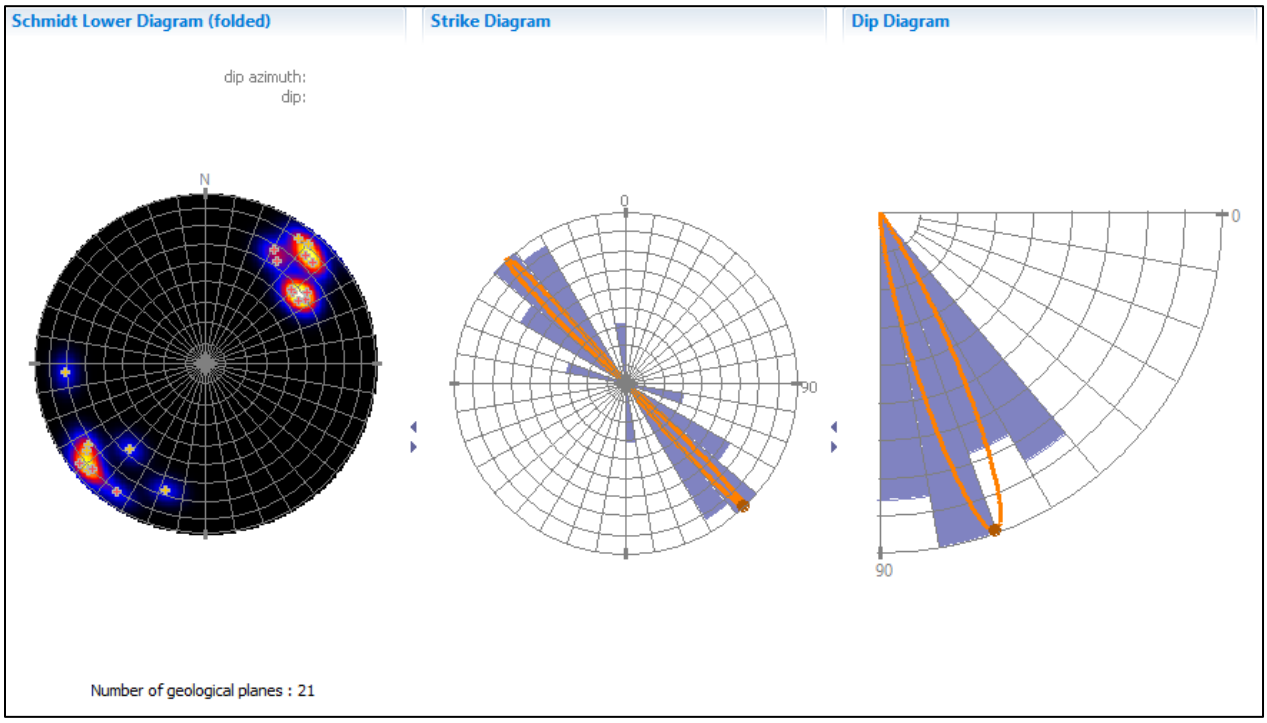

Figure 68: Resistive fracture distribution (Pole, Strike and Dip)

Well	Diffuse set name	Number of samples	Mean strike (°)	Mean dip (°)	Mean density (1/m)
Well-02	W2-N135-Cond	19	136	80	0.278
Well-02	W2-N108-Cond	1	108	67	5.295E-3
Well-02	W2-N177-Cond	1	177	71	5.355E-3
Well-02	W2-N106-Res	1	106	52	6.249E-3
Well-02	W2-N045-Break	5	45	87	0

Figure 69: Statistics related to the fractures and breakouts

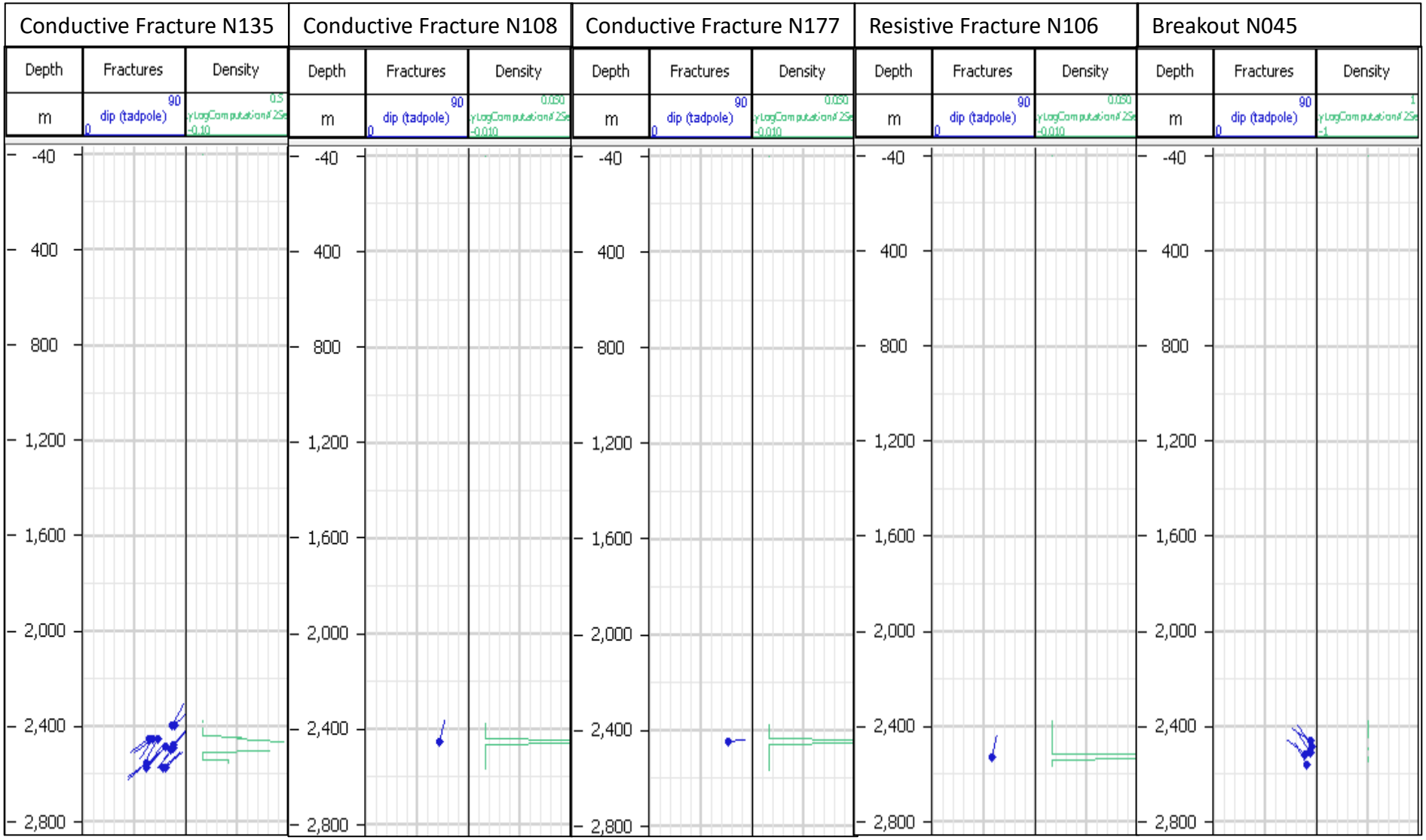

Figure 70: Fractures density and fracture distribution in the Well-2

V-2.2-Fracture analysis for the Well-3

In the Well-3, the stratification is represented by 16 measurements showing several strikes oriented N-S, NE-SW, and NW-SE, respectively. The dip is almost horizontal of all strikes (Fig.71). The breakouts are represented by 40 measurements and oriented N070 with an average dip equals to 62° (Fig.72). This indicates that the Maximum Horizontal Stress is oriented N160. Two conductive fracture sets were determined oriented N170 and N140 respectively (Fig.73).

The fracture set N170 is represented by three fractures with a dip around 90 degrees to WSW and ENE. The second fracture set N140 is represented by three fractures with a dip around 90 degrees to SW and NE. In addition, four semi-conductive fracture sets were determined oriented, N000, N070, N120 and N150 respectively (Fig.74).

The main fracture set is oriented N150 and N000 represented by 59 and 78 fractures respectively and having an average dip of 83°. No resistive fracture was detected in this well. The fracture density for the different fracture sets varies between 0.011 to 0.1 fracture/meter (Fig.75 & Fig.76).

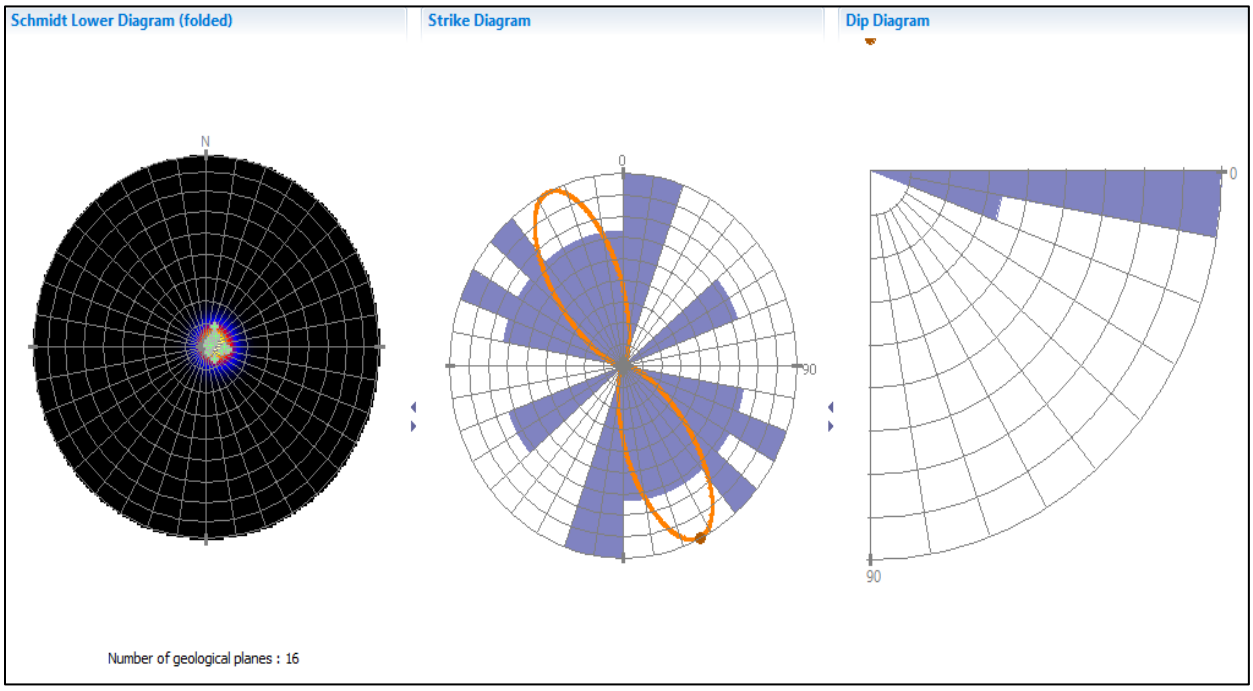

Figure 71: Stratification distribution (Pole, Strike and Dip)

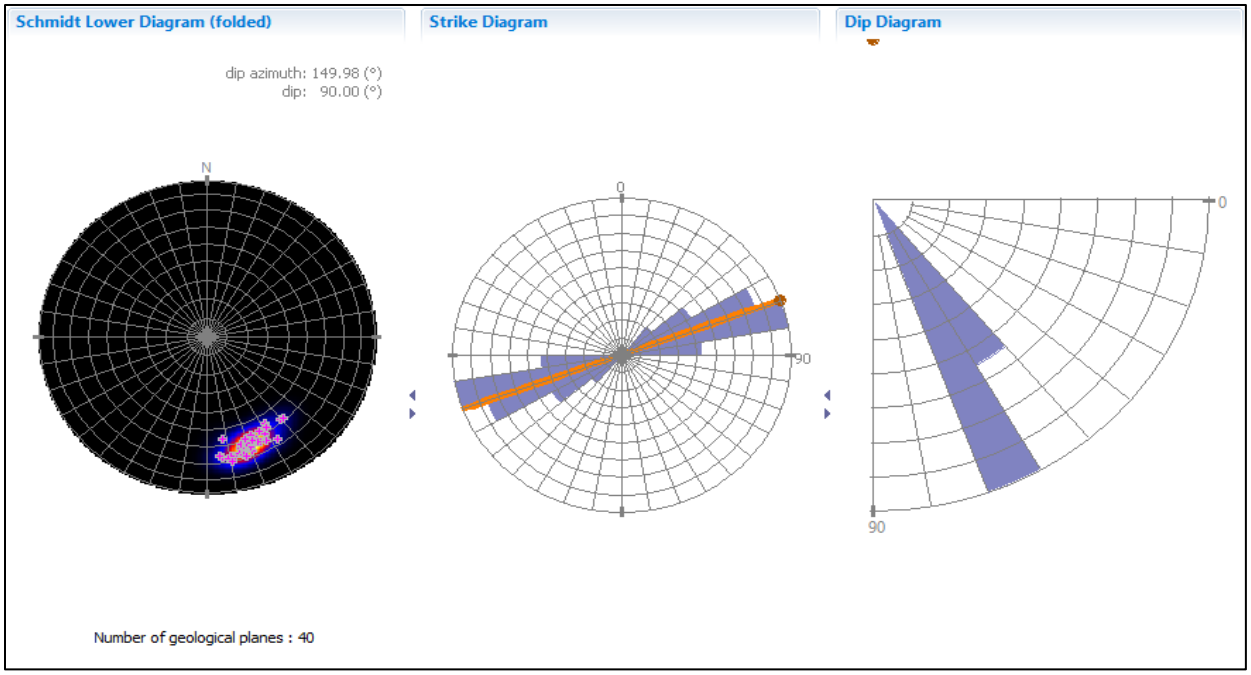

Figure 72: Breakouts distribution (Pole, Strike and Dip)

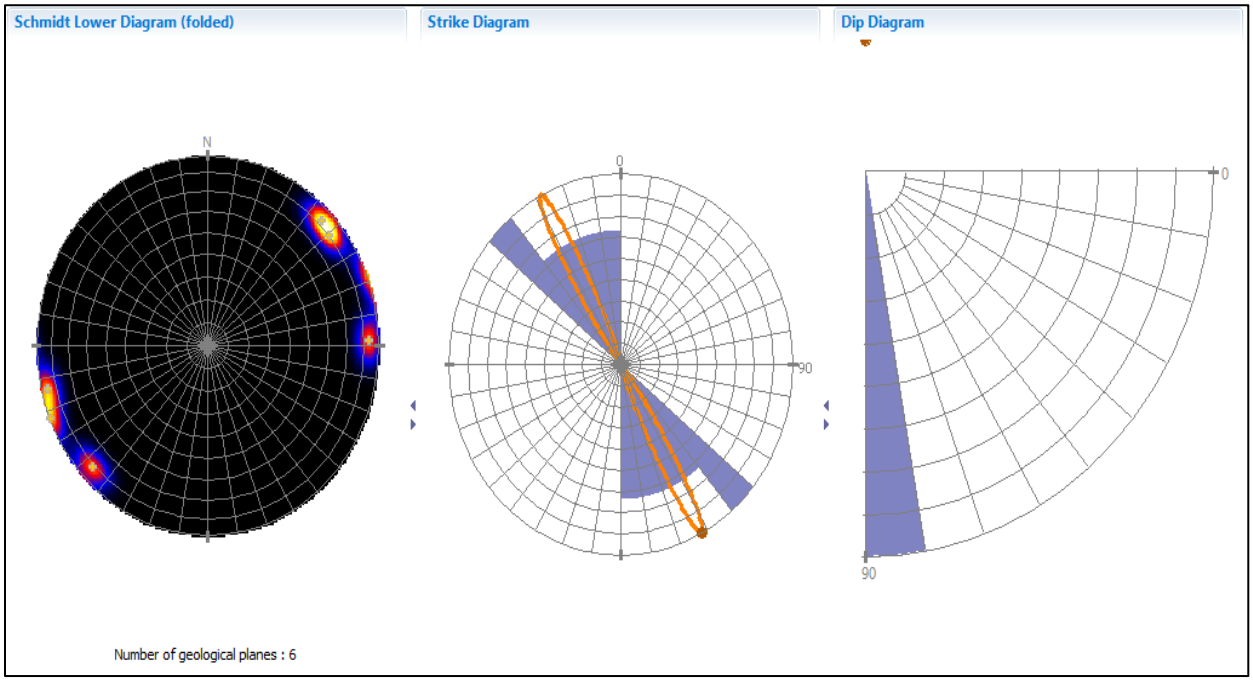

Figure 73: Conductive fracture distribution (Pole, Strike and Dip)

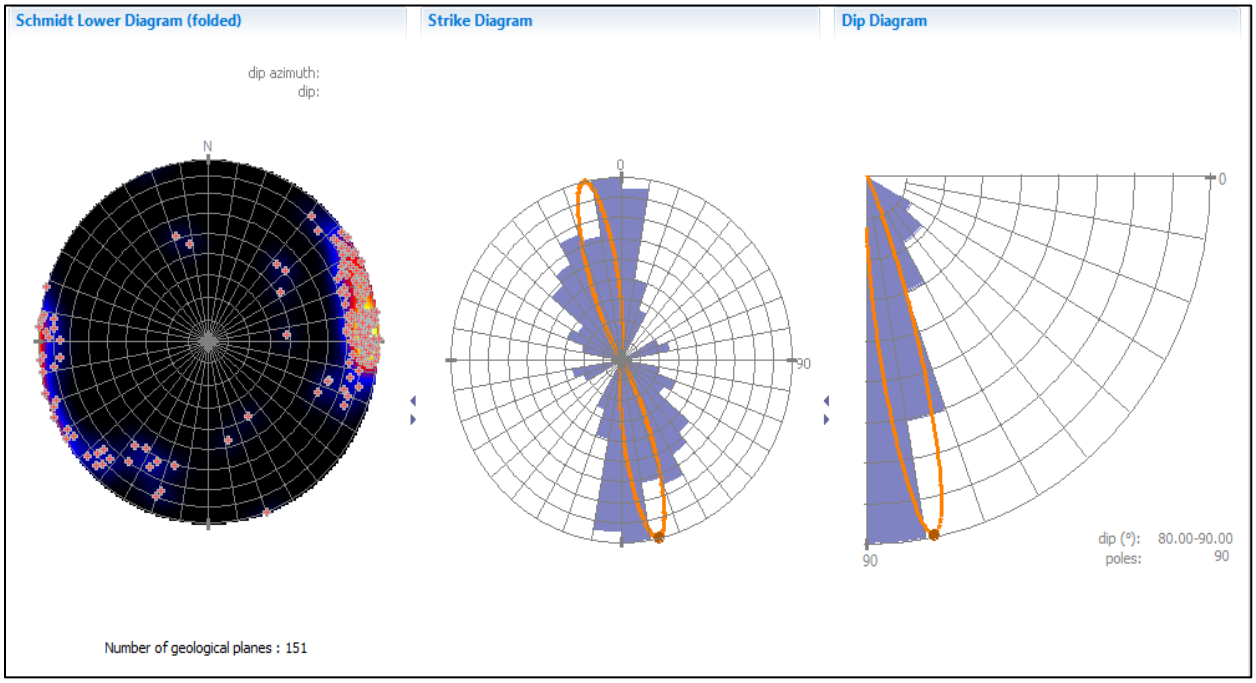

Figure 74: Semi-Conductive fracture distribution (Pole, Strike and Dip)

Well	Diffuse set name	Number of samples	Mean strike (°)	Mean dip (°)	Mean density (1/m)
Well-03	W3-N070-Break	40	70	62	0.274
Well-03	W3-N140-Cond	3	137	87	0
Well-03	W3-N170-Cond	3	167	89	0
Well-03	W3-N150-Sem_Cond	57	152	84	0.106
Well-03	W3-N000-Sem_Cond	78	1	83	0.023
Well-03	W3-N070-Sem-Cond	5	72	90	0.011
Well-03	W3-N120-Sem-Cond	9	117	66	0.034

Figure 75: Diffuse fracture statistics related to the Well-3

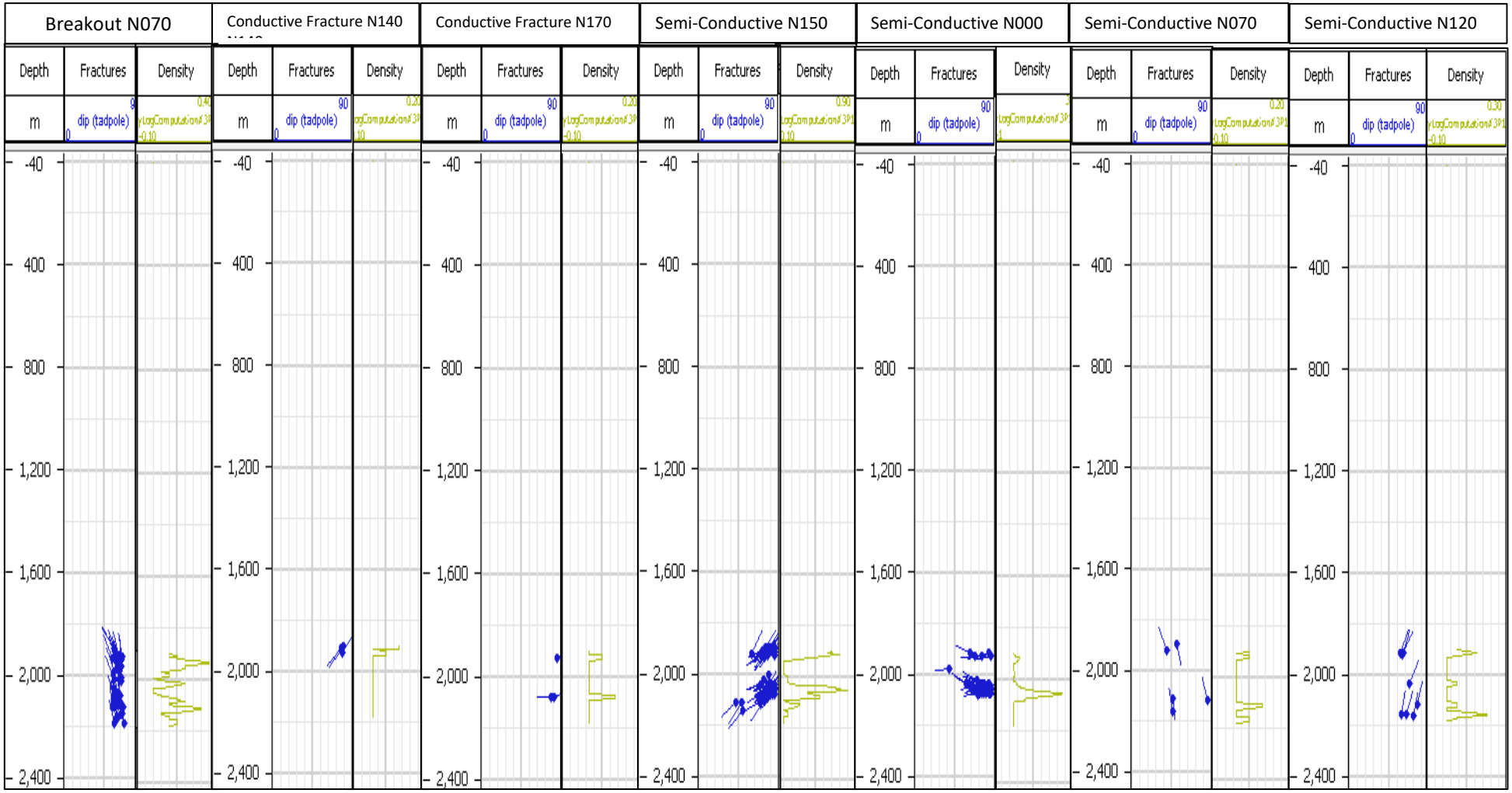

Figure 76: Fractures density and fracture distribution in the Well-3

V-2.3-Fracture analysis for the Well-4

In the well-4, the stratification is represented by more than 300 measurements showing several strikes oriented N-S, NE-SW, NW-SE, and E-W respectively. The dip is almost horizontal of all strikes (Fig.77). The breakouts represented by 14 measurements are oriented N056 with a dip equals to 89 degrees (Fig.78). This indicates that the Maximum Horizontal Stress is oriented N146. Four conductive fracture sets were determined oriented N136, N166, N027, and N60 respectively (Fig.79).

The N136 is the main fracture set represented by 15 fractures with a dip of 90 degrees. The N166, N027 and N060 are oblique fractures with a dip of 66, 68, and 52 degrees respectively. No resistive fracture was detected in this well. The fracture density varies between 0.002 to 0.007 fracture/meter (Fig.80 & Fig.81).

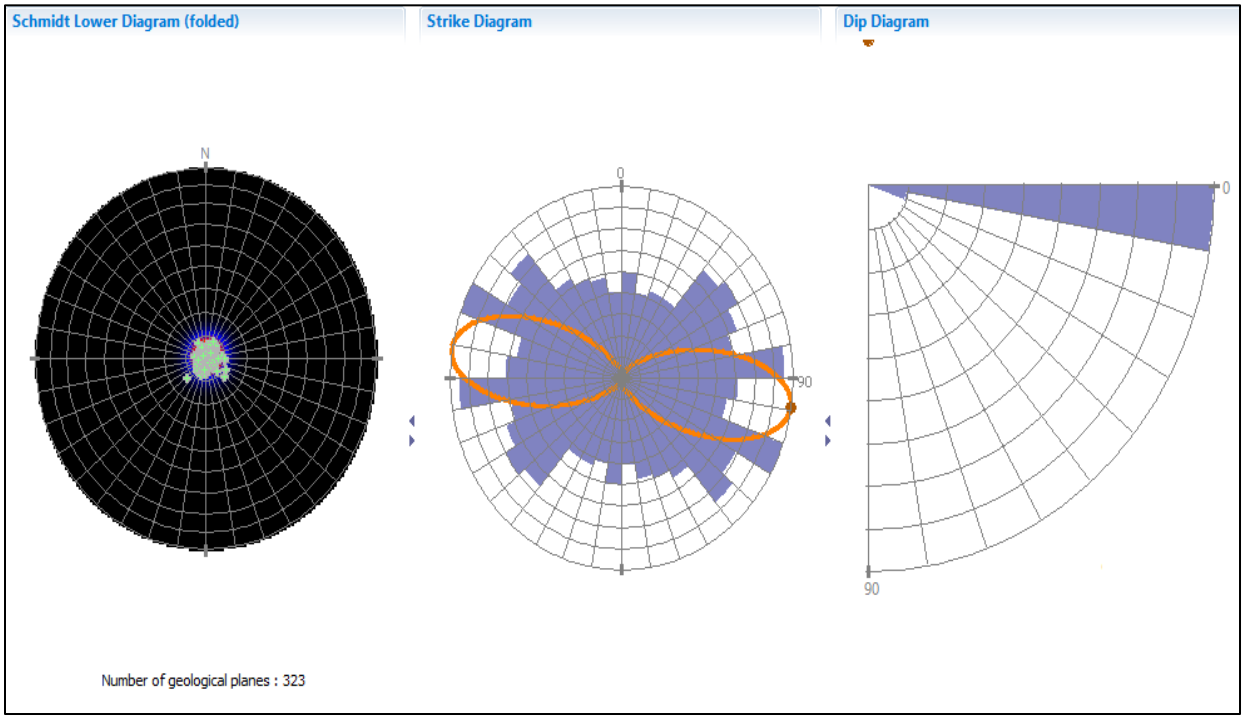

Figure 77: Stratification distribution (Pole, Strike and Dip)

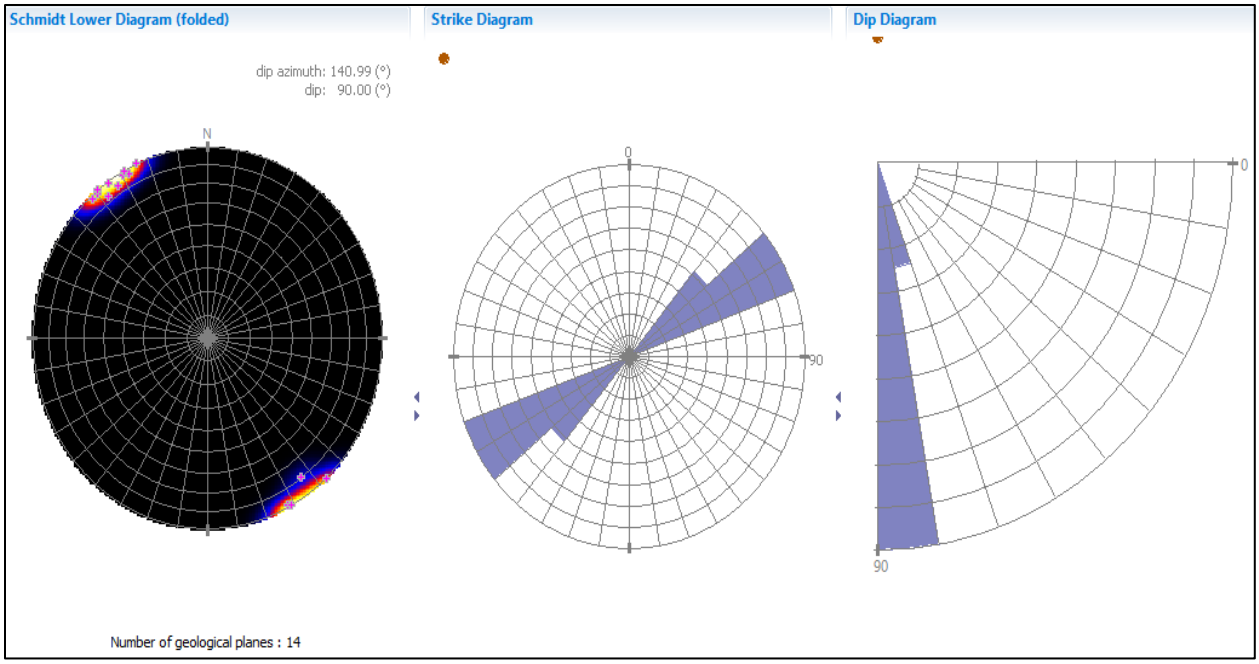

Figure 78: Breakouts distribution (Pole, Strike and Dip)

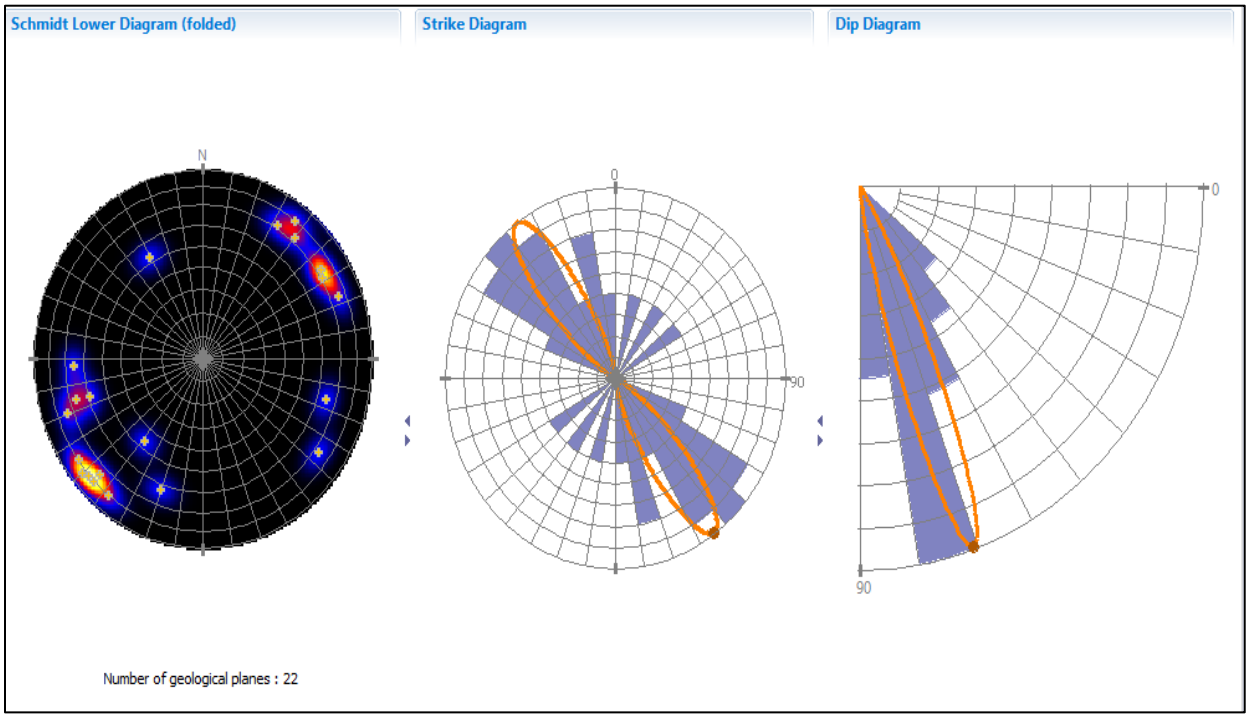

Figure 79: Conductive fracture sets distribution (Pole, Strike, and Dip)

Well	Diffuse set name	Number of samples	Mean strike (°)	Mean dip (°)	Mean density (1/m)
Well-04	W4-N056-Break	14	56	89	0
Well-04	W4-N140-Cond	15	136	90	0
Well-04	W4-N170-Cond	4	166	66	0.021
Well-04	W4-N030-Cond	2	27	68	7.836E-3
Well-04	W4-N060-Cond	1	59	52	2.787E-3

Figure 80: Statistics of fracture sets and breakouts in the Well-4

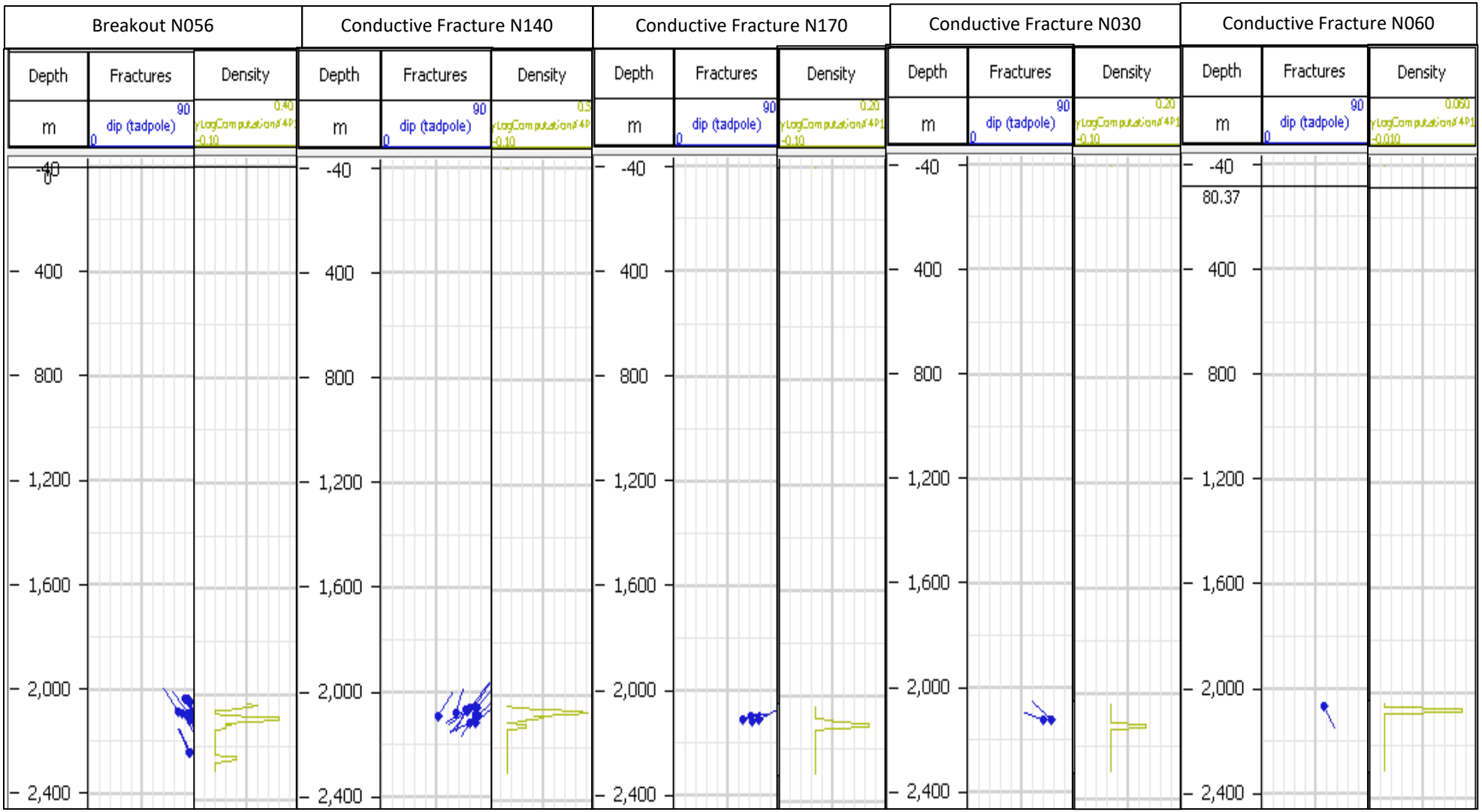

Figure 81: Fractures density and fracture distribution in the Well-4

V-3-Global Fracture Analysis

The three studied wells show mainly a horizontal stratification oriented NE-SW with a low dip ranges from 0 to 10 degrees toward the NW and sometimes toward the SE (Fig.82). Two types of fracture could be distinguished in these wells and they are conductive and semi-conductive fractures. Only one resistive fracture was described in the Well-2. The breakouts are represented by 60 measurements and they are oriented N070, which correspond to the Minimum Horizontal stress, with a dip ranges from 65 to 90 degrees (Fig.83). This permits to conclude that the Maximum Horizontal Stress in the area of study is oriented N160.

Thirty-six (36) conductive fractures were detected in the studied wells and they are oriented N140 and N160 respectively with an average dip of 80 degrees (Fig.84). On the other hand, 164 semi-conductive fractures were identified; they are mainly oriented N-S, and N140-N150 and having an average dip of 90 degrees (Fig.85). The density of the different fracture sets varies from 0.002 to 0.2 fracture/meter (Fig.86).

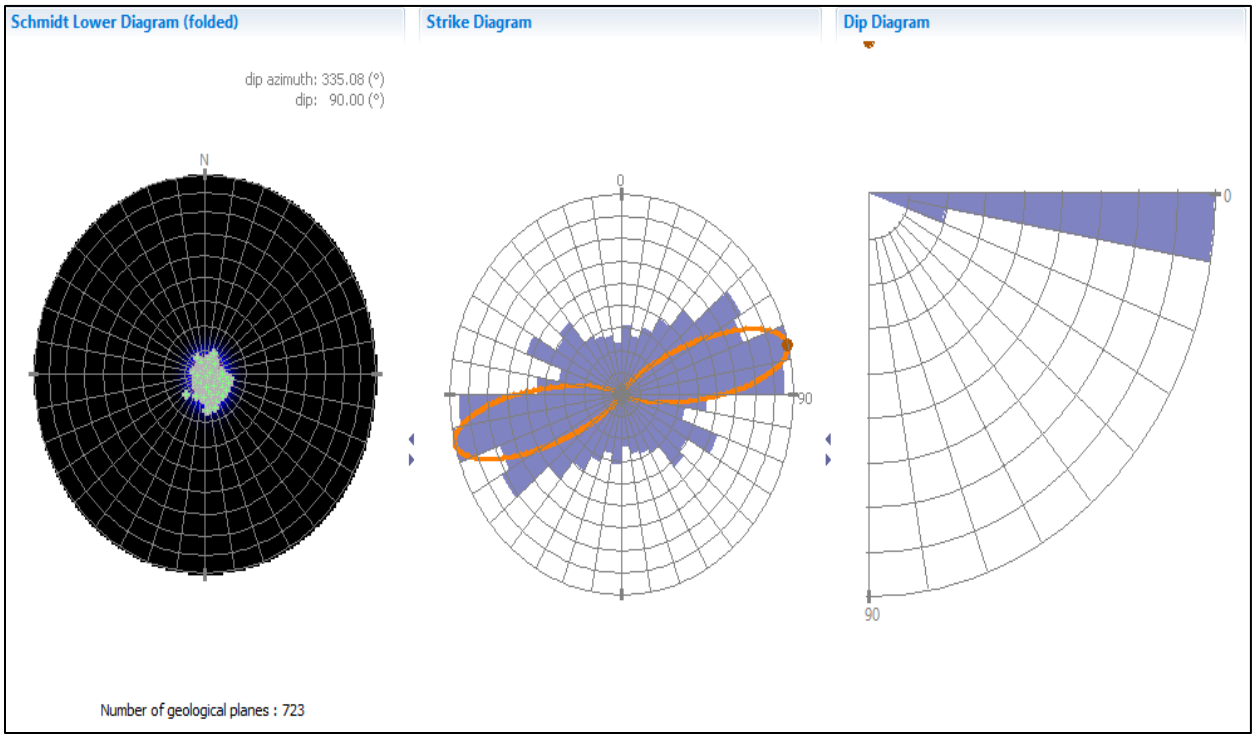

Figure 82: Global stratification distribution (Pole, Strike and Dip)

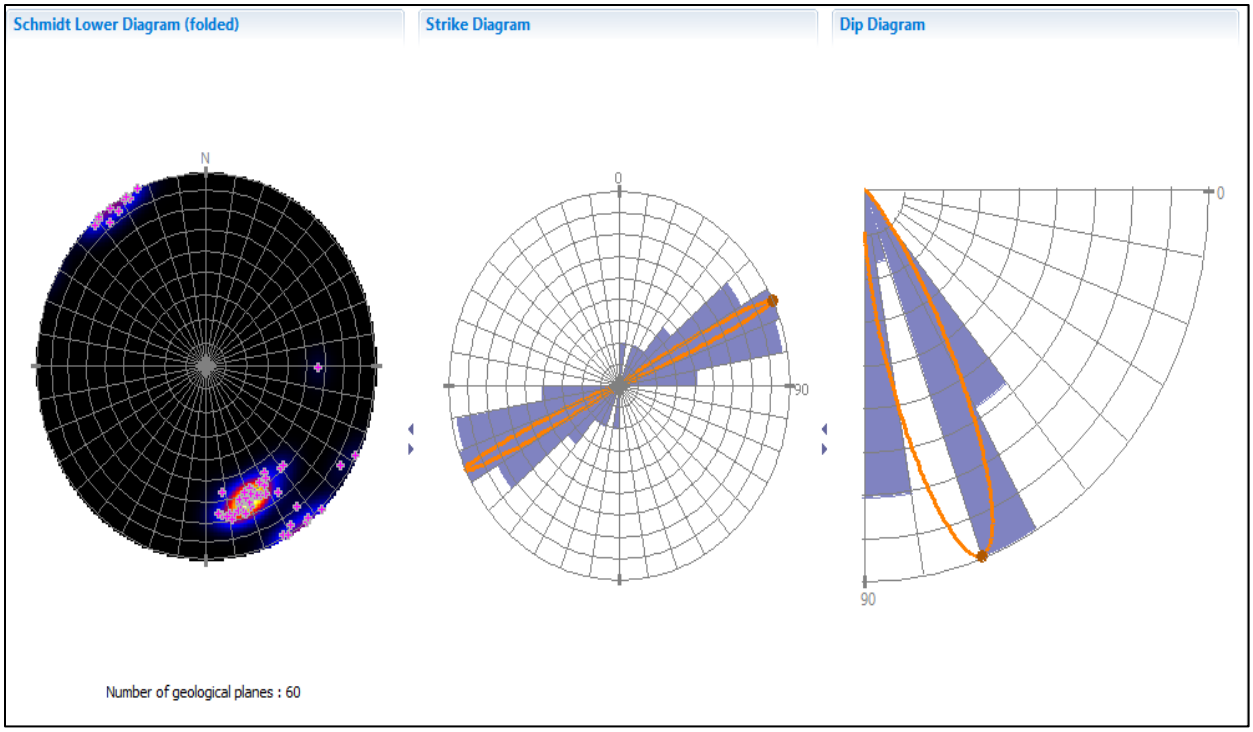

Figure 83: Global Breakouts distribution (Pole, Strike and Dip)

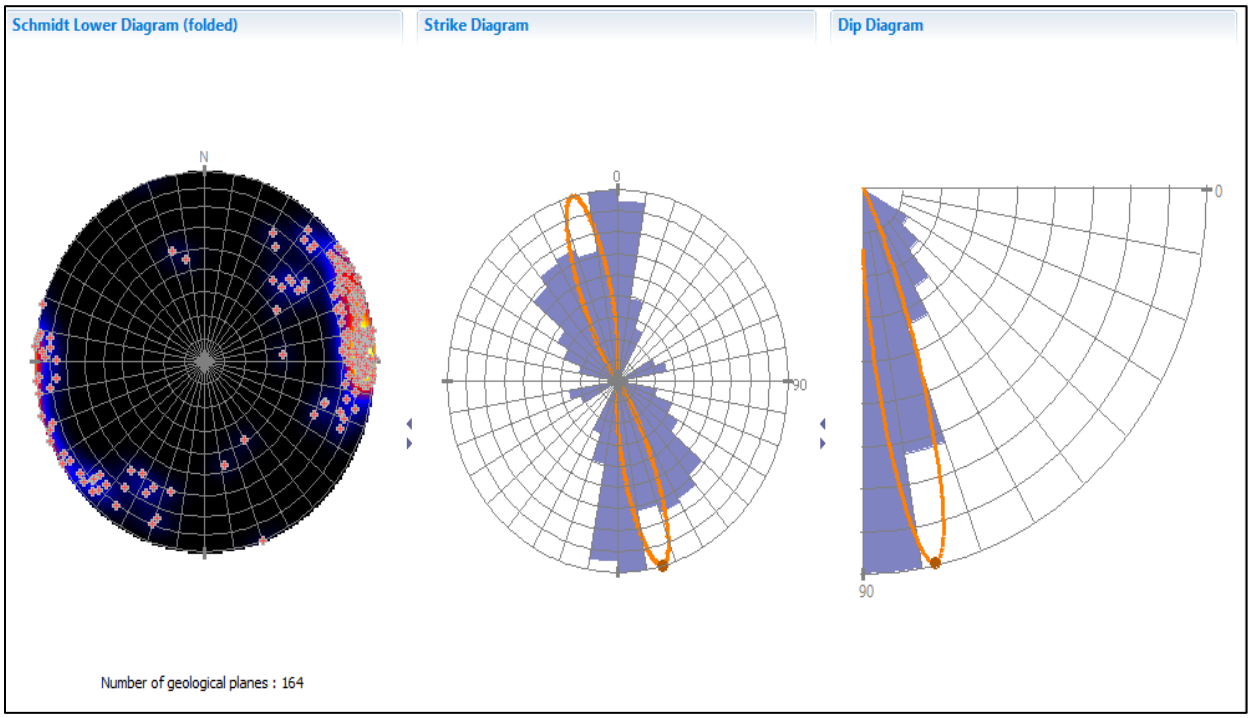

Figure 84: Global Conductive fracture distribution (Pole, Strike and Dip)

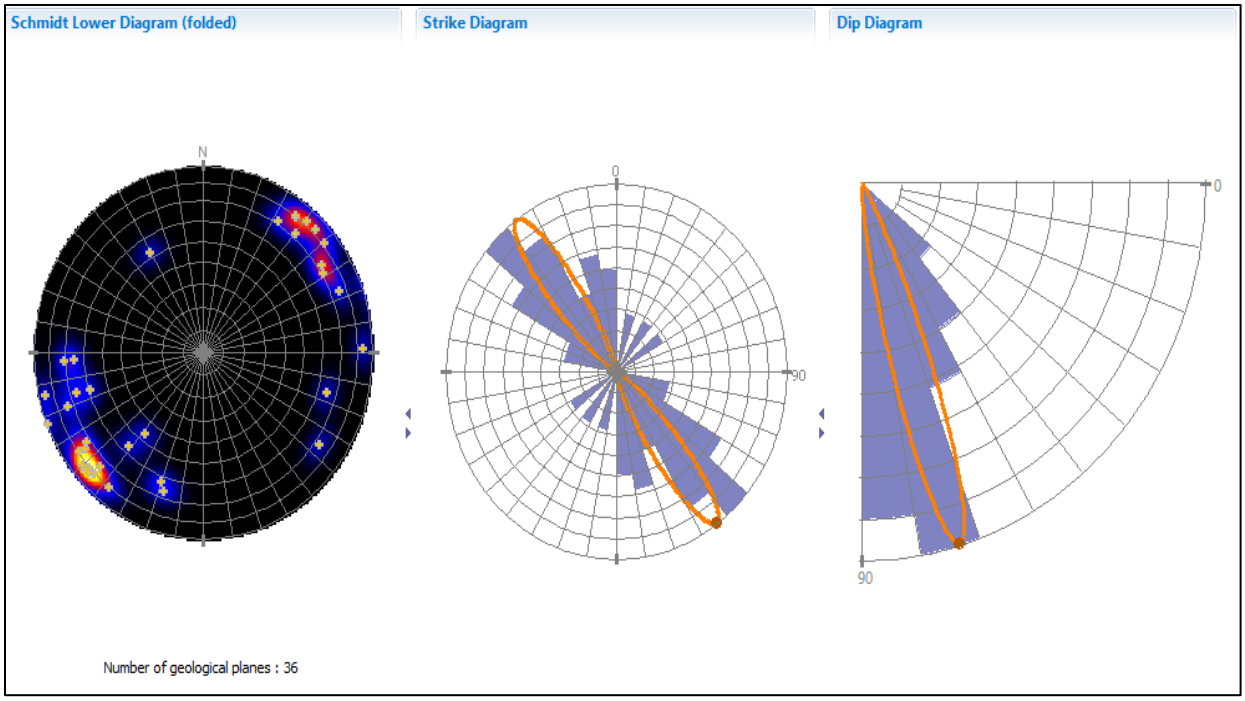

Figure 85: Global semi-conductive fracture sets distribution (Pole, Strike, and Dip)

Well	Diffuse set name	Number of samples	Mean strike (°)	Mean dip (°)	Mean density (1/m)
Well-02	W2-N135-Cond	19	136	80	0.278
Well-02	W2-N108-Cond	1	108	67	5.295E-3
Well-02	W2-N177-Cond	1	177	71	5.355E-3
Well-02	W2-N106-Res	1	106	52	6.249E-3
Well-02	W2-N045-Break	5	45	87	0
Well-03	W3-N070-Break	40	70	62	0.274
Well-03	W3-N140-Cond	3	137	87	0
Well-03	W3-N170-Cond	3	167	89	0
Well-03	W3-N150-Sem_Cond	57	152	84	0.106
Well-03	W3-N000-Sem_Cond	78	1	83	0.023
Well-03	W3-N070-Sem-Cond	5	72	90	0.011
Well-03	W3-N120-Sem-Cond	9	117	66	0.034
Well-04	W4-N056-Break	14	56	89	0
Well-04	W4-N140-Cond	15	136	90	0
Well-04	W4-N170-Cond	4	166	66	0.021
Well-04	W4-N030-Cond	2	27	68	7.836E-3
Well-04	W4-N060-Cond	1	59	52	2.787E-3

Figure 86: Global statistics of fracture sets and breakouts in Well-2, Well-3, and Well-4

V-4-Conclusion

The borehole imagery analysis of three wells in Hamra Quartzite reservoir in the eastern edge of the Ahnet basin shows that the stratification in the area of study is almost horizontal due the wells' position, which is located on the crest of the anticlines. Three main fracture sets are distinguished and oriented N030, N140, and N170 respectively with a dip of 80°. These fractures are conductive and semi-conductive. Only one resistive fracture was described in these three wells.

The core fracture analysis shows the predominance of tectonic fracture in term of number and length with a high index of fracturing. However, these fractures are usually cemented to partially cemented. The borehole imagery analysis reveals the presence of conductive and semi-conductive fractures. In many cases, it was difficult to distinguish between closed and opened fractures because of the type of cement. The huge amount of pyrite in fractures make them appearing like opened fractures but in fact, they are closed.

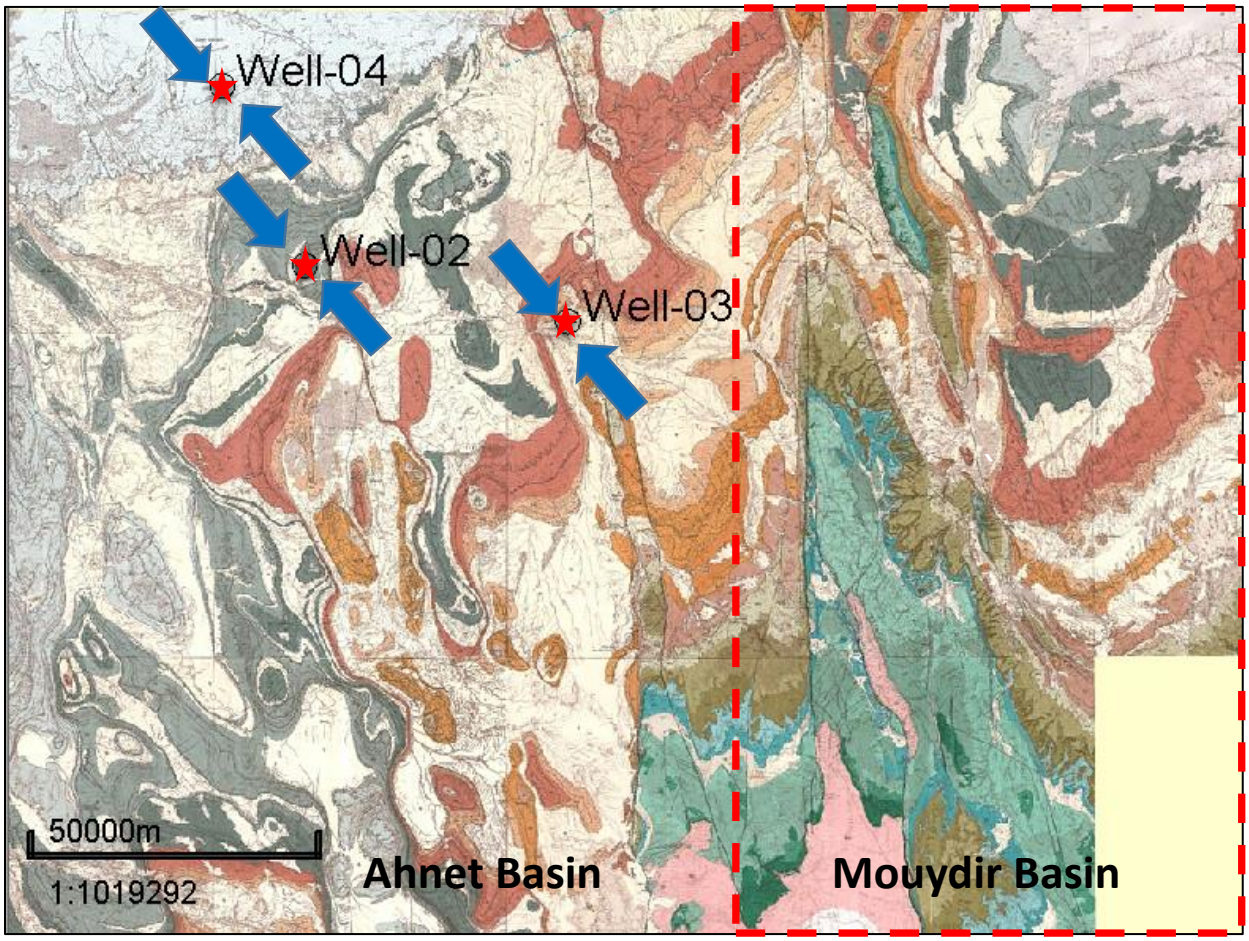

Figure 87: SHmax Orientation

The maximum horizontal stress (SHmax) is determined from the widths of wellbore breakouts. The SHmax inferred from the breakouts in the Ahnet basin is oriented NW-SE (Fig.87), which is conform to the SHmax well-known in the entire Saharan platform (Baghoul, 1992). Fractures having the same direction as the maximum horizontal stress are generally conducive (open) and thus contribute to the improvement of the petrophysical parameters of Cambro-Ordovician reservoir, whereas those perpendicular to the SHmax are generally resistive (closed) and therefore they may constitute permeability barriers.

Chapter VI: Reservoirs Quality

VI-1-Introduction

The overall distribution of petrophysical parameters was performed at the regional scale and at the scale of each well, based on the analysis of porosity and permeability measurements made on cores. The distribution of the samples is not homogeneous since the coring was not done systematically at all the sandstone and quartzite layers of the Cambrian and Ordovician reservoirs in all studied wells.

The general trend of core data cannot be representative in the Mouydir Basin, given the small number of wells drilled and their distribution, which remains random. The comparison between the core porosity and the log porosity could not be made because no elementary log analysis was performed due to lack of adequate well log curves.

The Cambrian reservoir, although compact, could be considered as a secondary objective in the Mouydir basin, especially to the southern part of the basin where it is at shallow depths. The sandstone units of the Ordovician are the main objective although their quality reservoir are average to low. The Ordovician reservoirs are the M'krata sandstones, the Oued Saret sandstone, El Atchane sandstone, and the Hamra Quartzites.

All the well tests realized on these reservoirs were negative. However, some wells had shown gas, traces of oil, and asphaltene in the Ordovician reservoir. In addition, other well tests yielded salt water in the north and fresh water to the south part of the basin.

VI-2-Cambrian Reservoir

In the Mouydir basin, only two wells have core-based petrophysical parameters. Given the small number of wells drilled through the Cambrian, it was useful to integrate the petrophysical measurements of the wells located in the immediate vicinity of the Mouydir basin, like those in the Ahnet, Oued Mya and Illizi basins. The use of such data will allow understanding the relationships between porosity and permeability and the impact of depth and natural fractures on them.

At the level of the Cambrian reservoir, the analysis of the logarithmic graph of the permeability as a function of the porosity shows that the two wells of the Mouydir basin are compact with permeability of the order of 0.01 and 0.1 mD and porosities hardly exceeding 3%.

The Cambrian at the level of the surrounding basins is also compact with permeability values very rarely exceeding 1 mD and average porosities of the order of 6% to 8% with the exception of one well where the permeability sometimes reaches 40 mD. These exceptionally permeability values have been attributed to the influence of fractures (Fig.88).

The analysis of the graphs relating to the permeability as a function of depth and the porosity as a function of the depth achieved at the level of the Cambrian reservoir reveals that there is little data to define the relationship between porosity and permeability at the Mouydir Basin. The two wells of the Mouydir Basin show that porosity and permeability are not affected by the effect of depth.

The Cambrian at the wells of basins bordering the Mouydir Basin display that porosity and permeability are not affected by the effect of depth, with the exception of one well where porosity increases with depth (Fig.89 and Fig.90).

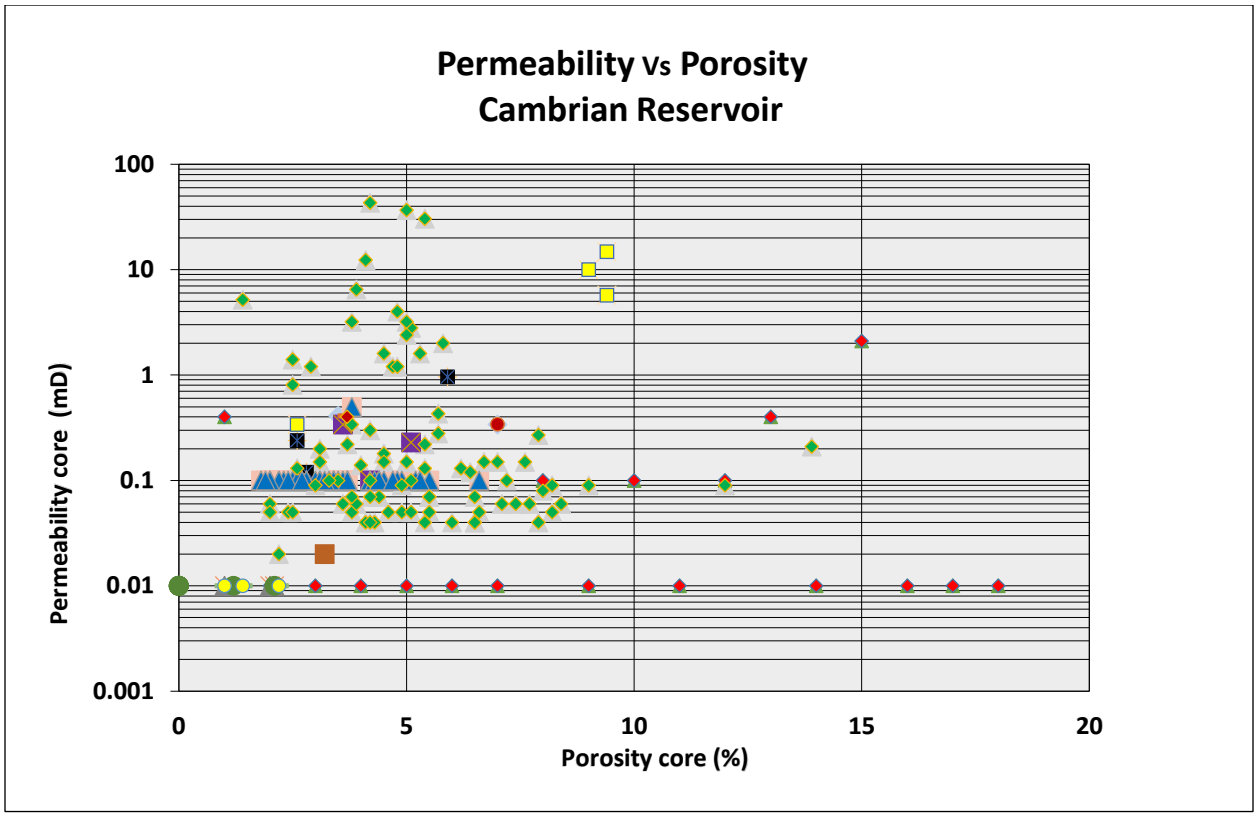

Figure 88: Porosity versus Permeability in the Cambrian reservoir

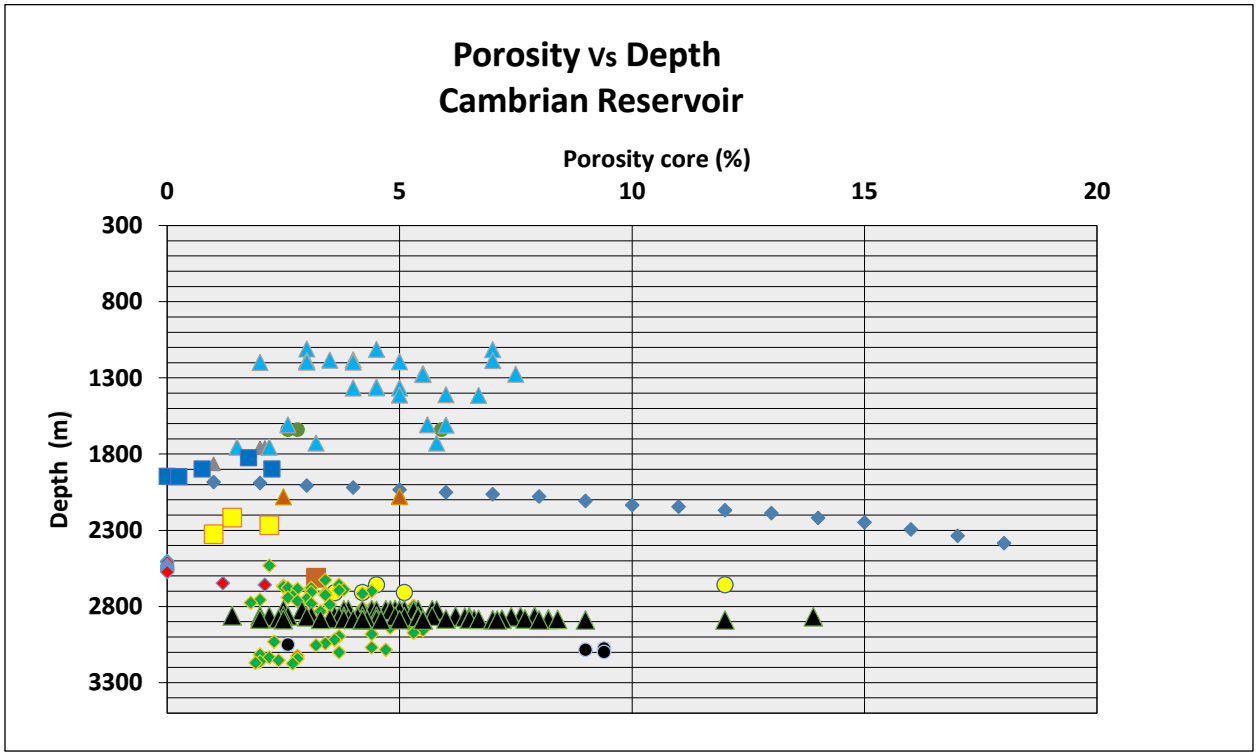

Figure 89: Porosity versus Depth in the Cambrian reservoir

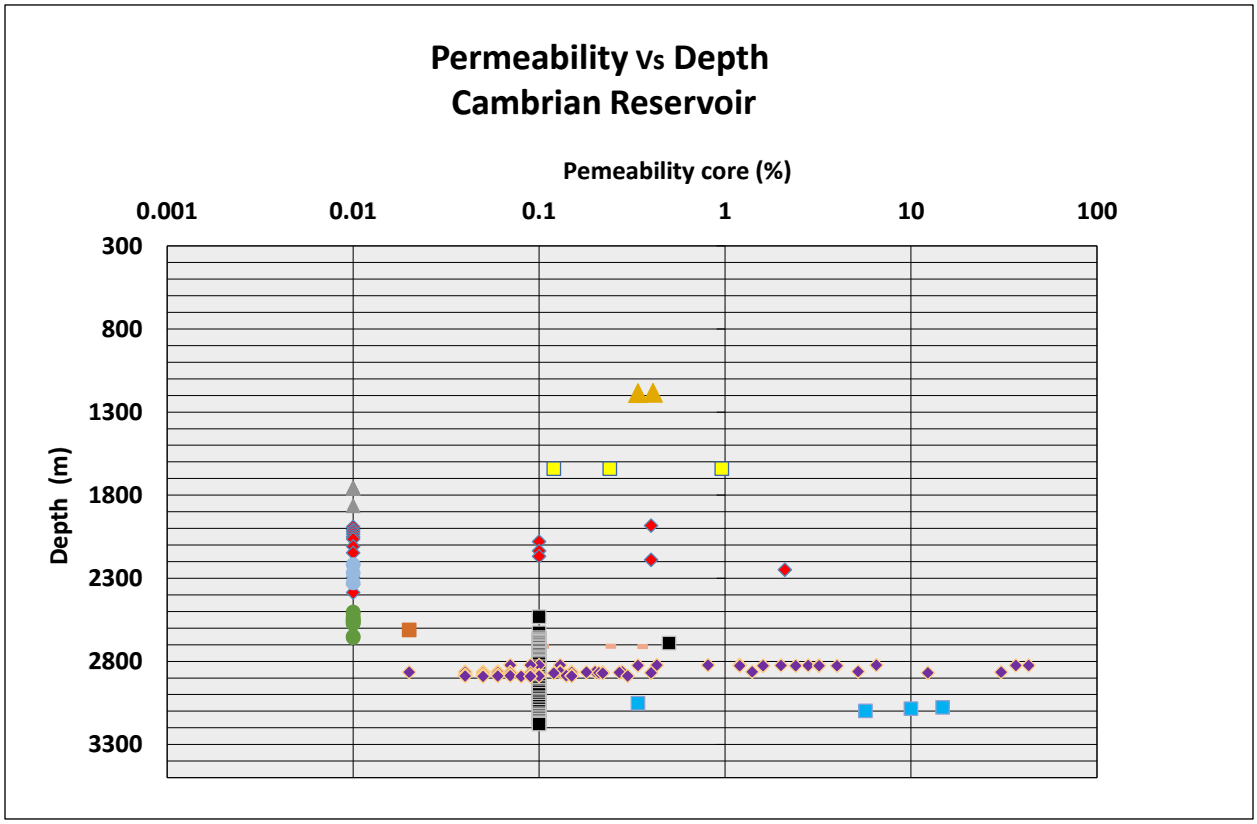

Figure 90: Permeability versus Depth in the Cambrian reservoir

VI-3-Ordovician Reservoir

In this analysis, it had been integrated both the core petrophysical data of the Ordovician reservoir for the wells drilled in the Mouydir basin than those of the surrounding basin. In the Mouydir basin, five wells have core-based petrophysical measurements. Analysis of the logarithmic graph of permeability as a function of porosity shows that the five wells in the Mouydir basin are compact with permeability ranging from 0.01 to 0.1 mD and porosities hardly exceeding 5%.

The petrophysical parameters of the Ordovician reservoir in the other wells appear also compact with permeability rarely exceeding 1 mD and average porosity of 6% to 8%. However, some wells show very high permeability and porosities of up to 18%. This high permeability, sometimes reaching values of 100 to 1000 mD, has been interpreted as due to the presence of fractures. In addition, their distribution shows an exponential relationship between porosity and permeability with a correlation coefficient of 0.5 (Fig.91).

Analysis of the permeability vs. depth and porosity vs. depth plots in the Ordovician reservoir reveal that the porosity and permeability are unaffected by the effect of the depth both for the Mouydir Basin wells and the wells surrounding basin (Fig.92 and Fig.93).

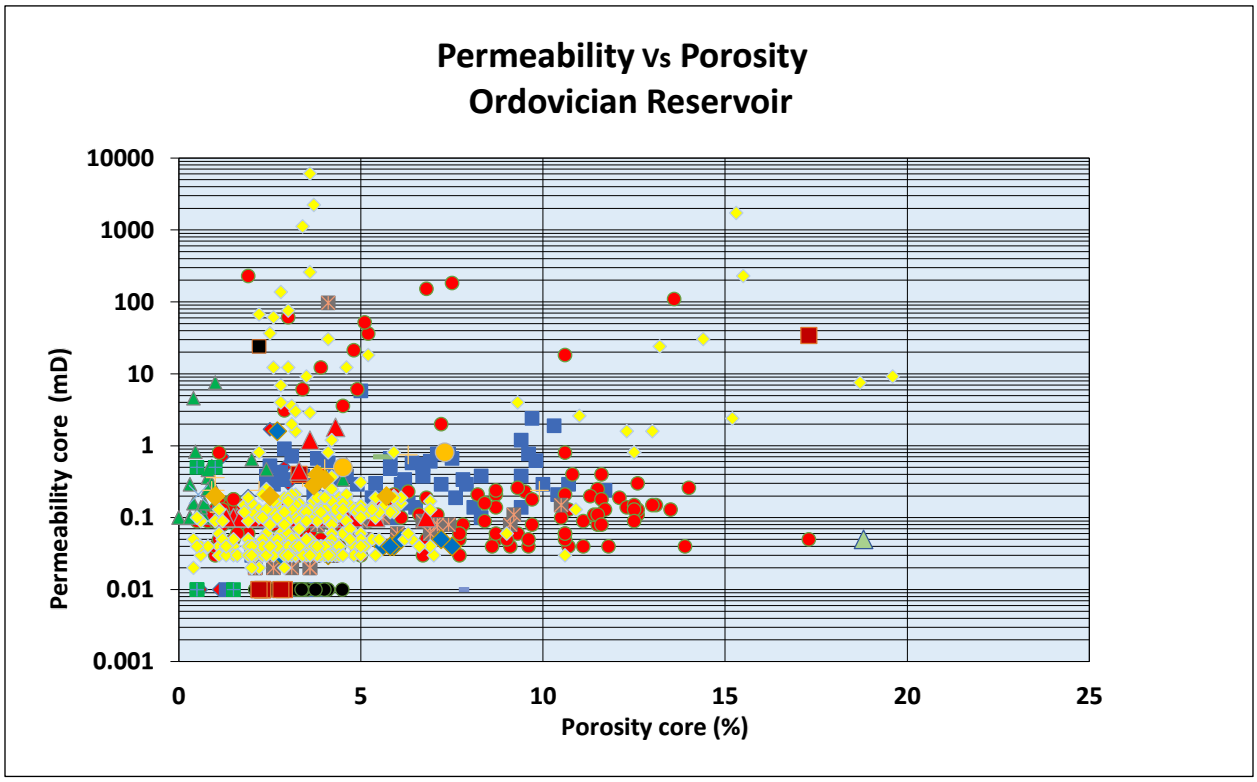

Figure 91: Porosity versus Permeability in the Ordovician reservoir

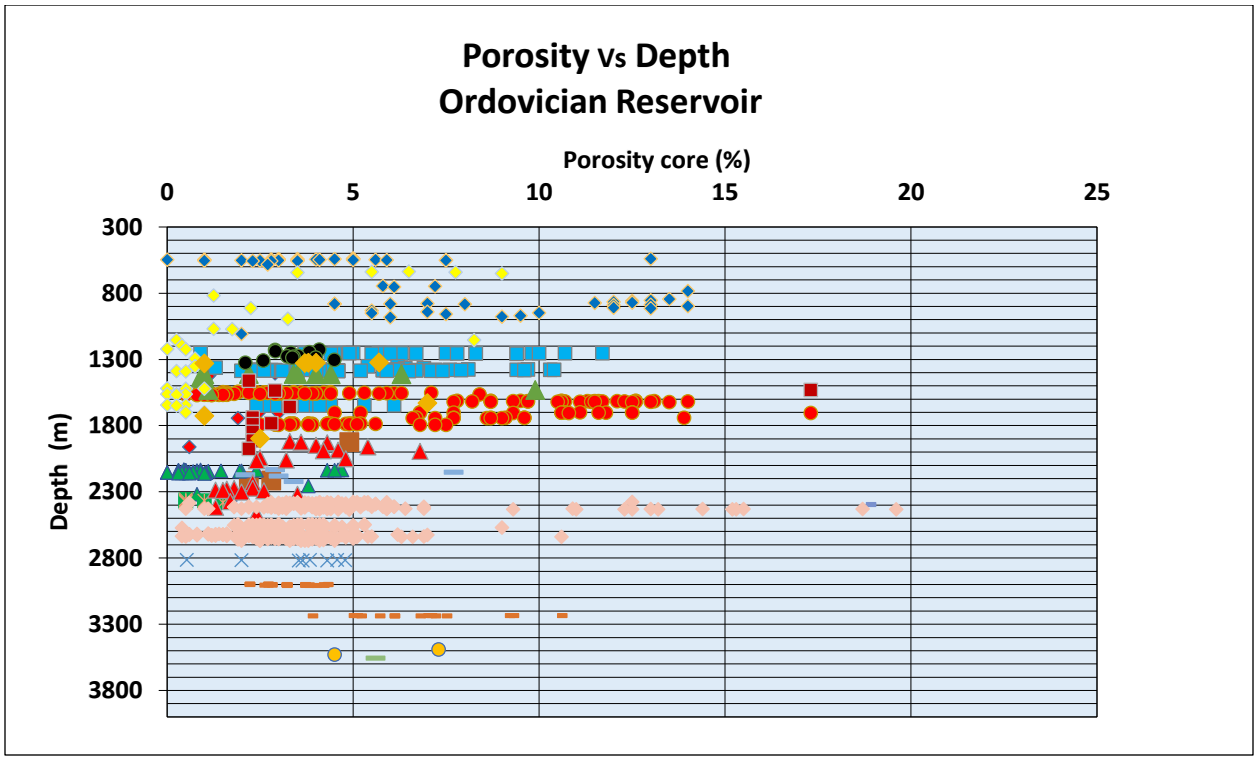

Figure 92: Porosity versus Depth in the Ordovician reservoir

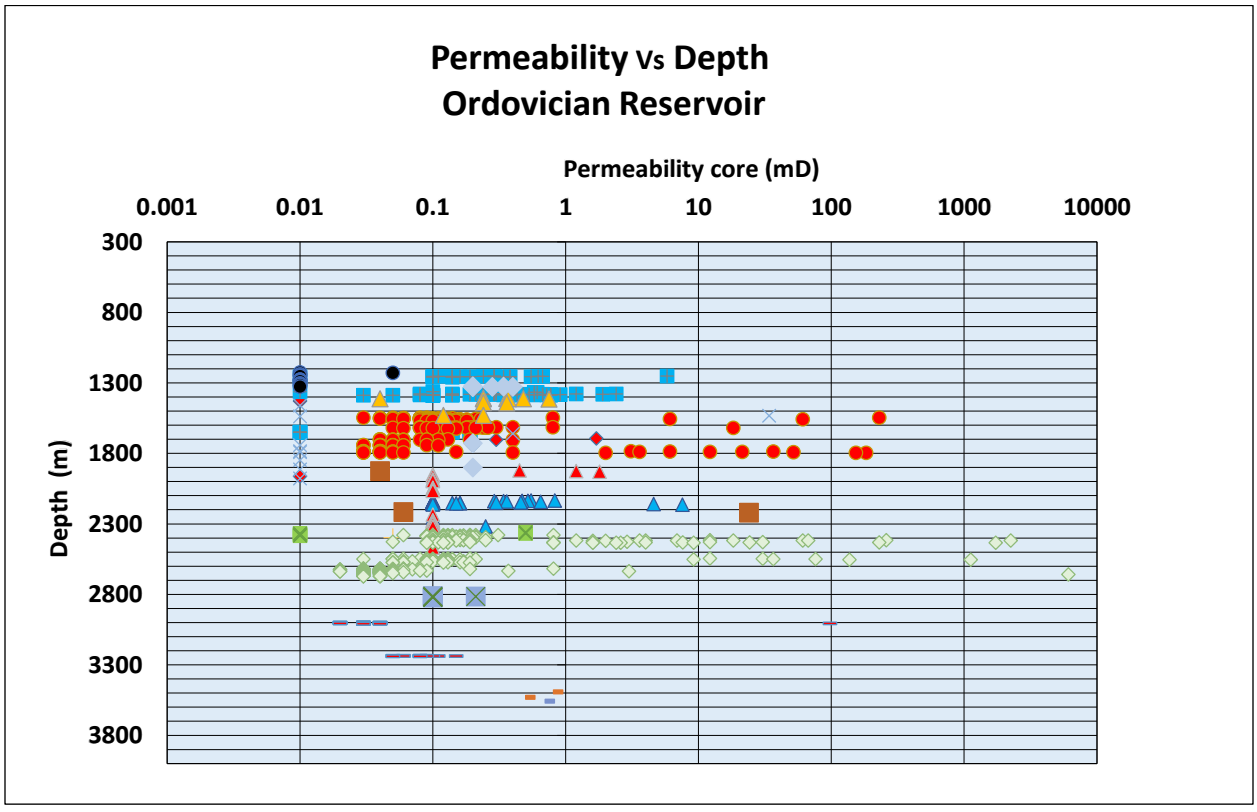

Figure 93: Permeability versus Depth in the Ordovician reservoir

VI-4-Conclusion

The overall distribution of petrophysical parameters was performed at the regional and well scale, based on the analysis of the porosity and permeability achieved on cores. The petrophysical measurements of core wells show a trend type tight sand for the majority of the studied wells with a permeability ranging between 0.01 to 0.1 mD. However, some core wells show a trend type conventional reservoir with a linear correlation between porosity and permeability.

In general, the porosity is ranged between 2% and 13% and permeability from 0.01 to 10 mD, primarily due to the effect of the compaction and cementation. Exceptional permeability values reach 100 mD due to the presence of fractures.

Chapter VII: Gravity, Seismic Data, and Structural Analysis

VII-1-Introduction

This chapter consists on the analysis of the gravity data, geological maps, 2D seismic profiles, and 3D seismic survey. The gravity data is used to determine the architecture of the subsurface in the Mouydir basin by highlighting the positive and negative anomalies and their geological signification.

The geological maps and 2D seismic profiles were both used to determine with exactitude the kinematics of different fracture sets that affect the area of study by analyzing them in the outcrops and in the subsurface. In addition, one 3D seismic survey is used to enhance and detect the reservoir's fracture network that affect the Ordovician by using several seismic attributes such curvature and Ant Tracking. The latter helps to extract and determine the fracture networks, its orientations, lengths, and density.

Firstly, the gravity data is used to determine the different positive and negative axes in the Mouydir basin. A comparison between the gravity data and geological maps is made to verify if there is an analogy between the two types of data.

Secondly, the fault network that affect the Mouydir basin is analyzed by determining the different fault sets, their length, their fractal dimension which help to generate a 3D fault model. The latter is merged with the outcrops fracture model to generate a unique 3D faults model that help to understand the origin and the extension of this fault network from the outcrops to the subsurface.

Thirdly, the major fault sets that affect the area of study are analyzed by using the geological maps to determine the age and the kinematics of these faults. In addition, the 2D seismic profiles that cross these faults we used in order to interpret their kinematics in the subsurface.

Fourthly, a 3D seismic survey located in the Ahnet basin and close to the area of study is used to illustrate the dense fracture network that affect the reservoir Ordovician and could be used as a reference analog for the future wells in the Mouydir basin.

VII-2-Gravity Data

The gravity field on the surface of the Earth is not homogenously the same in all places. It varies with the distribution of the form things underneath. This lateral change can be measured and interpreted in terms of likely relevant geology.

A Gravity survey is an indirect means of estimating the density property of subsurface constituents. The higher the gravity values, the denser the rock beneath (zonge.com). The gravity data was downloaded from the International Gravimetric Bureau website (http://bgi.omp.obs-mip.fr) by selecting the maximum and minimum latitude, and the maximum and minimum longitude of the zone of interest. The data was downloaded under zipped file including the gravity text file and image of the data in Tiff file.

The website offers data selection as free air (ocean) or Bouguer gravity anomaly (land). The interpretation of the gravity map of the Mouydir basin shows two positive anomalies oriented North-South. These anomalies correspond in fact to the edges of the basin represented by the Idjerane spur in the west and Amguid-Biod spur in the East (Fig.94).

In the middle of the basin there is another positive structure oriented also North-South where the well HL was drilled. These positive anomalies are separated by negative anomalies where several dry well were drilled. The positive anomalies have the same orientation as the major fault in the area of study and the show the same aspect as the geological maps (Fig.95).

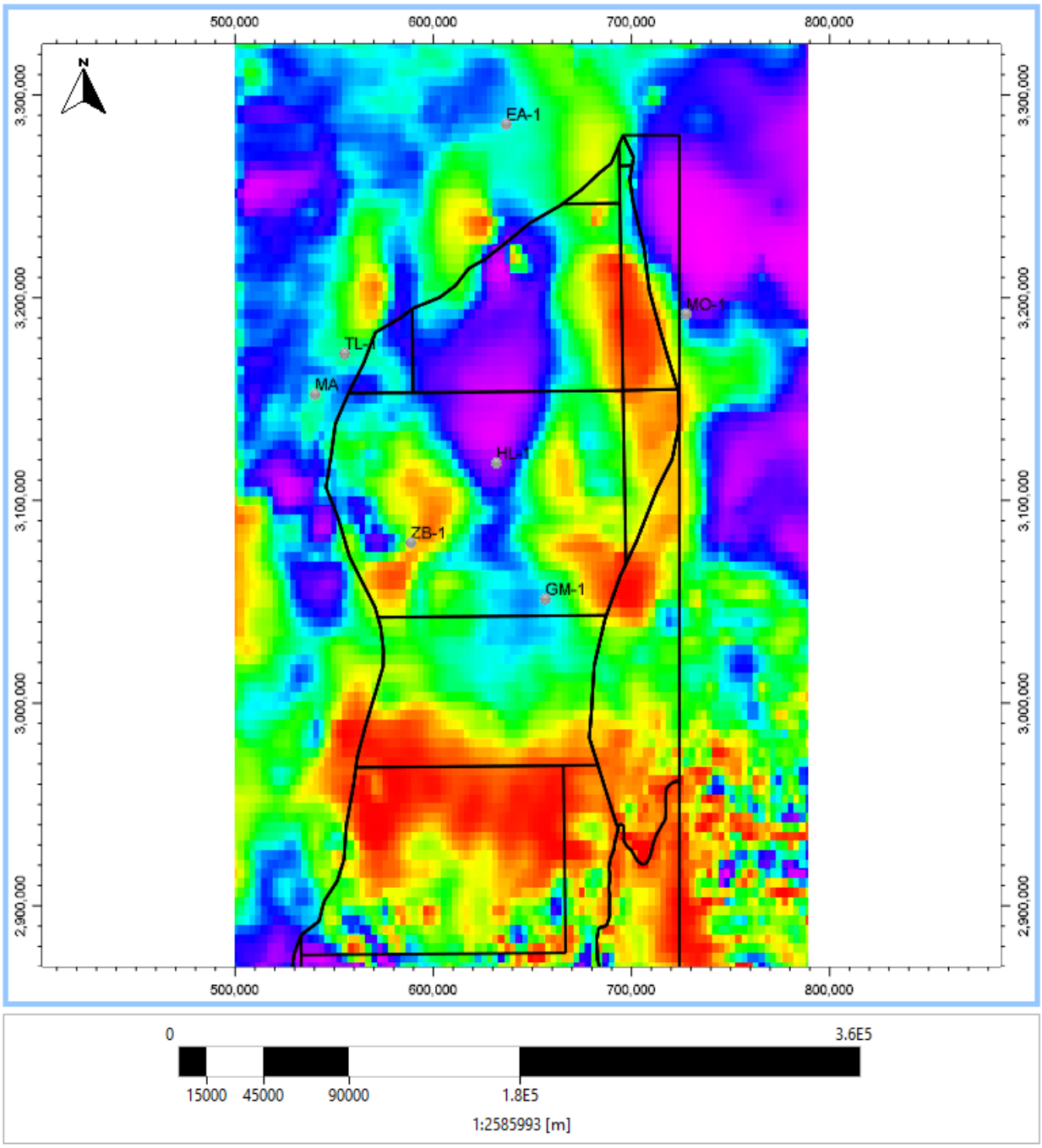

Figure 94: Gravity map in the area of interest.

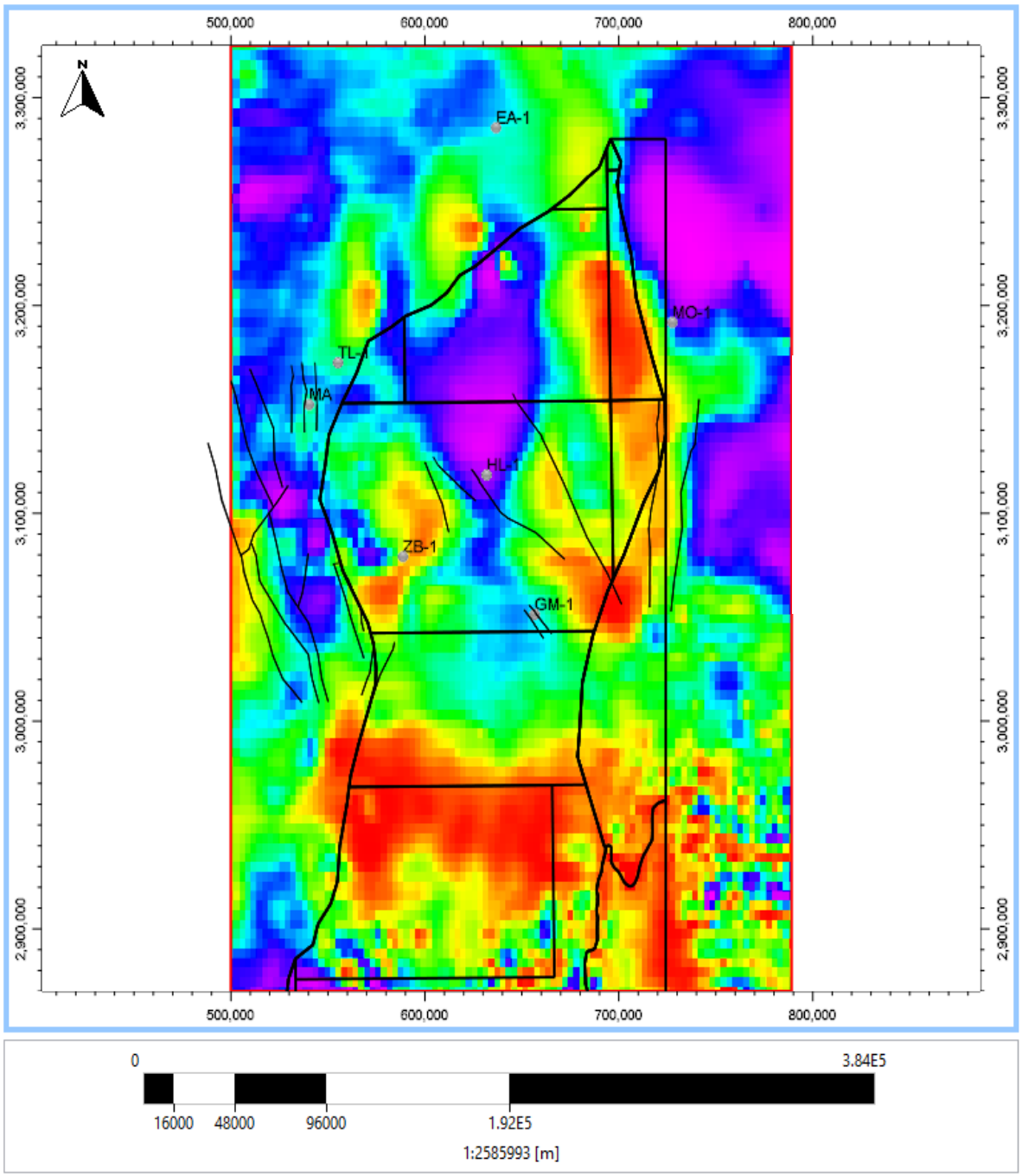

Figure 95: Gravity map and seismic faults in the Mouydir basin.

The superposition of the gravity map and the seismic fault show that the faults have the same orientation than the positive anomalies and they oriented North-South and NW-SE emphasizing the edges of the Mouydir basin.

VII-3-Fault Analysis

The fracture that affect the Mouydir basin are mainly mode II. These fractures are in an in-plane shear mode, where the displacements are in the plane of the discontinuities and could be normal/reverse faults, strike slip faults or combinations between both generating transpressional and transtensional faults. The pole diagrams are used in the fault analysis to better and faster analyze the faults' orientation. Each fault set is represented on stereo-diagram, which represent a group of poles built manually or automatically. In the area of study, faults represent the discontinuities where their lengths are plotted as normalized cumulative frequency distribution where Nb is the number of fractures with length greater than length, L per m2.

The logarithmic axes are used where a straight line indicates that the length distribution is power law with an exponent "a" given by the slope of the graph. The fault map is generated from the combination of different seismic 2D surveys. A fractal dimension approach is for the whole network and fault each fault set to determine whether or not the subsurface fault network has a fractal dimension.

Even though the lower quality of the 2D seismic data in the Mouydir basin, the top Ordovician and 27 faults were picked (Brahimi, 2015). The outputs were exported as ASCII files and loaded on FracaFlow^{TM} for analysis. The faults are gathered in four fault sets oriented N000, N020, N140 and N160 respectively (Fig.96). The global fractures length and the length of each fracture set were analyzed based on statistical parameters such as the most, least, and mean frequent lengths, correlation coefficient, and power law exponent. Their length varies between 3km to 8 km.

They are characterized by a power law distribution with coefficient oscillates between 1.7 and 2.65 and coefficient correlation ranges from 0.93 and 0.97 (Fig.97). FracaFlow software is used to analyze the fracture networks and calculate the fractal dimensions D_m using the center distance and the box-counting algorithms. Neither the whole network nor the different fault sets present a fractal dimension expect for the whole network which present a fractal dimension only using the box-counting method with a fractal dimension D_m equals to 1.25 (Fig.98). The 3D deterministic fault model for each formation was built to illustrate the fracture distribution in space to determine their origin and relationship, and predict their continuity in the subsurface (Fig.99).

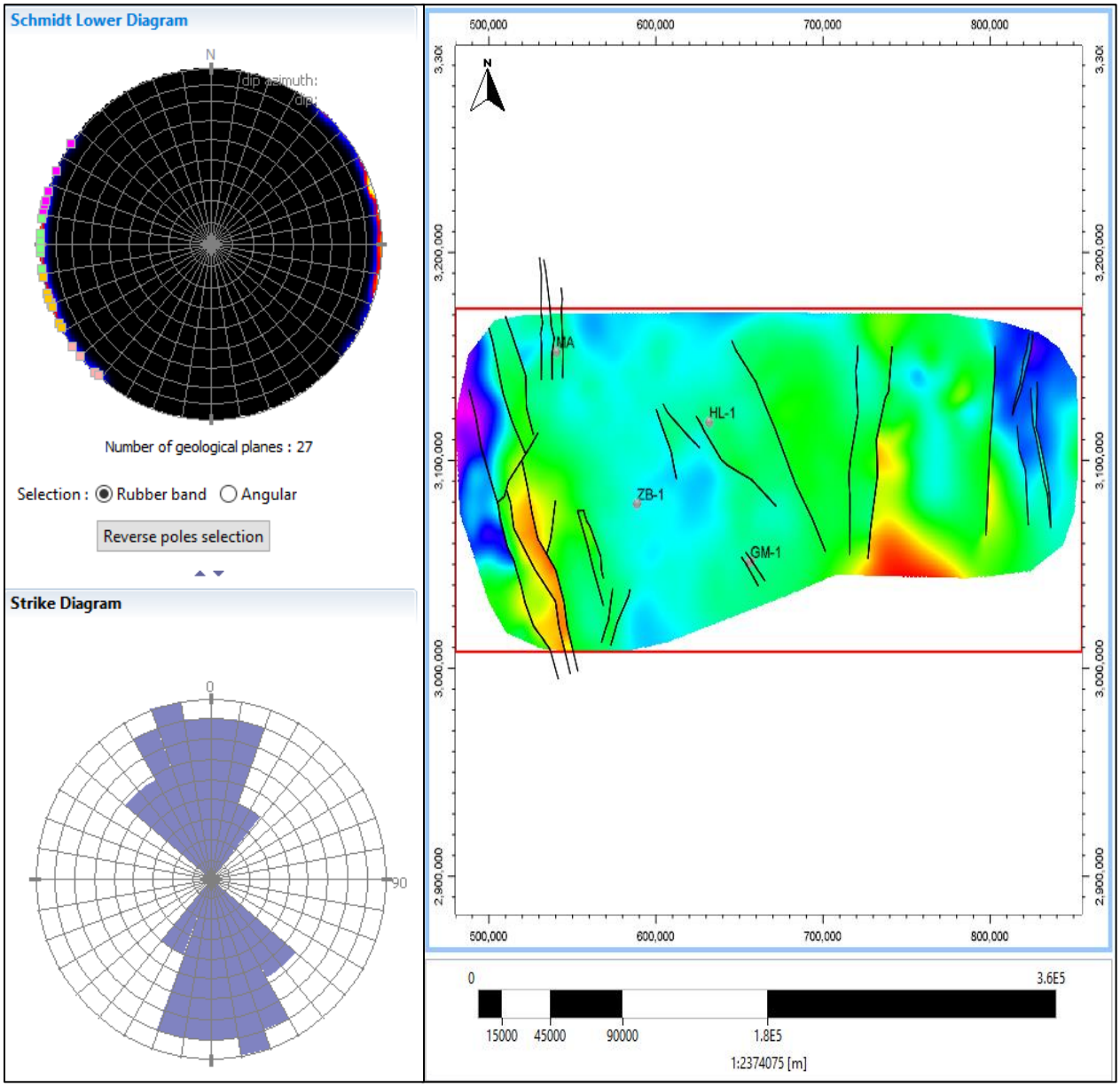

Figure 96: Sub-seismic faults distribution in the Mouydir basin

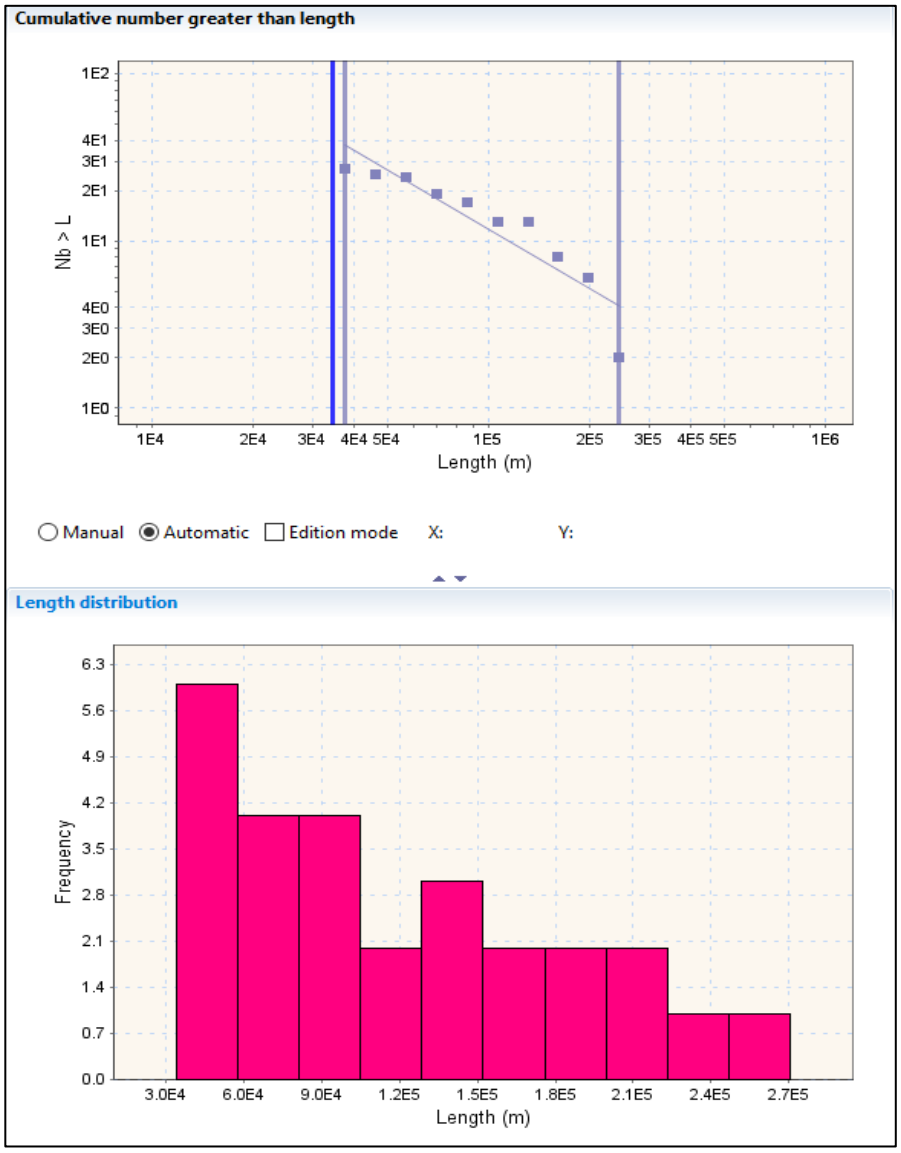

Data	Points	a	LMin (m)	LMax (m)	LMean (m)	Correlatio	Distribution
All Faults	27	2.17	3.75E+04	2.44E+05	7.91E+04	-0.92	Power law
N000	8	1.7	4.87E+04	1.92E+05	9.37E+04	-0.98	Power law
N020	6	2.23	5.35E+04	8.23E+04	6.56E+04	-0.77	Power law
N140	4	2.02	3.62E+04	1.23E+05	6.25E+04	-0.86	Power law
N160	9	2.65	7.65E+04	2.53E+05	1.22E+05	-0.91	Power law

Figure 97: Length distribution of the seismic fault in the Mouydir basin.

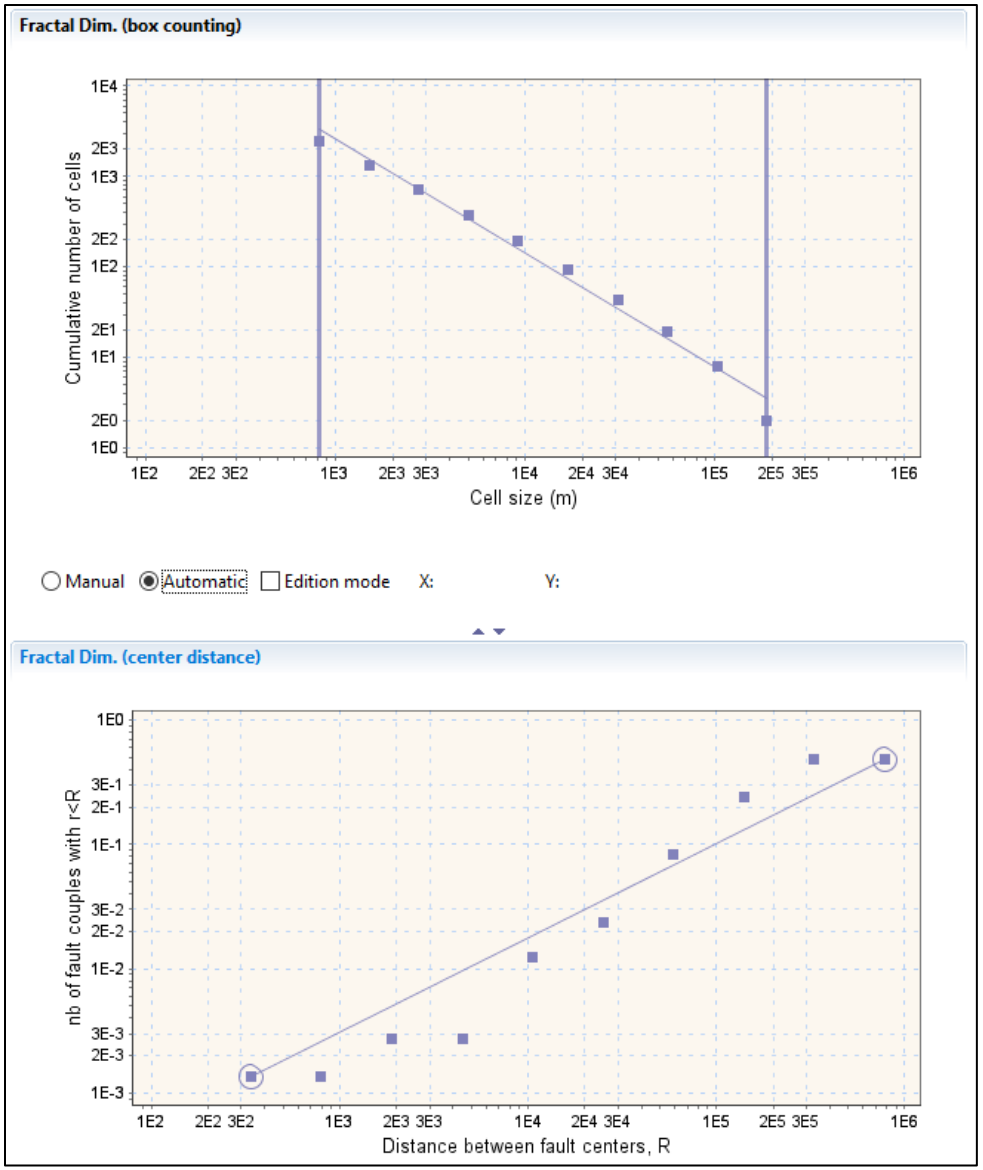

Figure 98: Fractal Dimension of the seismic faults in the Mouydir basin.

Data	Points	Fract dim.(center distance)	Fract dim.(box counting)	Rmin
All Faults	27	No value	1.2592	337.3212
N000	8	No value	No value	4.0138
N020	6	No value	No value	2.525
N140	4	No value	No value	3.8112
N160	9	No value	No value	3.8875

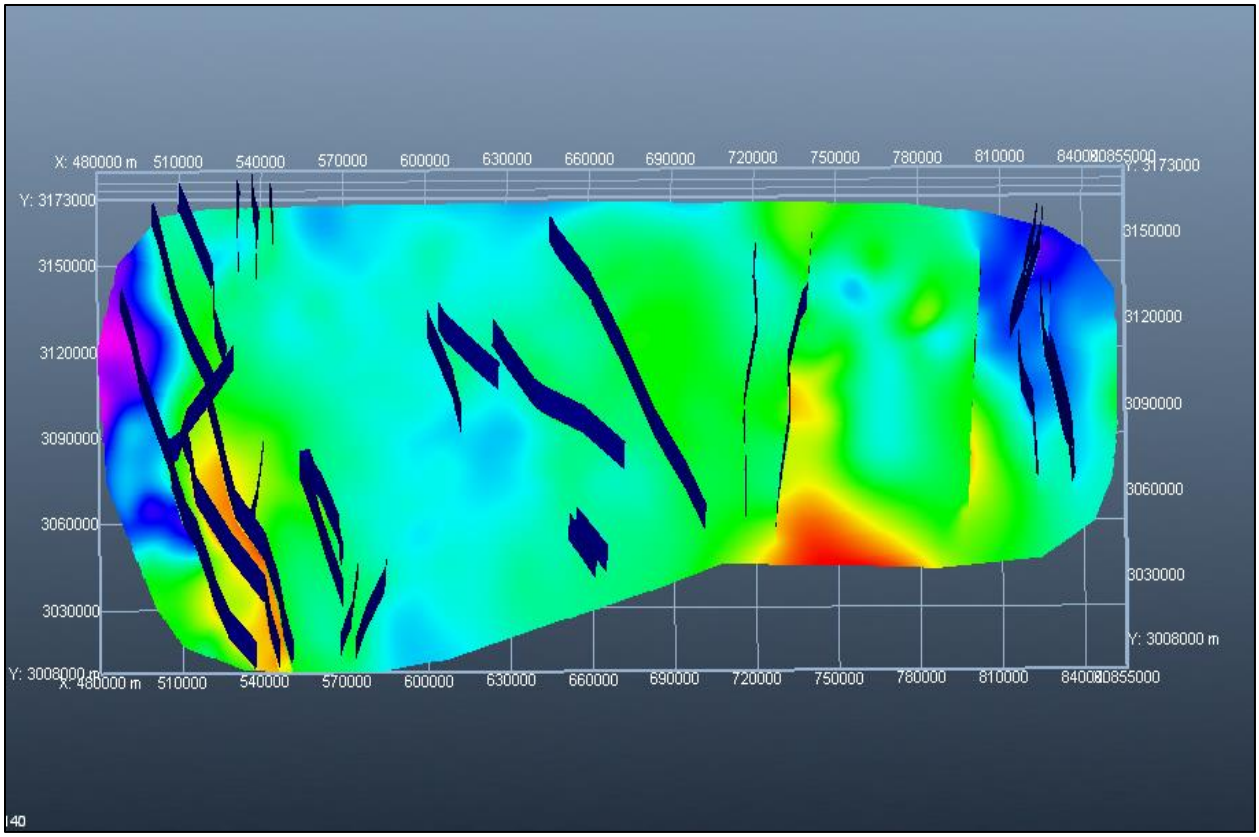

Figure 99: 3D fault model in the Mouydir basin.

The Cambro-Ordovician formations are characterized mainly by brittle tectonic style, linked with Major basement fractures inherited from the Pan-African orogeny, which is responsible for the creation of an extensive fracture network comprised of Major vertical fractures. These faults were reactivated during the Hercynian orogeny designing the actual architecture in horst and grabben of the Ahnet and Mouydir basins.

The analysis of geological maps shows that a dense fracture networks have affected the Paleozoic. Two Major fracture corridors can be distinguished which design the western and the eastern Mouydir basin's edges. They start from the basement in the Hoggar shield and continue to the north in divergent directions in the Saharan platform. They are oriented NNE to NS and NNW to NS constituting the Amguid and the Idjerane spurs respectively (Fig.100).

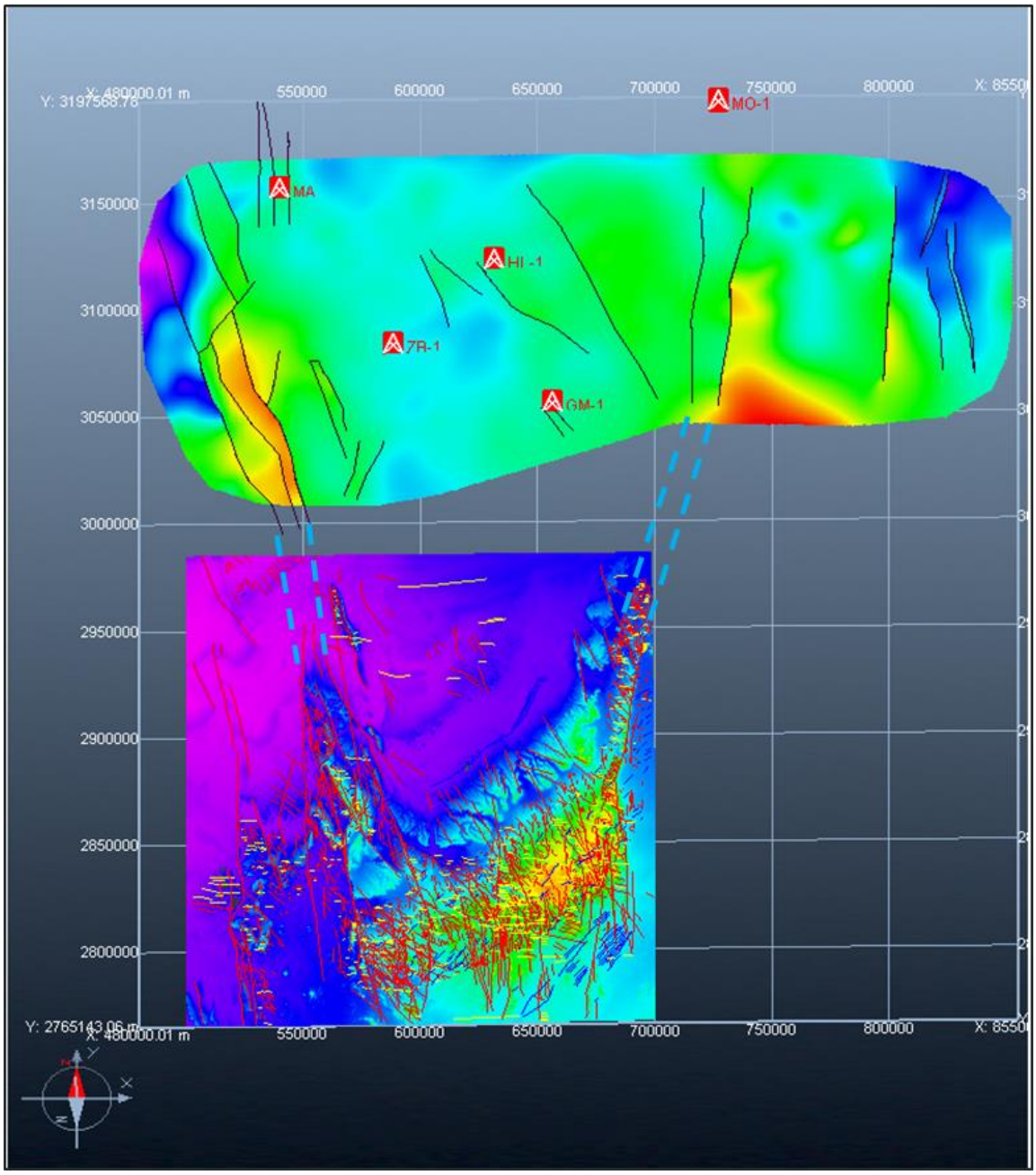

Figure 100: 3D merged fault model using outcrops and subsurface faults.

VII-4-Structural Analysis

The Paleozoic series overlay in the north part of the Hoggar shield. They located mainly in the south edges of Ahnet, Mouydir and Illizi basin (Fig.101). They are composed by the Cambro-Ordovician, Silurian, and Devonian formations. In this chapter, it will be focused into account only

the Major fractures that affected the basement and all the Paleozoic series. These fractures are Mode II fracture, characterized by long length and strike-slip kinematics, which affect all the Paleozoic series and continue in the subsurface in the Mouydir and Ahnet basins.

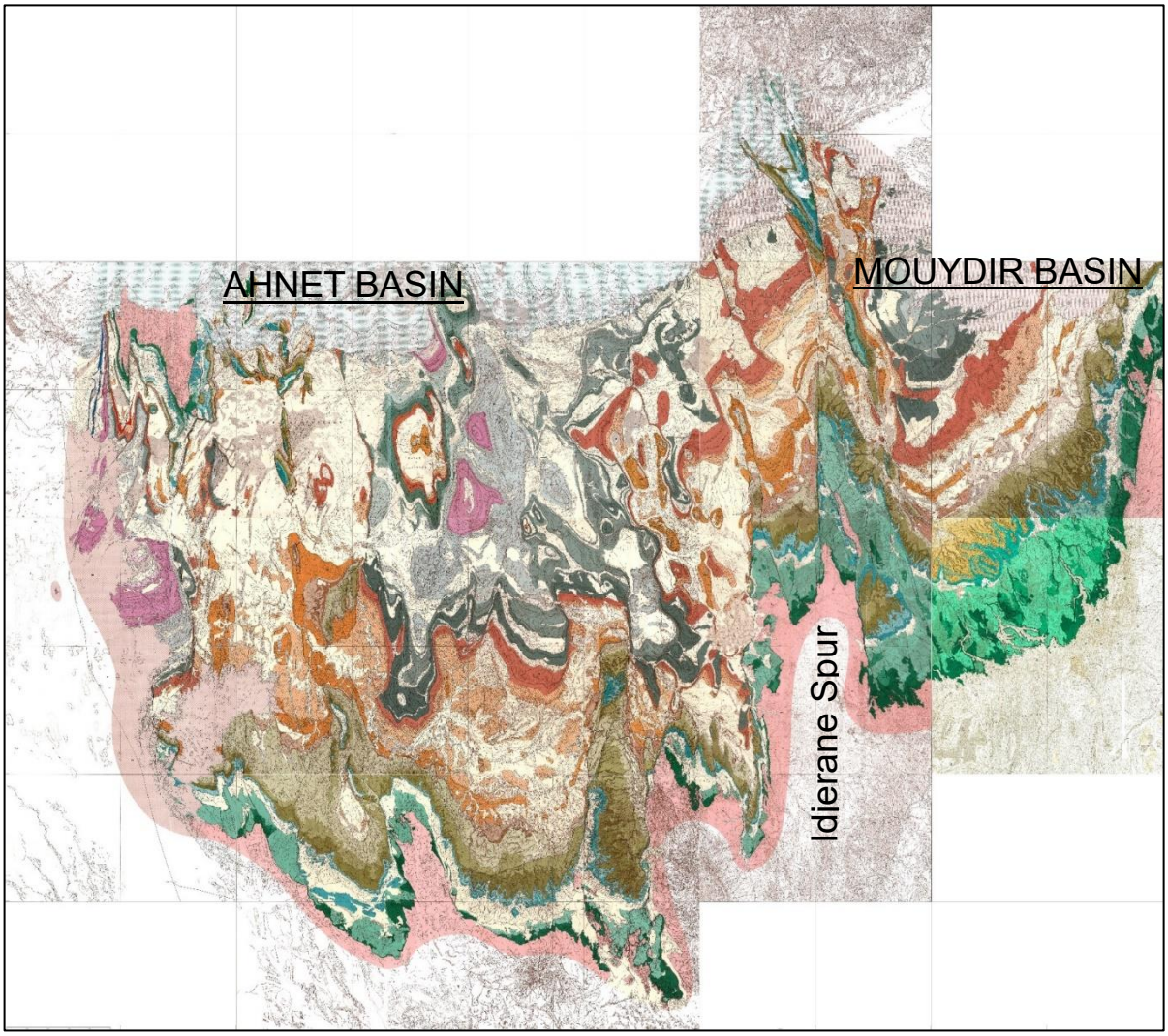

Figure 101: Geological map in the south edges of Ahnet and Mouydir basins.

The Cambro-Ordovician formations are characterized by brittle tectonic style, linked with Major basement fractures inherited from the Pan-African orogeny (Fig.102). The latter were reactivated during the Hercynian orogeny, creating the horst and grabben architecture in the Ahnet and Mouydir basins.

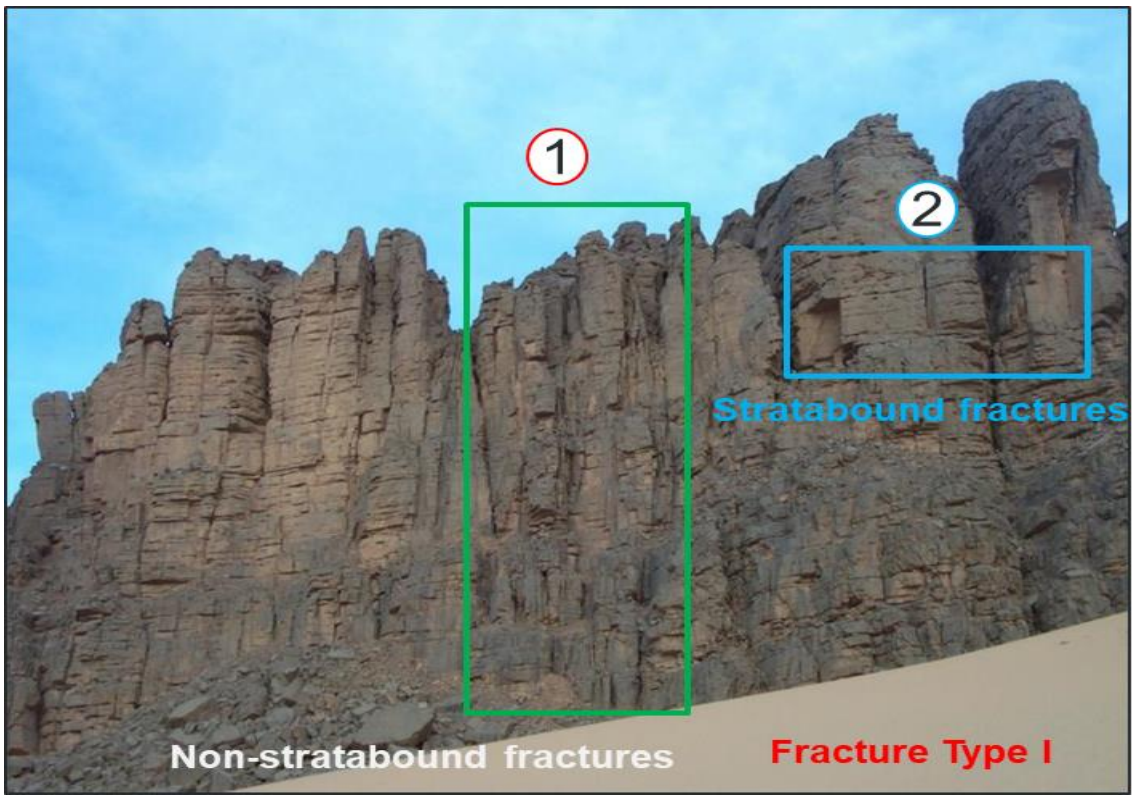

Figure 102: Hamra Quartzite reservoir analog in the area of study (Photo courtesy from N. Mokhtari).

The structural study revealed that the Saharan platform has been marked by several tectonic phases. The Hercynian orogeny that occurred at the end of the Carboniferous is the most important which structured the Saharan platform in horsts and grabens (Boudjema, 1987, Craig, 2006) (Fig.103).

In the area of study, the Hercynian orogeny has distorted and structured the Paleozoic cover of the domain in horst like Mole of Idjerane M'Zab in the west and the Amguid-Biod in the east, and graben like Mouydir basin (Zazoun, 2001).

The analysis of geological maps show that a dense fracture network has affected the Paleozoic series. The fracture network is composed by fracture sets oriented N-S, NNE-SSW, and NW-SE. The N-S fault network constitute large and long fracture corridors, which design the edges of the two basins namely Idjerane, Amguid spurs respectively. They start from the basement in the Hoggar shield and continue to the north in divergent directions in the Saharan platform. These faults are strike slip faults tending dextral and sinistral (Fig.104 & 105).

The NNE-SSW are also strike slip fault trending sinistral. The NW-SE are also strike slip faults tending dextral and sinistral (Fig.106 & 107). The Hercynian orogeny is well known in the Saharan platform. It is composed by two main tectonic events oriented N040 and N120 having age Visean and post-Namurian to post-Permian respectively (Zazoun, 2001).

According to Zazoun (2001) several authors have defined these two Hercynian events in different places. The N040 tectonic event aged Visean was identified by Bles (1969) in the Ougarta Mountains in Algeria, Ribeyrolles and Lavenu (1976), Pique and Michard (1981) in Morocco, Latrech (1982), Conrad and Lemosquet (1984) in the Bechar basin, Algeria, and Boudjema (1987) in the Illizi basin, Algeria.

On the other hand, the N120 tectonic event aged post-Namurian-pre-Permian is known by Ribeyrolles and Lavenu (1976) in Morocco, Conrad and Lemosquet (1984) in the Ougarta Mountains, Latreche (1982) in the Illizi basin, Boudjema (1987) in the Triassic province, Algeria and Lagarde (1985) in the 'Meseta Marocaine' in Morocco. The Hercynian Orogeny can be considered as a continuous deformation rather than tectonic events (Zazoun, 2001, Donzeau et al., 1981 and Donzeau, 1983).

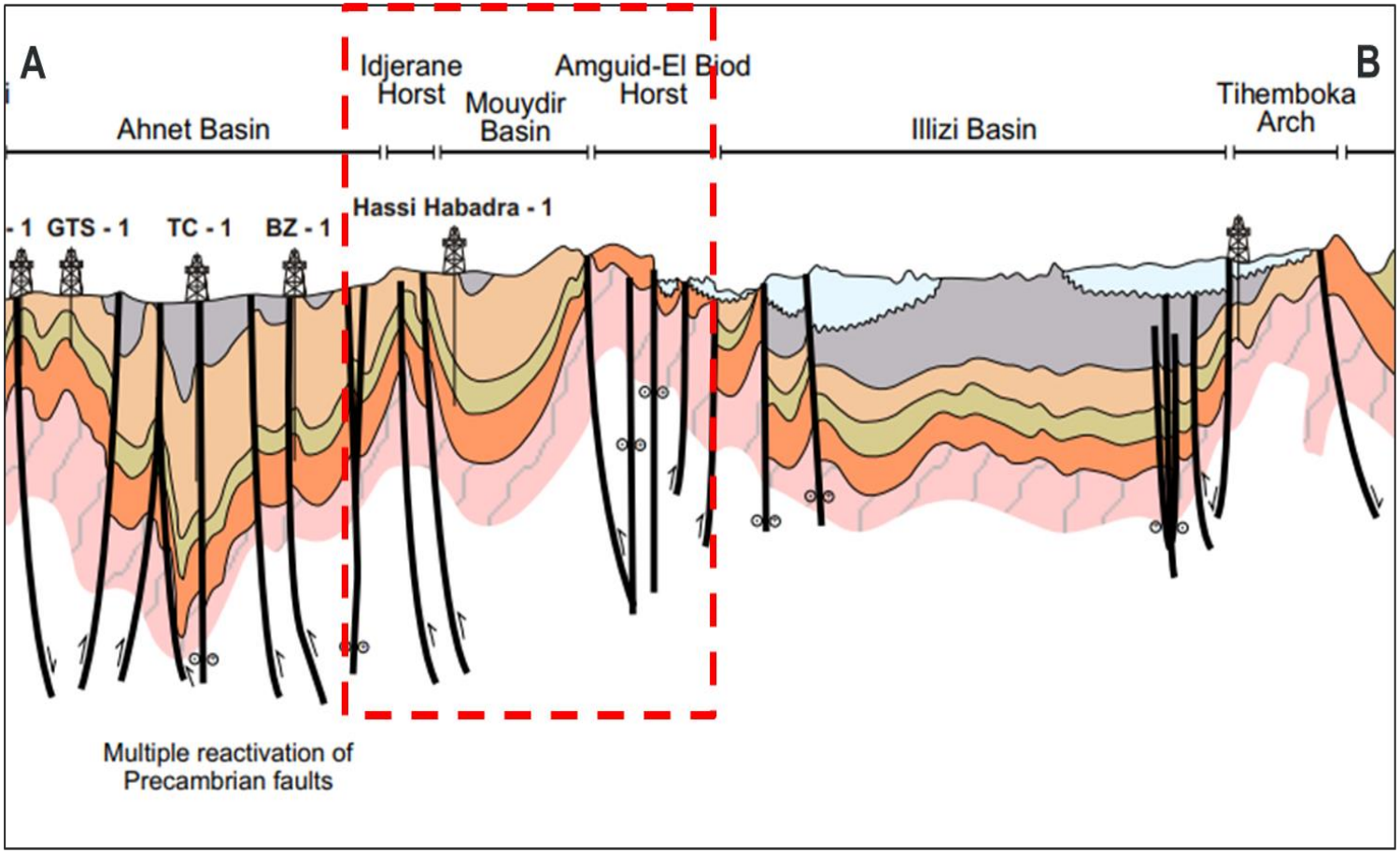

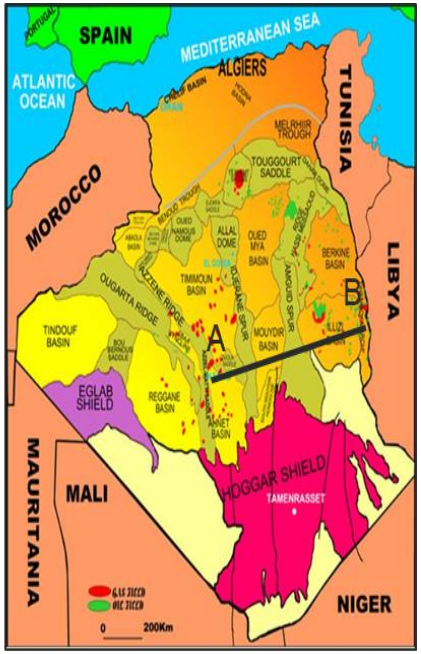

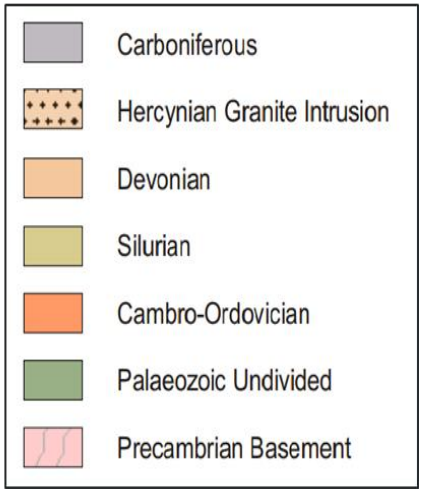

Figure 103: Geological cross section illustrating the main structural units in the Saharan platform (Craig et al, 2006)

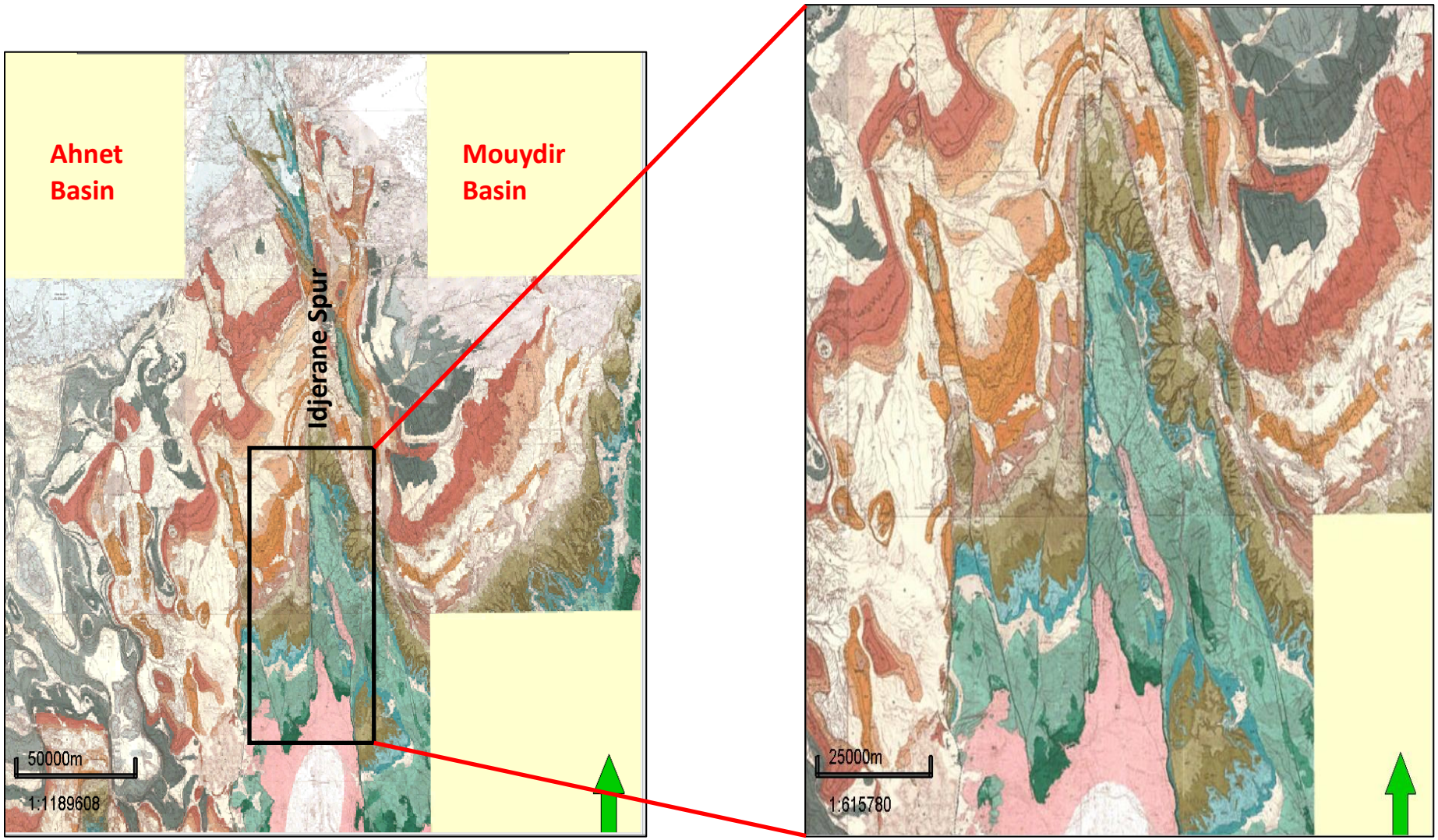

Figure 104: N-S and NW-SE faults in the area of study

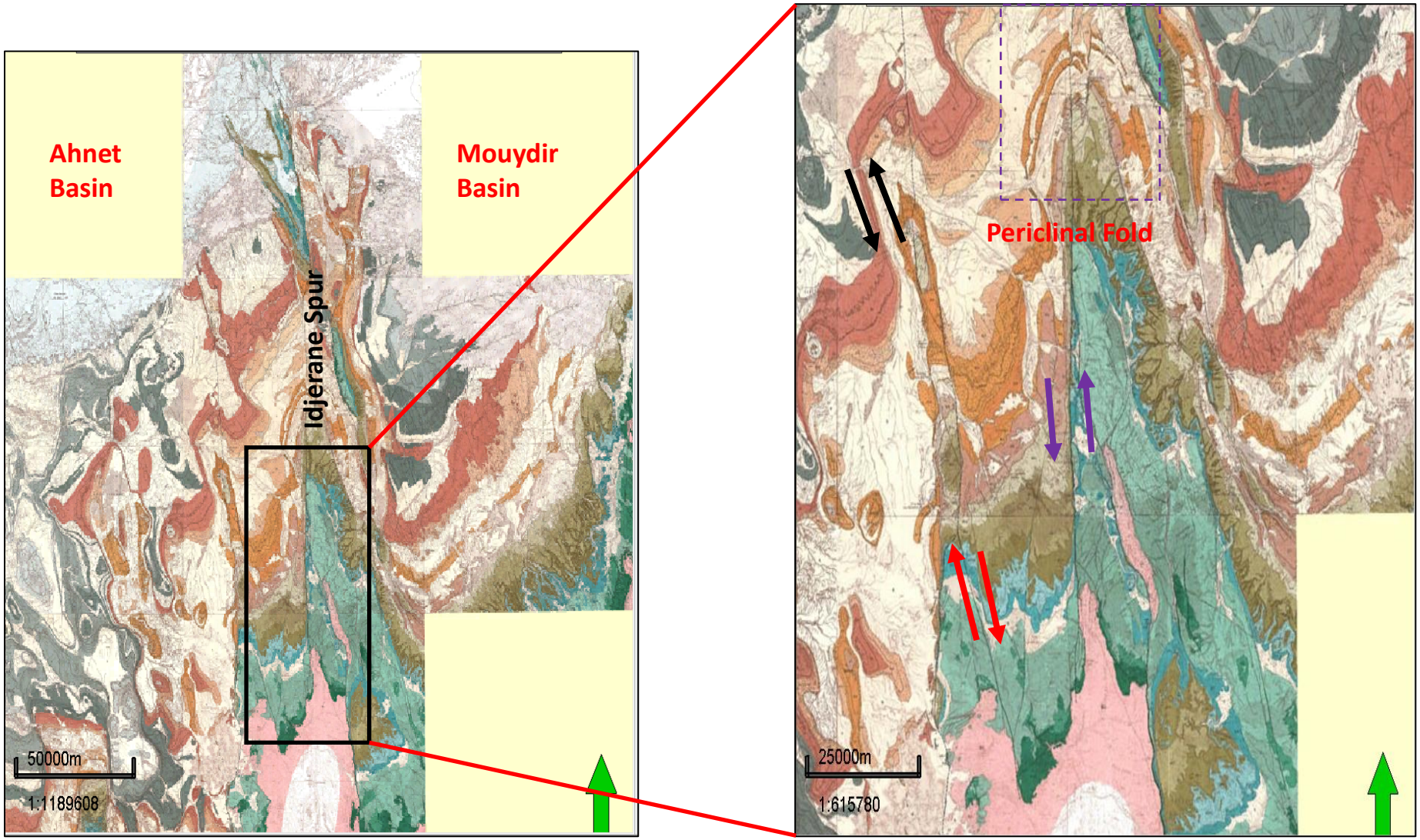

Figure 105: Kinematics of the N-S and NW-SE faults in the area of study.

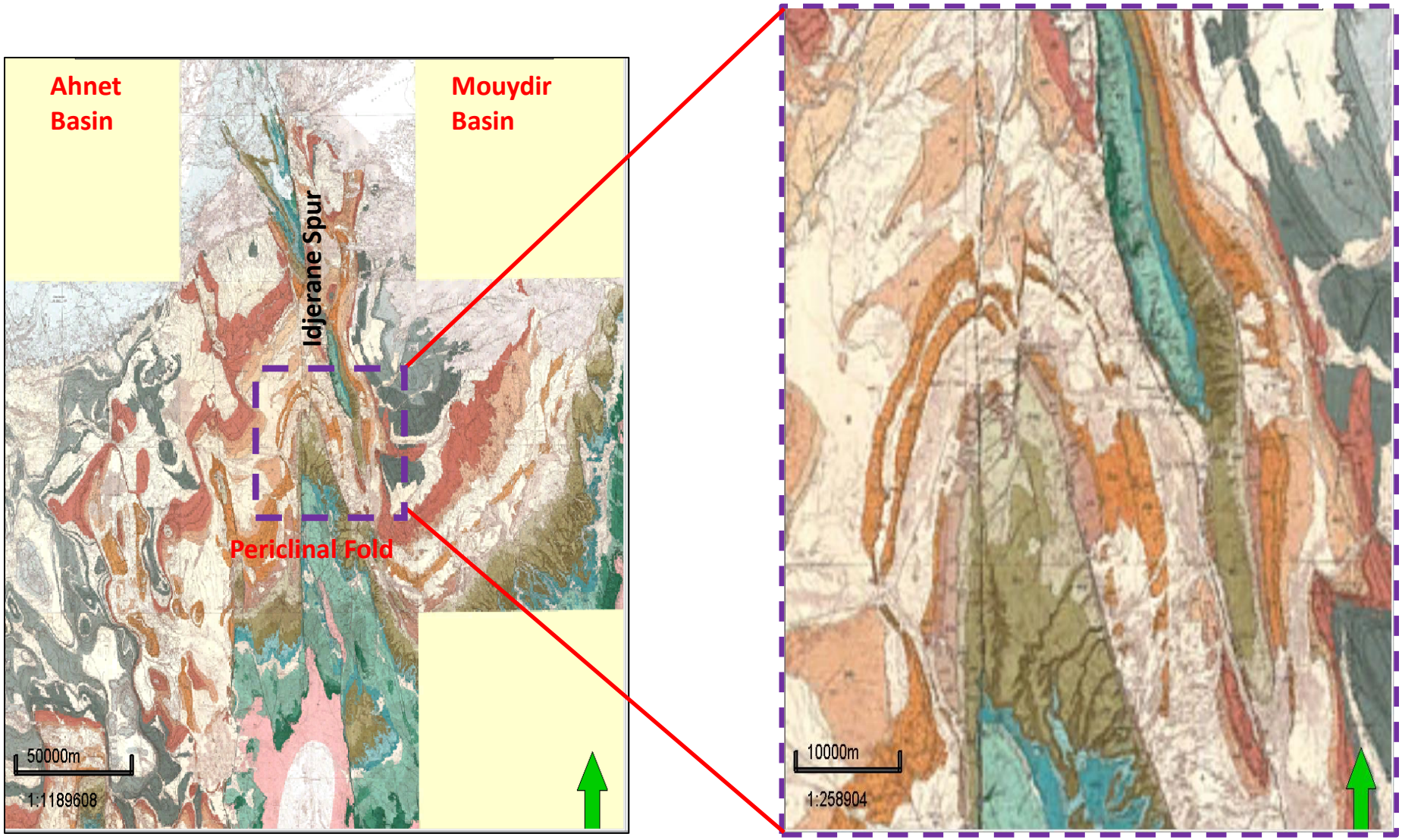

Figure 106: NNE-SSW, N-S, and NW-SE faults in Idjerane periclinal fold

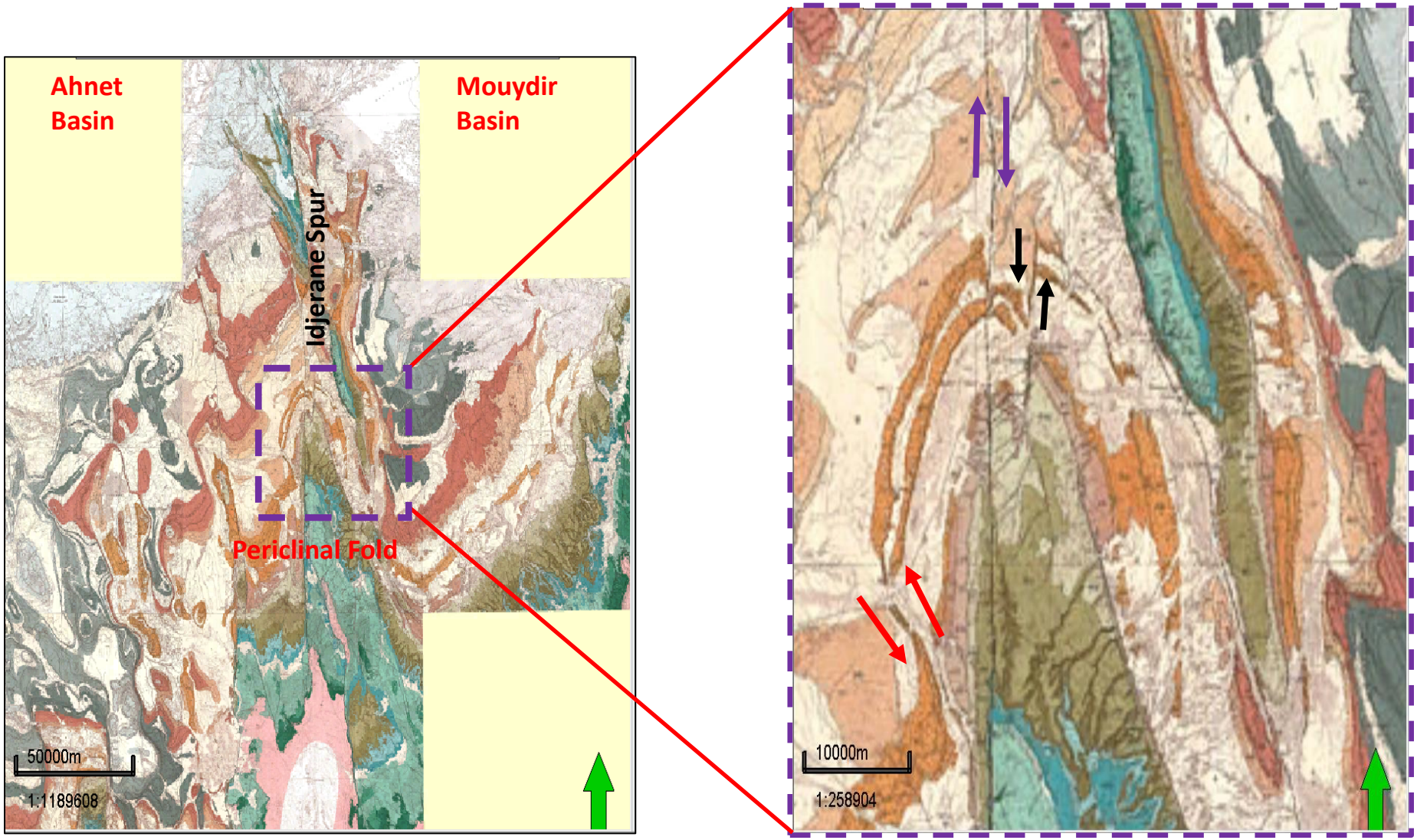

Figure 107: Kinematics of the NNE-SSW, N-S, and NW-SE faults in Idjerane periclinal fold.

VII-5-2D Seismic Analysis

A thick sedimentary cover including the basement, the Paleozoic series, Mesozoic formations, and the thin Cenozoic layers characterizes the Mouydir basin. Several unconformities are defined in the Mouydir basin separating the Paleozoic from the Mesozoic and the Mesozoic from the Cenozoic. These unconformities are namely, Hercynian, Austrian, and Mio-Pliocene respectively (Fig.108 & Fig.109).

The Mouydir subsurface is design as horst and grabben and confirm the architecture that appears in the gravity data. Two main horsts constitute the edges of the basin and are clearly visible in 2D seismic data. In addition, other horsts are visible and constitute the positive axis in the Mouydir basin. (Fig.110 & 111). This architecture in horst and grabben is sealed in the top by the Hercynian unconformity (Fig.112 & 113) which indicate that this structuration happened at the end of the Paleozoic era.

The 2D seismic profiles are used to highlight the subsurface architecture of the Mouydir basin and determine the exact kinematics, the dip, and the geometry of the major fault sets that affect the Ahnet and the Mouydir basins using the combination of the seismic 2D profiles and the geological maps. The selected 2D seismic profiles are perpendicular to these faults in order to determine their real dip and their kinematics.

The structural analysis of the different 2D seismic profiles attest that the deep strike slip faults that affected the Ahnet and Mouydir basin are not a pure strike slip trending only sinistral and dextral but they have also a vertical component trending as normal and reverse faults. They are mainly generated through transpressional and transtensional strain regimes that affected the area of study during the Hercynian orogeny.

The 2D seismic profiles show clearly that the area of study was affected at least by two tectonic events expressed by a compressive and distensive structures generation anticlines and reverse faults and synclines and normal faults (Fig.114-115, 116-117, 118-119, 120-121, & 122-123).

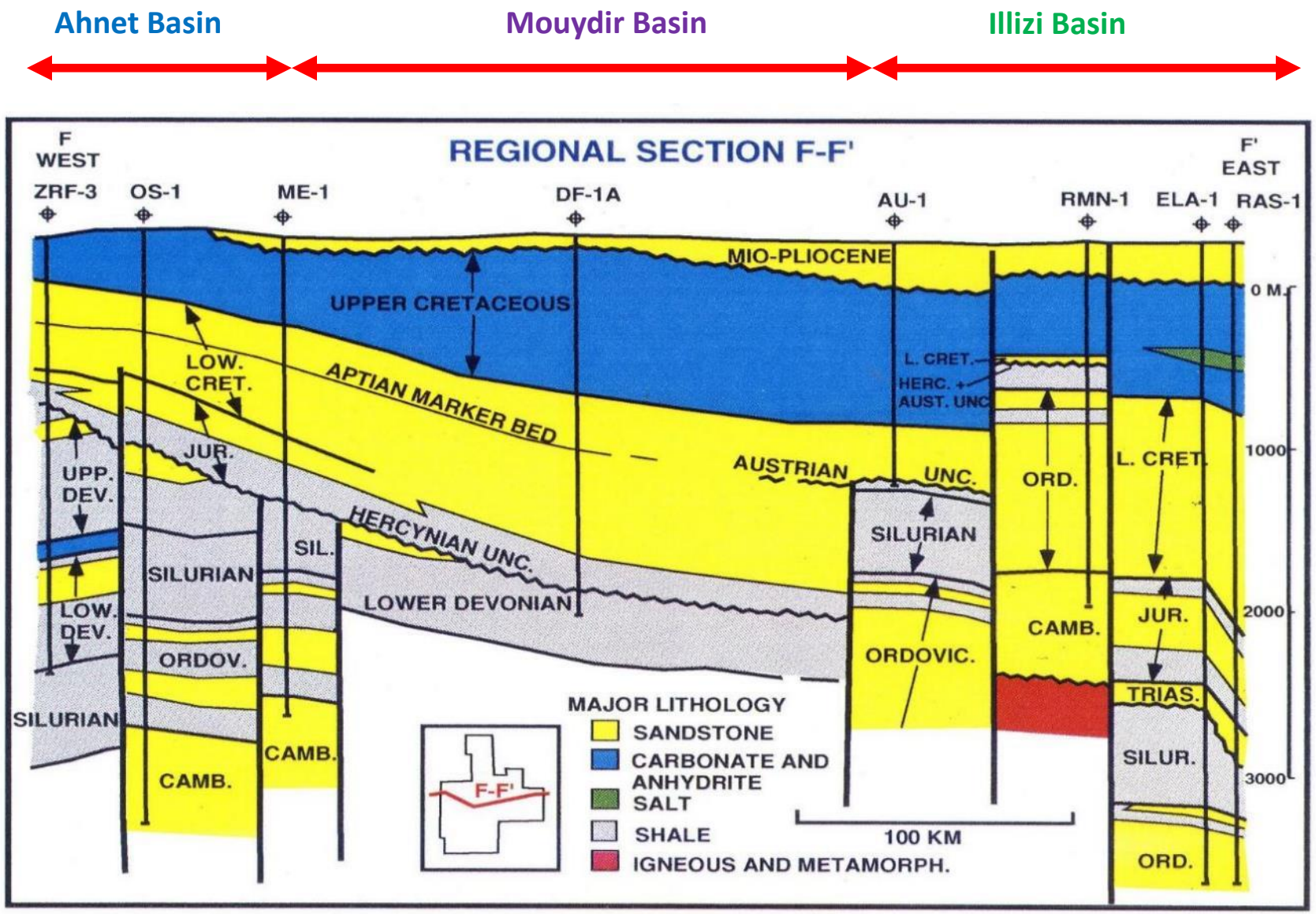

Figure 108: Schematic well cross section West-East in the Mouydir basin (Pecten, 2012)

Hoggar Shield ← Mouydir Basin → Oued Mya basin

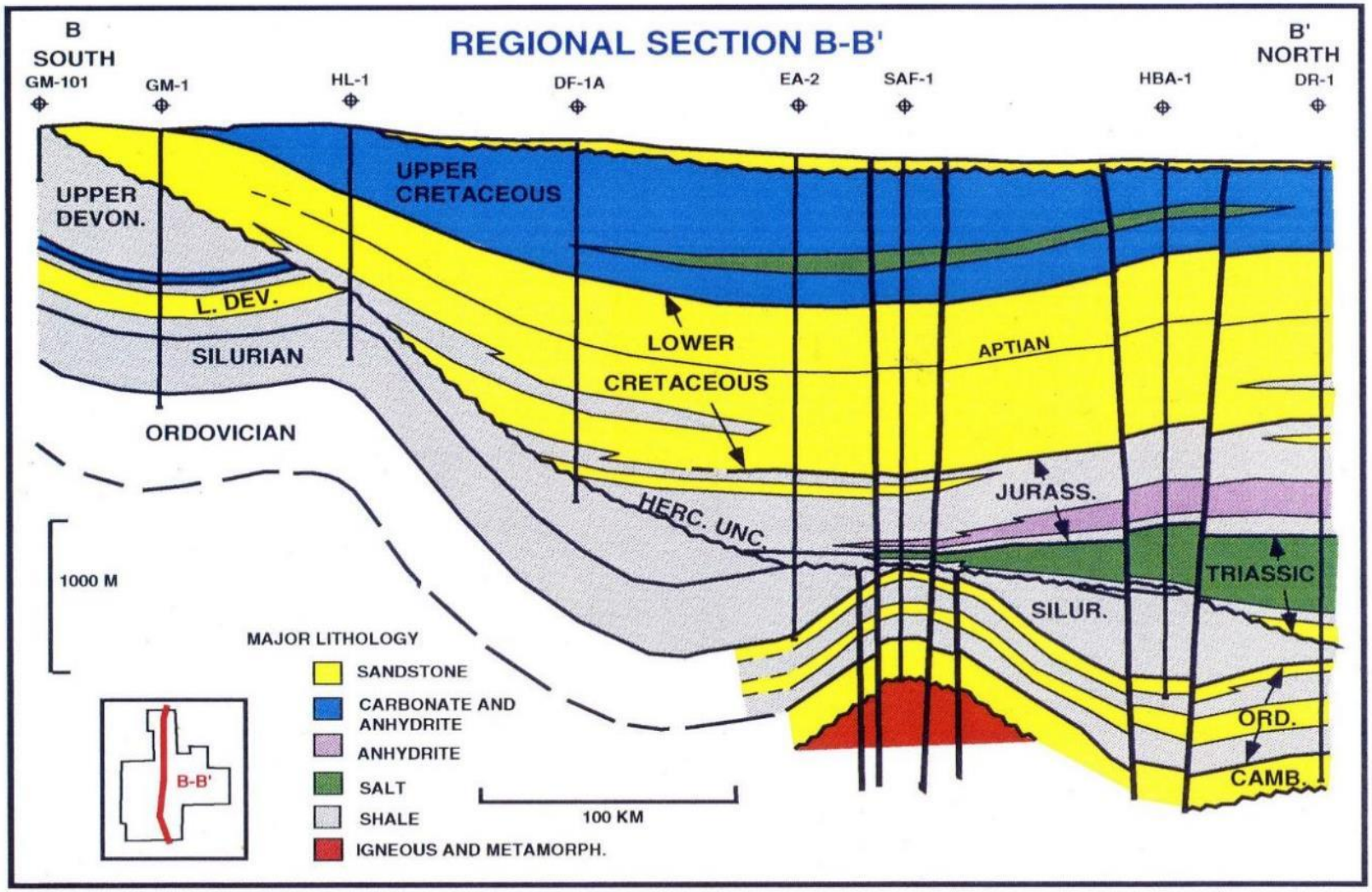

Figure 109: Schematic well cross section N-S in the Mouydir basin (Pecten, 2012)

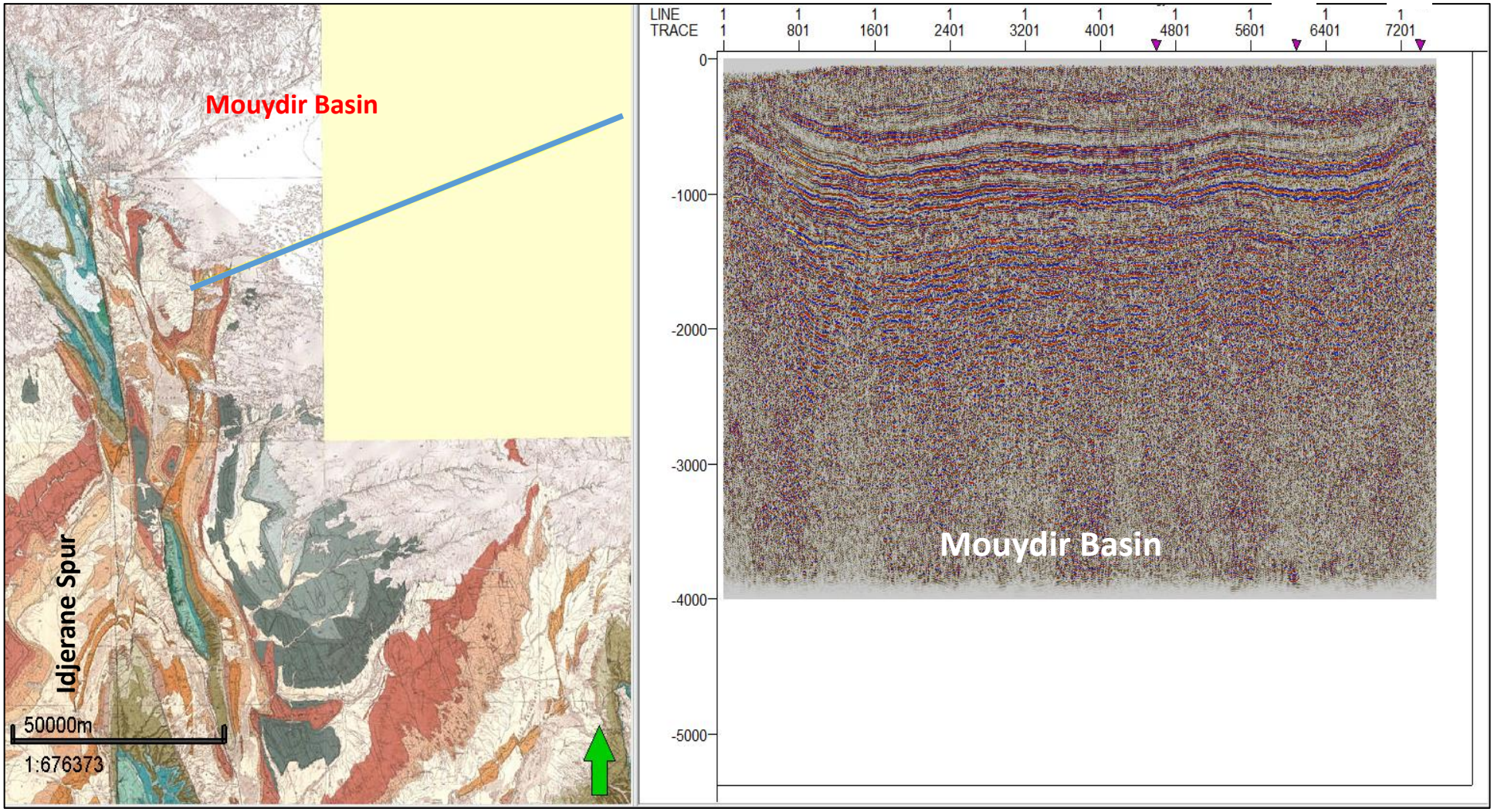

Figure 110: 2D seismic in the Mouydir basin

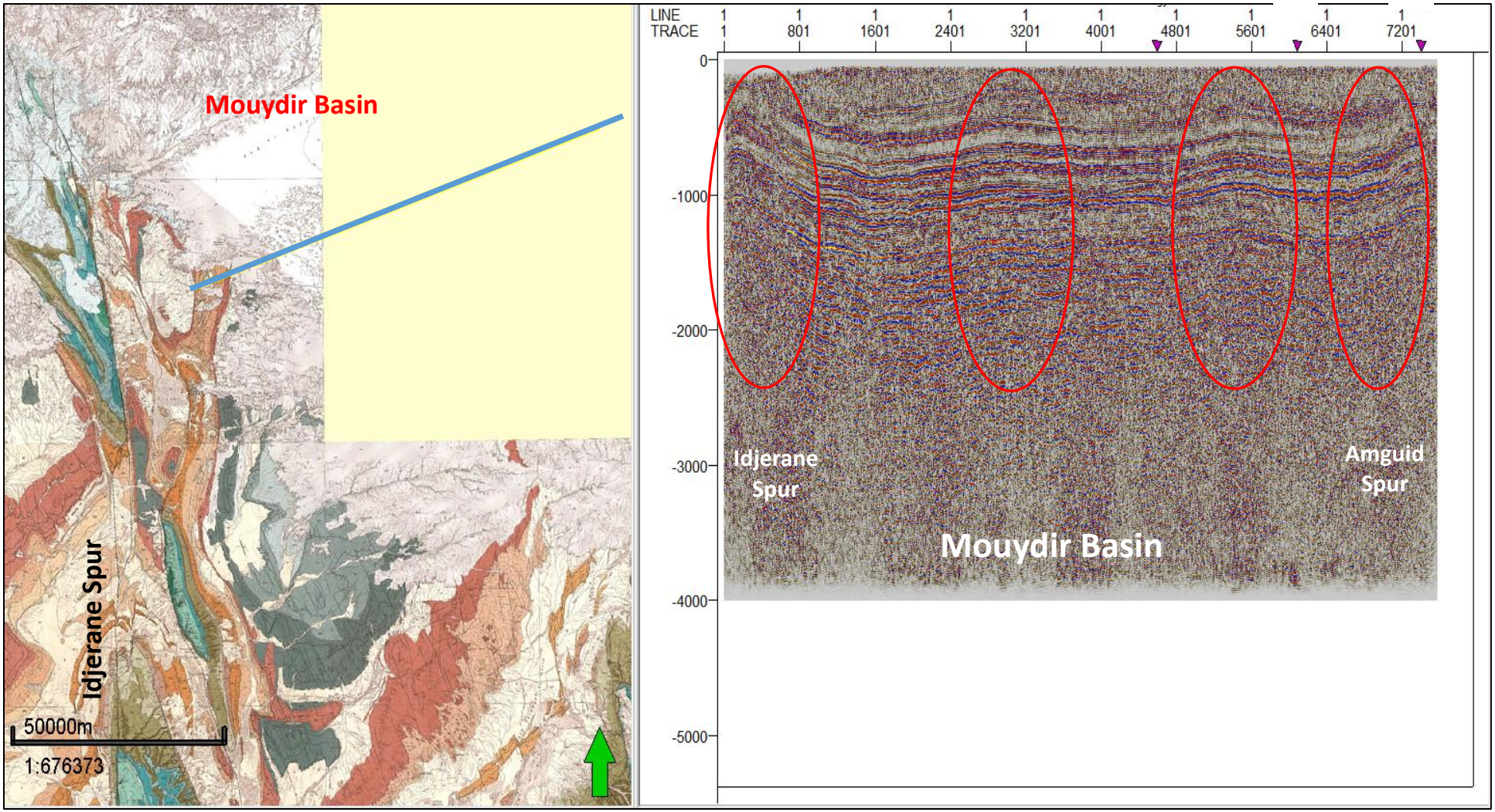

Figure 111: 2D seismic profile showing the different positive and negative structures in the Mouydir basin

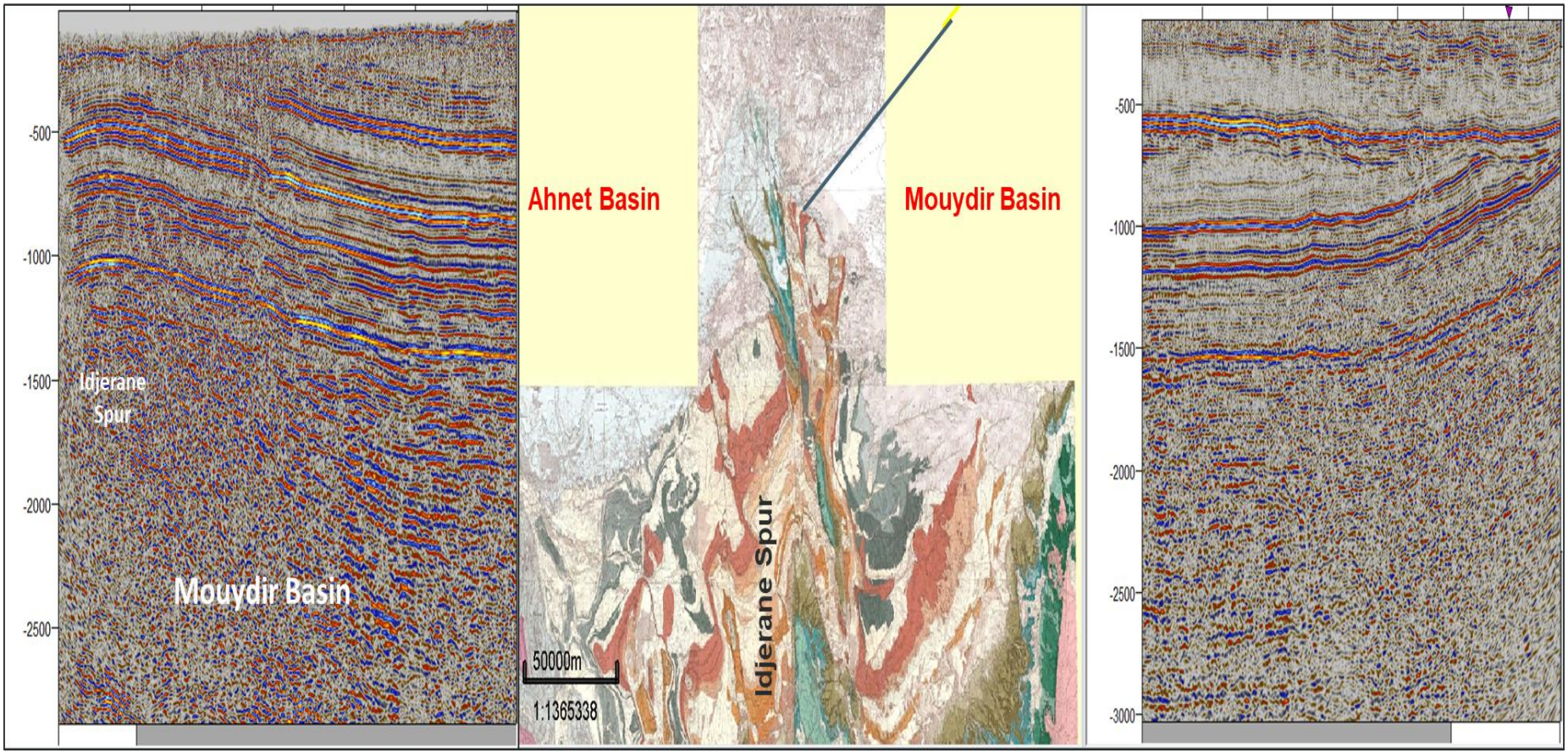

Figure 112: Composed 2D seismic profiles in Mouydir basin

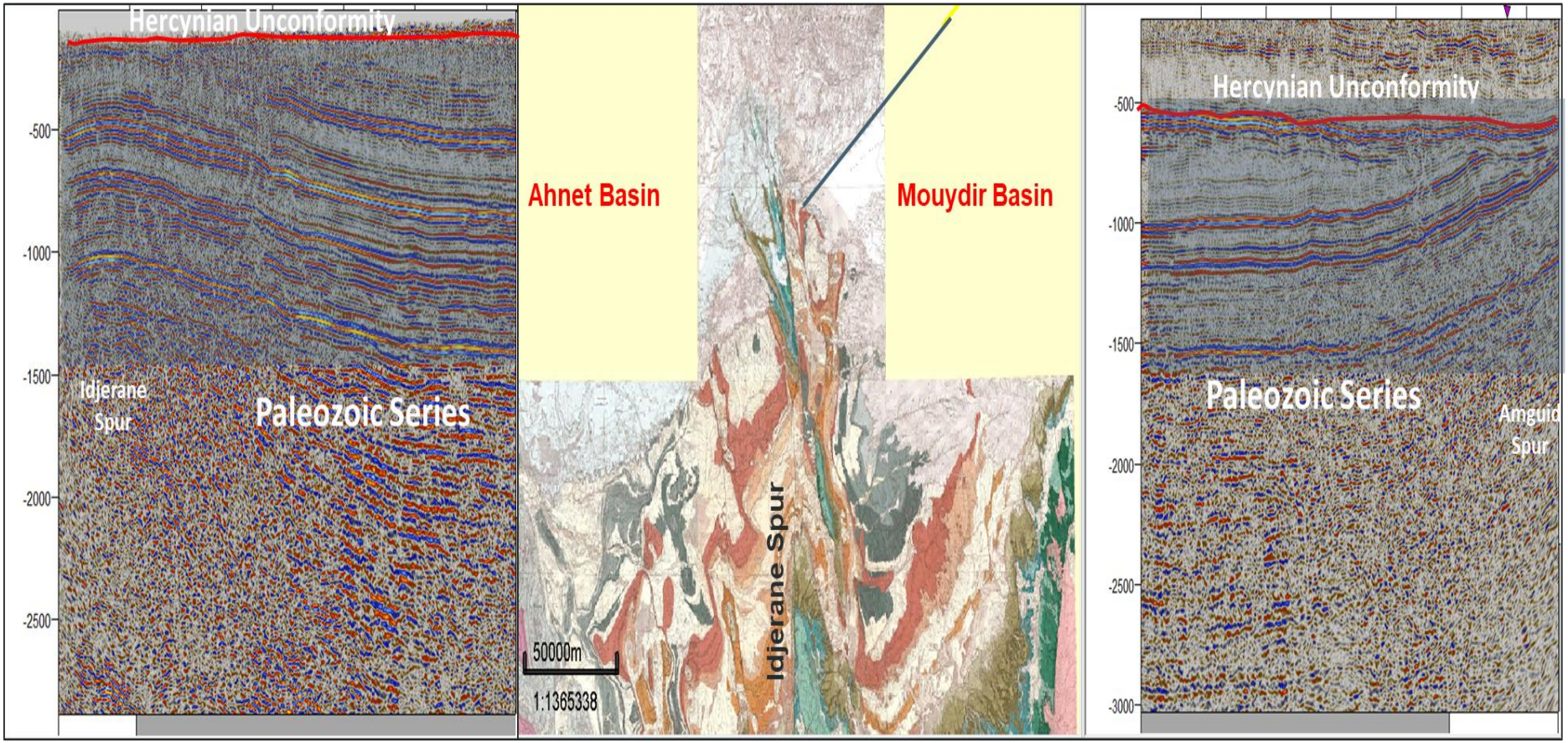

Figure 113: Composed 2D seismic profile showing the horsts architecture sealed by the Hercynian Unconformity in Mouydir basin.

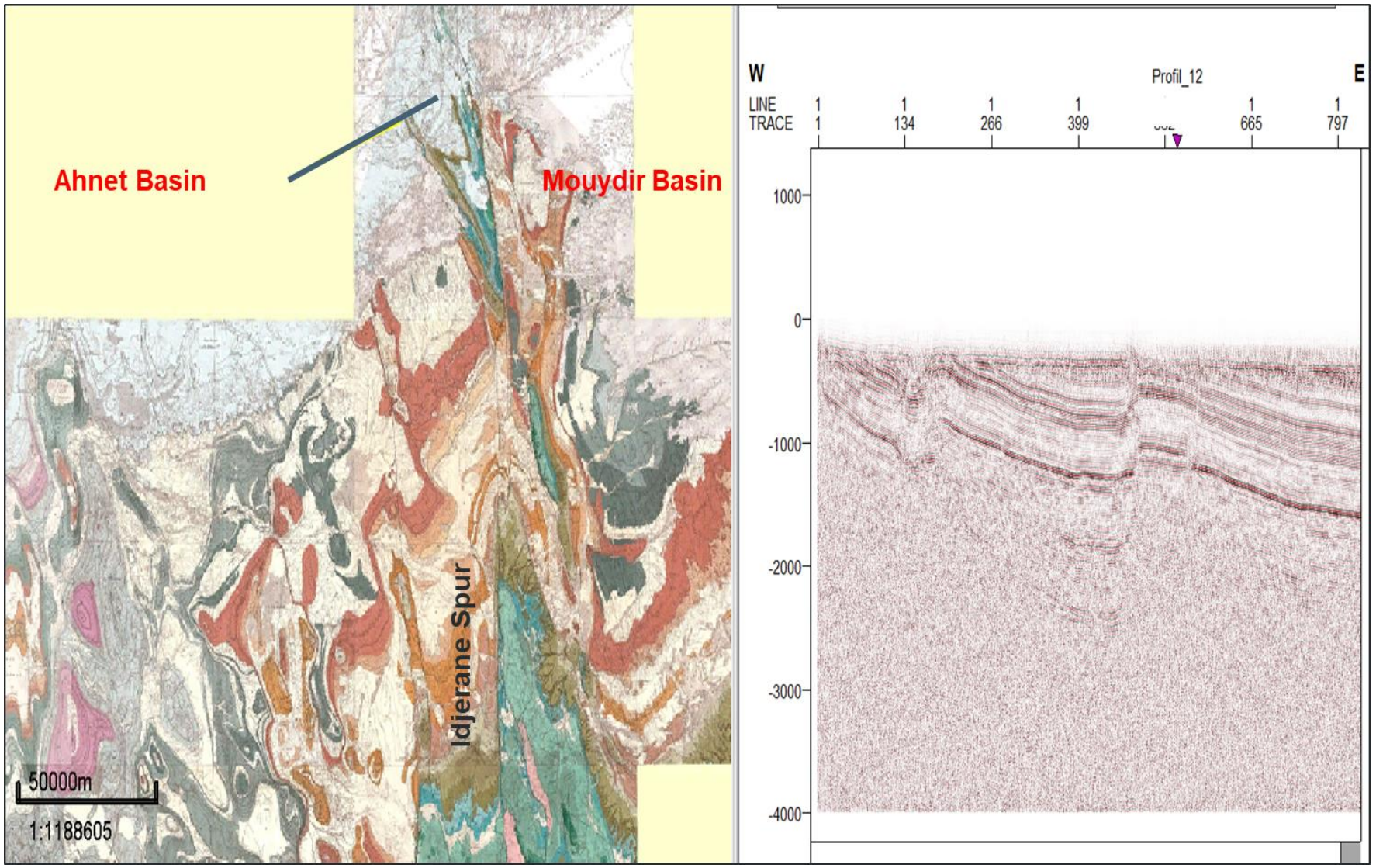

Figure 114: 2D seismic profile near Idjerane Spur

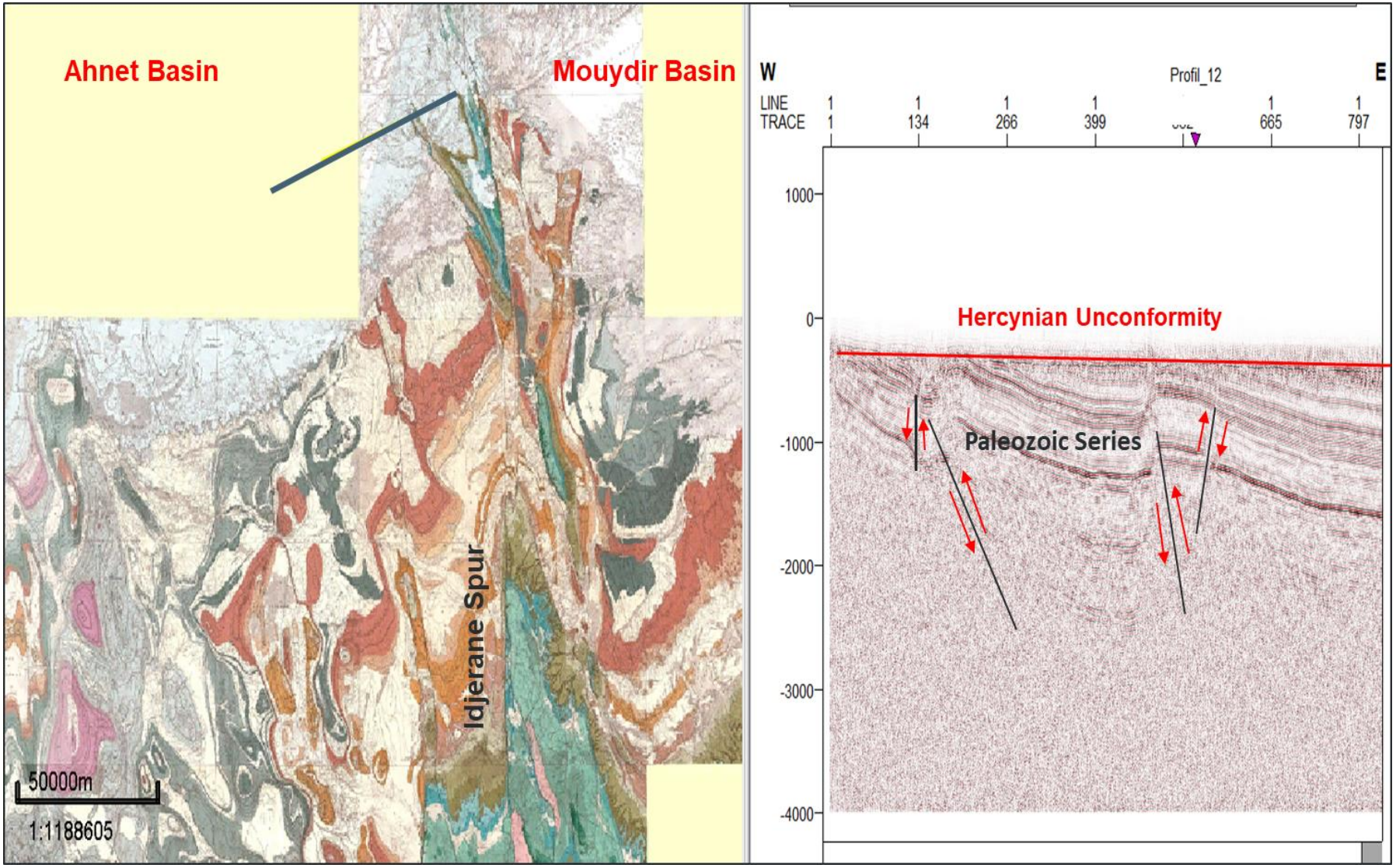

Figure 115: 2D seismic profile showing a compressive structure in a syncline sealed by the Hercynian unconformity.

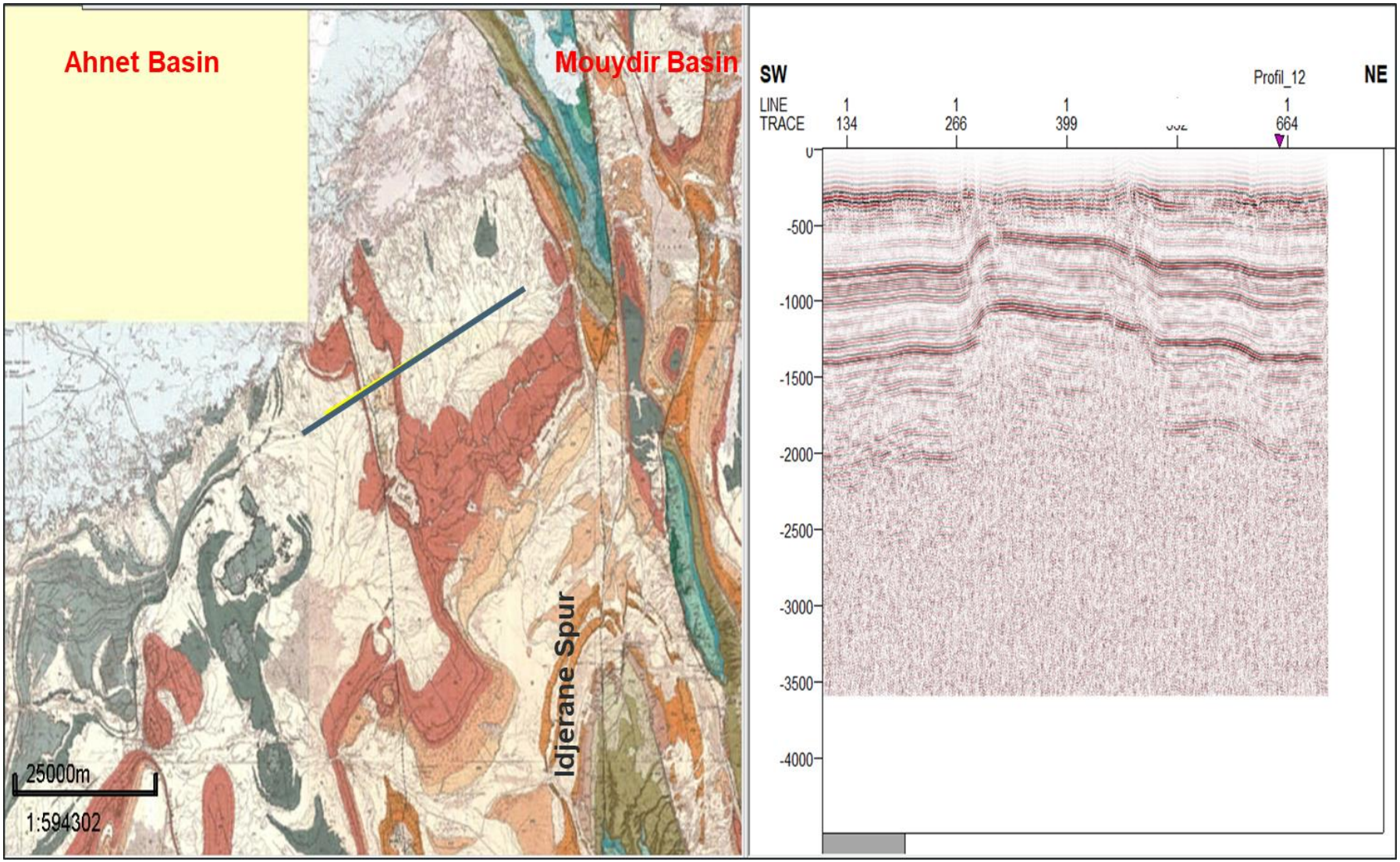

Figure 116: 2D seismic profile near Idjerane Spur

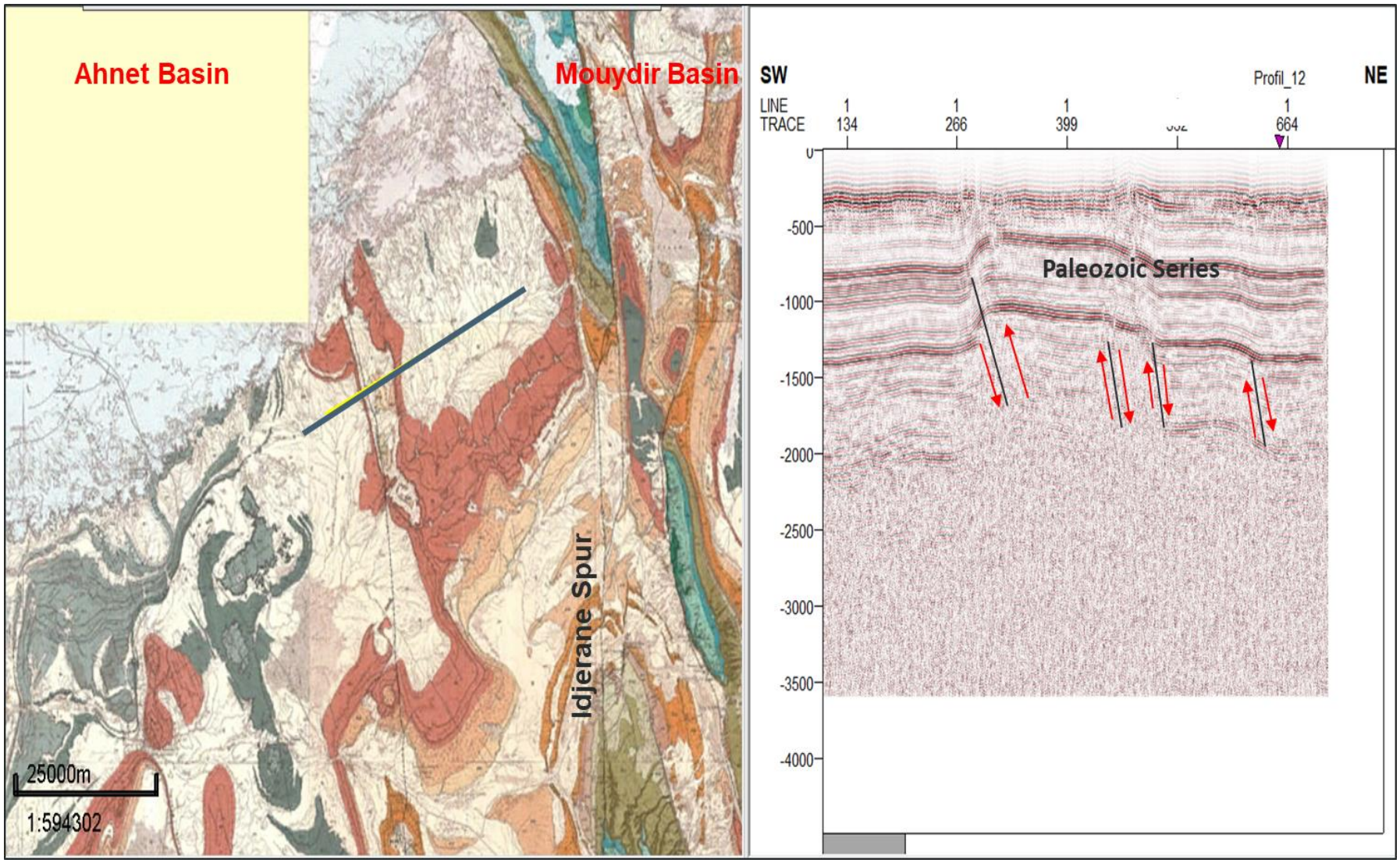

Figure 117: 2D seismic profile showing compressive and distensive structures

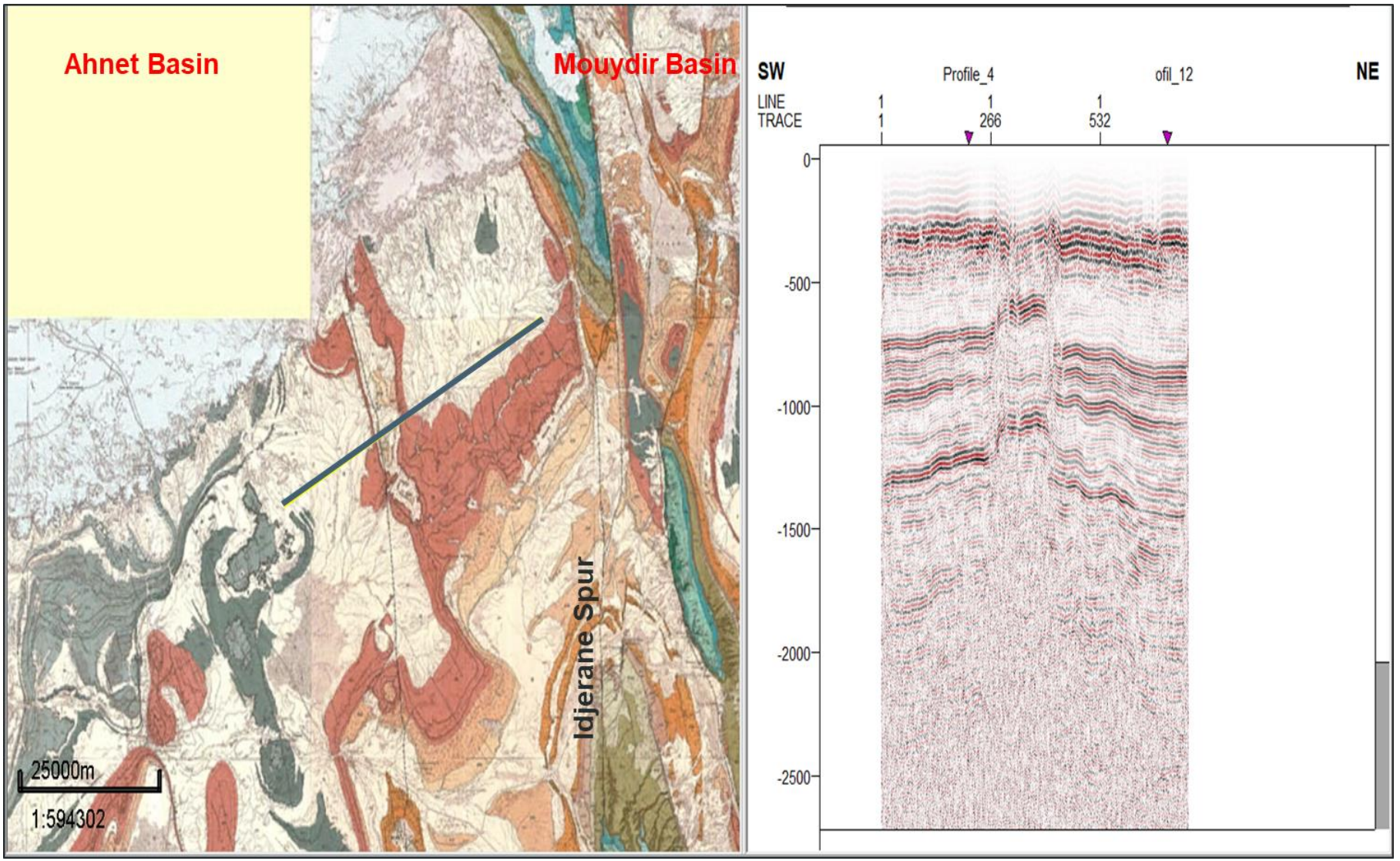

Figure 118: 2D seismic profile in Ahnet basin close to Idjerane spur

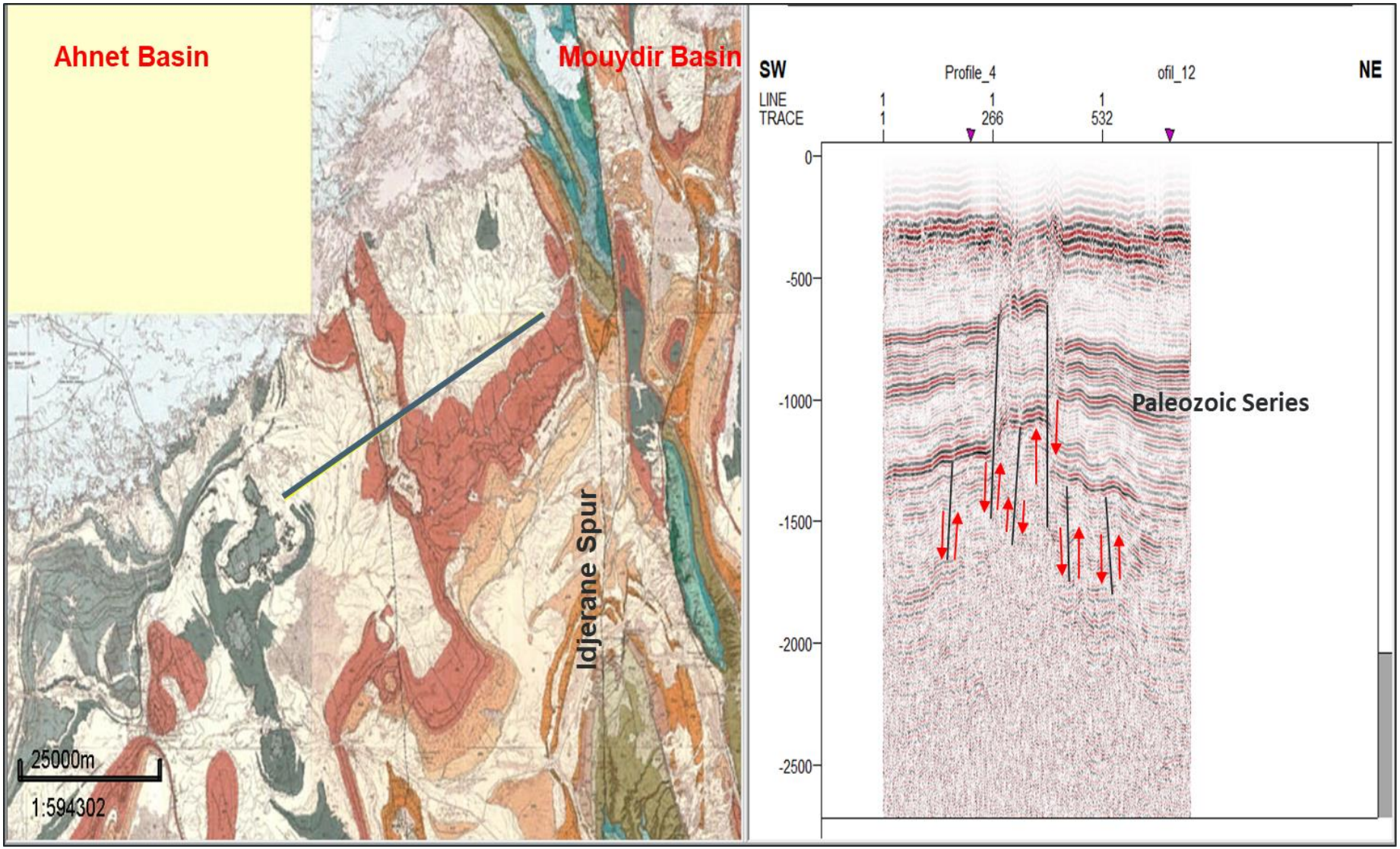

Figure 119: 2D seismic profile showing a Pop-Up structure.

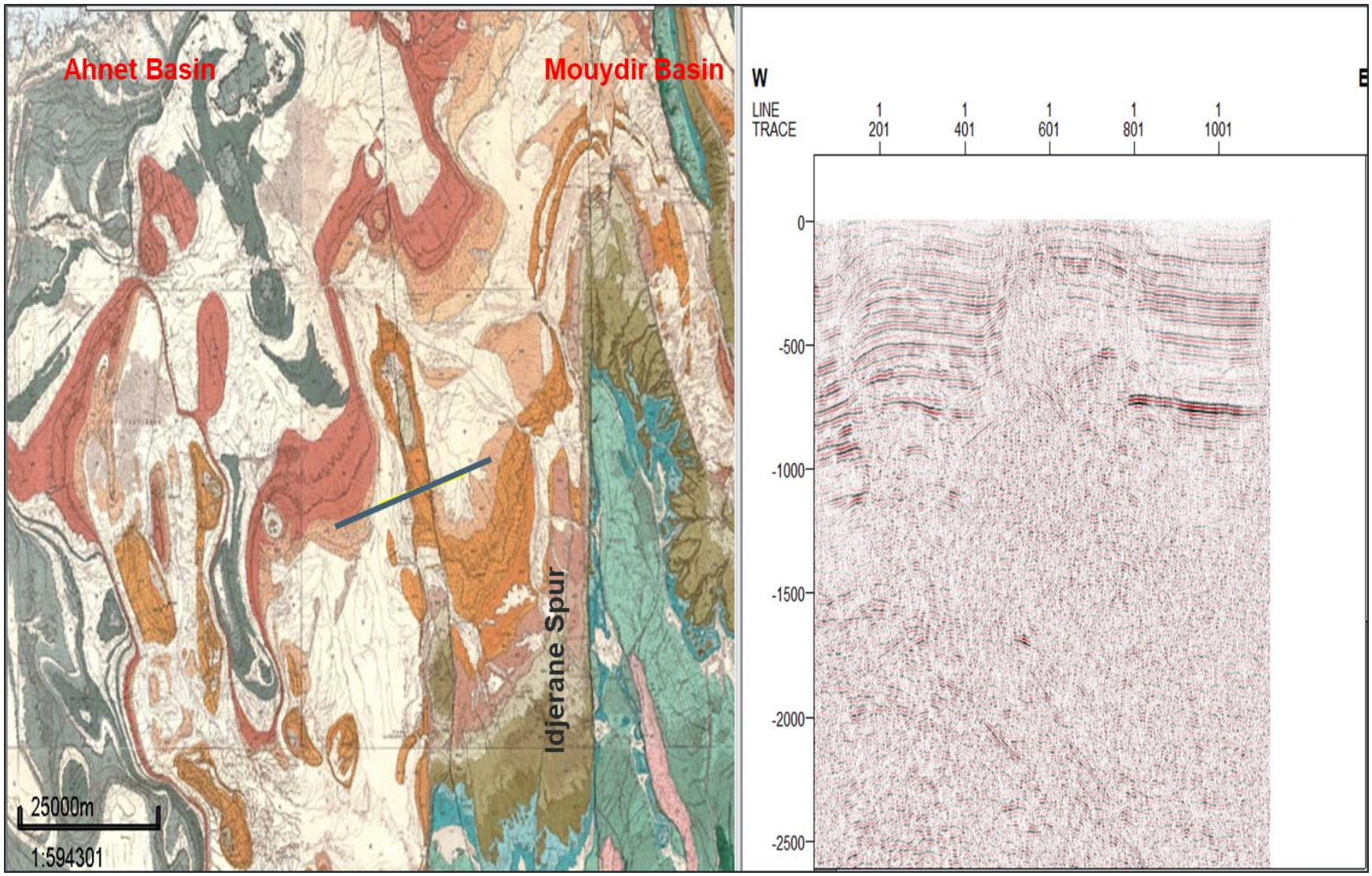

Figure 120: 2D seismic profile showing complex structures

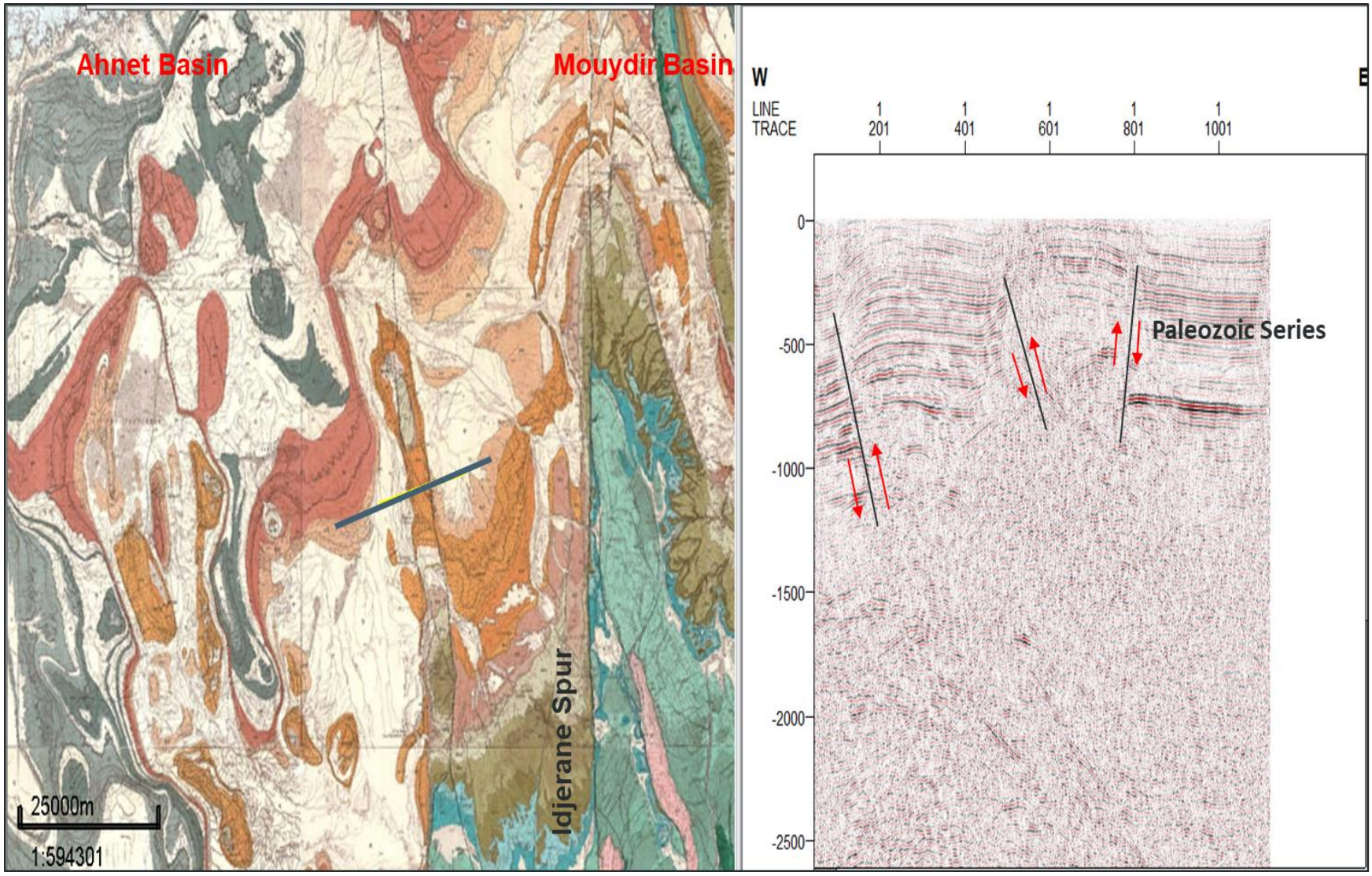

Figure 121: 2D seismic profile showing a succession of a compressive structures.

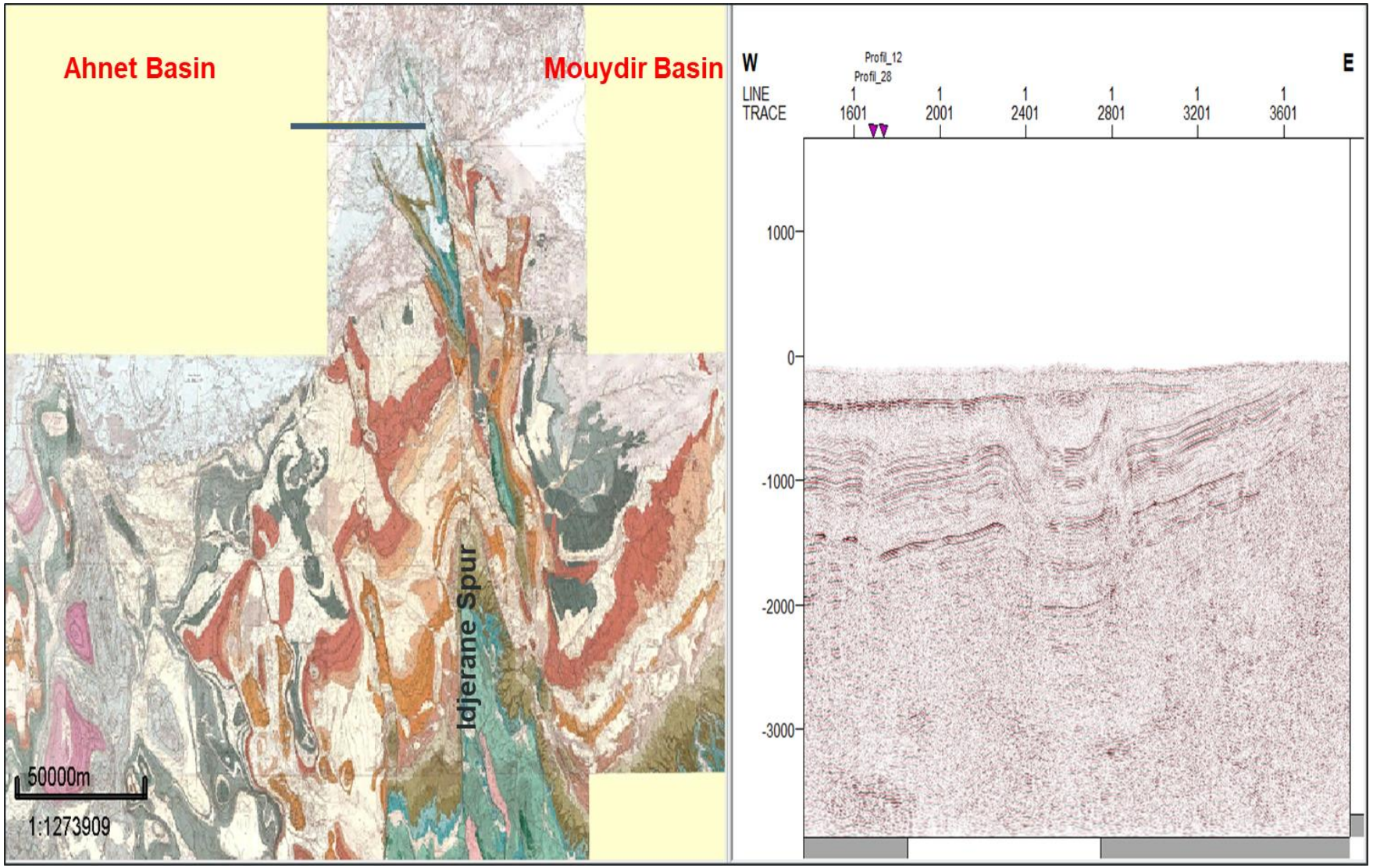

Figure 122: 2D seismic profile showing distensive and compressive structures

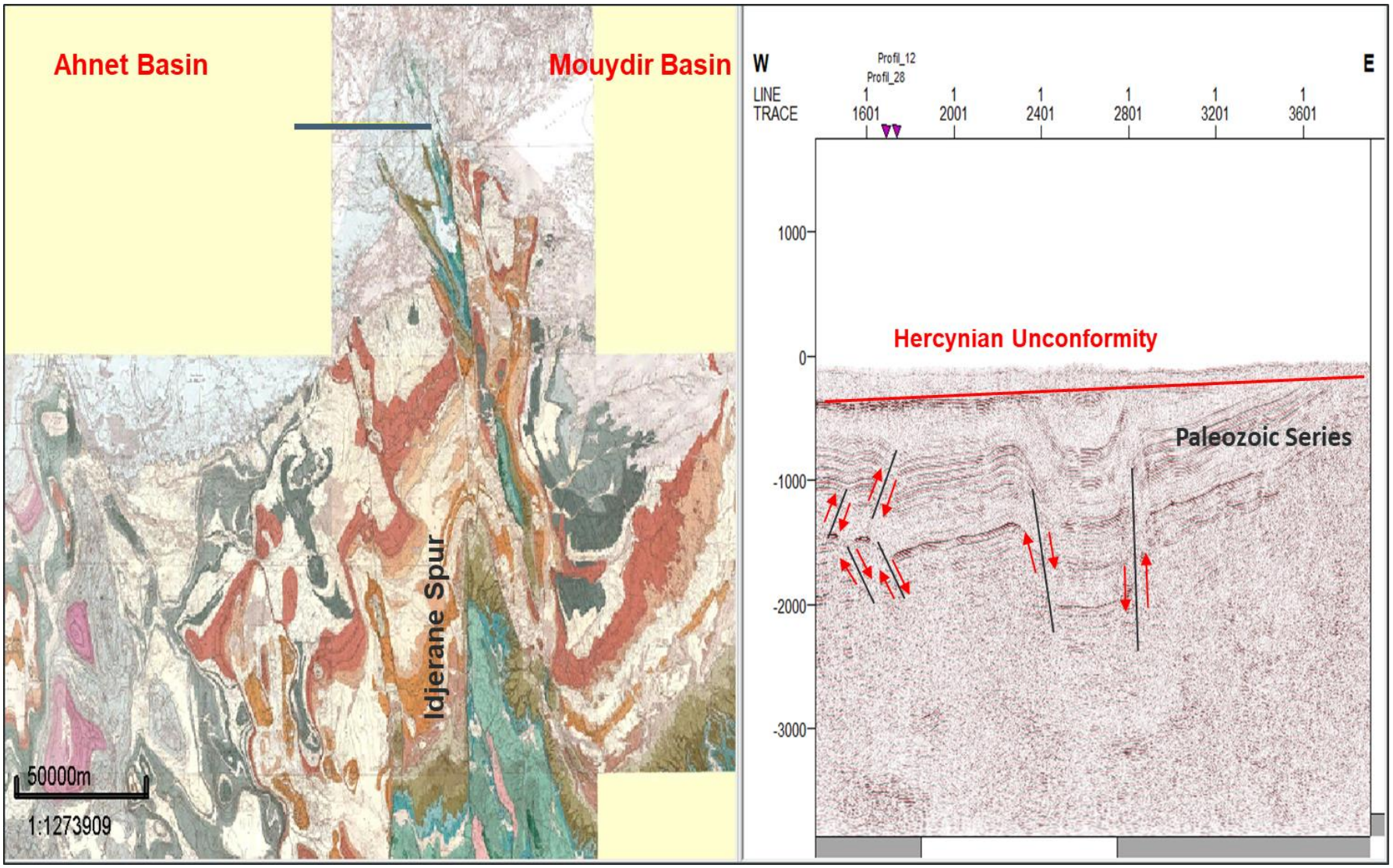

Figure 123: 2D seismic profile showing distensive and compressive structures sealed by the Hercynian Unconformity.

VII-6-3D Seismic Data Analysis

In the Mouydir, no 3D seismic data was acquired since the exploration oil and gas has started. Because of the lack of a 3D seismic data in the Mouydir basin and the low quality of the 2D seismic data, a 3D seismic volume in Ahnet basin was selected to understand the fracture aspect of the top of the Ordovician reservoir. This can serve as an analog to predict the fracture density and intensity in the top Ordovician in the Mouydir basin.

This 3D survey is close geographically to the area of study and can reflect the characteristics of the fracture distribution in the top Ordovician reservoir, which is considered as main gas objective in the Ahnet basin. Several attributes were applied on this 3D seismic volume in order to enhance and highlight the dense fracture network that affect this tight reservoir.

This 3D survey was recently acquired on an anticline in the eastern part of Ahnet basin where several productive gas wells were discovered in the Ordovician reservoir (Fig.124). The name of the 3D seismic volume will not be shown for a confidentiality purpose.

The 3D seismic analysis based on the analyses of Inline, Crossline and timeslice reveal an anticline structure where several faults trends are highlighted. The faults are oriented mainly NW-SE, N-S, NE-SW. The analysis of these faults in inline, crossline and timeslice sections shows that the main faults have strike slip components with reverse faults due to a transpressional strain regime (Fig.125).

The structure corresponds in fact to a popup generated by two main fault oriented N-S trending to the W and the East respectively. These two major faults are responsible of the generation of different fractures having the same trends.

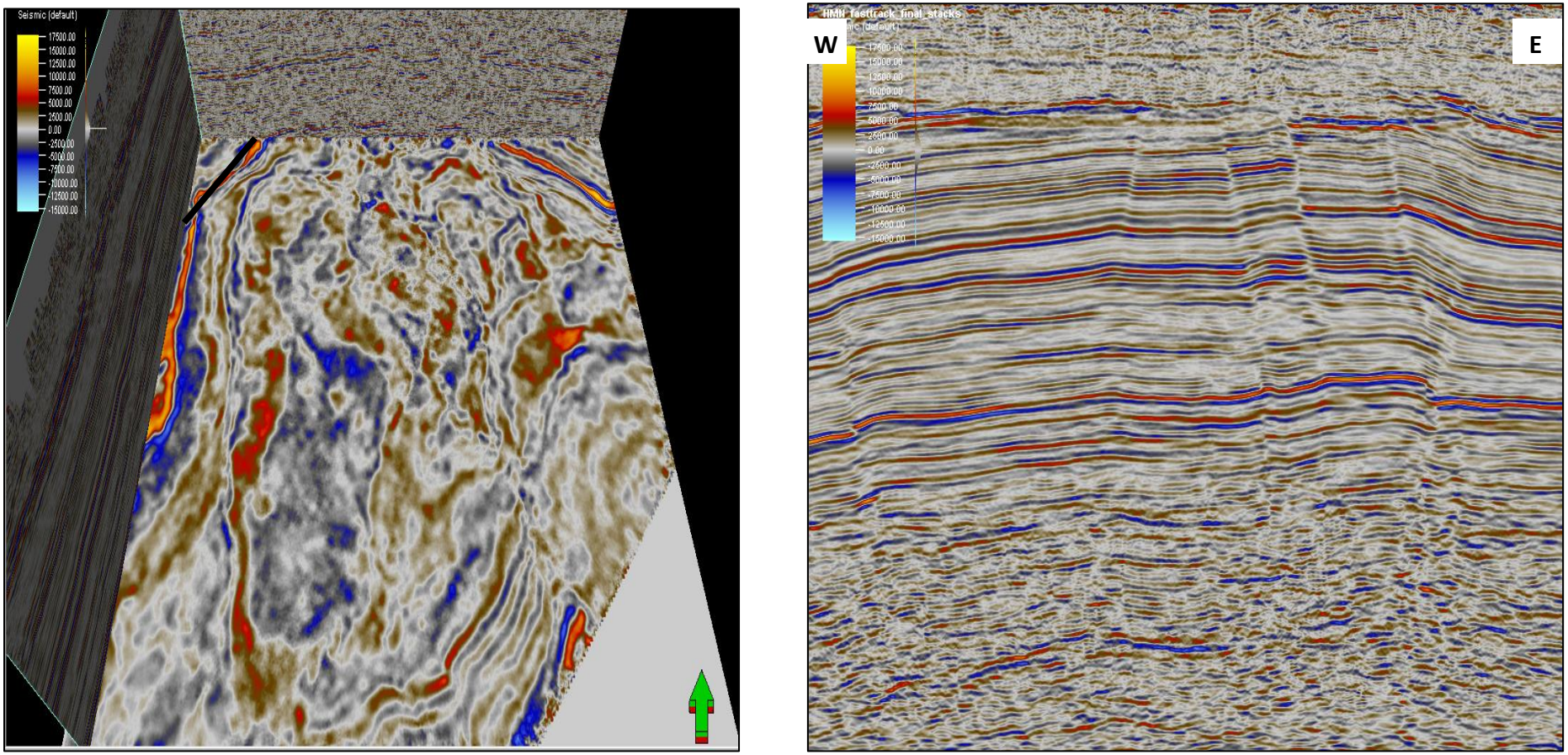

Figure 124: The 3D seismic volume

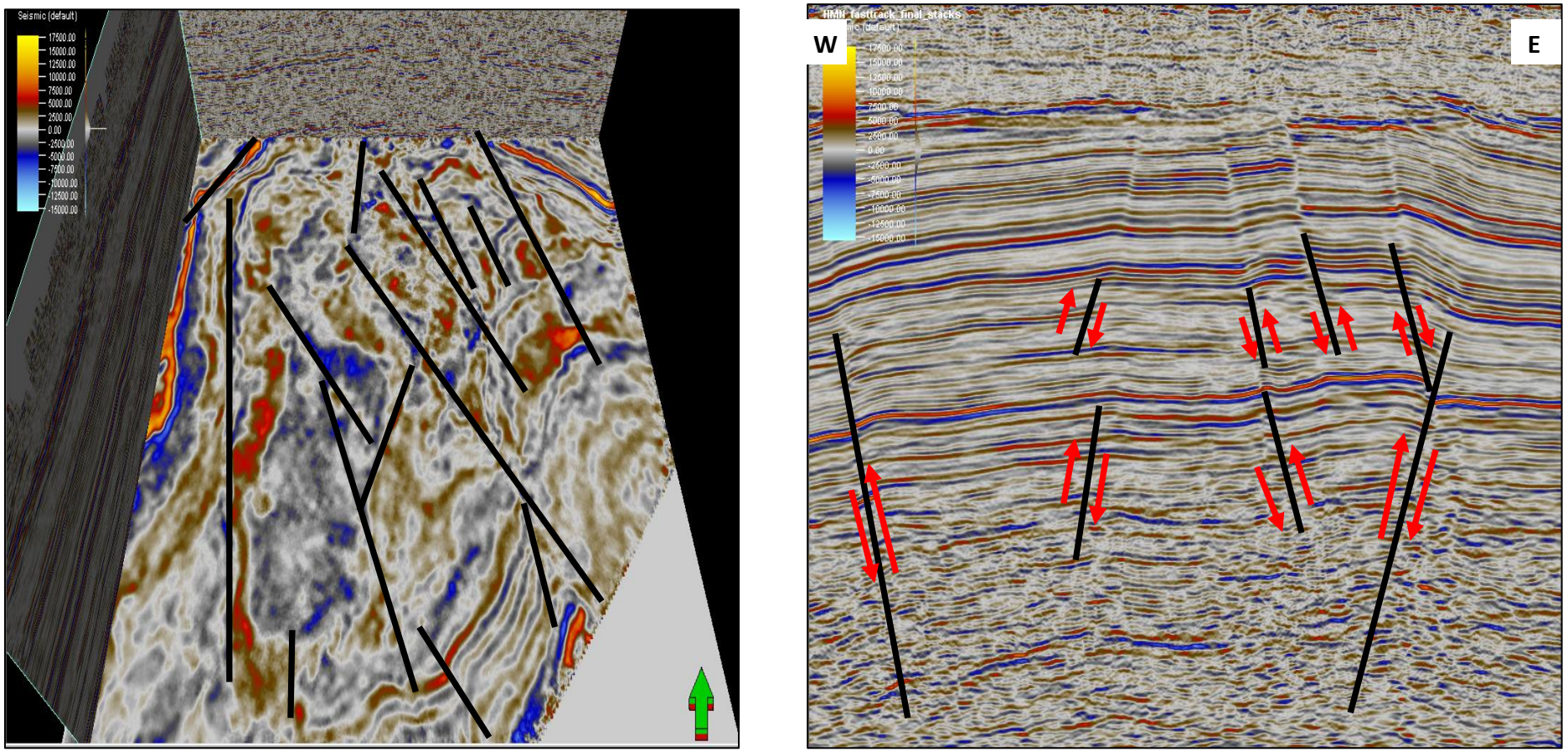

Figure 125: Structure shows an anticline with several fault sets which corresponds to a pop-up structure

The first attribute used is the variance attribute that can be used to isolate edges from the 3D seismic data (Fig.126). The term of edge means discontinuities in the horizontal continuity of amplitude. The variance is very interesting seismic attribute that can be used as a structural or a stratigraphic attribute. This attribute can highlight depositional features, including reefs, channels, and splays. To enhance the structural feature such faults the dip-guided variance is highly recommended (Schlumberger, 2018).

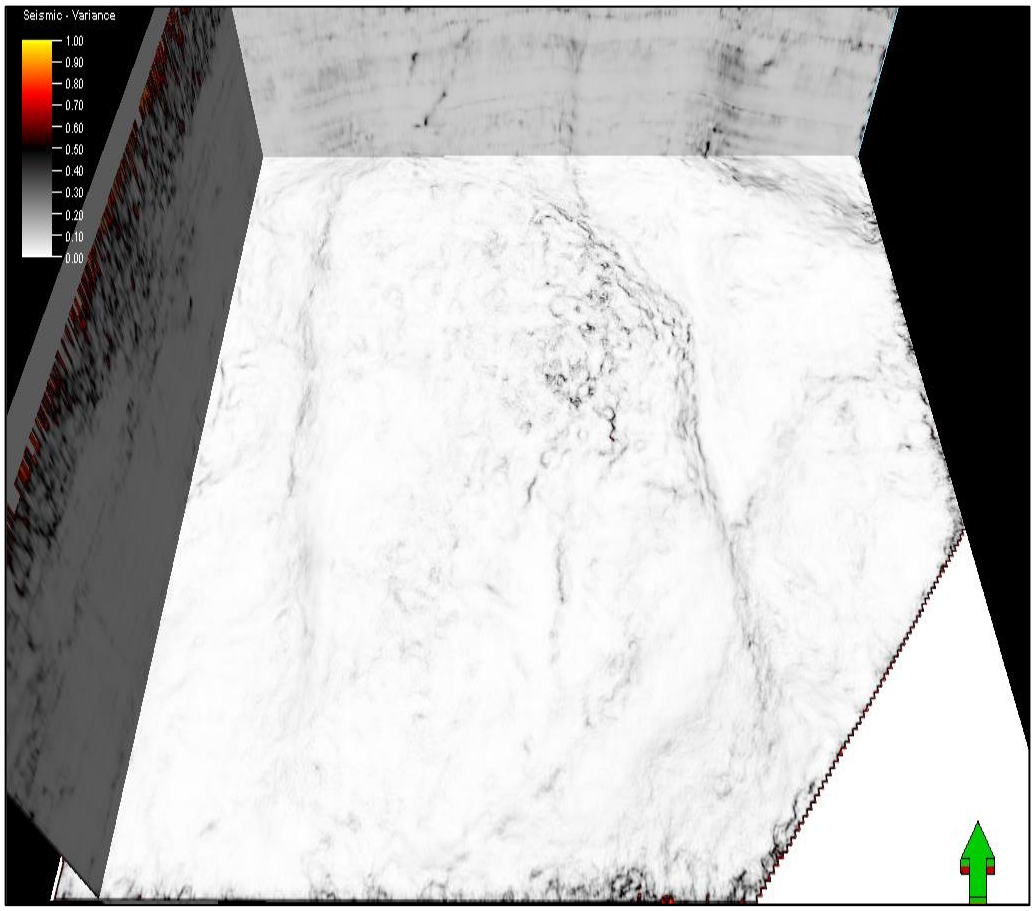

Figure 126: The 3D variance cube

In the area of study, this attribute highlights the anticline structure where several faults trends are illuminated. They are oriented mainly N-S, NE-SW. These trends are visible in inline, crossline and timeline intersections.

The second attribute used in this purpose is the curvature. The curvature is a seismic attribute that describes how bent a surface is at a particular point and is closely related to the second derivative of the curve defining the surface. The more bent a surface is, the larger the value of the

curvature attribute (Chopra, 2007). The surface curvature is well described by Roberts (Roberts, 2001). The surfaces of an anticline for example will yield positive curvature and the synclinal surface will yield negative curvature. On the other hand, the ridges will yield positive curvature in the direction across the ridge and zero curvature in the direction along the ridgeline (Klein et al., 2008). The largest curvature is named the maximum curvature and the curvature in the orthogonal azimuth is named the minimum curvature. The average of the minimum and maximum curvature is named the mean curvature and their product is called Gaussian curvature (Klein et al., 2008).

3D curvature can be used to bring out stratigraphic features in sedimentary environments, karst features or structural discontinuities. By tracking rapid changes in the orientation field, edges and subtle truncations become visible (Schlumberger, 2018). In the area of study this attribute enhances a dense faults network that affect the anticline. The main faults are oriented NW-SE, N-S, NE-SW. This fault network is well illustrated in timeline intersection (Fig.127).

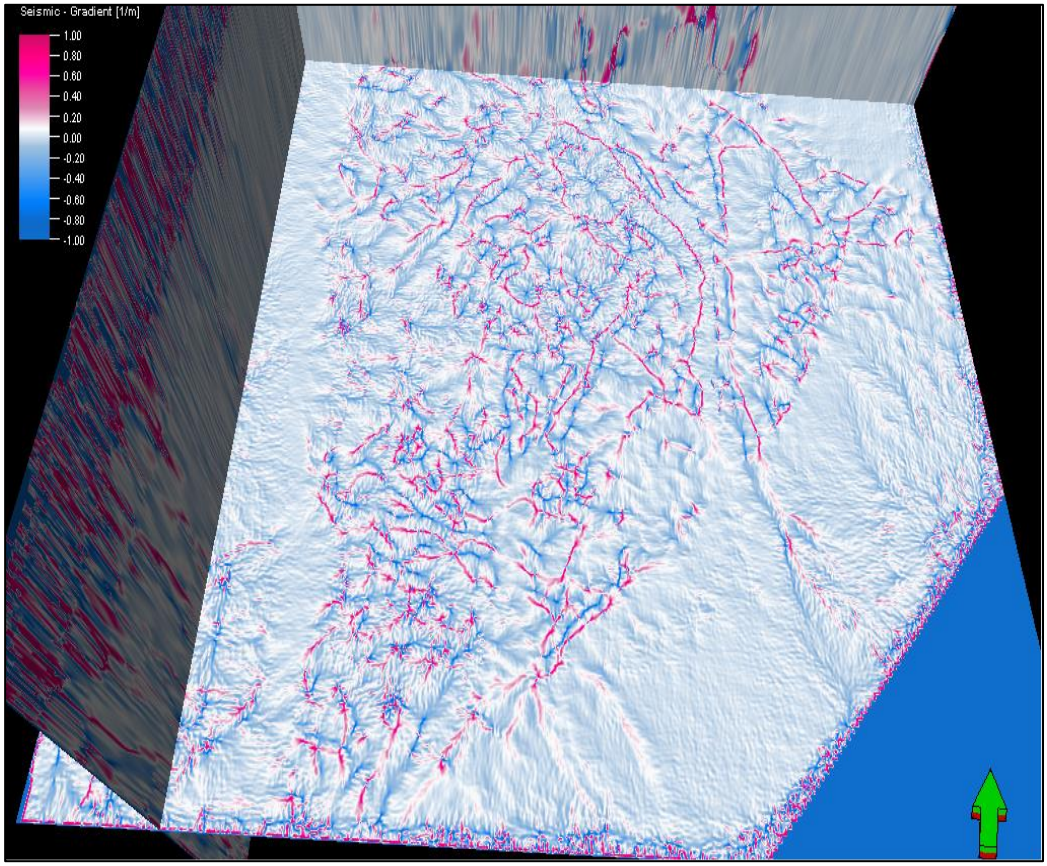

Figure 127: The 3D curvature cube

The third attribute used for this purpose is the dip deviation (Fig.128). This attribute uses a new dip estimation method and displays the calculations in two different views. A good dip estimation can reveal a lot about various structural geology in seismic. Discontinuities such as faults can easily be seen with a good dip estimate (Schlumberger, 2018).

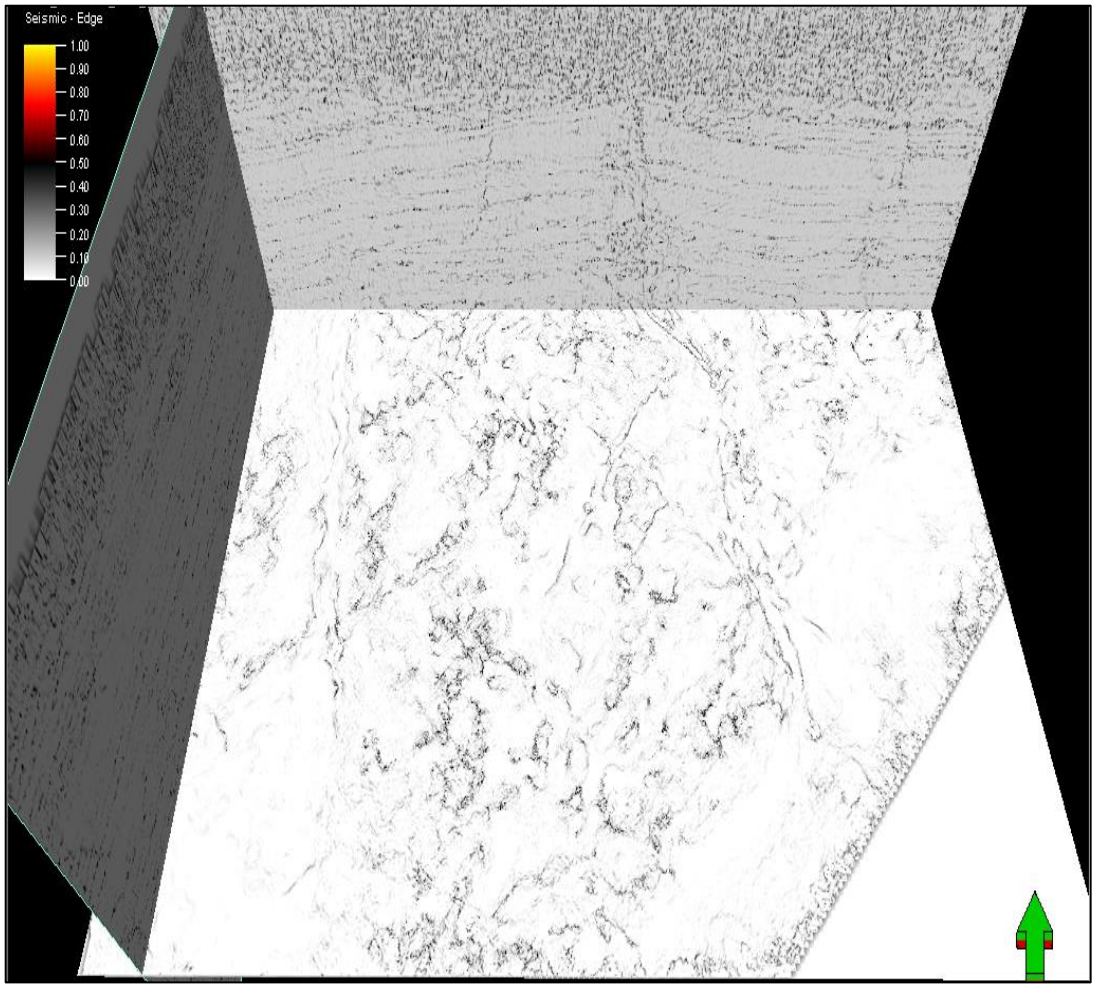

Figure 128: The 3D dip deviation cube

In the area of study, this attribute highlights the anticline structure where several faults trends are illuminated. They are oriented mainly NW-SE, N-S, NE-SW. These trends are visible in inline, crossline and timeline intersections.

The fourth attribute used to estimate the fracture intensity in the 3D seismic volume is the dip illumination (Fig.129). It is a good indicator of structural features such as faults, folds, and salt dome.

This attribute uses a dip estimation method and displays the calculations in two different views. Discontinuities such as faults, can easily be seen with a good dip estimate and a correct exploitation of the dip values. This attribute uses a cross correlation dip estimation method that has been modified with gradient decent to accelerate computations. The attribute gives you an option to display a directional view of the calculated dip, where the direction is in degrees and the dip magnitude (Schlumberger 2018).

This attribute highlights the anticline structure where several faults trends are illuminated. They are oriented mainly NW-SE, N-S, NE-SW. These trends are visible in inline, crossline and timeline intersections. The intensity of the shaded area can give an idea about the value of the dip. More the structure is shaded, the larger the dip value.

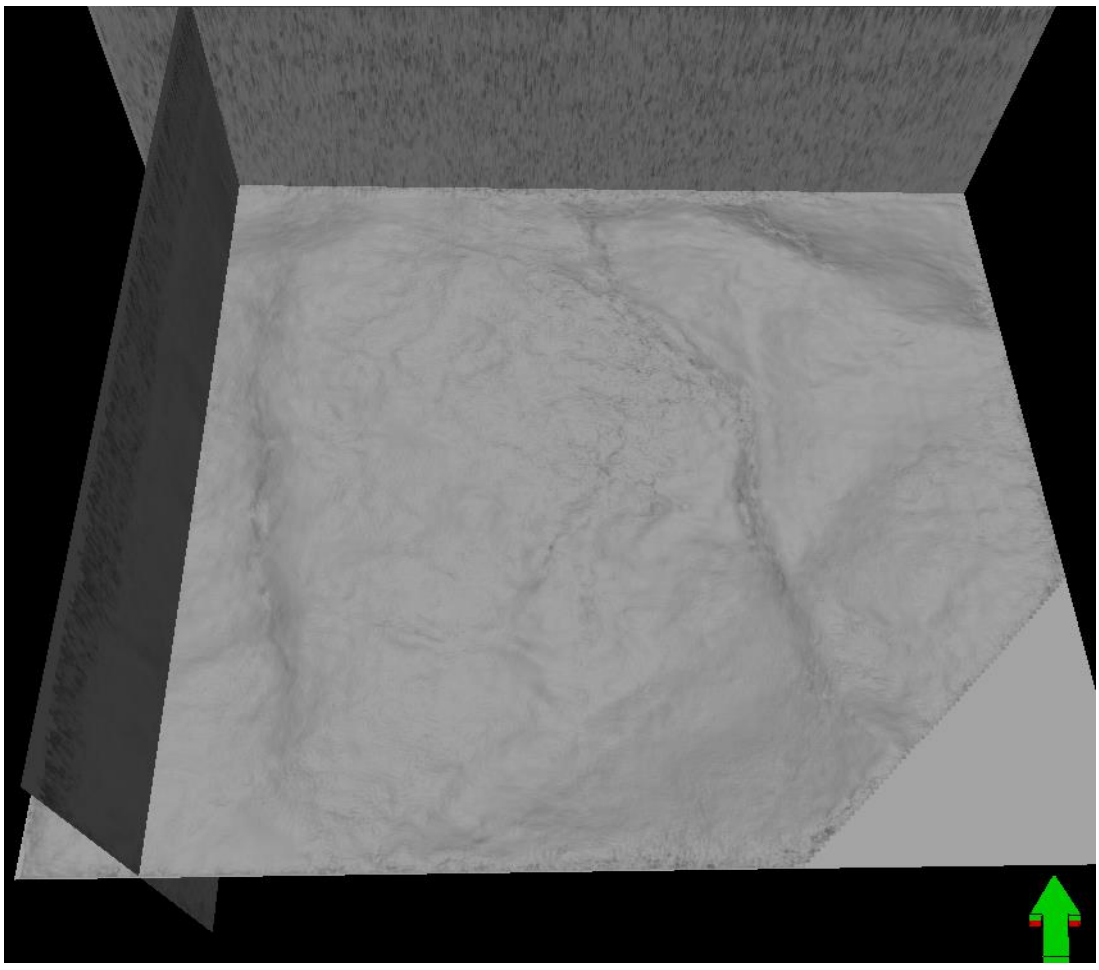

Figure 129: The 3D dip illumination cube

The fifth attribute used to estimate the fracture intensity and have an idea about the fractures' dip azimuth in the 3D seismic volume is the azimuth attribute (Fig.130). The estimation of local azimuth from the 3D seismic data contains three options. The first one is the Event where the downslope azimuth varies between 0 to, 360 of the estimated event and the gradient is assumed to be perpendicular to the event. The second one is the gradient where the azimuth varies from 0 to 360 of the instantaneous gradient of the sample neighborhood. The third one is the Principal Component where the local azimuth is estimated from the principal component analysis of gradient covariance matrix (Schlumberger, 2018).

The local structural dip and azimuth attributes are powerful both for capturing properties of the 3D seismic data. This attribute highlights the anticline structure where several faults trends are highlighted. In the eastern and western flanks, the anticline shows structures with an azimuth dipping to the East and the West. On the other hand, in the northern part of the anticline, two structures dipping to the NE and NW are also illuminated.

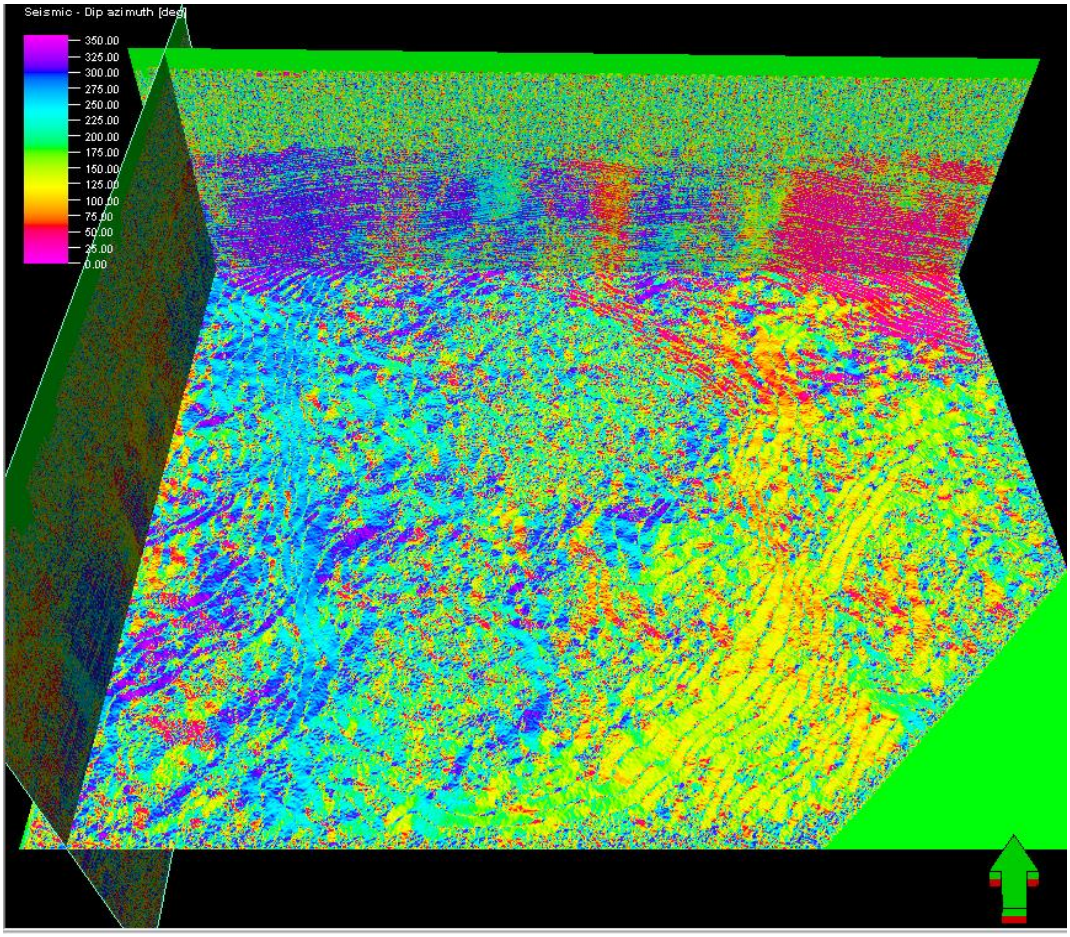

Figure 130: The 3D Azimuth cube

The sixth attribute used for this purpose is the Ant Tracking (Fig.131). This algorithm has been developed by Schlumberger to extract fault surfaces from fault attributes. This algorithm uses the principles from ant colony systems to extract surfaces appearing like trends. The approach is fully 3D and can take advantage of surface information in the surrounding voxels. By writing the extracted surfaces back to a volume is referred to the ant track cube. This cube contains only what is likely to be true fault information. Through this volume, fault surfaces could be extracted via an automatic fault extraction (Schlumberger, 2018).

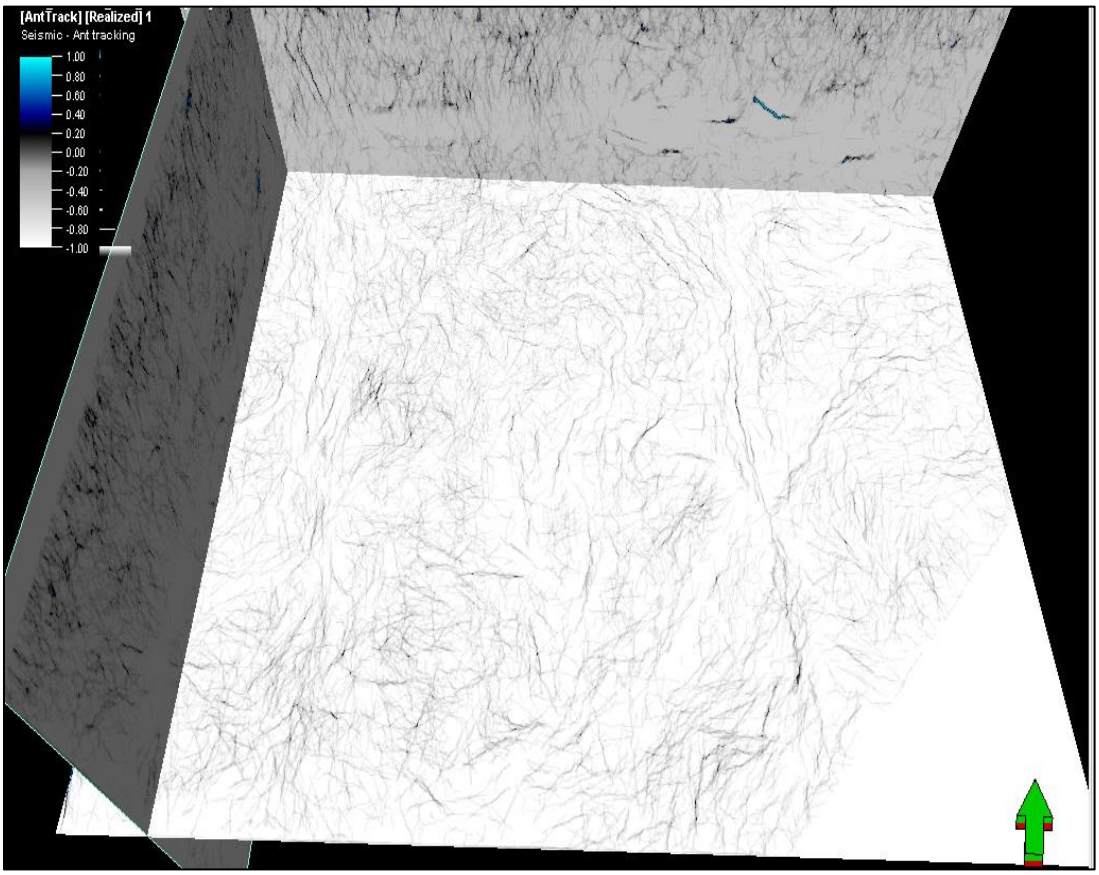

Figure 131: The 3D Ant Tracking cube

In the area of study, the Ant tracking was generated based on the Variance volume with an aggressive ant detector in order to illuminate all the fault patterns that affect this anticline. The application of the Ant Tracking attribute highlights a dense fault network that affect the crest and the two flanks of the anticline. This fault network designs a lozenge fault pattern that appears in inline, crossline and timeline intersections. The faults are oriented mainly N-S, NE-SW. An automatic fault extraction was applied on the Ant Tracking volume in order to extract, display,

analyze, and edit fault-patches. The fault patches were created from the variance volume. All the extracted surfaces are displayed and give an overview of the possible fault systems that affect the top Ordovician. The outcome shows that top Ordovician is affected by a very dense fault network oriented NW-SE, N-S, NE-SW and E-W (Fig.132 & Fig.133).

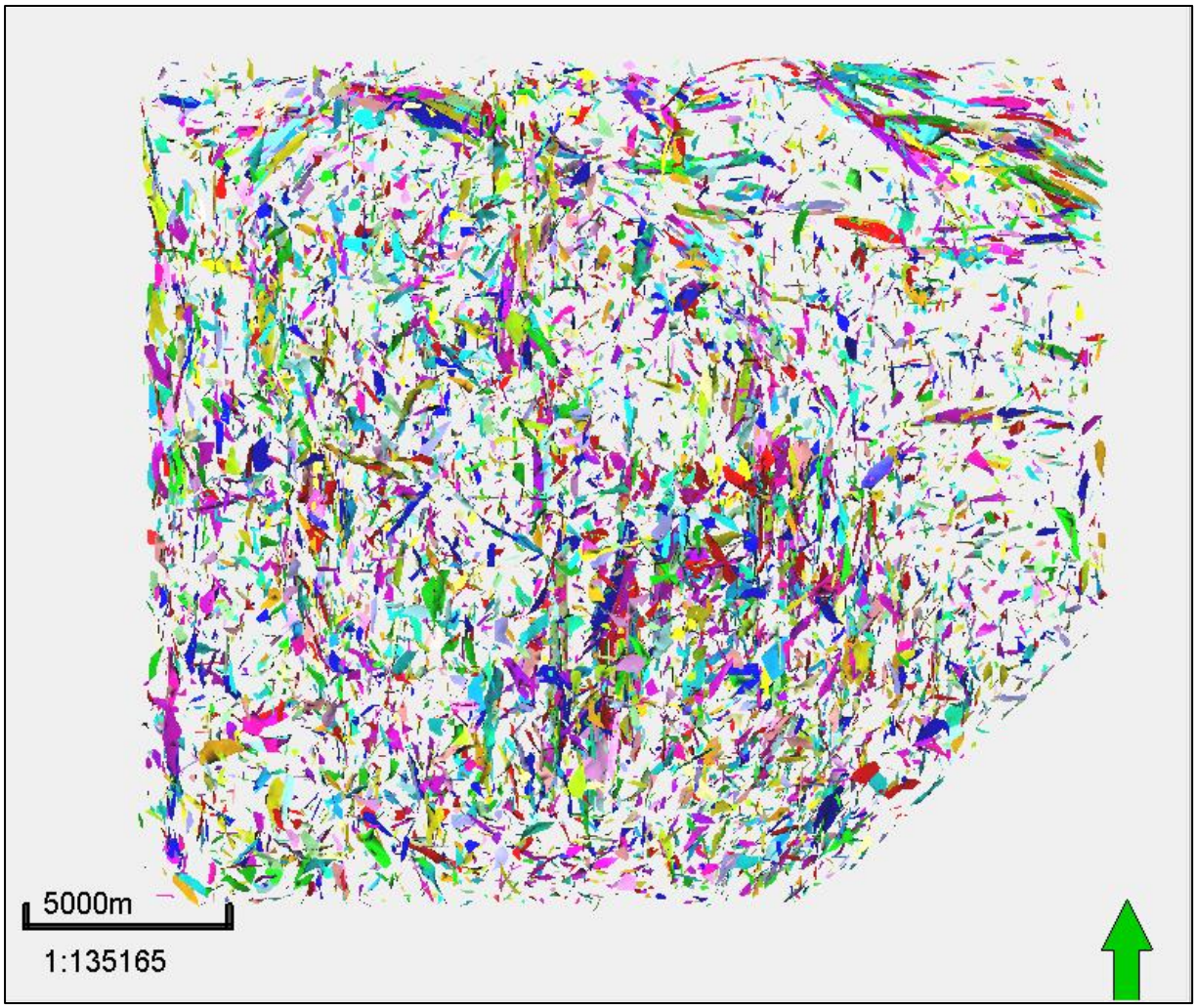

Figure 132: The Fault network in 2D dimension

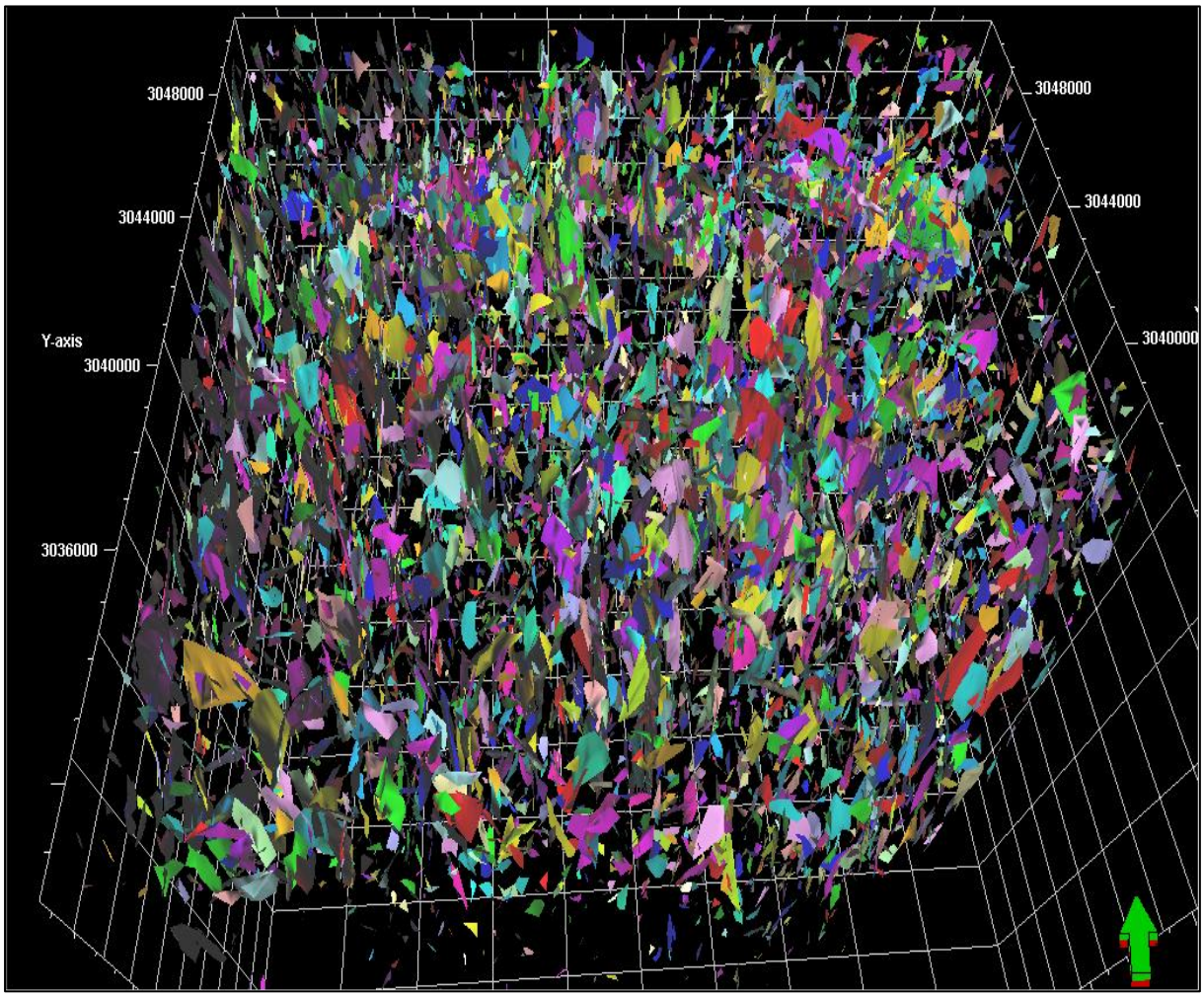

Figure 133: The Fault network in 3D dimension

The analysis of the fracture patches shows that the fractures have a dip ranges between 60 and 90 degrees with a mean equals to 80 degrees (Fig.134). The analysis of the dip azimuth shows that the main fractures have a dip azimuth 270 and 90 which indicate that the strike of these main fractures have strike N-S dipping to the West and the East (Fig.135). The fractures' length analysis show that the main frequent fault length averages 300 meters (Fig.136).

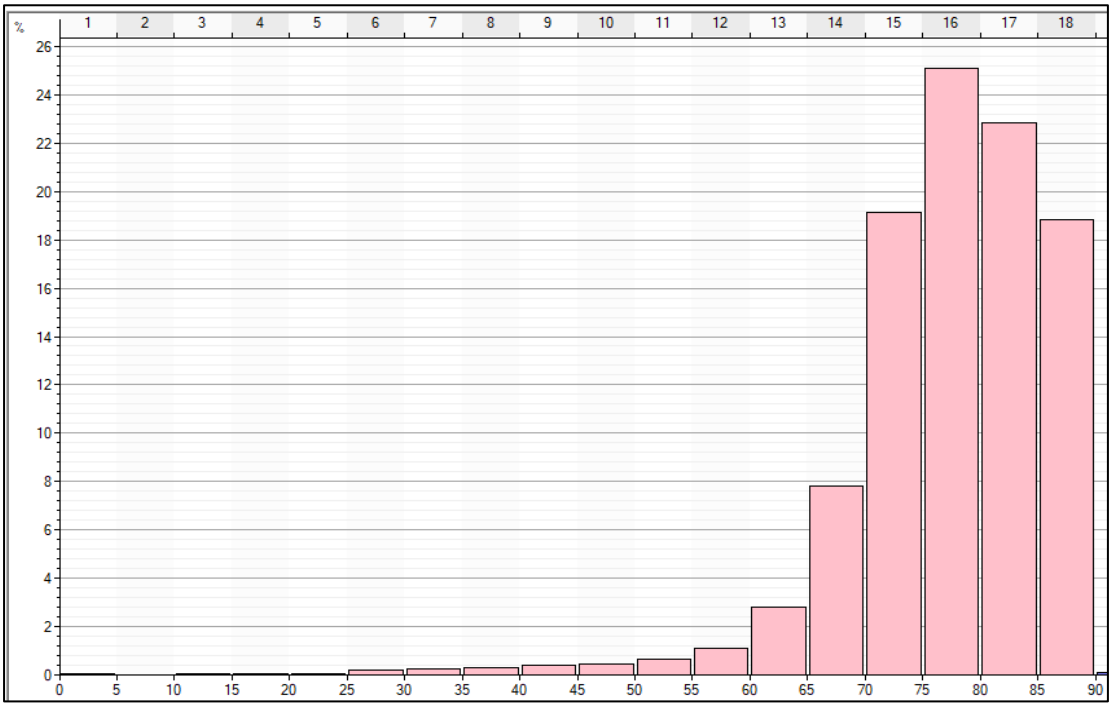

Figure 134: Faults' dip ranges

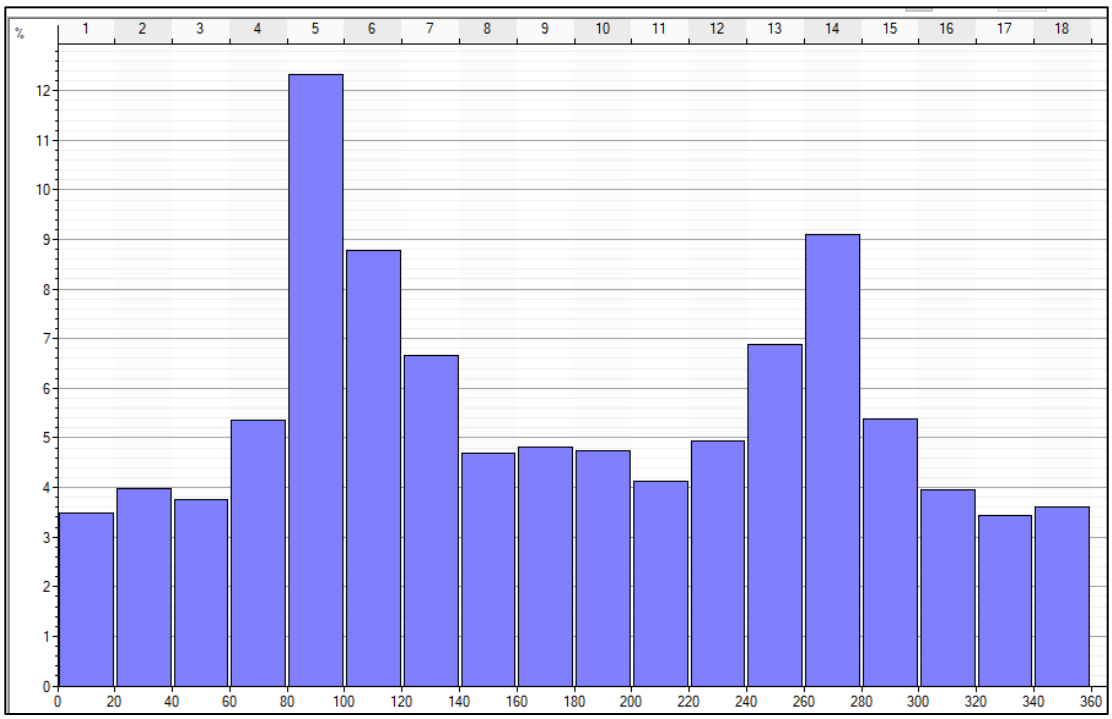

Figure 135: Faults' dip azimuth ranges

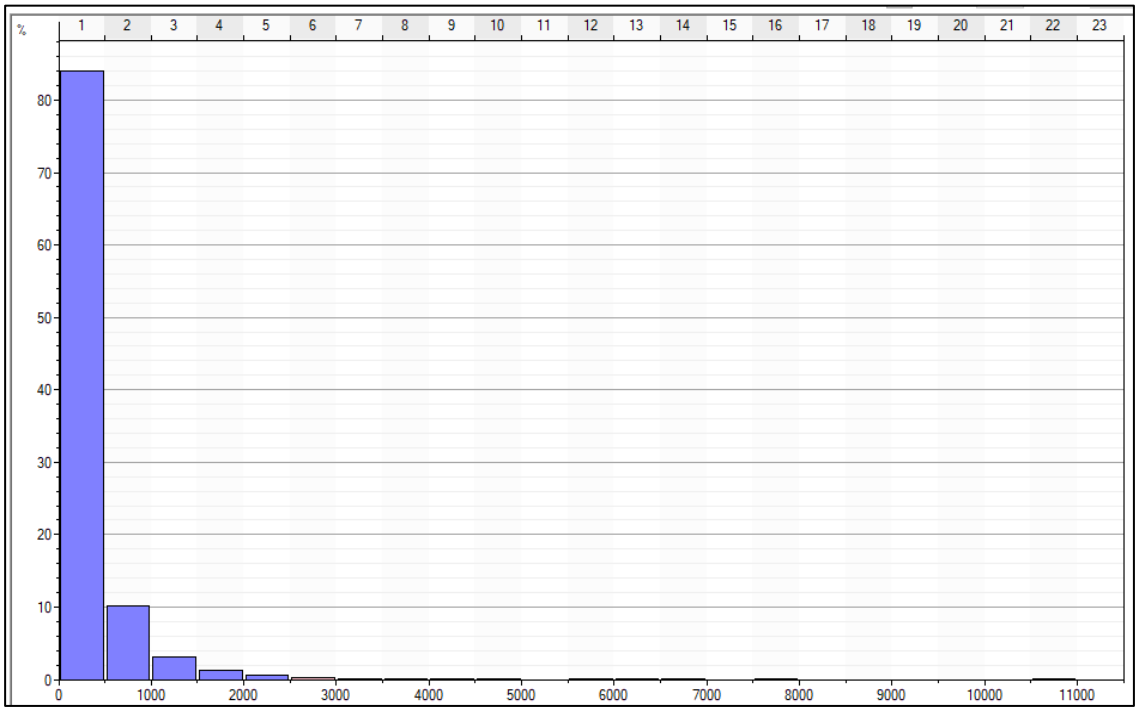

Figure 136: Faults' length distribution

VII-7-Conclusions

The structures in the Ahnet and Mouydir basins appear to be the results of the two Hercynian events sealed by the regional angular discordance named Hercynian unconformity (Boudjema, 1987, Donzeau, 1983, Haddoum et al., 2001, Issad et al., 2011, Zazoun, 2001, Zegrir, 2014). In the Mouydir and Ahnet basins, the Hercynian orogeny has structured the Paleozoic formations horsts and grabens (Boudjema, 1987, Haddoum et al., 2001, Zazoun, 2001, Issad et al., 2011, Zielinski, 2011).

Base on the geological maps, it appears clearly that a dense fracture network affects the Paleozoic series. The fracture network is composed by fracture sets oriented N-S, NNE-SSW, and NW-SE. The N-S fault network constitute large and long fracture corridors, which design the edges of the two basins. These faults are strike slip faults tending dextral and sinistral. The NNE-SSW are also strike slip fault trending sinistral. The NW-SE are also strike slip faults tending dextral and sinistral which can attest that these faults were reactivated several times during the Paleozoic era. The Hercynian orogeny which is well known in the Saharan platform is composed by two main tectonic events oriented N040 and N120 having age Visean and post-Namurian to post-Permian respectively (Boudjema, 1987, Donzeau, 1983, Haddoum et al., 2001, Issad et al, 2011,

Zazoun, 2001). The Hercynian Orogeny can be considered as a continuous deformation rather than tectonic events (Donzeau et al., 1981, Donzeau, 1983, Zazoun, 2001,).

The 3D seismic analysis based on different attributes shows that Ordovician is affected by a very dense fracture network oriented NW-SE, N-S, NE-SW and E-W. The faults analysis shows that the structure corresponds in fact to a popup generated by two main fault oriented N-S trending to the W and the East respectively. These two faults are responsible of the generation of different fractures having the same trends the faults have a mean dip equals to 80 degrees and dip azimuth equals 270 and 90 degrees respectively.

The structural analysis of the different 2D seismic profiles attest that the deep strike slip faults that affected the Ahnet and Mouydir basin are not a pure strike slip trending only sinistral and dextral but they have also a vertical component trending as normal and reverse faults. They are mainly generated through a transpressional and a transtensional strain regimes that affected the area of study during the Hercynian orogeny.

The 2D seismic profiles show clearly that at least two tectonic events expressed by a succession of distensive and compressive events respectively and generation of synclines and normal faults, and anticlines and reverse faults affected the area of study.

These approaches allow up understanding the geological processes that affect the area of study, which are responsible for the generation of the complex fracture patterns. These approaches will help to predict the occurrence of these fracture patterns in the area where no data is available. This information will help to plan a new exploration strategy in the Mouydir basin where the natural fractures would play a tremendous role in the productivity of the Ordovician reservoir.

Chapter VIII: Discussion and Conclusions

The Cambro-Ordovician in the Algerian Saharan platform is characterized by tight sandstone formations with very low petrophysical characteristics where the natural fractures play an important role in their productivity. The Mouydir basin is the less explored basin where a poor quality of seismic 2D surveys and few wells with limit set of logs are available. They were drilled on structures defined on the field observations, the gravity data, the geological maps, and the seismic refraction data. Unfortunately, these wells were all negative.

The Mouydir basin is limited in the west by the Ahnet and Timimoun basins, which are considered as the main gas provinces in the western part of the Saharan plate-form. Also, The Mouydir basin is limited in the north and the east by Oued Mya and Illizi basins respectively, which are considered as prospective oil and gas provinces. These basins have the same petroleum system as the Mouydir basin where the Ordovician reservoir produces tremendous quantity of oil and gas from natural fractures.

A specific and an innovative workflow was proposed to analyze and characterize the natural fractures in the Cambro-Ordovician reservoir using a surface analog that appears in the southern edge of the Mouydir basin in order to bring a new insight and guide the future exploration wells in this basin. This workflow integrates multiple sources of data to build a deterministic fracture model. This model highlights the major and minor fractures that aid to understand the basin's geological evolution as well as the impact of the basement's fractures on the basin's structuration and on the sedimentary cover.

The 3D fracture model is used to understand the fractures' distribution, their connectivity, and their kinematics. The outcomes could be used to predict fractures' extension and occurrence in the subsurface and could be used to explain the negative results of the drilled wells. In addition, borehole imagery and 3D seismic data from the Ahnet basin were used to complete the lack of data in the Mouydir basin and understand the intensity, the density and typology of fractures in the Ordovician fractured reservoir by interpreting different attributes.

The unique deterministic fracture model illustrates the fractures' distribution and helps to distinguish the mechanical units of the Cambro-Ordovician and the relationship between them. The Tamadjert formation appears to be the most fractured unit due to the lithological

characteristics. On the other hand, the In-Tahouite is the least fractured formation due probably to its shaly components.

The basement's faults had a huge impact on the sedimentary cover and they had structured the Cambro-Ordovician units. The Cambro-Ordovician formations are characterized mainly by brittle tectonic style, linked with Major basement fractures inherited from the Pan-African orogeny, which is responsible for the creation of an extensive fracture network comprised of Major vertical fractures.

The analysis of geological maps shows that a dense fracture networks had affected the Paleozoic series. The Major structures correspond to N-S-trending dextral strike-slip fractures and NNW-SSE trending sinistral strike-slip fracture. Two Major fracture corridors can be distinguished which design the western and the eastern Mouydir basin's edges. They start from the basement in the Hoggar shield and continue to the north in divergent directions in the Saharan platform. They are oriented NNE and NNW constituting the Amguid and the Idjerane spurs respectively. The fractures' length distribution shows a power law distribution with a coefficient ranging between 2.31 and 2.69 and high correlation coefficients averaging 0.96.

The fractal analysis of the entire 2D fracture networks and the different fracture sets that affect the basement and the Cambro-Ordovician units show fractal dimensions based on both the center distance and the box-counting algorithms with values ranging between 1 and 2. Though, very few fracture sets do not show any fractal dimension. The fractal dimension using the box-counting algorithm is 0.2 to 0.3 less than the fractal dimension using the center surface algorithm for the different networks and in the different fracture sets.

At the level of the Cambrian reservoir, the core analysis shows a poor reservoir quality where the permeability ranges from 0.01 and 0.1 mD and porosities hardly exceeding 3%. The petrophysical parameters of the Ordovician reservoir rarely exceed 1 mD with an average porosity of 6 to 8%.

The analysis of the core's fractures of the three wells of the Mouydir basin shows that the fracture density varies from 2.14 fractures/meter to 0.07 fractures/meter, whereas their openings vary from one millimeter to one centimeter. A proportion of 20% of fractures appear partially cemented with essentially quarzitic cements and 70% of fractures are totally cemented with quartz with presence of pyrite and rarely with calcite. The density of the fractures sometimes exceeds 1 / m of fracture in the different reservoir levels, assuming an ideal level of connectivity, would

produce a network of significant permeability. Most of the fractures are steeply dipping, and the observation of some intersections of core fractures probably illustrates the presence of a network of connected fractures. The global distribution of fracture types per reservoir shows that the studied wells are generally moderately fractured with a predominance of vertical fractures

The borehole imagery analysis in Hamra Quartzite reservoir in the Ahnet basin shows three main fracture sets oriented N030, N140, and N170 respectively with a dip of 80°. These fractures are conductive and semi-conductive. The maximum horizontal stress (SHmax) is determined from the widths of wellbore breakouts. The SHmax inferred from the breakouts in the eastern edge of Ahnet basin, is oriented NW-SE. Fractures having the same direction as the maximum horizontal stress are generally conducive (open) and thus contribute to the improvement of the petrophysical parameters of Cambro-Ordovician reservoir, whereas those perpendicular to the SHmax are generally resistive (closed) and therefore they may constitute permeability barriers.

On one hand, the core fracture analysis shows the predominance of tectonic fracture in term of number and length with a high index of fracturing. However, these fractures are usually cemented to partially cemented. On the other hand, the borehole imagery analysis reveals the presence of conductive and resistive fractures. In many cases, it was difficult to distinguish between closed and opened fractures because of the type of cement and the existence of pyrite. Three main directions of conductive and semi-conductive fractures were highlighted N030, N140, and N170 respectively with a dip of 80°.

Mouydir basin shows two positive anomalies illustrated in the gravity map oriented North-South. These anomalies correspond the edges of the basin represented by the Idjerane spur in the west and Amguid-Biod spur in the East. In the middle of the basin there is another positive structure oriented also North-South where the well HL was drilled.

The geological maps show a dense fault sets oriented N-S, NNE-SSW, and NW-SE. These faults are strike slip faults tending dextral and sinistral which can attest that these faults were reactivated at least two times during the Paleozoic era.

The structures in the Ahnet and Mouydir basins appear to be the results of the two Hercynian events sealed by the regional angular discordance named Hercynian unconformity (Boudjema, 1987, Donzeau, 1983, Haddoum et al., 2001, Issad et al., 2011, Zazoun, 2001, Zegrir, 2014). The Hercynian orogeny has structured the Paleozoic formations in horsts and grabens (Boudjema, 1987, Haddoum et al., 2001, Zazoun, 2001, Issad et al., 2011, Zielinski, 2011). The

Hercynian orogeny is composed by two main tectonic events oriented N040 and N120 having age Visean and post-Namurian to post-Permian respectively (Boudjema, 1987; Donzeau, 1983; Haddoum et al., 2001; Issad et al, 2011; Zazoun, 2001). The Hercynian Orogeny can be considered as a continuous deformation rather than two tectonic events (Donzeau et al., 1981; Donzeau, 1983; Zazoun, 2001).

The structural analysis of the different 2D seismic profiles attest that the deep strike slip faults that affected the Ahnet and Mouydir basin are not a pure strike slip trending only sinistral and dextral but they have also a vertical component trending as normal and reverse faults. They are mainly generated through transpressional and transtensional strain regimes during the Hercynian orogeny.

The seismic attributes show that Ordovician is affected by a very dense fracture sets oriented NW-SE, N-S, NE-SW and E-W. The faults analysis illustrate that the structure corresponds to a popup generated by two main faults oriented N-S trending to the West and the East respectively.

In the Mouydir basin, the Silurian is the main source rock and it is a type II kerogen. The Total Organic Carbon (TOC) values range from 2% to 4% and reach up 11.65% (Issad et al., 2011). The Silurian source rock is in dry gas phase (Ro> 2%). The generation of oil in the Mouydir Basin began in the early Carboniferous and stopped at Stephanian, while the gas generation continued until the Hercynian event and even post-Hercynian event (Issad et al., 2011).

According to Lounissi (1992), a decrease in potentiometric pressures is observed in the Mouydir basin from south to north. The Cambro-Ordovician complex contains water of different types, from a fresh water hydro-carbonated sodium to a salt-water chlorinated calcium. Chlorinated calcium waters dominate, but to the south; the waters are characterized by their low salinity, which can be explained by the infiltration of fresh water coming from the southern outcrops.

The drilling of a horizontal pilot well having as target the Cambro-Ordovician reservoir in the depocenter of the Mouydir basin, on positive structures already discovered such as HL, and parallel to the Minimum Horizontal stress, could be a decelerator of a new exploration era in the Mouydir basin (Fig.137).

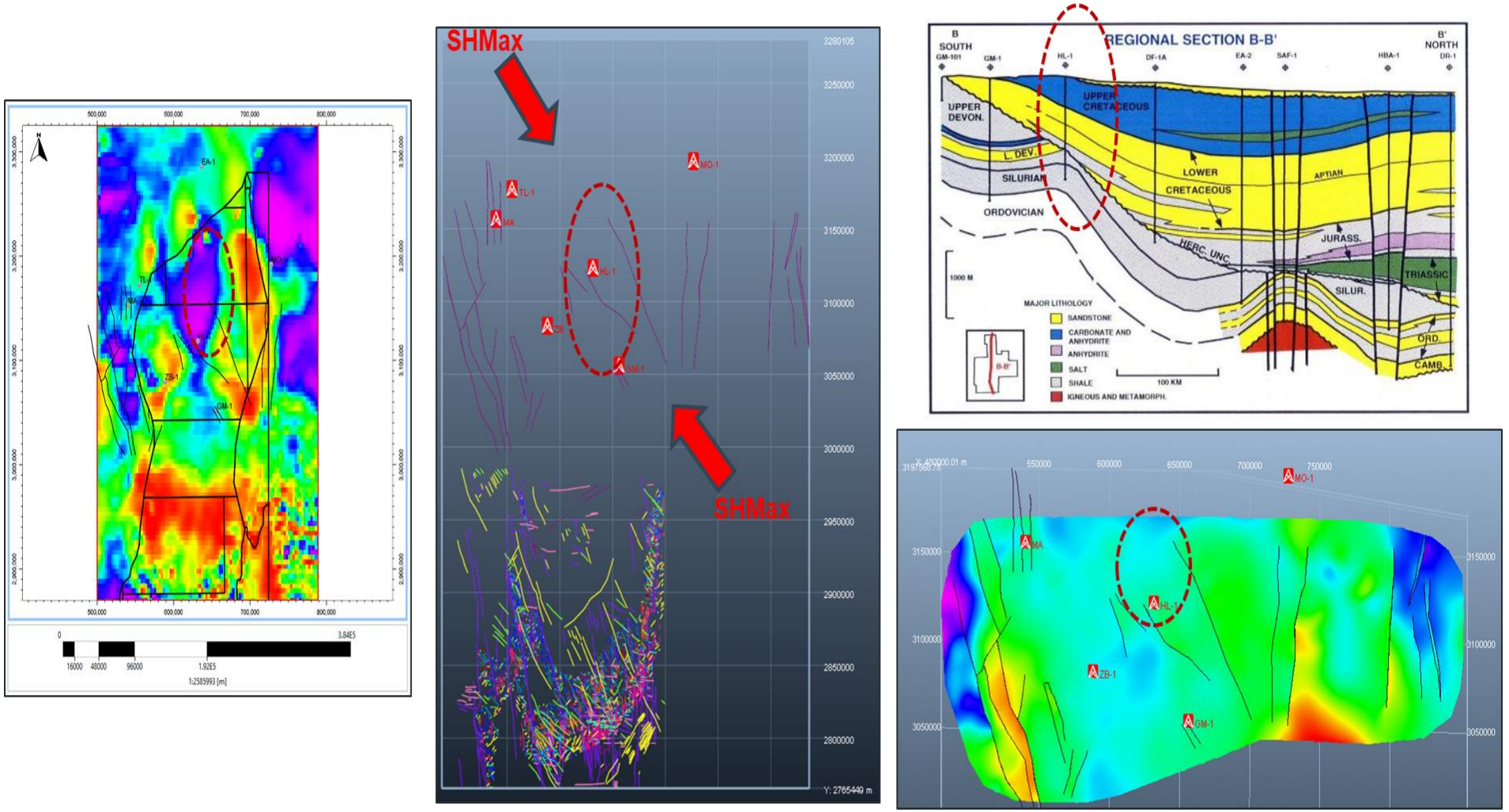

Figure 137: The proposed sweet spot (horizontal well perpendicular to SHmax)

References

Aliev, M., Ait Laoussine, N., Avrov, V., Aleksine, G., Barouline, G., Iakovlev, B., Korj, M., Kouvikine, J., Makarov, V., Medvedev, E., Mkrtchiane, O., Moustafinov, R., Oriev, L., Oroudjeva, D., Oulmi, M., Saıd, A., 1971. In: Altamira-Rotopress, S.A. (Ed.), Structures geologiques et perspectives en petrole et en gaz du Sahara algerien,

Arab, M., Djezzar, S., 2011. Gas Potential Evaluation, Reggane Basin, Southwestern Algeria. Oil Mediterranean Conference and Exhibition (OMC), Ravena, Italy.

Badsi M. (1998): Fracturation naturelles des roches: Application au bassin de l'Ahnet (Algérie) (Thèse de Doctorat).

Balberg, I and Binenbaum, N. 1983. Computer study of the percolation threshold in a two-dimension anisotropic system of conducting sticks Physical Review, 28 (1983), pp. 3799-3812

Balberg, I., Berkowitz, B., Drachsler, G.E., 1991. Application of a percolation model to flow in fractured hard rocks. Journal of Geophysical Research 96B, 10015–10021

Basseto, D., Ben Salah, A., Beuf, S., Gabriel, O., Lacot, R.,Moussine-Pouchkine, A., Philippe, G., 1974a. Carte geologique de Aoulef El-Arab, Ahnet et Mouydir. Service de la Carte Geologique, Algerie, jeu de 13 feuilles, Echelle 1: 200 000, NG 31, No. 941, p. 14.

Basseto, D., Ben Salah, A., Beuf, S., Gabriel, 0. Lacot, FL. Moussine-Pouchkine, A., Philippe, G., 1974b. Carte geologique de Reggane. Ahnet et Mouydir. Service de la Carte Geologique, Algerie, jeu de 13 feuilles, Echelle 1: 200 000, NG 31, No. 941, p. 13.

Beghoul M.S. (1991): Apport et contribution de l'analyse de diagraphies à la connaissance d'un bassin sédimentaire, Application au bassin de Timimoun (Algérie, Thèse de Doctorat).

Beicip, 2018. FracaFlow Tutorial.

Bennacef, A., Beuf, S., Biju-Duval, B., De Charpal, O., Gariel, O., Rognon, P., 1971. Example of cratonic sedimentation: Lower Palaezoic of Algerian Sahara. The American Association of Petroleum Geologists Bulletin 55 (12), 2225–2245.

Bensalah, A. Beuf, S. Gabriel, O. Philippe, G. Lacot, r. Paris, A. Basseto, D. Conrad, J. Moussine-Pouchkine, M.A. 1972. Carte Géologique de l'Algérie: Arak, feuille NG-31-X et NG-31-IV. Ministère de l'Industrie et de l'Energie.

Bensalah, A. Beuf, S. Gabriel, O. Philippe, G. Lacot, r. Paris, A. Basseto, D. Conrad, J. Moussine-Pouchkine, M.A. 1972. Carte Géologique de l'Algérie: Ain Tadjoubar, feuille NG-31-XVI. Ministère de l'Industrie et de l'Energie.

Bensalah, A. Beuf, S. Gabriel, O. Philippe, G. Lacot, r. Paris, A. Basseto, D. Conrad, J. Moussine-Pouchkine, M.A. 1972. Carte Géologique de l'Algérie: Khanget El Hadid, feuille NG-31-XVII. Ministère de l'Industrie et de l'Energie.

Bensalah, A. Beuf, S. Gabriel, O. Philippe, G. Lacot, r. Paris, A. Basseto, D. Conrad, J. Moussine-Pouchkine, M.A. 1972. Carte Géologique de l'Algérie: Ifetessene, feuille NG-31-XI. Ministère de l'Industrie et de l'Energie.

Berkowitz, B. Bour, O. Davy, P. Odling, N. 2000. Scaling of fracture connectivity in geological formations Geophysical Research Letters, 27 (14) (2000), pp. 2061-2064

Beuf, S., Biju-Duval, B., De Charpal, D., Rognon, R., Bennacef, A., 1971. Les grès du Paléozoïque inférieur au Sahara. Sédimentation et discontinuité: évolution structurale d'un craton. In: Technip-Institut Français du pétrole, vol. 18. Collection Sciences et Techniques du Pétrole, Paris, p. 464.

Biju–Duval, B. M. Deynoux, M. Rognon, P. 1974. Essai d'interprétation des "fractures en gradins" observées dans les formations glaciaires Précambriennes et ordoviciennes du Sahara Revue de Géographie Physique et de Géologie Dynamique, Paris, 16 (1974), pp. 503-512

Black R, Latouche L, Liégeois JP, Caby R, Bertrand JM (1994) Pan-African displaced terranes in the Hoggar shield (central Sahara). Geology 22:641–644

Boualam, A., Djezzar, S., Rasouli, V, Rabiei, M. 2019. 3D Modeling and Natural Fractures Characterization in Hassi Guettar Field, Algeria. 53rd US Rock Mechanics/Geomechanics Symposium New York, NY, USA, 23–26 June 2019.

Boudjema, A., 1987. Evolution structurale du bassin pétrolier 'Triasique' du Sahara Nord Oriental (Algérie). These Doctorat Etat, Paris XI-Orsay, France, 290p.

Bour, O., Davy, P., 1997. On the connectivity of random fault networks following a power law length distribution. Water Resources Research 33, 1567–1583.

Bour, O., Davy, P., 1998.On the connectivity of three-dimensional fault networks. Water Resources Research, 34 (1998), pp. 2611-2622

Brahimi, F., 2015. Etude Geophysique de la structure Zeriba. Document interne, Sonatrach.

Brown, S.R., Bruhn, R.L., 1998. Fluid permeability of deformable fracture networks. J. Geophys. Res. Solid Earth 103 (B2), 2489-2500.

Cacas, M.C. Daniel, J.M. Letouzy J. 2001. Nested geological modeling of naturally fractured reservoirs Petroleum Geoscience, 7 (2001), pp. 43-52

Chilés, J.P., 1988. Fractal and geostatistical methods for modeling of a fracture network. Mathematical Geology 20 (6), 631–654.

Chopra, S., Marfurt, K.J. (2007). Seismic attributes for prospect identification and reservoir characterization. Society of Exploration Geophysicist. pp. 481

Clark-Lowes, D.D. (Eds.), Petroleum Geology of North Africa. Geological Society of London, pp. 97–108. Special Publication 132.

Coward, M.P., Ries, A.C., 2003. Tectonic development of North Africa basins. In: Arthur, T.J., Macgregor, D.S., Cameron, N.R. (Eds.), New Themes and Developing Technologies. Geological Society of London, pp. 61–83. Special Publication 207.

Craig, J., Rizzi, C., Said, F., Thusu, B., Lüning, S., Asbali, A.I., Keeley, M.L., Bell, J.F., Durham,M.J., Eales, M.H., Beswetherick, S., Hamblett, C., 2008. Structural styles andprospectivity in the Precambrian and Palaeozoic hydrocarbon systems of NorthAfrica. In: Salem, M.J. (Ed.) The Geology of East Libya Vol. IV. Gutenberg Press,Malta, pp. 51–122.

Daoudi M. & S.Djezzar (2011): Caractérisation des réservoirs du Dévonien inferieur dans la partie nord du bassin de Reggane. Rapport Interne Sonatrach.

Darcel, C. Bour, O. Davy, P. 2003. Stereological analysis of fractal fracture networks Journal of Geophysical Research, 108 (B9), p. 2451.

Davy, P. 1993. On the fault-Length frequency distribution of the San Andreas fault system Journal of Geophysical Research, 98 (12) (1993), pp. 141-151

Davy, P. Sornette, A. Sornette, D. 1992. Experimental discovery of scaling laws relating fractal dimensions and the length distribution exponent of fault systems Geophysical Research Letters, 19 (1992), pp. 361-363

Davy, P. Sornette, A. Sornette, D. 1990. Some consequences of a proposed fractal nature of continental faulting Nature, 348 (1990), pp. 56-58

Dershowitz,W.S., Herda, H.H., 1992. Interpretation of fracture spacing and intensity. In: The 33th US Symposium on Rock Mechanics (USRMS). American Rock Mechanics Association.

Durham, M.J., Eales, M.H., Beswetherick, S., Hamblett, C., 2004. Structural styles and prospectivity in the Precambrian and Palaeozoic hydrocarbon systems of North Africa. In: Conference Proceedings, Geology of East Libya Symposium, Maghreb Petroleum Research Group, Binghazi, Lybia. 110 p.

Djezzar, S., Rasouli, V, Boualam, A., Rabiei, M. 2019. A New Method for Reservoir Fracture Characterization and Modeling using Surface Analog. 53rd US Rock Mechanics/Geomechanics Symposium New York, NY, USA, 23–26 June 2019.

Djezzar, S., Rasouli, V, Boualam, A., Rabiei, M. 2019. Size Scaling and Spatial Clustering of Natural Fracture Networks Using Fractal Analysis. 53rd US Rock Mechanics/Geomechanics Symposium New York, NY, USA, 23–26 June 2019.

Djezzar, S., Rasouli, V, Boualam, A., Rabiei, M. 2019. Fractal Analysis of 2-D Fracture Networks of Naturally fractured Reservoirs Analog in south Algeria. Joint Geological Society of America, Section Meeting South-Central, North-Central, and Rocky Mountain Sections. 25–27 March 2019, Manhattan, Kansas.

Djezzar, S., Rasouli, V, Boualam, A., Rabiei, M. 2019. Fractography Analysis of Cambro-Ordovician Reservoirs through Surface Analog. Mouydir Basin, Algeria. Joint Geological Society of America, Section Meeting South-Central, North-Central, and Rocky Mountain Sections. 25–27 March 2019, Manhattan, Kansas.

Djezzar, S., Rasouli, V, Boualam, A., Rabiei, M. 2019. Integration of Seismic Curvature and Illumination Attributes in Fracture Detection on a Digital Elevation Model: Methodology and Interpretational Implications. Joint Geological Society of America, Section Meeting South-Central, North-Central, and Rocky Mountain Sections. 25–27 March 2019, Manhattan, Kansas.

Djezzar, S., Rasouli, V, Boualam, A., Rabiei, M. 2019. An integrated workflow for multiscale fracture analysis in reservoir analog. Arabian Journal of Geosciences (in process).

Djezzar, S., Mahdjoub, Y., Mokhtari, N., 2016. 3D fracture modeling of Cambro-Ordovician reservoirs using surface analog to predict the sub-surface fractures in Mouydir basin, Algeria. The First Arab Geosciences Union (ArabGU) International Conference (AIC-1), USTHB, Algeria.

Djezzar, S., Goucem, N., 2015. 3D fracture Modeling in Hassi Guettar field, Hassi Messaoud, Algeria. The 10th Edition of Sonatrach Technical & Scientific Days (JST10), Oran, Algeria.

Djezzar, S., 2012. Impact de la fracturation naturelle dans la productivité des reservoirs du Dévonien inférieur dans le basin de Reggane. Memoire de Magister, Institut des Sciences de la Terre. Université des Sciences et Technologie Houari Boumediene (USTHB). Bab-Ezzouar. Algérie.

Donzeau, M., Fabre, J., Moussine Pouchkine, A., 1981. Comportement de la dalle saharienne et orogenese varisque. Essai d'interpretation. Bulletin Societe Histoire Naturelle Afrique Nord 69 (3-4), 171-184.

Donzeau, M., 1983. Tectonique des monts de'Ougerta. In: Fabre, J, (Ed), Afrique de l'Ouest. Introduction Geologique et Termes Startigraphiques. Lexique Stratigraphique International, Nouvelle Serie 1. Pergamon Press, Oxford, UK, pp. 118-120.

Durham, M.J., Eales, M.H., Beswetherick, S., Hamblett, C., 2004. Structural styles and prospectivity in the Precambrian and Palaeozoic hydrocarbon systems of North Africa. In: Conference Proceedings, Geology of East Libya Symposium, Maghreb Petroleum Research Group, Binghazi, Lybia. 110 p.

Fabre, J., 2005. Géologie du Sahara occidental et central. Musée Royale de l'Afrique Centrale (Ed.), Tervuren, Belgique, 572 p.

Follot, J., 1952. Ahnet et Mouydir. 19eme Congres international de Geologic, Alger. Monographie Regionale, Serie 1, 1, pp. 1-6.

Fekirine, B., Abdellah, H., 1998. Palaeozoic lithofacies correlatives and sequence stratigraphy of the Saharan Platform, Algeria. In: Macgregor, D.S., Moody, R.T.J.,

Gao, D., 2013, Integrating 3D seismic curvature and curvature gradient attributes for fracture detection: Methodologies and interpretational implications: Geophysics, 78, no. 2, O21–O31

Haddoum, H., Guiraud, R., Moussine Pouchkine, A., 2001. Hercynian compressional deformations of the Ahnet-Mouydir Basin, Algerian Saharan platform: far-field stress effects of the late palaezoic orogeny. Terra Nova 13, 220–226.

Healy, D., Rizzo, R.E., Cornwell, D.C., Farrell, N.J.C., Watkins, H., Timms, N.E., Gomez-Rivas, E. & Smith, M., 2017. FracPaQ: a MATLAB™ toolbox for the quantification of fracture patterns. Journal of Structural Geology, 95, pp1-16.

Issad M., 2003. Structural model of Bahar El Hamar. Rapport Interne Sonatrach.

Issad M, Amia, Z., Djezzar, S., Mahiedine, D., Brahimi, F., Doussas, N., Goucem N., 2011. Reevaluation du potential petrolier du basin du Mouydir. Rapport Interne Sonatrach.

Klein, P., Richard, L., and James, H.,(2008). 3D curvature attributes: A new approach for seismic interpretation. EAGE, First Break, Volume 26.

Legrand, Ph., 1962. Comparaison des séries Cambro-Ordoviciennes reconnues en affleureument dans la région d'Amguid et en forage au centre du basin saharien occidental. Bulletin de la Société Géologique de France 7 (IV), 132–135.

Legrand, Ph., 1985. Lower Palaeozoic rocks of Algeria. In: Holland, C.H. (Ed.), Lower Palaeozoic of North-Western and West-Central Africa. John Wiley and Sons, New York, pp. 6–84.

Legrand, Ph., Nabos, G., 1962. Contribution à la stratigraphie du Cambro-Ordovicien dans le bassin saharien occidental. Bulletin de la Société Géologique de France 7, 123–131.

Liégeois JP, Benhallou A, Azzouni-Sekkal A, Yahiaoui R, Bonin B, 2005. The Hoggar swell and volcanism: reactivation of the Precambrian Hoggar shield during Alpine convergence and West African Cenozoic volcanism. In: Foulger, GR, Natland, JH, Presnall, DC, Anderson, DL (Eds), Plates, plumes and paradigms Geol Soc America Spec, Paper, vol. 388, pp. 379–400

Liégeois JP. 2019. A New Synthetic Geological Map of the Hoggar Shield: An Overview of Its Global Structure and Geological Evolution. In: The Geology of the Arab World-An Overview, A. Bendaoud et al. (eds.), Springer Geology, pp. 83-107

Lisle, R.J., 1994, Detection of zones of abnormal strains in structures using Gaussian curvature analysis: AAPG Bulletin, v. 78/12, p. 1811-1819

Long, J.C.S., Remer, J.S., Wilson, C.R., Witherspoon, P.A., 1982. Porous media equivalents for networks of discontinuous fractures. Water Resour. Res. 18 (3), 645-658.

Lounissi, R., 1992. Hydrogéologie du Mouydir. Rapport Interne Sonatrach.

Mandelbrot, B. 1975. Les objets fractals Flammarion, (Ed.), Paris, 212p.

Mandelbrot, B. 1982. The Fractal Geometry of Nature Freeman (Ed.), San Francisco, 461p.

Manzocchi, T., 2002. The connectivity of two-dimensional networks of spatially correlated fractures. Water Resour. Res. 38 (9).

Markovaara-Koivisto, M., Laine, E., 2012. MATLAB script for analyzing and visualizing scanline data. Comput. Geosci. 40, 185e193.

Mauldon, M., Dunne, W.M., Rohrbaugh, M.B., 2001. Circular scanlines and circular windows: new tools for characterizing the geometry of fracture traces. J. Struct. Geol. 23 (2), 247-258.

Mokhtari, N., Mahdjoub, Y., Djezzar, S., 2016. Fracture characterization in the flat laying domain: Tassili N'Ajjer, SE Algeria. The First Arab Geosciences Union (ArabGU) International Conference (AIC-1), USTHB, Algeria.

Moore, D.E., Lockner, D.A., 1995. The role of microcracking in shear-fracture propagation in granite. J. Struct. Geol. 17 (1), 95-114.

Oda, M., 1983. A method for evaluating the effect of crack geometry on the mechanical behavior of cracked rock masses. Mech. Mater. 2 (2), 163-171.

Odling, N.E. Gillespie, P. Bourgine, B. Castaing, C. Chilés, J.P. Christensen, N.P. Fillion, E. Genter, A. Olsen, C. Thrane, L. Trice, R. Aarseth, E. Walsh, J.J. Watterson. J.1999. Variations in fracture system geometry and their implications for fluid flow in fractured hydrocarbon reservoirs Petroleum Geoscience, 5 (1999), pp. 373-384

Pecten Algeria Company (1992): Exploration potential of the district 6/2 convention area Algeria

Porteous, W.G., 1973. A breccia pipe in the Dalradian series, East Kincardineshire. Scott. J. Geol. 9 (3), 233-237.

Rabai, G., Benbakhti I., Djemai, S., Djezzar, S., 2016. Lower Devonian reservoirs of the northeastern part of Reggane Basin: Structure and hydrocarbon potential. The First Arab Geosciences Union (ArabGU) International Conference (AIC-1), USTHB, Algeria.

Rives, T., Razack, M., Petit, J.P., Rawsley, K.D., 1992. Joint spacing: analogue and numerical simulations. Journal of Structural Geology 14 (8–9), 925–937.

Rizzo, R.E., Healy, D. & De Siena, L. (2017a). Benefits of a Maximum Likelihood Estimator for fracture attribute analysis. Journal of Structural Geology, 95, pp.17-31.

Rizzo, R. E., Healy, D., Farrell, N. J., & Heap, M. J. (2017b). Riding the right wavelet: Quantifying scale transitions in fractured rocks. Geophysical Research Letters.

Roberts, A., 2001, Curvature attributes and their application to 3-D interpreted horizons: First Break, v. 19/2, p. 85-100

Rohrbaugh Jr., M.B., Dunne, W.M., Mauldon, M., 2002. Estimating fracture trace intensity, density, and mean length using circular scan lines and windows. AAPG Bull. 86 (12), 2089-2104.

Sanderson, D.J., Nixon, C.W., 2015. The use of topology in fracture network characterization. J. Struct. Geol. 72, 55-66.

Segall, P. Pollard, D. 1983.Joint formation in granitic rock of the Sierra Nevada Geological Society of America Bulletin, 94 (1983), pp. 563-575

Schlumberger, 2018. Petrel tutorial.

Suzuki, K., Oda, M., Yamazaki, M., Kuwahara, T., 1998. Permeability changes in granite with crack growth during immersion in hot water. Int. J. Rock Mech. Min. Sci. 35 (7), 907-921.

Vecoli, M., Videt, B., Paris, F., 2008. First biostratigraphic (palynological) dating of Middle and Late Cambrian strata in the subsurface of northwestern Algeria, North Africa: implications for regional stratigraphy. Review of Palaeobotany and Palynology 149 (1–2), 57–62.

Well Evaluation Conference (WEC, 2007). Well Evaluation Conference, Internal report, "Joint documents of Sonatrach and Schlumberger", Algeria, p.489

Wendt, J., Kaufmann, B., Belka, Z., Klug, C., & Lubeseder, S. (2006). Sedimentary evolution of a Palaeozoic basin and ridge system: The Middle and Upper Devonian of the Ahnet and Mouydir (Algerian Sahara). Geological Magazine, 143(3), 269-299.

Woodcock, N.H., 1977. Specification of fabric shapes using an eigenvalue method. Geol. Soc. Am. Bull. 88 (9), 1231-1236.

Zazoun, R.S., 2001. La tectogenèse hercynienne dans la partie occidentale du basin de l'Ahnet et la région de Bled El-Mass, Sahara Algérien: un continuum de déformation. Journal of African Earth Sciences 32 (4), 869–887

Zazoun, R.S., 2008. The Fadnoun area, Tassili-n-Azdjer, Algeria: fracture network geometry analysis. Journal of African Earth Sciences 50 (5), 273–285.

Zeeb, C., Gomez-Rivas, E., Bons, P.D., Virgo, S., Blum, P., 2013a. Fracture network evaluation program (FraNEP): a software for analyzing 2D fracture trace-line maps. Comput. Geosci. 60, 11-22.

Zeeb, C., Gomez-Rivas, E., Bons, P.D., Blum, P., 2013b. Evaluation of sampling methods for fracture network characterization using outcrops. Am. Assoc. Pet. Geol. Bull. 97 (9), 1545-1566.

Zegrir, H. 2014. Distribution de la fracturation dans les reservoirs compacts du Cambro-Ordovicien: Méthodologie d'intégration des données de surface au modèle de sub-surface (Bassin de l'Ahnet-plate forme saharienne-Algérie). Memoire de Magister, Faculté des Hydrocarbures et de la Chimie. Université M'hamed Bougara, Boumerdès, Algérie.

SEGWiki, 2019. www.wiki.seg.org

Zieliński, M., 2011. Reconstruction of thermal history of the Ahnet and Mouydir basins (southern Algeria). PhD thesis, Institute of Geology, Faculty of Geographical and Geological Sciences, Adam Mickiewicz University, Poznan